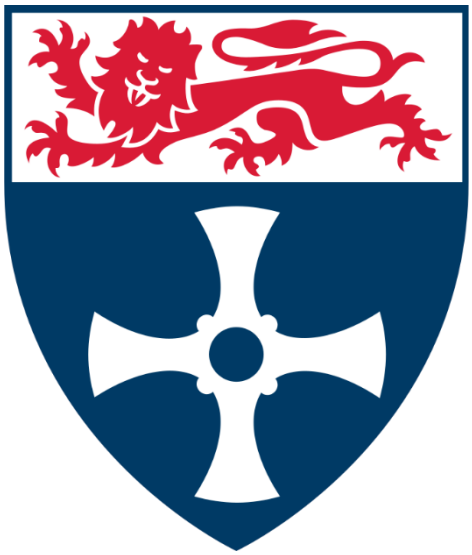

Predictive QSAR tools to aid in early process development of monoclonal antibodies

John Micael Andreas Karlberg

Published work submitted to Newcastle University for the degree of

Doctor of Philosophy in the School of Engineering

November 2019

Abstract

Monoclonal antibodies (mAbs) have become one of the fastest growing markets for diagnostic and therapeutic treatments over the last 30 years with a global sales revenue around $89 billion reported in 2017. A popular framework widely used in pharmaceutical industries for designing manufacturing processes for mAbs is Quality by Design (QbD) due to providing a structured and systematic approach in investigation and screening process parameters that might influence the product quality. However, due to the large number of product quality attributes (CQAs) and process parameters that exist in an mAb process platform, extensive investigation is needed to characterise their impact on the product quality which makes the process development costly and time consuming. There is thus an urgent need for methods and tools that can be used for early risk-based selection of critical product properties and process factors to reduce the number of potential factors that have to be investigated, thereby aiding in speeding up the process development and reduce costs.

In this study, a framework for predictive model development based on Quantitative Structure-Activity Relationship (QSAR) modelling was developed to link structural features and properties of mAbs to Hydrophobic Interaction Chromatography (HIC) retention times and expressed mAb yield from HEK cells. Model development was based on a structured approach for incremental model refinement and evaluation that aided in increasing model performance until becoming acceptable in accordance to the OECD guidelines for QSAR models.

The resulting models showed that it was possible to predict HIC retention times of mAbs based on their inherent structure. Further improvements of the models are suggested due to performance being adequate but not sufficient for implementation as a risk assessment tool in QbD. However, the described methodology and workflow has been proven to work for retention time prediction in a HIC column and is therefore likely to be applicable to other purification columns.

List of publications resulting from this research

Karlberg, M., von Stosch, M. and Glassey, J., 2018. “Exploiting mAb structure characteristics for a directed QbD implementation in early process development.” *Critical reviews in biotechnology*, 38(6), pp.957-970

Kizhedath, A., Karlberg, M. and Glassey, J., 2019. “Cross interaction chromatography based QSAR model for early stage screening to facilitate enhanced developability of monoclonal antibody therapeutics”. *Biotechnology journal*, Accepted

Karlberg, M., Kizhedath, A., Glassey, J., 2019. “QSAR model for Hydrophobic Interaction Chromatography behaviour from primary sequence of monoclonal antibodies”. *Biotechnology Journal*, Submitted

Karlberg, M., de Souza, J., Kizhedath, A., Bronowska, A, Glassey, J., 2019. “QSAR model for Hydrophobic Interaction Chromatography behaviour from 3D structure of monoclonal antibodies”. *Biotechnology Journal*, Submitted

List of conference contributions

Karlberg, M, von Stosch, M, McCreath, G, Glassey, J. “Early Bioprocess development using PAT approaches”, ESBES, Sep 2016, Dublin, Ireland

Karlberg, M, “Exploiting mAb structure characteristics for a directed QbD implementation in process development”, XIII BioProcess UK”, Nov 2016, Newcastle, UK

Karlberg, M, Kizhedath, A., von Stosch, M, Wilkinson, S, Glassey J. “Exploiting mAb structure characteristics for rapid screening and a directed QbD implementation in process development”, ACS Biot 253rd meeting, Apr 2017, San Francisco, USA

Karlberg, M, von Stosch, M, Glassey, J. “Exploiting mAb structure characteristics for a directed QbD implementation in process development”, WCCE ECAB, Oct 2017, Barcelona, Spain

Karlberg, M and Glassey, J. “Exploiting MAB structure characteristics for a directed QbD implementation in process development”, ESBES, Sep 2018, Lisbon, Portugal

Acknowledgements

Many people have supported me during the past three years, and I have greatly enjoyed working with all of them. Especially, I would like to thank my main supervisor and friend, Jarka Glassey for pushing me to always do better and for providing encouragement to keep on going. Without this, I would not have learned as much as I now know today for which I am truly grateful. I would like to thank secondary supervisor Agnieszka Bronowska for showing me the cool world of Molecular Dynamics and the endless potential it holds for use in process development of biologics. I also want to thank Joao Victor de Souza Cunha for taking the time in teaching me the theory and application of Molecular Dynamics which added great value to the project. I also want to thank my former supervisor Moritz von Stosch for all the fruitful discussion on multivariate data analysis.

In the city of Newcastle and at Newcastle University, I would like to thank my friends Arathi, Andre, Ana, Sylvester and Joao, who made every day an adventure. I truly enjoyed coming to university every day.

From Fujifilm Diosynth in Billingham, UK, I would also like to thank the people who supported and helped me during my secondment. I truly appreciate the industrial insight and fruitful discussion that they provided as this clarified the problem statement of this project and encouraged me to continue research on this topic.

I would also like to thank my family and friends in Sweden for their continued support and encouragement when writing up this thesis. During the three years of the project I had the pleasure and honour of becoming godfather to my beloved nephew Gabriel and niece Maja for which I will definitely tell tall tales and stories about my great adventure across the seas.

This project received funding from the European Union's Horizon 2020 Research and Innovation Programme under the Marie Skłodowska-Curie Grant Agreement No 643056 (Biorapid project).

Table of Contents

List of Figures

List of Tables

Abbreviations

Process Development

CMO	Contract Manufacturing Organisation
EMA	European Medicine Agency
FDA	Food and Drug Administration
PAT	Process Analytical Technology
QbD	Quality by Design
QTPP	Quality Target Product Profile
CQA	Critical Quality Attribute
QA	Quality Attribute
CPP	Critical Process Parameter
PP	Process Parameter
FMEA	Failure Mode and Effect Analysis
USP	Upstream Process
DSP	Downstream Process
HIC	Hydrophobic Interaction Chromatography
AEX	Cation Exchange Chromatography
CEX	Anion Exchange Chromatography
BLA	Biologics License Application
MAA	Market Authorisation Application

Antibody Structure

mAb	Monoclonal Antibody
Fab	Antigen-Binding Fragment
Fc	Crystallizable Fragment
V_H	Variable Domain in Heavy Chain
C_H1	First Constant Domain in Heavy Chain
C_H2	Second Constant Domain in Heavy Chain
C_H3	Third Constant Domain in Heavy Chain
V_L	Variable Domain of Light Chain
C_L	Constant Domain in Light Chain
CDR	Complementary Determining Region
FR	Framework Region
VDJ	Variety, Diversity and Joining gene recombination
PTM	Post-Translational Modification

Predictive Modelling and Statistics

QSAR	Quantitative Structure-Activity Relationship
EDA	Exploratory Data Analysis
PCA	Principal Component Analysis
PLS	Partial Least Squares
PLS-DA	Partial Least Squares Discriminant Analysis
SVM	Support Vector Machines
SVC	Support Vector Machines for Classification

SVR	Support Vector Machines for Regression
OvO	One versus One
OvR	One versus Rest
MCC	Matthew Correlation Coefficient
RMSD	Root Mean Square Deviation

Protein Structure Prediction

NMR	Nuclear Magnetic Resonance
Cryo-EM	Cryogenic-Electron Microscopy
BLAST	Basic Local Alignment Search Tool
PSI-BLAST	Position-Specific Iterative – Basic Local Alignment Search Tool
NCBI	National Centre for Biotechnology Information
HMM	Hidden Markov Model
WAM	Web Antibody Modelling
PIGS	Prediction of ImmunoGlobulin Structures
MOE	Molecular Operating Environment
PDB	Protein Data Bank
DOPE	Discrete Optimisation Protein Energy
RMSD	Root Mean Square Deviation
RMSF	Root Mean Square Fluctuation

Protein Dynamics

QM	Quantum Mechanics
TDSE	Time Dependent Schrödinger Equation

MM	Molecular Mechanics
MD	Molecular Dynamics
GPU	Graphical Processing Unit
CPU	Central Processing Unit
HPC	High Performance Computing
PME	Particle Mesh Edwald
PBC	Periodic Boundary Condition
EM	Energy Minimisation
NVT	constant Number of atoms, constant Volume, constant Temperature
NPT	constant Number of atoms, constant Pressure, constant Temperature
ACPYPE	AnteChamber Python Parser
GAFF	General Amber Force Field
HTMD	High-Throughput Molecular Dynamics
RSA	Relative Surface Area
SASA	Solvent Accessible Surface Area
TAE	Transferable Atom Equivalent

Nomenclature

$\boldsymbol{X}$	2-D matrix of independent variables
$\boldsymbol{x}$	1-D row or column vector containing the independent variables for a specific sample or variable, respectively
$\boldsymbol{Y}$	2-D matrix of dependent variables/responses
$\boldsymbol{y}$	1-D input vector of dependent variables/responses
$\boldsymbol{T}$	2-D matrix containing the scores of the $\boldsymbol{X}$ block
$\boldsymbol{t}$	1-D column vector containing the scores of the $\boldsymbol{X}$ block
$\boldsymbol{P}$	2-D matrix containing the loadings of the $\boldsymbol{X}$ block
$\boldsymbol{p}$	1-D row vector containing the loadings of the $\boldsymbol{X}$ block
$\boldsymbol{E}$	2-D matrix containing the residual values of the $\boldsymbol{X}$ block
$\boldsymbol{U}$	2-D matrix containing the scores of the $\boldsymbol{Y}$ block
$\boldsymbol{u}$	1-D column vector containing the scores of the $\boldsymbol{Y}$ block
$\boldsymbol{Q}$	2-D matrix containing the loadings of the $\boldsymbol{Y}$ block
$\boldsymbol{q}$	1-D row vector containing the loadings of the $\boldsymbol{Y}$ block
$\boldsymbol{W}$	2-D matrix of weights used in PLS and PLS-DA
$\boldsymbol{w}$	1-D row vector of weights used in PLS and PLS-DA
$\boldsymbol{H}$	2-D matrix containing the residual values of the $\boldsymbol{Y}$ block
$d(\boldsymbol{x}_i, \boldsymbol{x}_j)$	Distance between sample i and j
$P(C_c\|\hat{y}_i)$	Posterior probability of being class c given sample i
$P(\hat{y}_i\|C_c)$	Likelihood of sample i belonging to class c
$P(C_c)$	Probability of class c occuring

$P(\hat{y}_i)$	Probability of sample i occuring
$\boldsymbol{\Sigma}$	2-D matrix containing covariance values
$\boldsymbol{V}$	2-D matrix containing eigenvectors
$\boldsymbol{\Lambda}$	Diagonal 2-D matrix containing eigenvalues
$\boldsymbol{\omega}$	1-D row vector containing weights for support vectors
C and λ	Regularisation parameters
ϵ	Insensitive loss
ξ	Slack variable
α and β	Lagrange multipliers

Introduction

Monoclonal antibodies (mAbs) are therapeutic proteins that have gained increasing popularity and importance over the last three decades mainly due to their clinical specificity and safety as treatments, but also because they can be applied to a wide spectrum of different ailments. The Process Analytical Technology (PAT) initiative and the Quality by Design (QbD) paradigm have become an integral part of process development of mAbs in today's pharmaceutical industries with the goal of increasing process understanding and control in order to deliver a consistent product quality (Rathore, 2014, Zurdo et al., 2015). Continuous improvements are constantly being made to increase the effectiveness and applicability of these frameworks for the production of biopharmaceuticals (Glassey et al., 2011). However, many challenges still impede the successful implementation of QbD due to limited process and product understanding in early process development. This has led to an increased need of tools to aid in risk assessment of mAb candidates in order to speed up process development but also to evaluate their manufacturing feasibility.

In the last decade, much focus has been directed to the development of *in silico* methods that can aid in risk assessment and speed up the process development. The Quantitative structure-activity relationships (QSAR) framework, which can use knowledge from previous mAb production processes, appears to be one of the most promising frameworks for the development of predictive tools. The main strength of the QSAR framework is its ability to effectively link structural properties and features of the protein structure, which are commonly known as descriptors, to those of the biological response or mAb behaviour in unit operations. This therefore has the potential of increasing the product understanding of new mAb candidates in early process development by aiding in the risk assessment and process route selection and allowing for a more efficient process development.

The aim of this project was therefore to explore the available methods in the QSAR framework that could be used to address the lack of process and product knowledge in early process development. A list of project objectives has been presented below:

1. Generation and exploration of suitable structural descriptors that can be used for predictive QSAR models.
2. Development of a robust and structured framework with critical evaluation of classification and regression methods to determine their applicability in relevant process development settings.
3. Testing the proposed modelling framework and descriptors generation workflow on relevant process development data. In this research HIC retention times and mAb yields of 137 mAbs was used and acquired from a data set published by Jain et al. (2017).

Thesis structure

The thesis starts with an extensive review of the QbD and QSAR frameworks in Chapter 1. Methodology and implementation of predictive modelling methods and techniques are overviewed in Chapter 2. The remaining chapters of the thesis can logically be divided into two parts based on the methodology used to acquire structural descriptors that were used in the predictive modelling. The first part investigates structural descriptors derived directly from the primary sequence (amino acid sequences) of the mAbs and is described in Chapter 3, Chapter 4 and Chapter 5. The second part investigates structural descriptors derived from the 3D structure of the mAbs and is described in Chapter 6 and Chapter 7.

Chapter 1: Literature Review

The literature review provides a background of the current state-of-the-art in process development of mAbs according to the QbD paradigm. Attrition and current challenges in the paradigm are addressed which mainly originates in the limited knowledge of both the process and product available in early process development. The QSAR methodology was proposed for predictive model development of mAb behaviour in unit operations.

Chapter 2: Modelling Development and Assessment

This chapter provides an overview of the multivariate techniques used in this research to develop and test predictive QSAR models. Examples of successful implementation of these methods and their applicability to specific problems are highlighted and reviewed.

Chapter 3: Primary Sequence-based Descriptors

In this chapter the structure and sources of sequence variation in a mAb are assessed and reviewed. The methodology for generating descriptors based on the primary sequence is presented with the corresponding software used in this research.

Chapter 4: Impact of mAb isotypes and species origins on primary sequence-based descriptors

The generated descriptors from Chapter 3 are investigated with exploratory methods with regards to structural variations related to the heavy and light chain isotype as well as the species origins. This provided insight into sources of variations that were present in the primary sequence-based descriptors sets and was used for identifying systematic structural variation that negatively impacted model performance in Chapter 5.

Chapter 5: QSAR model development: Primary sequence-based descriptors

In this chapter the applicability of the primary sequence-based descriptors in predictive modelling of HIC retention times and mAb yields was assessed. A statistical analysis investigating the impact of the heavy and light chain isotypes as well as species origins on the two responses was performed. The statistical analysis coupled with the exploratory analysis in Chapter 4 was used as a foundation for sample selection in order to reduce systematic variation in the descriptors that was detrimental to the performance of the developed models.

Chapter 6: 3D Structure Descriptors

In this chapter a methodology for generating descriptors from the 3D structure of mAbs is presented. To this end, methods for generating 3D structures from the primary sequence is assessed as well as options for protein dynamics simulations for structure relaxation and modifications are reviewed and covered in detail.

Chapter 7: QSAR model development: 3D Structure Descriptors

The applicability of the 3D structure descriptors from Chapter 7 is assessed in predictive modelling of HIC retention times and mAb yields. Exploration of structural variations related to the light chain isotypes as well as the species origins are performed to investigate potential systematic variation that may be detrimental to the performance of the developed models. A comparison between models developed using the primary sequence-based descriptors and the 3D structure descriptors was carried out to evaluate their applicability in an industrial setting.

Chapter 8: Conclusion and Future Perspectives

This chapter concludes the work presented in this thesis as well as providing suggestions for improvement with regards to both predictive modelling and descriptor generation for future applications.

Chapter 1

Literature review

1.1 Antibody Market

The increasing popularity of mAbs can be seen in Figure 1.1a where the number of approved mAbs by the European Medicine Agency (EMA) in EU (blue line) and the Food and Drug Administration (FDA) in US (green line) has drastically increased over the last 30 years (ACTIP, 2017, May 15, Reichert, 2012). In the last five years a new trend has emerged where manufacturing of generic mAbs, known as biosimilars, has gained more attention due to the expiration of patents on mAbs introduced to the market earlier. The first biosimilar of infliximab (better known as Remicade) was first approved and then marketed in 2013 by the EMA and later approved by FDA in 2016, thus opening the door for manufacturing of generic mAbs. As of 2017, a total number of 11 biosimilars has been approved by either EMA, FDA or both. These are biosimilars of infliximab, adalimumab, trastuzumab and rituximab (Grilo and Mantalaris, 2019). A list of currently approved mAbs is presented in Table A.1 in Appendix A.

The market sales have enjoyed an increasing growth ever since the first mAb was launched in 1986. Recent reports on the mAb market show an increase in revenue from around $39 billion in 2008 to around $89 billion in 2017 illustrated in Figure 1.1b, making mAbs one of the fastest growing bioproduct groups (Ecker et al., 2015, Grilo and Mantalaris, 2019). The market is expected to grow further with a predicted worldwide revenue of between $130-200 billion by 2022 (EvaluatePharma®, 2018, Grilo and Mantalaris, 2019).

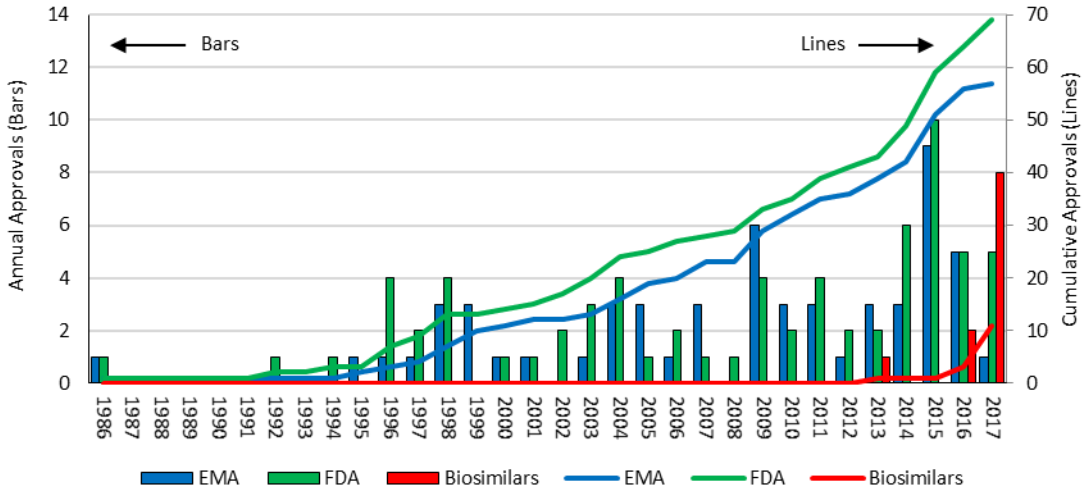

(a)

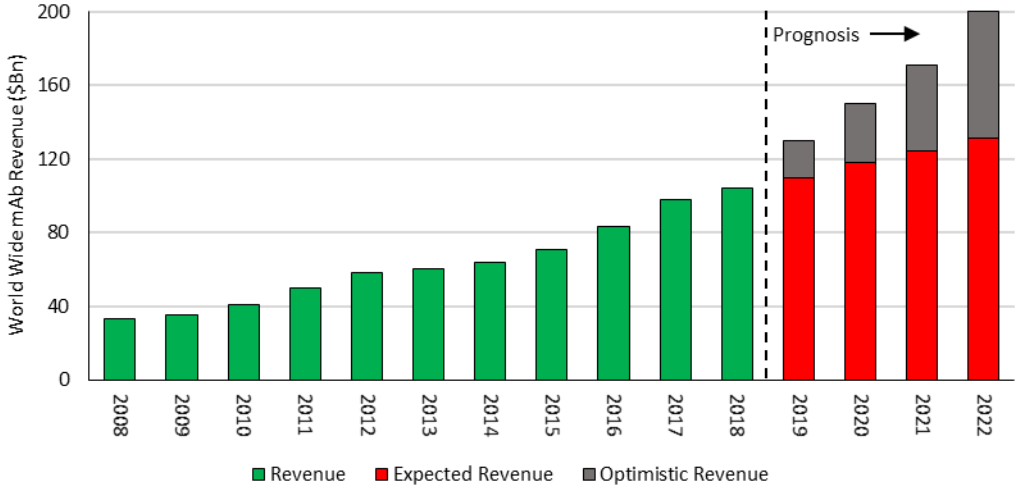

(b)

Figure 1.1. Approval and market trends of mAbs. **(a)** History of approved mAbs by EMA (blue) and FDA (green) annually (bars) and cumulative (lines) as well as approved biosimilars by either EMA, FDA or both shown in red. **(b)** History of market revenue from 2008 to 2018 (green bars) and prognosis of the expected market revenue between 2019 and 2022 (red bars) where an optimistic revenue prognosis has been included (grey bars). Based on market data from EvaluatePharma® (2018) and Grilo and Mantalaris (2019).

Due to their popularity and market revenue, many advances in improving the mAb manufacturing processes have been made including process optimisation (Fischer et al., 2015, Kunert and Reinhart, 2016) and process control (Karst et al., 2017). Frameworks, such as QbD, have gained popularity during recent years due to their ability to expedite the process development of mAbs through increased process understanding (Rathore et al., 2018). However, the manufacturing of mAbs is cost-intensive due to the high product quality and regulatory requirements that must be met to make the product clinically safe. This is especially pronounced in the downstream processes due to the need of high product purity of the end product (Hammerschmidt et al., 2014, Hou et al., 2011). Industries still struggle with the development of the manufacturing processes due to high complexity of both the underlying

biological system and the behaviour of the mAb molecules, which hampers the implementation of PAT and QbD (Krummen, 2013, Mercier et al., 2014). In particular, the sensitivity of the product quality in mAbs to changes in the processing conditions requires a high level of understanding of the product and process in order to implement effective control. There is thus an increased need for better tools to aid process development. Due to its popularity in pharmaceutical industries, the QbD framework is reviewed in detail in this chapter and some of its limitations and challenges are highlighted.

1.2 State of the Art in mAb manufacturing

In 2004, FDA introduced a new regulatory initiative called Process Analytical Technology (PAT) with the aim to design and develop well understood processes that consistently ensure a predefined quality of a drug at the end of the manufacturing process (U.S. Department of of Health and Human Services, 2004). The PAT principles are used to gain information relating to physical, chemical and biological attributes of the product to increase process understanding to create a foundation for the implementation of monitoring, optimisation and control of the process (Glassey et al., 2011). The QbD paradigm was introduced in 2004 and is a systematic approach that aligns with the PAT principles and aims to build quality into the product through product and process understanding. The framework is especially useful for process development of mAbs, which consists of many different steps (unit operations). A typical mAb process can be divided into two parts: The upstream (USP) or the cell culture where the mAbs are expressed and the downstream (DSP) or purification where the mAbs are isolated and contaminants removed. Typically, a mAb process will consist of between 15-20 different unit operations which must be characterised in order to deliver consistent quality and safety of use (Rathore et al., 2018). The guideline for implementation of QbD is outlined in the International Conference on Harmonisation Guidelines: ICH Q8 (ICH Harmonised Tripartite Guideline, 2009), ICH Q9 (ICH Harmonised Tripartite Guideline, 2005) and ICH Q10(ICH Harmonised Tripartite Guideline, 2008). The general outline and the nomenclature of the QbD methodology are illustrated in Figure 1.2 and is discussed further in this chapter.

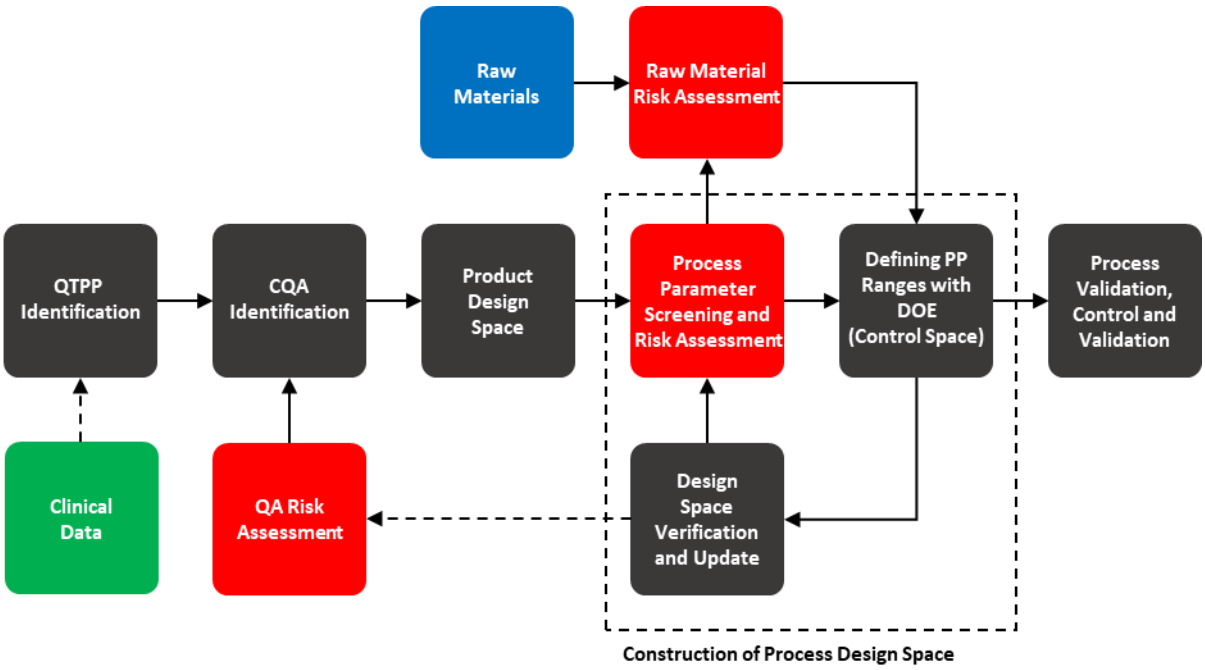

Figure 1.2. General outline of the QbD methodology. The process design space is shown as the dashed box where the effects of process parameters and raw material input (blue box) on the product quality is characterised. Steps highlighted in red indicate risk assessment of either product quality attributes, process parameters or raw materials. The green box indicates availability of clinical data which can be used to better define the QTPP (adapted from Chatterjee (2012)).

1.2.1 Implementation of QbD

The implementation of QbD starts by defining the Quality Target Product Profile (QTPP) which forms the basis of the design for the development and contains information about the drug quality criteria such as delivery mechanisms, intended use, route of administration for the intended product to ensure clinical safety and efficacy. The QTPP is generated from knowledge based on literature research, clinical trials and existing experience from industry or academia (Herwig et al., 2015, Rathore, 2014). For mAbs, the QTPP relates to the product's intended use and properties that can affect patients and need to be clearly stated in order to avoid adverse effects in patients. These should include antigen binding, pharmacokinetics, effector function, stability and half-life of the mAb (Rathore, 2009, Alt et al., 2016). However, much of this information does not become available until later when clinical data has been obtained. Thus, instead many aspects of the QTPP are based on prior knowledge in early process development of an mAb. Recently, computational prediction and simulation of the mAb structure have been shown to be a valuable tool for mAb design due to their ability to provide estimates of behaviour and protein stability which can aid in more accurate QTPP specification (Yamashita, 2018, Tiller and Tessier, 2015).

Based on the QTPP, the Critical Quality Attributes (CQAs) are identified from a list of Quality Attributes (QAs) using risk-based analysis in accordance with the ICH Q9 guideline to

investigate properties that might affect product quality. The CQAs are physical, chemical or biological properties of the drug product that need to be within appropriate ranges to ensure the desired product quality. These ranges, similarly to the generation of QTPP, are obtained through literature research, clinical data and previous experience but they are also updated during the process development as new information from characterisation studies becomes available. The most frequently used method for risk assessment in industries is Failure Mode and Effect Analysis (FMEA) where the impact of different unit operations in the process on the QAs are listed. Each effect is ranked according to a Severity rating (S), an Occurrence rating (O) and a Detectability rating (D). A final Risk Priority Number (RPN) is calculated by multiplying the ratings which are then ranked to identify the effects that potentially affect the product quality and efficacy (Zimmermann and Hentschel, 2011, Harms et al., 2008). Tailored risk assessment methods have also been proposed for biopharmaceuticals by Zalai et al (2013) where the authors argued that traditional methods do not take into account the "complexity" of how a process might affect the product or the "uncertainty" which includes the quality of the input material as a possible source of risk and which need to be added as additional factors to the risk assessment (Zalai et al., 2013). A list of potential CQAs adapted from the work of Alt et al (2016) is presented in Table 1.1 which gives a non-exhaustive overview of the different structural variants that can occur in mAbs and can affect their structure, stability and activity. It is therefore important that the CQAs are controlled in order to achieve the desired product quality (Alt et al., 2016).

All categories of variants in Table 1.1, except the "structure" category, are caused by so-called post-translational modifications (PTMs). This means that modifications of the protein structure occurs after the mAb has been expressed in the cells and which are therefore highly dependent on the environment (Yang et al., 2013). For clarification, a few of the PTMs are described in more detail. The low molecular weight species (LMW) is an incomplete mAb structure where a part or parts of the structure are missing. This is most commonly caused by missing disulphide bonds between chains (see Section 3.1 for description of mAb structure) or enzymatic/non-enzymatic cleavage of the amino acid sequence (Wang et al., 2018). Additionally, if cleavage occurs at the C-terminal residue, which is most often a lysine in mAbs, a basic charge variant will be produced as well, due to loss of a basic residue. However, other charge variants can still occur without the sequence cleavage. For example, deamidation of sterically free asparagine into aspartate is one such PTM which is promoted if the asparagine is followed by a glycine (Khawli et al., 2010). It is important to remember that the majority of the PTMs require the site or the residue that is modified to be accessible on the surface of the mAb structure and therefore in contact with the solvent (Sydow et al., 2014). It should be noted that Table 1.1 does not take

into consideration the quality of the input material and its effect on the product quality as well as various process related QAs, such as contaminants e.g. host cell proteins (HCPs) and DNA, which also need to be characterised.

Table 1.1. List of potential CQAs related to common structural variants in mAbs (adapted from Alt et al. (2016)).

Category	**Quality Attribute**
Size related	High Molecular Weight Species (HMWs)
	Low Molecular Weight Species (LMWs)
Acidic Charge Variants	Deamidation in CDRs regions
	Deamidation in non-CDR regions
	Glycation in CDR regions
	Glycation in non-CDR regions
Basic Charge Variants	Aspartic Acid isomerisation in CDR regions
	Aspartic Acid isomerisation in non-CDR regions
	C-terminal Lysine cleavage
	N-terminal leader sequence
	N-terminal pyroglutamic acid
Oxidation	Oxidation of Methionine and Tryptophan in CDR regions
	Oxidation of Methionine in non-CDR regions
Fc Glycosylation	Afucosylation
	Galactosylation
	High-Mannose
	Sialylation
	Non-glycosylated Heavy chain
Structure	Cysteine variants
	Sequences variants
	Protein structure

Once the CQAs have been selected, a process design space is defined by screening process parameters (PPs) for each of the unit operations in the process that have a significant effect on the CQAs. PPs that have a significant impact on the CQAs are called Critical Process Parameters (CPPs) and are identified and controlled through the use of the following steps:

1. Similar to identification of CQAs, risk analysis methods, such as FMEA, are used to reduce the large number of PPs to those that may affect CQAs.
2. Systematic experimental studies using Design of Experiments (DoE) over a range of PP settings are carried out in small scale to obtain experimental data for process characterisation to identify CPPs and their optimal ranges which. This is referred to as the control space.

3. Multivariate data analysis (MVDA) is used for implementation of appropriate real-time monitoring and control strategies needed for the defined CQAs and CPPs to ensure product quality. Movement outside of the defined control space would cause the product quality to drop below that of the desired quality stated in the QTPP.

The use of statistical DoE is preferred in process development of pharmaceuticals over univariate analysis as it can generate qualitative and quantitative information about important process parameters and their impact on the product quality (Leardi, 2009). Response Surface Modelling (RSM) and leverage plots are often used on generated DoE data to investigate the significance of PPs on the explored CQAs as well as define allowed ranges for the identified CPPs (Rathore, 2016). Several different experimental designs exists and selecting an appropriate design is critical in order to maximise the information gained from the experiments. Kumar et al. (2014) compared different experimental designs for the DoE of downstream unit operations to demonstrate how these affect the response surface of each unit operation (Kumar et al., 2014). Tai et al. (2015) showed that a well-chosen experimental design can lead to diverse and informative data about the system and when combined with high-throughput experimentation techniques, can be a powerful tool when defining the process design space.

Process validation is performed when the design space has been characterised to demonstrate that the desired product quality is delivered when operated within the design space and is usually performed on larger scale. In order to ensure consistent quality, the CQAs need to be within the defined control space of the process. This is done through monitoring and control of identified CPPs that have a dynamic behaviour and effect on the CQAs e.g. pH, temperature, flow rates etc. (Read et al., 2010, Golabgir et al., 2015). MVDA methods such as Principal Component Analysis (PCA) and Partial Least Square (PLS) are commonly employed in order to monitor and control CQAs (Ferreira and Tobyn, 2015). For examples of MVDA implementations for monitoring and control, refer to "modelling based approaches" under Section 1.2.3. However, implementation of monitoring and control strategies is usually not necessary for all CPPs e.g. trace elements in the basal media might need to be characterised, depending on the product, to achieve the desired product quality, but they do not necessarily need to be monitored in real time. The control of the CPPs should always be in the form of a dynamic control scheme to ensure that product quality is kept constant, even if there is variability introduced by the input raw materials used in the process. The QbD framework is an iterative process where the QTTP, CQAs and CPPs need to be constantly revaluated in order to characterise all sources of variability that can impact the final product quality.

As mentioned previously, many aspects of the QTPP might not be known in early process development and only become available once clinical trials have been performed. This means that the process development is closely linked to the clinical phases, as illustrated in Figure 1.3. Once clinical data becomes available, better decisions regarding the potential redesign of the product and re-evaluation of the QTPP, CQAs and CPPs can be made (Cooney et al., 2016). A short summary of investigation goals and scope of each trial phase is presented in Table 1.2 which was based on the ICH E8 guidelines for clinical trials (ICH Harmonised Tripartite Guideline, 1997a).

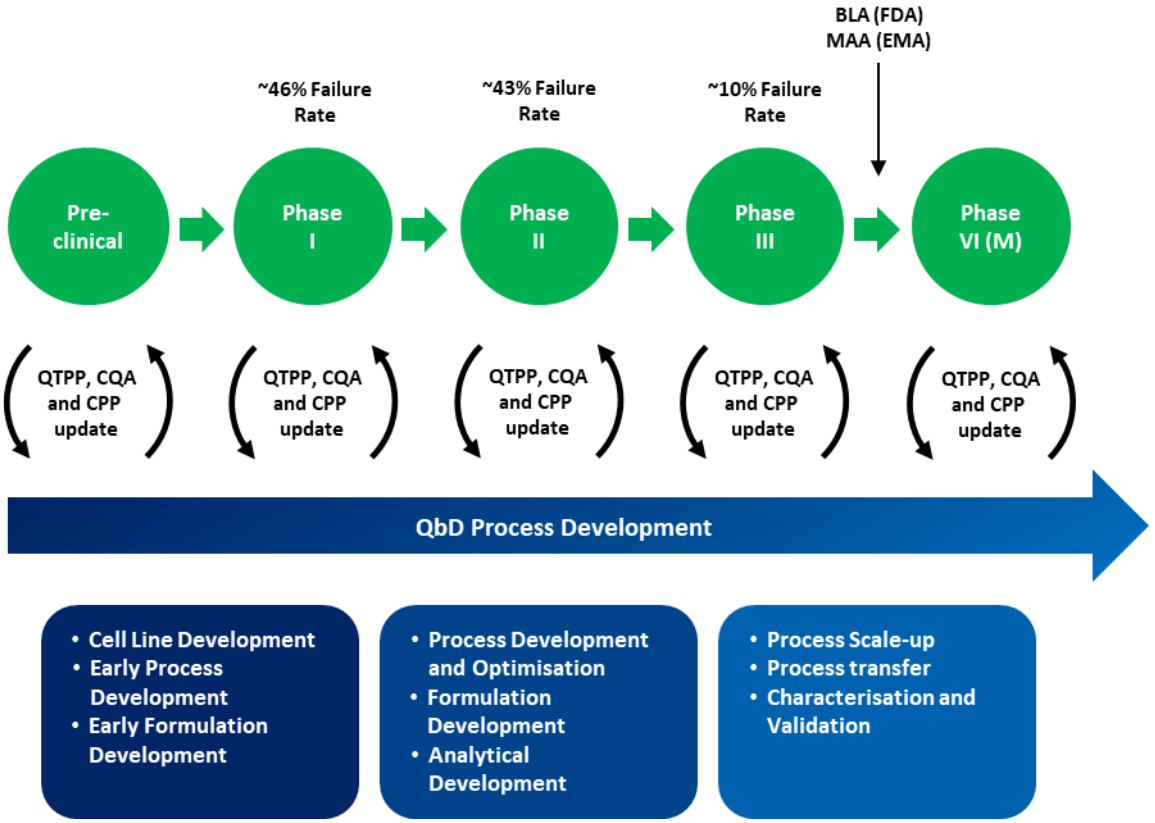

Figure 1.3. Overview of the parallelisation between the clinical trials and the process development (adapted from Li and Easton (2018) as well as Mercier et al. (2013))

Generally, early process development always starts in small scale and is subsequently scaled up as the mAb advances through the different clinical phases which provides two benefits: 1) it provides an economic safety if the mAb product fails in the clinical trial and termination of the drug candidate is likely, 2) it is more cost-effective due to the early clinical trials (pre-clinical and phase I) not requiring large quantities of the mAb for clinical testing. Process knowledge gained from earlier trials is used to build a foundation of process understanding and is applied when scaling up the process which aids in reducing uncertainty in subsequent process characterisation steps. Control and monitoring strategies for characterised CQAs and CPPs also starts to be implemented in Phase II and III (Li and Easton, 2018). If a mAb passes Phase III in

the clinical trials, enough evidence is usually available to start a Biologics Licensing Application (BLA) in the US or a Market Authorisation Application (MAA) in the EU. The process is then transferred to full production, which is also known as Phase VI or manufacturing phase and is implemented according to Good Manufacturing Practice (GMP). Additional clinical data is gathered after the mAbs have been marketed in order to investigate additional adverse effects that were not apparent during the Phase I to Phase III.

Table 1.2. Overview of the clinical phases for an mAb candidate with their corresponding research goals and scope (adapted from the ICH E8 guidelines).

Phase	**Goals**	**Scope**
Pre-clinical	Animal Testing Assessment of safety Estimation of biological activity	Laboratory and animal studies
I	human Pharmacology Assessment of tolerance and safety Estimation of biological activity Estimation of pharmacodynamics and pharmacokinetics.	20-100 (healthy or with disease/condition)
II	Therapeutic Exploratory Estimate dosage for subsequent studies Further assessment of safety and efficacy Side effects	Hundreds (with condition/disease)
III	Therapeutic Confirmatory Confirmation of efficacy Establish safety profile Establish dose-response relationship Provide basis for benefits and risks to support licensing	300-3000 (with condition/disease)
VI (M)	Therapeutic Use Refine understanding of benefits and risks Identify less common side effects Refinement of dosage	Thousands (with condition/disease)

Throughout the process development it is important to note that scale-up can have an impact on the product quality. More generally, CPPs that have been identified to have an effect on product quality in small scale might not necessarily have that same effect in larger scale and may therefore impact the product quality differently. This was thoroughly investigated in the works of Le et al. (2012) and Mercier et al. (2013), where scale dependent effects on CPPs were characterised and had a significant effect on the product quality. This shows that the importance and the ranges of CPPs determined in smaller scales cannot necessarily be transferred to larger scales directly. Consequently, this implies that characterisation of these CPPs needs to be performed every time the scale is increased.

A case study of QbD implementation was published in 2009 by CASSS and ISPE on A-mAb bioprocess development (CASSS and ISPE, 2009). The study gave a broad overview from identification and risk assessment of CQAs to the construction of the design space for both upstream and downstream unit operations. It presented a systematic approach to designing a well-controlled process which assures high product quality and has been used as a foundation for applying the QbD framework to other biopharmaceutical products. Further details on the implementation of QbD in biopharmaceutical manufacture can be found in literature (Rathore and Winkle, 2009, Rathore, 2009, Rathore, 2014, Sadowski et al., 2016).

1.2.2 Challenges in QbD implementation

Effective implementation of QbD and PAT is still a significant challenge in biopharmaceutical industries due to the complex relationships between PPs and product quality. This becomes more apparent when considering the potential structural variants presented in Table 1.1 that commonly occur during the process development. It is therefore important that sources causing structural variability are investigated in order to minimise the risk of harmful effects on patients. However, this requires extensive experimental studies to characterise the CPPs and ranges (Eon-Duval et al., 2012, Mercier et al., 2014).

The glycan in the mAb structure is a good example of this due to being very important for the efficacy and stability of the protein. It is therefore important to determine the impacting factors which need to be monitored and controlled, but this proved to be challenging (Boyd et al., 1995, Raju and Jordan, 2012, Costa et al., 2014). It has been shown that the glycan structure can be controlled through changing the composition of the basal and feed media (Kildegaard et al., 2016, Rathore et al., 2015) or optimisation of the mammalian cell line used for expression (del Val et al., 2010) in order to drive the glycosylation towards the desired structure.

As previously described, heuristic approaches are often used by industries for process development based on experience gained from previous process implementations. However, these rarely succeed in delivering good correlation between PPs and QAs (Zalai et al., 2015). An example of this was the QbD application filing of the mAb Perjeta (pertuzumab) at the end of 2012 by Genentech & Roche (Krummen, 2013). This application was rejected due to the design space not being properly characterised as demonstrated by the following:

1. Not all CQAs, such as the effect of different glycosylation patterns on the Antibody-Dependent Cell-mediated Cytotoxicity (ADCC) which introduced residual clinical risks from different glycosylation variants, were identified. This was mainly due to the

previous ranges from an existing mAb process being used and other CQAs not being considered.

2. Not all CPPs were identified and the effects on the glycosylation profile could not be determined.
3. The proposed control strategy for the CQAs was not appropriate.

Another challenge for pharmaceutical industries is the high failure rates of mAb candidates in the clinical trials coupled together with the high development costs. DiMasi et al. (2016) state that the failure rates of all mAb candidates in the clinical phases I, II and III were around 46%, 43% and 10%, respectively, as illustrated in Figure 1.3. An estimation of total investment needed for a mAb to reach the market was calculated to be around $2.558 billion which includes purchase of necessary equipment and facilities. Of this, $1.098 billion was expected to be invested in the pre-clinical phase and includes discovery and testing of several candidates. The remaining $1.460 billion is invested in the process development and clinical trials (Figure 1.3). This means that the revenue of successful mAb candidates is used to drive the development of other potential candidates making the approved mAbs usually very expensive for the consumer. There is therefore a growing need for additional tools to aid in both clinical assessment and process development of mAbs in order to bring development costs and times down.

1.2.3 Current Focus and Improvements in Process Development

To address the challenges presented in Section 1.2.2, many different approaches and advances have been developed as briefly discussed in the following sections.

Cell-line and media considerations:

Grainger and James (2013) argued that a cell line selection should include product quality such as the glycosylation and not focus only on cell growth and product yield. They illustrated the possibility of choosing cell line and customising the media to achieve high product quality. However, as the glycosylation is cell line specific, no one media composition fits all, but needs to be characterised for each cell line which requires a significant number of experiments. Bruhlmann et al. (2015), who investigated the effects of media supplements on QAs of mAbs (i.e: post-translational modifications such as glycosylation, glycation, deamidation, isomerisation, oxidation, aggregation, LMW species, C- and N-terminal modifications) argued, that media development could greatly increase the quality of the product without the need for extensive cell line engineering. However, the number of media components that need to be characterised requires extensive experimentation to understand the impact of the components on the CQAs. In the case of Genentech & Roche, not carrying out exhaustive studies or risk

assessment analysis to identify CQAs and CPPs had a negative impact on the process understanding of how the CPPs affected the CQAs, e.g. the effect of the glycosylation profile. Due to these reasons the highest level of PAT and QbD in the form of product and process understanding for complex pharmaceuticals has not been reached yet (Mercier et al., 2014).

High-throughput approaches:

Sustained effort has gone into the development of more efficient high-throughput screening methods for both upstream and downstream processing to reduce use of resources, costs and to speed up process development (Bhambure et al., 2011). This includes high-throughput screening of cell lines across different fed-batch scales (Rouiller et al., 2016), high-throughput media development for increased cell growth, viability and product yield for both basal and feed media (Rouiller et al., 2013), high-throughput screening of basal media and feed component effects on post-translational modifications (Rouiller et al., 2014), high-throughput process development in upstream by using parallel small scale reactor systems (Tai et al., 2015), model-based high-throughput screening to find optimal ion exchange chromatography columns by using both mechanistic models and experimental designs to bring down the amount of experiments (Khalaf et al., 2016) or high-throughput screening of an ion chromatography step for process characterisation (Bhambure and Rathore, 2013).

DSP platform orientation and streamlining:

Over the last decade, the mAb DSP have become more platform oriented and also shifted towards continuous processing in order to reduces bottlenecks in production. Several purification strategies used by large pharmaceutical companies, such as Amgen (Shukla et al., 2007), Genentech (Trexler-Schmidt et al., 2009), Biogen (Ghose et al., 2013) and KBI Biopharma (Shukla et al., 2017), indicate a general layout of the DSP platforms for mAbs that are very similar, as illustrated in Figure 1.4.

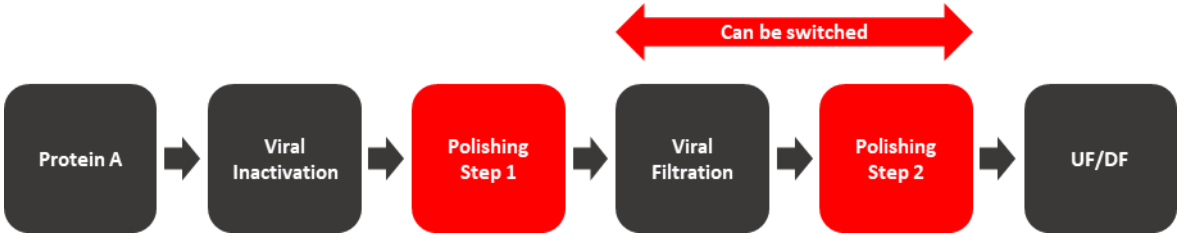

Figure 1.4. General overview of platform-oriented purification of mAbs. The black boxes represent chromatographic columns and steps that are always included, whereas the red boxes represent chromatographic polishing steps that change depending on the behaviour and quality requirements of the mAb. The order of the second polishing step and the viral filtration can be switched (adapted from Shukla et al. (2017)) .

As illustrated in Figure 1.4, Protein A chromatography is used almost exclusively as the first step in the DSP due to its high specific binding to IgG1, IgG2 and IgG4 mAbs where the protein A ligand binds primarily to the region between the CH2 and CH3 domains in the Fc part of the antibody (see section 3.1 for more information on the antibody structure). Due to its high binding specificity towards mAbs, protein A chromatography is able to remove the majority of impurities such as HCPs, DNA and viruses from the cell culture supernatant. A monomeric mAb purity between 90-95% can thus be expected in many cases where protein A chromatography has been used (Shukla et al., 2007). Elution of the mAbs from the protein A column is performed by lowering the pH (to 2.5 - 4.0), thereby disrupting the binding between the protein A ligands and the mAbs.

A natural step after the protein A chromatography is the viral inactivation step, as illustrated in Figure 1.4, due to the low pH which effectively inactivates enveloped virus particles. An important factor in this step is the hold time which is usually around two hours in order to inactivate the majority of the retained virus particles (Mattila et al., 2016). However, it has been shown that low pH can promote aggregation of mAbs and it is therefore important to thoroughly characterise both the protein A chromatography step and the viral inactivation step in order to minimise the loss of mAb product (Mazzer et al., 2015).

Additional chromatographic steps, also known as polishing steps, are used after the viral inactivation for further removal of contaminants and undesired mAb variants. However, selection of chromatographic columns for polishing is very dependent on the characteristics of the desired mAb product and remaining contaminants in order to maximise retention of the final drug product. Commonly used columns are cation exchange chromatography (CIEX) and anion exchange chromatography (AIEX) which can separate mAb variants according to charge and weight as well as facilitate the additional removal of HCPs, DNA and viruses (Liu et al., 2010). More specifically, the CIEX column contains ligands that are negatively charged and bind more efficiently to positively charged proteins, whereas the AIEX column contains positively charged ligands which bind more efficiently to negatively charged proteins. Therefore, depending on the charge of the mAb, the column can be selected to promote binding. Another commonly used polishing step is a hydrophobic interaction chromatography (HIC) which can be used to reduce high molecular weight species and host cell proteins. The HIC column contains hydrophobic ligands that bind to hydrophobic patches on the surface of the protein. The binding is promoted further by adding salts, such as ammonium sulphate, that lower the protein stability and allow for hydrophobic residues to surface (Gagnon, 1996a).

The viral filtration step illustrated in Figure 1.4 is performed to remove the majority of the remaining viral particles from the product in order to reduce the risk of viral infection in patients (ICH Harmonised Tripartite Guideline, 1997b). This step is placed towards the end of purification in order to avoid fouling of the filtration membrane as the majority of larger particles, such as aggregates and DNA, have been removed in earlier steps. This allows for the desired mAb product to pass through the membrane while larger virus particles are retained in the membrane pores or on the retention side of the membrane (Kern and Krishnan, 2006). In the final step, ultrafiltration/diafiltration (UF/DF), as illustrated in Figure 1.4 is applied in order to concentrate the final mAb as well as to exchange the buffer for increased stability and shelf life time (Liu et al., 2010).

Modelling based approaches:

The use of MVDA methods for process development and monitoring of QAs increased significantly during the last years. This gives increased insight into correlation between PPs and QAs that might otherwise go undetected. Mercier et al. (2013) showed with PCA and PLS that the scalability had a significant effect on performance which was not considered before. Ivarsson et al. (2015) showed how the metabolic flux inside of the cells shifted with different pH and how it affected growth and production rate by using Flux Metabolic Analysis (FMA) which is especially important in scale-up where compartmentalisation of the reactor is likely to happen. Sokolov et al. (2016) illustrated how process characterisation could be performed for biosimilars with the use of PCA and Decision Trees (DT) on characterisation data to find optimal set points in order to get as close as possible to quality specifics of the originator. Rathore et al. (2015) used PCA and PLS to link PPs and amino acids concentrations in the media to their impact on the glycosylation in batch, fed-batch and fed-batch with microaeration. In a similar study by Green and Glassey (2015), the authors illustrated how the amino acid concentrations in the growth media as well as process parameters could be used to predict the glycosylation forms of mAbs with PLS. Another approach is to use knowledge-based modelling, such as presented by Khalaf et al. (2016) where the authors used mechanistic model whose parameters were estimated from experimental data to create a high-throughput screening of ion exchange columns. This is similar to hybrid modelling in process monitoring and control that is based on mechanistic models but whose parameters are estimated from a DoE data set (Glassey and Von Stosch, 2018). The advantage is that compared to other mechanistic models with static parameters, the hybrid models can dynamically adjust the parameters from the DoE data set (von Stosch et al., 2014). The cause for the slow integration of other MVDA methods

into industries can be speculated, but one of the main reasons is the broadly formulated framework of QbD and the lack of a clear implementation path to follow.

Product understanding:

The fundamental principle of the QbD framework is to increase process understanding in terms of the effect that PPs have on product quality. Zurdo (2013) suggested that the QbD framework needed to be extended to incorporate product understanding in terms of the developability of the pharmaceutical which would include manufacturability, safety, pharmacology and biological activity. The author argued that by using *in silico* risk assessment tools based on structural features of the mAbs and historic development data, predictions concerning manufacturability of an mAb could be made. In a later publication two case studies were presented where structural properties of mAbs were successfully linked to CQAs related to aggregation and half-life (Zurdo et al., 2015). Such tools can add great value to early process development of mAbs when implementing the QbD framework where very little is known about both the process and product. Thus, a more in-depth investigation of Quantitative Structure-Activity Relationship (QSAR) framework and its potential benefits for QbD integration is explored here.

1.3 Quantitative Structure-Activity Relationship

The QSAR framework relates structural properties and features (also known as descriptors) of a compound to biological or physicochemical activity (Dehmer et al., 2012, Dudek et al., 2006). This methodology was first introduced by Hammet in the 1930s and was later refined by Hansch and Fujita and has become a standard tool for small drug discovery (Du et al., 2008). A method derived from QSAR, referred to as Quantitative Sequence-Activity Modelling (QSAM), has been introduced in recent years and focuses on relating structural descriptors of proteins, peptides and nucleic acids to activity (Zhou et al., 2010). The only difference between QSAR and QSAM is the development of descriptors whereas the guidelines for the predictive model development remain the same. Given the proteinaceous character of the mAbs, the QSAM methodology for descriptor generation will be of more relevance and the workflow described below will therefore focus more on protein based rather than small molecule based QSAR.

1.3.1 Descriptor generation

One of the most important steps in QSAR is how the structures of the pharmaceuticals in question can be described numerically in order to use them in correlation studies with prediction outputs of interest. For proteins, such as mAbs, two approaches to generate descriptors are discussed here: 1) descriptors generated from the amino acid primary sequence and 2)

descriptors generated from three-dimensional models of the mAbs. It has been shown that a combination of both physicochemical and 3D structure descriptors works best and also ensures that the model is not overly reliant on a single type of a descriptor (Hechinger et al., 2012).

Amino acid composition-based descriptor generation:

Extensive research has been carried out to develop new informative descriptors for peptides and proteins generated from their primary sequence (Zhou et al., 2008). This was first introduced by Sneath (1966) who derived amino acid descriptors for the 20 naturally occurring amino acids from qualitative data. Later on, Kidera et al. (1985) used 188 properties of the 20 naturally occurring amino acids, which were converted into ten orthogonal new descriptors to describe the amino acids. Later the Z-scale, which consists of 3 new amino acid descriptors derived by applying PCA to 29 physiochemical properties (Hellberg et al., 1986, Hellberg et al., 1987a), was introduced. Other amino acid scales, which were also derived through PCA, include the extended Z-scale and T-scale (Sandberg et al., 1998, Tian et al., 2007). Other descriptors include the so called isotropic surface area (ISA) and the electronic charge index (ECI), which are derived from the 3D structures of the amino acids (Collantes and Dunn, 1995). All these descriptors were tested and performed well in respective studies on small peptides. In a two-part review by van Westen et al (2013a, 2013b) many of the existing amino acid scales were benchmarked and compared. The authors demonstrated that the different scales described different physiochemical and topological properties which is useful when deciding on which scales to use (van Westen et al., 2013a, van Westen et al., 2013b). Doytchinova et al. (2005) applied the Z-scales descriptors to successfully predict ligand binding of peptides and Obrezanova et al. (2015) used several such amino acid scale to predict mAb aggregation propensity based on the primary sequence. However, even though amino acid descriptors explain the differences in the primary sequence, they do not take into consideration potential interaction between the amino acids in or between primary chains. It has been argued that this simplification can lead to a loss of information concerning properties of secondary and tertiary structure in larger proteins (Zhou et al., 2008).

Descriptors can also be generated by using empirical equations on the entire primary sequence to infer protein properties such as the isoelectric point, hydrophobicity, molecular weight, physico-chemical properties and secondary structure content, to name a few. Many such tools and applications are available on bioinformatics sites, such as ExPASy (Gasteiger et al., 2005) and EMBL-EBI (Li et al., 2015).

Homology modelling and molecular dynamics for descriptor generation:

Descriptors capturing structural and surfaces properties can be generated by using existing crystal or NMR structures or by building models using homology modelling. The latter is performed by finding proteins with existing 3D structures that have a high level of similarity to the primary sequence of the protein of interest. These proteins are then used as templates to predict the likely structure of the queried protein (Liao et al., 2011). This has been successfully used in many publications where information such as surface areas, angles and surface properties were extracted (Sharma et al., 2014, Sydow et al., 2014, Buyel et al., 2013). The method is especially useful when no crystal structure exists. Caution needs to be exercised, however, as the homology models are only predicted structures. Breneman et al. (1995) introduced a methodology for generating 2D surface descriptors, also called transferable atom equivalent (TAE) descriptors, by reconstructing the electronic surface properties of the molecular structures from a library of atomic charge density components. This has the advantage of representing surface variations such as hydrophobicity and charge distributions numerically, which is of great importance when studying for example protein binding to an anion exchange chromatographic column packing using different salts (Tugcu et al., 2003). Breneman et al. (2003) later introduced the Property-Encoded Surface Translator (PEST) algorithm which is a further development to better describe the surfaces of the proteins when applying the TAE molecular surface descriptors. However, it is important to note that the PEST algorithm need 3D models in order to generate the descriptors of interest. PEST, together with TAE descriptor, has been successfully applied in a QSAR study where the generated model was able to accurately predict protein separation from HCPs (Buyel et al., 2013). Robinson et al. (2017) used the TAE descriptors to relate the structural differences between several Fab fragments to predict column performance between different chromatographic systems. It has been argued, however, that caution needs to be exercised when using library-based descriptors as these are usually directly related to a specific state of a compound that was measured in a unique environment. This means that these descriptors should only be applied if experiments were carried out in an identical or similar environment. Otherwise, this might cause the descriptors to be biased (Hechinger et al., 2012). Other structural properties, such as molecular angles and solvent accessible surface areas extracted from homology models, were used by Sydow et al. (2014) to determine the risk of degradation of asparagine and aspartate in mAbs as PTMs. Similarly, Sharma et al. (2014) investigated the risk of oxidation of surface accessible tryptophans.

Due to the flexibility and size of the mAbs it is very difficult to produce good 3D structures based on X-ray crystallography and NMR. Instead, homology modelling has proven to be a good alternative to circumvent this problem. However, due to the size and the many flexible parts, such as loops, in the mAbs, pure homology models might not give a sufficiently accurate representation of the reality. Molecular dynamics (MD) is a useful tool that can be used to minimise the energy of the entire protein and to simulate the dynamics of the protein of interest in different environments (Brandt et al., 2010). MD simulations have also shown very high similarities in the internal dynamics of mAbs when comparing the simulated results to those observed in reality (Kortkhonjia et al., 2013). It can therefore be argued that MD simulation should be applied to all homology models before descriptors are generated to mimic the environment of the samples that are used in QSAR studies.

1.3.2 QSAR for protein behaviour prediction

The QSAR framework has been applied to a diverse range of challenges where structural properties of pharmaceuticals have been used directly for the prediction of different process related aspects such as the prediction of isotherm parameters in ion-exchange chromatography (Ladiwala et al., 2005), ligand-binding in ion-exchange chromatography under high salt concentrations (Yang et al., 2007a), binding of proteins in ion-exchange chromatography under different pH conditions (Yang et al., 2007b), protein surface patch analysis for the choice of purification methods (Insaidoo et al., 2015), chromatographic separation of target proteins from HCPs (Buyel et al., 2013), viscosity, clearance and stability prediction for mAbs (Sharma et al., 2014) and degradation prediction of asparagine and aspartate in mAbs (Sydow et al., 2014) to mention a few. This also showcases one of the main strengths of the QSAR/QSAM framework with its ability to link structural features to many different forms of prediction outputs. It is important to note, however, that identical experiments must have been performed on different pharmaceuticals in order to compare the differences in structure and their effect on the output. Equally important is that sufficient excitation is present in the output data in order for the effects to be linked to the corresponding structural feature (Bishop, 2006).

1.4 Towards mAb process development by bridging QbD and QSAR

There have been significant advances in computational prediction methods and they are starting to become more common in process development (Jiang et al., 2011). As mentioned by Zurdo et al (2015), the ability to predict product related characteristics that strongly relate to the QTPP and/or CQAs can greatly simplify process development, especially in the early stages when the product or process knowledge is limited. The implementation of QSAR in process related areas, such as protein purification, has been researched extensively (Chen et al., 2008, Yang et al.,

2007a, Yang et al., 2007b, Ladiwala et al., 2005, Woo et al., 2015a, Hou et al., 2011, Robinson et al., 2017). Though not all the mentioned examples concern mAbs specifically, the outlined methodology used in the different research articles is still applicable. Given the significant proportion of mAb development cost that is incurred during downstream processing, considerable advantages can be gained by being able to predict the performance of chromatographic columns and their effect on product quality early in the process development. In the case of mAbs much of the cost is incurred during the purification due to the strict regulations surrounding clinical safety of the end product (Hammerschmidt et al., 2014, Farid, 2007). Examples of regulations for mAbs include removal of harmful structural variants, such as those presented in Table 1.1, while retaining the desired structure based on evidence from clinical trials. The removal of contaminants, such as HCPs, DNA and viruses, is also necessary in order to avoid undesired immune responses in patients. Thus, for therapeutic use, a mAb purity of >99% is required in the final formulation (European Medicines Agency, 2016). Therefore, the integration of QSAR into QbD is proposed based on the valuable insight that QSAR can provide in early process development and is illustrated in Figure 1.5 which also shows how the QbD framework can add to and improve the QSAR modelling with addition of new data.

Two main approaches of integrating the QSAR framework into the QbD paradigm can be considered. The first approach is by only using generated structural descriptors for development of models able to predict protein behaviours. An example of this was published by Obrezanova et al. (2015) where the authors developed a model with the adaBoost algorithm based on decision trees that was able to predict the probability of mAb aggregation based on the structure of the primary sequence. The method is however more constrained as it requires data generated from identical experimental setups, and therefore identical PP settings in order to assume that the observed effect is caused only by the differences in structure between the proteins. Therefore, models developed this way are better for assessing the manufacturing feasibility and/or potential CQAs before starting the process development. The second approach is to use the PPs of interest, taken from previous mAb processes to use directly in the model development by either 1) adding the PPs together with the generated structural descriptors as inputs (Rodrigues de Azevedo et al., 2017) or 2) structural descriptors are calculated to be dependent on the PPs, meaning that the values of the descriptors will change with changing values of the PPs (Yang et al., 2007b). The latter is easiest done by generating descriptor from MD simulations where changes in the soluble environment can be implemented. This however requires that data is gathered from similar experimental setups where only the PPs of interest have been varied. This would usually not be a problem when gathering historic data generated

from the QbD paradigm as it will often conform to experimental designs based on DoEs where the experimental environment is strictly controlled. The added benefit of this approach is that the developed model will be able to account for both the structural differences as well as the impact from the studied PPs when predicting protein behaviour. This can potentially have great value in process development of new mAbs as PP ranges can be assessed in silico and therefore greatly aid in reducing the number of needed experiments, seen as grey arrows in Figure 1.5.

The methods described above provide a reference for further risk assessment and characterisation to be performed in the QbD framework, as they provide information, such as the behaviour of the product in different scenarios and increase the product understanding. As additional information from new mAb processes becomes available, models can be improved by expanding the data sets used in the model development. This in turn will aid in providing more accurate predictions due to lowering the sparsity by incorporating more protein structures. Available characterisation research studies can also be used as additional sources of data in order to improve the models by expanding the data set for model development.

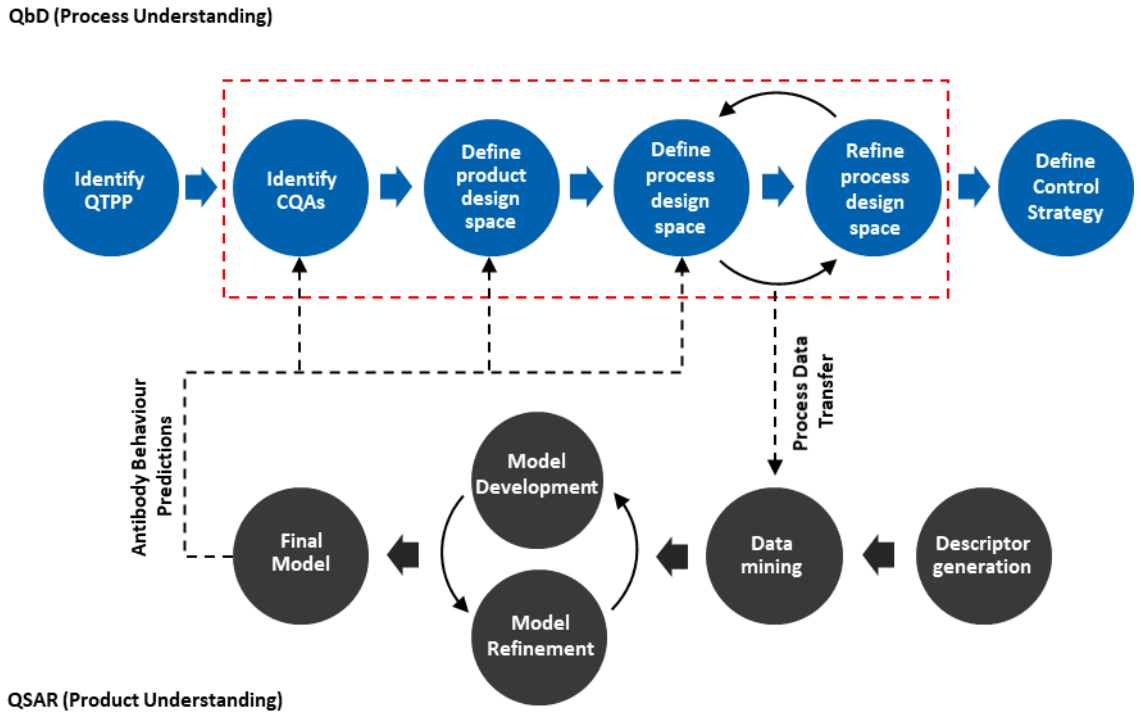

Figure 1.5. Proposed integration of QSAR into QbD where the upper half illustrates the simplified framework of QbD (blue) and the lower half illustrates a simplified version of the QSAR framework (black). Transfer of characterisation data from previous mAb processes can be used directly for model development using QSAR. Depending on the purpose of the developed QSAR model, it can be used to directly aid in assessing CQAs or provide insight into PPs and ranges.

1.5 Scope of this study

This study focused on developing a QSAR framework that could aid in early stage process development of monoclonal antibody therapeutics to facilitate rapid developability. The

application of QSAR for proteins other than mAbs is not new and has been reported extensively in the past. An example of this is prediction of chromatographic performance of CIEX columns (Ladiwala et al., 2003, Malmquist et al., 2006), AIEX columns (Song et al., 2002, Tugcu et al., 2003), HIC columns (Ladiwala et al., 2006, Chen et al., 2007, Chen et al., 2008) and multimodal columns (Chung et al., 2010, Woo et al., 2015a, Woo et al., 2015b). In the listed examples, the proteins used in the studies were all of unique sizes, structures and functions. However, the implementation of QSAR for the prediction of mAb behaviour in process related settings is still relatively new where areas such as aggregation propensity (Lauer et al., 2012, Obrezanova et al., 2015), chromatography performance of HIC (Robinson et al., 2017), chromatography performance of CIEX (Kittelmann et al., 2017) and degradation of solvent accessible asparagine and aspartate in the variable regions of the mAb structure (Sydow et al., 2014) have been explored recently.

It is important to note that descriptor generation of mAb focused research have adhered to workflows used for QSAR models developed for the prediction of general protein behaviour where proteins were of different sizes, properties and functions such as those examples mentioned in the beginning of this section. However, due to the high sequence and structure similarities between mAbs, such descriptors might not necessarily capture the more subtle differences between mAbs that might be needed for accurate prediction with QSAR. For this reason, descriptors in this research were developed based on structural features and properties inherent to all mAbs as presented in Chapter 3 and Chapter 6 for primary sequence-based descriptors and 3D structure descriptors, respectively. Also, to date, no exploration of structural variations originating from different mAb isotypes and species origins has been performed. These structural variations were therefore explored in order to characterise their effect on generated descriptors (Chapter 4) and their potential impact on model performance in terms of a response of interest (Chapter 5 and Chapter 7).

Another concern with previously published research is the lack of mAb samples used for model development, which was in many cases below 40 samples (Robinson et al., 2017, Kittelmann et al., 2017). Due to the large structural variability of mAbs, a smaller dataset will be limiting and might not necessarily contain the structural variability needed for accurate model prediction. In this study, a larger dataset published by Jain et al. (2017) was used, consisting of 137 unique mAbs with 12 experimental assays performed for each mAb. This allowed for greater structural variation between mAbs to be included in the model development compared to previously published research. Out of the 12 experimental assays provided by Jain et al. (2017), HIC retention time and mAb yield were selected as responses to be used in model

development due to representing important factors of the DSP and USP, respectively, in industrial process development of mAbs. As mentioned previously in Section 1.2.3, HIC is a common polishing step in mAb purification but also allows for the investigation of their stability based on retention times as more hydrophobic mAb would elute later (Haverick et al., 2014). As for the mAb yield, this parameter is important in order to ensure that enough product can be extracted cost effectively, given of course that the majority of the expressed mAb structures fulfils the QTPP and CQA requirements for the intended drug.

The potential impact of successful prediction of mAb behaviour based on their structure is invaluable in biopharmaceutical industry as it can provide critical information pertaining to their stability (Obrezanova et al., 2015), behaviour in operational units (Robinson et al., 2017) and potential structural variants (Sydow et al., 2014), to mention a few. This can aid in early process development of new mAb candidates and in turn in a more informed risk assessment and process route selection, thereby reducing the number of required experiments to characterise the process, resulting in lower development costs and lead times.

1.6 Summary

Due to the high efficacy and safety of the mAbs, their market has grown considerably during the last three decades. This has led to an increased focus on improvement and optimisation of the process development in order to manufacture mAbs cheaper and faster.

The QbD framework was reviewed as a means to increases the process understanding through characterisation of PPs and their effect on the product quality. However, due to the numerous PPs that need to be characterised, the QbD framework still faces challenges in implementation. Much research has been performed in areas such as high-throughput platforms and process optimisation to reduce attrition in the process development. More importantly, one of the biggest problems with QbD is the lack of knowledge about both the process and product in early process development where the manufacturability of an mAb might not be possible.

The use of *in silico* methods for prediction of protein and mAb behaviour in different unit oprations has proven to be efficient to increase product knowledge. Based on the QSAR framework, historic process data from established and failed mAb processes can be used and linked with structural properties of the mAbs in order to investigate potential behaviour during processing. Different strategies for generating structural properties or descriptors of an mAb have been suggested and reviewed based on the amino acid composition, homology modelling and MD simulation.

The integration of QSAR and QbD frameworks is therefore proposed here to increase product and process understanding which is especially important in early process development.

Chapter 2

Modelling Development and Assessment

In this Chapter, an overview of some of the current and more traditional techniques used for data exploration, classification and regression is presented. The theory of each method is explained with references to further detailed literature and some examples of applicability are highlighted. Model training and validation with cross-validation in particular are reviewed and their importance in model training and validation is critically discussed. The material in this chapter acts as a foundation for all model development performed in this thesis and it also provides a useful overview of the tools for tackling a wide variety of different modelling problems in other disciplines and industrial sectors.

2.1 Matrix, vector and index notations

For consistency and to avoid confusion, specific naming conventions is used throughout for the independent and dependent variables in this chapter to describe the structure of vectors and matrices used in the different multivariate techniques explained below. Additional matrix, vector or index notations specific to individual methods are specified and explained in connection with the method in question.

2.1.1 Independent data

The independent data will be referred to as $\boldsymbol{X}$ shown in eq.(2.1) where the rows correspond to individual samples and the columns to individual independent variables. The term structural descriptors defined in QSAR modelling is equivalent to that of the independent variables

$$\boldsymbol{X} = \begin{bmatrix} x_{11} & x_{12} & \cdots & x_{1M} \\ x_{21} & x_{22} & & x_{1M} \\ \vdots & & \ddots & \vdots \\ x_{N1} & x_{N2} & \cdots & x_{NM} \end{bmatrix} \tag{2.1}$$

Index notation for samples in this thesis will use $i, j = 1, \dots, N$ where i and j are individual arbitrary samples and N is the total number of samples in the data set. Index notation for variables/descriptors will use $k, l = 1, \dots, M$ where k and l are individual arbitrary variables/descriptors and M is the total number of variables/descriptors in $\boldsymbol{X}$. Small letter $\boldsymbol{x}$ in bold in this chapter indicates either a column vector for a single variable eq.(2.2) or a row vector for a single sample eq.(2.3) and can be identified based on the index notation belonging to either the variables or the samples.

$$\boldsymbol{x}_k = \begin{bmatrix} x_{1k} \\ x_{2k} \\ \vdots \\ x_{Nk} \end{bmatrix} \tag{2.2}$$

$$\boldsymbol{x}_i = [x_{i1} \quad x_{i2} \quad \cdots \quad x_{iM}] \tag{2.3}$$

2.1.2 Dependent data

The dependent variables or response variables will be referred to as $\boldsymbol{Y}$ shown in eq.(2.4) where the rows correspond to individual samples and the columns to the individual response variables.

$$\boldsymbol{Y} = \begin{bmatrix} y_{11} & y_{12} & \cdots & y_{1D} \\ y_{21} & y_{22} & & y_{1D} \\ \vdots & & \ddots & \vdots \\ y_{N1} & y_{N2} & \cdots & y_{ND} \end{bmatrix} \tag{2.4}$$

Index notation for response variables will use $f, g, h = 1, \dots, D$ where f, g and h are individual arbitrary responses and D is the total number of response variables in $\boldsymbol{Y}$. Small letter $\boldsymbol{y}$ in bold in this chapter indicates either a column vector for a single response eq.(2.5) or a row vector for a single sample eq.(2.6) and can be identified based on the index notation belonging to either the variables or the samples.

$$\boldsymbol{y}_f = \begin{bmatrix} x_{1f} \\ x_{2f} \\ \vdots \\ x_{Nf} \end{bmatrix} \tag{2.5}$$

$$\boldsymbol{y}_i = [y_{i1} \quad y_{i2} \quad \cdots \quad y_{iD}] \tag{2.6}$$

2.2 Exploratory Data Analysis

Exploratory data analysis (EDA) is applied to better understand the main characteristics of a data set and can therefore provide an overview of the variables and samples in a study used to identify similarities/dissimilarities, systematic trends and outlies (Biancolillo and Marini, 2018). EDA is therefore a crucial step prior to any predictive modelling in order to identify sources of variation that can potential impact on model performance. In this research, Principal Component Analysis (PCA) has been reviewed due to being one of the most commonly used techniques EDA.

2.2.1 Principal Component Analysis

PCA is one of the oldest and most widely used data exploration tools in fields of statistics, biology and chemometrics. The idea behind PCA was first introduced by Pearson in 1901 who proposed the that lines could be placed in a high dimensional variable space that had a best fit to a set of sample points. The direction of the lines in the original variable space were placed in such a way that the correlations between the lines and the original variables were maximised, thus ensuring that most of the variation in the data was captured (Pearson, 1901). The method was later improved upon by Hotelling in 1933 who instead of using lines, used linear transformations to transform the data to a new coordinate system where the new axes were linear combinations on the original variables (Hotelling, 1933).

2.2.1.1 Theory

Given a data matrix, e.g. $\boldsymbol{X}$, a new set of variables called Principal Components (PCs) are calculated which describe the variation of the original variables according to:

$$\boldsymbol{X} = \boldsymbol{T}\boldsymbol{P}^T + \boldsymbol{E} = \boldsymbol{t}_1\boldsymbol{p}_1^T + \boldsymbol{t}_2\boldsymbol{p}_2^T + \cdots + \boldsymbol{t}_R\boldsymbol{p}_R^T + \boldsymbol{E}, \quad r = 1, \dots, R \tag{2.7}$$

where $\boldsymbol{T} = [\boldsymbol{t}_1 \quad \dots \quad \boldsymbol{t}_R]$ (N x R) is the sample score matrix and R is the number of components, $\boldsymbol{t}_r$ (N x 1) is the score vector of component r, $\boldsymbol{P} = [\boldsymbol{p}_1 \quad \cdots \quad \boldsymbol{p}_R]$ (M x R) is the loadings matrix, $\boldsymbol{p}_r$ (M x 1) is the loading vector of component r and $\boldsymbol{E}$ (N x M) is the residual error matrix not explained by the PCs.

The loading vectors are linear combinations of the original variables are pair-wise orthogonal. When stronger correlations between the original variables are present, fewer PCs are required to explain the majority of the variation in $\boldsymbol{X}$. Also, due to the orthogonality, each PC has an

individual contribution to the explained variation according to eq.(2.8). Thus, increasing the number of PCs will in turn increase the total variation explained.

$$\begin{aligned}\|\boldsymbol{TP}^{\boldsymbol{T}}\|^2 &= \left\|\boldsymbol{t}_1\boldsymbol{p}_1^{\boldsymbol{T}}\right\|^2 + \left\|\boldsymbol{t}_2\boldsymbol{p}_2^{\boldsymbol{T}}\right\|^2 + \cdots + \left\|\boldsymbol{t}_R\boldsymbol{p}_R^{\boldsymbol{T}}\right\|^2 = \\ &= \|\boldsymbol{X}\|^2 - \|\boldsymbol{E}\|^2\end{aligned} \tag{2.8}$$

PCA relies on the calculation of the covariance matrix, $\boldsymbol{\Sigma}$, as it describes the covariance between pairs of variables in $\boldsymbol{X}$. The covariance between two variables is calculated according to:

$$\begin{aligned}\mathrm{cov}(\boldsymbol{x}_k, \boldsymbol{x}_l) &= \frac{1}{N-1}\sum_{i=1}^{N}(x_{ik} - \bar{x}_k)(x_{il} - \bar{x}_l)\,, \\ & k, l = 1, \ldots, M\end{aligned} \tag{2.9}$$

The full covariance matrix, $\boldsymbol{\Sigma}$, is defined in eq.(2.10) where the diagonal elements become the variances for the individual variables, $\mathrm{cov}(\boldsymbol{x}_k, \boldsymbol{x}_k) = \sigma_k^2$. Eq.(2.10) can be simplified as according to eq.(2.11) by first mean-centring the $\boldsymbol{X}$ block (see Section 2.7).

$$\boldsymbol{\Sigma} = \begin{bmatrix} \sigma_1^2 & \mathrm{cov}(\boldsymbol{x}_1, \boldsymbol{x}_2) & \cdots & \mathrm{cov}(\boldsymbol{x}_1, \boldsymbol{x}_M) \\ \mathrm{cov}(\boldsymbol{x}_2, \boldsymbol{x}_1) & \sigma_2^2 & & \mathrm{cov}(\boldsymbol{x}_2, \boldsymbol{x}_M) \\ \vdots & & \ddots & \vdots \\ \mathrm{cov}(\boldsymbol{x}_M, \boldsymbol{x}_1) & \mathrm{cov}(\boldsymbol{x}_M, \boldsymbol{x}_2) & \cdots & \sigma_M^2 \end{bmatrix} \tag{2.10}$$

$$\boldsymbol{\Sigma} = \frac{1}{N-1}\boldsymbol{X}_{Cent}^{T}\boldsymbol{X}_{Cent} \tag{2.11}$$

In order to find the directions and importance of the PCs, the eigenvalues, λ_k, and eigenvectors, $\boldsymbol{v}_k$ (M x 1), are calculated from $\boldsymbol{\Sigma}$. For details on calculation and properties of eigenvalues and eigenvectors, refer to Appendix D.1. The eigenvectors calculated from covariance matrix play a central role in the calculation of the PCs as they are pair-wise orthogonal and represent the directions in the original variable space in which the data variations are the highest.

The eigenvalues on the other hand determines the importance of their corresponding eigenvector where a higher eigenvalue indicates a larger data variation in the direction of the eigenvector. The covariance matrix, $\boldsymbol{\Sigma}$, can then be decomposed using the eigenvectors and eigenvalues which is known as eigen-decomposition according to:

$$\boldsymbol{\Sigma} = \boldsymbol{V}\boldsymbol{\Lambda}\boldsymbol{V}^T \tag{2.12}$$

where $\boldsymbol{V} = [\boldsymbol{v}_1 \quad \boldsymbol{v}_2 \quad \cdots \quad \boldsymbol{v}_M]$ is the eigenvector matrix and $\boldsymbol{\Lambda} = \text{diag}(\lambda_1, \lambda_2, \ldots, \lambda_M)$ is a diagonal matrix consisting of the eigenvalues where $\lambda_1 \geq \lambda_2 \geq \cdots \geq \lambda_M$. Based on the definition of PCA stated in eq.(2.7), the PC loadings are equal to the eigenvector matrix due to their orthogonality according to eq.(2.13). An example of the placement of two eigenvectors is illustrated in Figure 2.1c. The PC scores are then calculated as the product of the mean centred $\boldsymbol{X}$ matrix and the loadings, $\boldsymbol{P}$, according to eq.(2.14). Figure 2.1d illustrates the new placement of samples on two PCs where the red and blue dashed lines represents the scores on the first PC and second PC for sample i. The representation is also known as a score plot.

$$\boldsymbol{P} = \boldsymbol{V} \tag{2.13}$$

$$\boldsymbol{T} = \boldsymbol{X}_{Cent}\boldsymbol{V} = \boldsymbol{X}_{Cent}\boldsymbol{P} \tag{2.14}$$

Alternatively, the principal components can be calculated using Singular Value Decomposition (SVD) which is present in Appendix D.2.

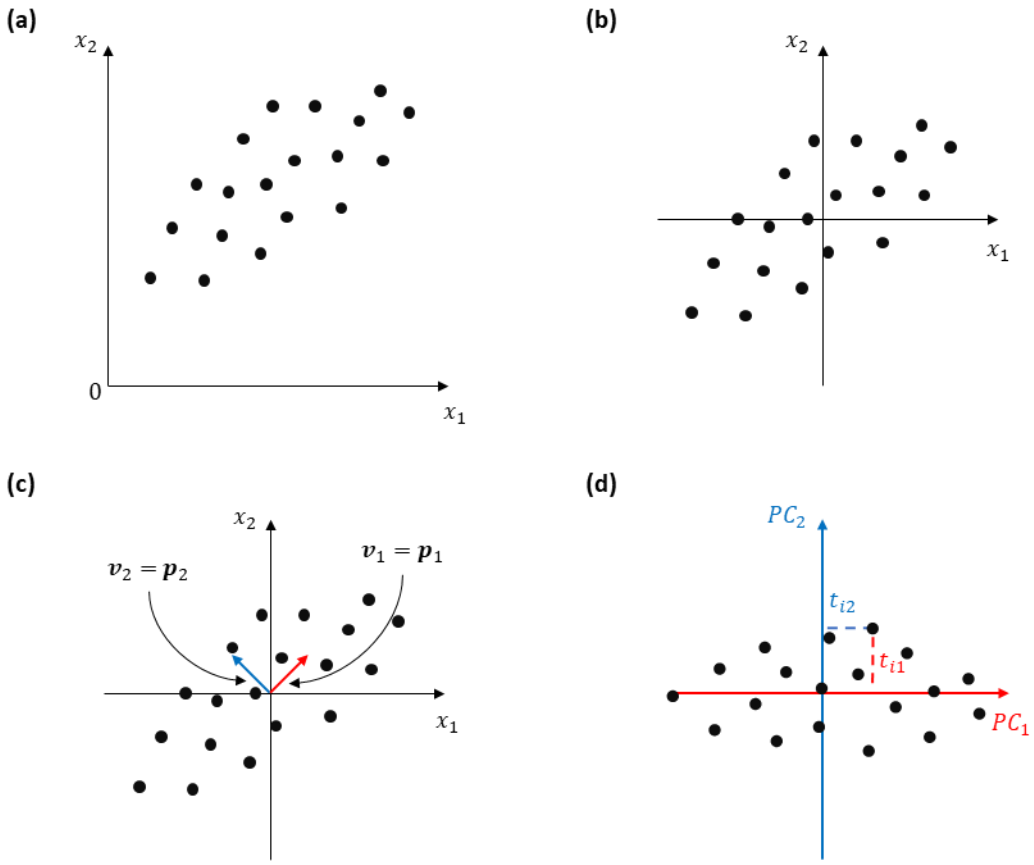

Figure 2.1. Overview and critical steps of data decomposition with PCA in two dimensions. **(a)** The raw data is first **(b)** pre-treated by mean centring the samples around the origin**. (c)** Linear combinations of the original variables, x_1 and x_2, known as eigenvectors are then calculated where the first eigenvector, $\boldsymbol{v}_1$ (red), lies in the direction of the greatest data variation and the second eigenvector, $\boldsymbol{v}_2$ (blue), in the direction of the second greatest data variation. **(d)** Final transformation of samples to the PC_1 (red line) and PC_2 (blue line) axes where each sample is represented by its individual scores (adapted from O'Malley (2008))

2.2.1.2 Applicability of PCA in this research

PCA is a very useful tool for visualisation and exploration of high dimensional data set due to its ability to reduce the variable dimensionality and to capture strong correlations between variables which might otherwise be difficult to explore. PCA also has powerful diagnostic capabilities for detection of outliers based on residual values and the calculation of Hotelling T^2 (Hotelling, 1933). This provides evidence for characterisation of not only ill-fitted samples with high residual values, but can be used to identify extreme samples that are forcing the direction of the PCs. Thus, PCA aids in the identification of samples which require further investigation due to different behaviour compared to the other samples in the data set (Bro and Smilde, 2014).

PCA has been extensively used over the years within bio-related research for applications ranging from the effects of raw material variations in media composition (O'Kennedy, 2016), characterisation of fermentation process (Sokolov et al., 2016, Rathore et al., 2015), fault detection in fermentation (Gunther et al., 2006) and effects of scalability on bioprocesses

(Mercier et al., 2013) to mention a few. In all applications, PCA was shown to be an effective method used to identify sources of variation that impacted upon the individual problem statements. The authors also highlighted the importance of selecting the right number of components in order to filter out noise and keep application related variation.

The selection of the number of PCs to use when decomposing $\boldsymbol{X}$ depends mainly on the problem statement as well as the data. In the visualisation of the scores, class information can be incorporated by colouring samples according to the available classes which might aid in determining the number of PCs needed to find a good separation class separation (Biancolillo and Marini, 2018, Bro and Smilde, 2014). However, due to being unsupervised and depending only on the data variation in $\boldsymbol{X}$, PCA will not necessarily lead to a good separation of classes if the data variation is not directly correlated to the class information. Alternatively, a scree test can be performed where the eigenvalues or the captured variation are plotted against their corresponding PCs. The number of PCs are chosen based on when the decrease in eigenvalues becomes linear, indicating that the model is starting to capture noise (D'Agostino Sr and Russell, 2005). Another method is the Broken stick method where a line based on the broken stick distribution is added to the scree plot (MacArthur, 1957). The line mimics the behaviour of eigenvalues calculated from a completely randomised data set, thus effectively representing noise. If eigenvalues in the PCA model lies above the line this is an indication that the PC capture structured variation. The last reviewed approach is to define a limit for the minimum total explained variance which must be captured by the PCA model (Bro and Smilde, 2014).

In this research, a limit for the minimum total explained variance was used due to two reasons: 1) The components in PCA are additive, meaning that even if extra components are added to the model, the structure of the initial components will remain unchanged. 2) PCA was only used for exploration and therefore a strict number of components does not need to be defined. Bro and Smilde (2014) argued that this allows for greater exploration of the behaviour in the individual components. However, it is mportant to remember that it also inadvertently increases the chances of including components that only capture noise.

It is important to note that PCA will only perform well if the relationship between correlated variables is linear, meaning for non-linear correlations PCA will not be able to capture the correlation between variables.

2.3 Classification

When distinct classes exist in the data set and clear discrimination is needed, dedicated classification methods may be more appropriate for the task and can be used to investigate

potential correlation between variables in $\boldsymbol{X}$ and the sample classes. The theory of the popular classification methods PLS-DA and SVC has been covered in this research and their applicability assessed.

2.3.1 Partial Least Square – Discriminant Analysis

PLS-DA like the name implies, is a combination of Partial Least Squares (PLS) and Linear Discriminant Analysis (LDA). However, only LDA will be covered in this section due to being the classifier whereas PLS is strictly a regression method (see section Section 2.4.1). As for the LDA algorithm, Bayes decision rule was used in this research due to being better suited to the problem statement (see Section 2.3.1.2). The method theory has been covered below

2.3.1.1 Theory

Before describing the theory of the Bayes´ method, it is important to understand the structure of the input data into the DA algorithm. Prior to the classification, a PLS regression model will be trained with $\boldsymbol{X}$ and $\boldsymbol{Y}$**.** The matrix $\boldsymbol{Y}$ (N x C) contains the class memberships of the samples and is represented in the form of dummy variables. An example of $\boldsymbol{Y}$ in a binary classification problem ($D = 2$) with classes C_1 and C_2 is presented in Figure 2.2a. Two dummy variables have been generated as column vectors representing each class where the class membership of each sample, $\boldsymbol{x}_i$, is assigned with values of either one and zero. A value of one indicates membership to the class represented in the dummy variable while a value of zero indicates membership to another class, e.g. if $y_{i1} = 1$ then the sample $\boldsymbol{x}_i \in C_1$.

However, the predictions from the PLS model, $\widehat{\boldsymbol{Y}}$, will not be predicted perfectly as ones and zeros but will instead have predictions close to the original values of $\boldsymbol{Y}$. An example of PLS predictions is presented in Figure 2.2b.

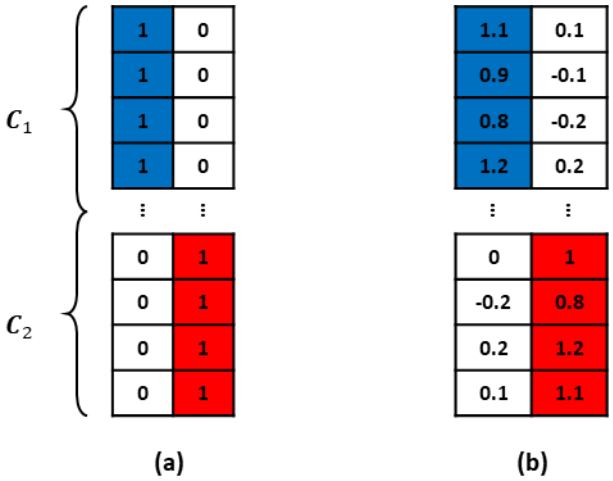

Figure 2.2. The structure of the response vector $\boldsymbol{Y}$ in a binary classification problem used in PLS-DA. **(a)** Dummy variables are used to construct $\boldsymbol{Y}$ and assign class memberships of samples to either C_1 (blue) and C_2 (red). **(b)** Example predictions from the PLS regression.

A binary classification problem however will not need two dummy variables in order to represent the classes due to all samples being listed as either ones or zeros in each column. The PLS-DA algorithm will build two classifiers based on each dummy variable. The solutions of these classifiers however will be identical due to the class membership of the samples being retained regardless of which column in $\widehat{\boldsymbol{Y}}$ is used as well as the individual class means and variances of C_1 and C_2 being identical in both columns (Brereton and Lloyd, 2014). Therefore, in order to avoid confusion, Bayes method will be explained in relation to the second column in $\widehat{\boldsymbol{Y}}$ which, for convenience, will be referred to as $\hat{\boldsymbol{y}} = (\hat{y}_1, \hat{y}_2, \dots, \hat{y}_N)$.

Bayes´ theorem for discrimination of two classes can be formulated according to:

$$P(C_c|\hat{y}_i) = \frac{P(\hat{y}_i|C_c)P(C_c)}{P(\hat{y}_i)} \propto P(\hat{y}_i|C_c)P(C_c) \qquad (2.15)$$

$P(\mathrm{C}_c|\hat{y}_i)$ is the posterior probability of a sample i belonging to class C_c given a particular value of $\hat{y}_i$ where $c = 1{,}2$. The $P(\hat{y}_i|\mathrm{C}_c)$ term is the likelihood or the probability of observing $\hat{y}_i$ given C_c. The $P(C_c)$ term is the prior probability of class C_c, or more specifically, the probability of observing class C_c. $P(\hat{y}_i)$ is the probability of observing $\hat{y}_i$. The posterior probability is directly proportional to the numerator in eq.(2.15) due to that $P(\hat{y}_i)$ will not change regardless of the class defined in the posterior.

The likelihood, $P(\hat{y}_i|\mathrm{C}_c)$, can be defined as a gaussian function according to:

$$P(\hat{y}_i|\mathrm{C}_c) = \frac{1}{\sqrt{2\pi\sigma_c^2}} \exp\left(-\frac{(\hat{y}_i - \bar{y}_c)^2}{\sigma_c^2}\right) \tag{2.16}$$

where σ_c is the standard deviations of samples belonging to class C_c and $\bar{y}_c$ is the sample mean of class C_c. An example of the likelihood functions is illustrated in Figure 2.3a for class C_1 (blue line) and C_2 (red line) where the predicted values are centred around zero and one, respectively. The prior class probabilities are calculated as the ratio of samples belonging to a specific class and all samples in the data set according to:

$$\sum_{c=1}^{2} P(\mathrm{C}_c) = 1, \qquad P(\mathrm{C}_c) = \frac{N_c}{N} \tag{2.17}$$

where N_c is the number of samples belonging to class C_c. The sum of all priors needs to be equal to one. The probability of observing $\hat{y}_i$ is the sum of the likelihoods weighted by their corresponding class priors according to:

$$P(\hat{y}_i) = \sum_{c=1}^{2} P(\hat{y}_i|C_c)P(C_c) \tag{2.18}$$

An example of the distribution of $P(\hat{y}_i)$ is illustrated in Figure 2.3a as the grey dashed line and it can be observed that the peaks of the likelihoods are preserved in the distribution which was weighted with $P(C_1) = P(C_2) = 0.5$ in order for the distribution area to become equal to one. The posterior probabilities for class C_1 and C_2 are illustrated in Figure 2.3b as the blue and red line, respectively. It can be observed that samples around zero on the $\hat{y}$ axis will be classified as C_1 while samples around one be classified as C_2. A point of interest is where $P(C_1|\hat{y}) = P(C_2|\hat{y})$, which is known as the decision boundary, d.

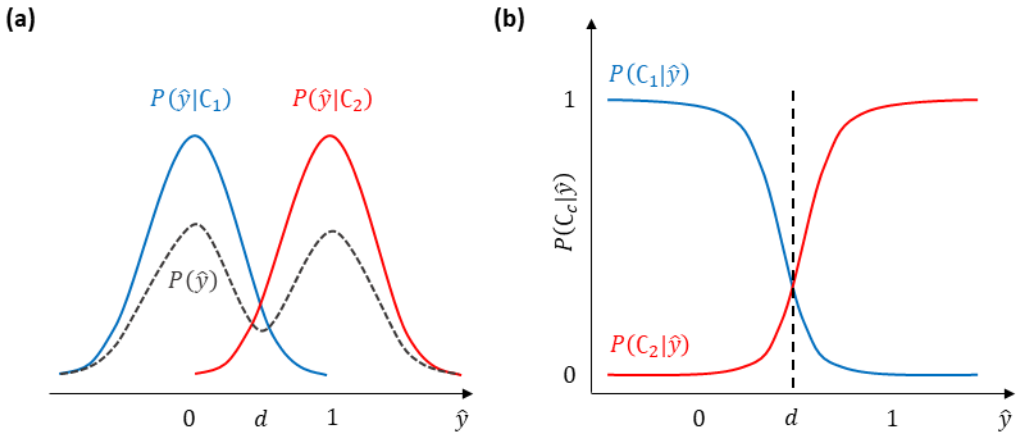

Figure 2.3. Probability distributions used in Bayes theorem. (a) Examples of the likelihood distributions of $\hat{y}$ belonging to class C_1 (blue line) and C_2 (red line) centred around zero and one, respectively. The distribution of $\hat{y}$ (dashed grey line) with equal samples sizes, $P(C_1) = P(C_2) = 0.5$. (b) The posterior probabilities of a sample belonging to either to class C_1 (blue line) or C_2 (red line) based on $\hat{y}$ with the decision boundary, d (dashed black line) (adapted from Pérez et al. (2009)).

Two options exist for classification of samples once the posterior probability functions have been calculated: 1) the decision boundary can used directly to determine the class of a sample i based on $\hat{y}_i$ from the PLS model, or 2) the probabilities of a sample i is calculated using the posterior probability function according to eq.(2.15) and the class with the highest probability is assigned to the sample. In this research, the latter option has been used.

2.3.1.2 Applicability of PLS-DA in this research

If the goal is to investigate discrimination between sample classes, PLS-DA will be much more useful compared to PCA due to the maximisation of covariance between $\boldsymbol{X}$ and $\boldsymbol{Y}$ (Ballabio and Consonni, 2013).Numerous PLS-DA algorithms with different decision boundary rules and their application in the PLS algorithm have been developed in the past (Povey et al., 2014, Chen et al., 2018). It is therefore important to consider the different aspects and choices available for PLS-DA with regards to the problem statement in order to develop meaningful models. Several decision rules exist which can be used in PLS-DA to generate the decision boundary where the two most common ones are: 1) Fisher's LDA which minimises the variance in the individual classes while maximising the distance between the class means and assumes Gaussian distribution and equal variance between classes (Barker and Rayens, 2003). 2) Bayes decision rule which allows for prior class probabilities to be used. Bayes rule applies Gaussian distribution fit to the individual classes, but does not assume the class variances to be equal (Indahl et al., 2007, Pérez et al., 2009). For LDA, class imbalances have a negative impact on the model due to that the decision boundary will be moved closer to the class containing the most samples which consequently can cause a higher misclassification rate if the class variance is large (Brereton and Lloyd, 2014). This is however not a problem with Bayes rule due to

assignment of class weights based on the prior probabilities of the class occurrence within the data set as seen in eq. (2.15). As a result, Bayes decision rule will modify and place the decision boundary in the centre between the two classes (Indahl et al., 2007). For this reason, Bayes decision rule was therefore chosen in this research as the data set available from Jain et al. (2017) demonstrated uneven class representation.

Kjeldahl and Bro (2010) as well as Gromski et al. (2015) reported on a common misconception about PLS-DA where many publications report model performance based on R^2 and Q^2 (see Section 2.6.1). This is often misleading as these describes the model fit with regards to regression and give no information pertaining to correct classification and misclassification of a sample. In this research, performance metrics conforming to classification problem statements are strictly used (see Section 2.6.2).

Another important aspect to consider is the contribution of random chance-correlation between $\boldsymbol{X}$ and $\boldsymbol{Y}$ in PLS-DA. Perez and Narasimhan (2018) showed that the accuracy of PLS-DA fitted on randomly generated variables increased when the number of variables became much greater than the number of samples in the data set ($M \gg N$). This is caused by random chance-correlation between $\boldsymbol{X}$ and $\boldsymbol{Y}$, thus making it appear as if PLS-DA resulted in a clear discrimination of classes but where in reality, none should exist. Perez and Narasimhan (2018) as well as Westerhuis et al. (2008) highlighted the importance of rigorous cross-validation (see Section 2.5) in order to ensure that PLS-DA captures the true underlying pattern in the data.

In reviews by Gromski et al. (2015) and Brereton and Lloyd (2014), the authors stated that PLS-DA is often outperformed by other classification methods such as Support Vector Machines for classification (SVC). PLS-DA might therefore not be the optimal choice of classifier to apply in many problem statements. However, PLS-DA has unparalleled diagnostic capabilities compared to other methods due to the PLS component in the algorithm which can assess sample and variable contributions to the predictions (see Section 2.4.1 for more information). Therefore, PLS-DA should be seen as an intermediate step in classification model development to be used for outlier detection and investigation of highly contributing variables prior to model development with an alternative classifier (Brereton and Lloyd, 2014, Gromski et al., 2015).

2.3.2 Support Vector Machines for Classification

Support Vector Machines (SVM) for classification (SVC) were first introduced by Boser et al. (1992) as a linear or non-linear classification method that maximises the separation of classes through calculation of optimal placement of the decision boundary. The method is based on the

original work of Vapnik who first introduced the method in 1963 as the "generalised portrait algorithm" (Vapnik and Lerner, 1963).

The aspect that the SVC algorithm addresses, that many classification techniques do not, is that of over-fitting. As previously discussed, when training a classifier to maximise correct classification it is possible to fit the classifier over-fit to the training set. This has the effect of degrading the performance of the classifier when presented with unseen data. In a binary classification problem, the SVC algorithm trains a decision function that maximises the generalisation between the classes. In doing so, this makes the algorithm more robust.

In literature, the abbreviations of SVM and SVC are used interchangeably so in order to avoid confusion, this research uses SVC to distinguish SVM for classification from that of SVM for regression (SVR) which has also been applied in this research (see Section 2.4.2).

2.3.2.1 Theory

In a binary classification problem that is linearly separable, for any given data set, e.g. $\boldsymbol{X}$, where each sample is assigned a class according to $y_i \in \{-1,1\}$, the SVC algorithm will always find the largest margin or the "widest street" that separates the two classes. The separation is illustrated in Figure 2.4a of positive samples (red dots) and negative samples (blue dots) according to a defined hyperplane shown as the black line.

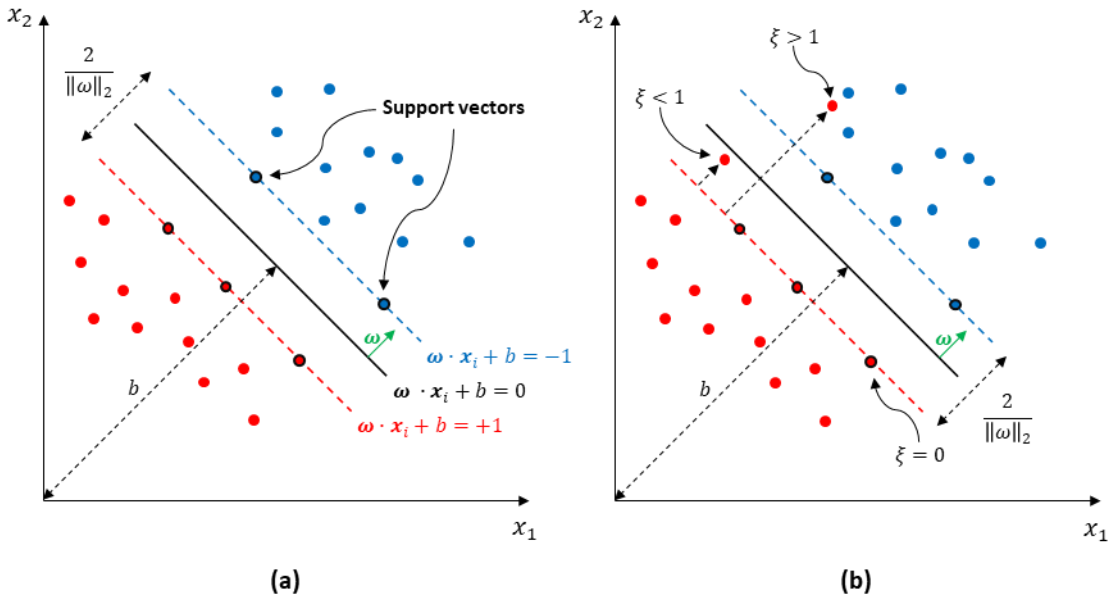

Figure 2.4. SVC placement of the decision boundary (black line) generated from selected samples that act as support vectors (black circles) which maximises class discrimination in a problem that is **(a)** linearly separable and **(b)** not linearly separable. The SVC constraints for separating positive and negative class samples are shown as the red dashed line and blue dashed line, respectively (adapted from Boser et al. (1992))

The SVC algorithm defines the boundaries for each class according to:

$$\boldsymbol{\omega} \cdot \boldsymbol{x}_i^+ + b \geq 1 \tag{2.19}$$

$$\boldsymbol{\omega} \cdot \boldsymbol{x}_i^- + b \leq -1 \tag{2.20}$$

where $\boldsymbol{\omega} = (\omega_1, \omega_2, \ldots, \omega_M)$ (M x 1) is the normal vector of the desired hyperplane, b is the distance from the origin to the hyperplane and is parallel to $\boldsymbol{\omega}$, $\boldsymbol{x}_i^+$ are samples for which $y_i = 1$ and $\boldsymbol{x}_i^-$ are samples for which $y_i = -1$. For simplicity, eq.(2.19) and eq.(2.20) can be rewritten as a single expression through multiplication of y_i according to:

$$y_i(\boldsymbol{\omega} \cdot \boldsymbol{x}_i + b) - 1 \geq 0 \tag{2.21}$$

The orientation and placement of the hyper plane in the variable space is defined by a subset of samples, positive and negative, called support vectors (SVs) that defines the boundaries according to:

$$y_{SV}(\boldsymbol{\omega} \cdot \boldsymbol{x}_{SV} + b) - 1 = 0 \tag{2.22}$$

The maximal width of the margin is defined by the SVs and will always be equal to $2/\|\boldsymbol{\omega}\|_2$ where $\|\boldsymbol{\omega}\|_2$ is the magnitude of $\boldsymbol{\omega}$. Therefore, in order to maximise the separation of samples, $\|\boldsymbol{\omega}\|_2$ needs to be minimised. Based on the defined width of the margin and the decision boundary in eq.(2.21), the primal optimisation problem can be formulated according to:

$$\begin{aligned} \underset{\boldsymbol{\omega},b}{\text{minimise}} \quad & \frac{1}{2}\|\boldsymbol{\omega}\|_2^2 \\ \text{subject to} \quad & y_i(\boldsymbol{\omega} \cdot \boldsymbol{x}_i + b) - 1 \geq 0 \end{aligned} \tag{2.23}$$

where $\frac{1}{2}\|\boldsymbol{\omega}\|_2^2$ is the objective function for which $\boldsymbol{\omega}$ and b are the variables that needs to be optimised and eq.(2.21) has been added as linear constraints. As can be observed, the original minimisation of $\|\boldsymbol{\omega}\|_2$ has been slightly modified to $\|\boldsymbol{\omega}\|_2^2$ instead which transforms the optimization into a quadratic programming (QP) problem, meaning that the solution space becomes convex and a global solution can always be produced. The primal can be solved directly using QP designed solvers to find the minimum value in the objective function. However, solving the primal can be computationally cumbersome if M is large which is usually

the case where data sets today can consist of thousands of variables. The QP problem in eq.(2.23) can instead be reformulated by using Lagrange Multipliers to define the dual problem according to:

$$\begin{aligned} \underset{\boldsymbol{\alpha}}{\text{maximise}} \quad & W(\boldsymbol{\alpha}) = \sum_{i=1}^{N} \alpha_i - \frac{1}{2} \sum_{i,j=1}^{N} \alpha_i \alpha_j y_i y_j \boldsymbol{x}_i \cdot \boldsymbol{x}_j \\ \text{subject to} \quad & \alpha_i \geq 0, \qquad i = 1, \dots, N \\ & \sum_{i=1}^{N} \alpha_i y_i = 0 \end{aligned} \tag{2.24}$$

where $W(\boldsymbol{\alpha})$ is the new optimisation function called Wolf's dual and $\boldsymbol{\alpha} = (\alpha_1, \alpha_2, \dots, \alpha_N)$ (N x 1) are multipliers for the constraints in expression eq.(2.23). For detailed formulation of the dual with Lagrange Multipliers (see Appendix D.3). It can be observed in expression eq.(2.24) that the dual is only dependent on the samples in the data set to form of the inner product between pairs of samples. This is an especially beneficial quality of the dual formulation due to $N \ll M$ in many data sets today. For support vectors, the values of α_i will be non-zero and $\boldsymbol{x}_i \in \boldsymbol{x}_{SV}$ while samples laying further away from the boundaries will have α_i equal to zero. The optimal solution for $\boldsymbol{\alpha}$ is obtained by using the Sequential Minimal Optimisation (SMO) algorithm which is specially designed to handle QP problems in SVC for both classification and regression (Platt, 1998, Shevade et al., 2000). The variables $\boldsymbol{\omega}$ and b can then be solved using the identified support vectors.

Class prediction of an unknown sample, $\boldsymbol{x}_u$, can then be performed according to:

$$D(\boldsymbol{x}) = \text{sign}(\boldsymbol{\omega} \cdot \boldsymbol{x} + b) = \text{sign}\left(\sum_{i=1}^{N} \alpha_i y_i \boldsymbol{x}_i \cdot \boldsymbol{x}_u + b \right) \tag{2.25}$$

where $D(\boldsymbol{x})$ is the decision function for a sample $\boldsymbol{x}$. Substitution of $\boldsymbol{\omega}$ has been performed with eq.(D.13) in the last equality of eq.(2.25). This also shows that the solution of the hyper plane is dependent only on the samples.

2.3.2.2 Soft Margin

So far only cases that are linearly separable have been discussed. For non-separable classification problems such as the example illustrated in Figure 2.4b where a positive sample (red) is mixed in with the negative samples (blue) the QP problem in eq.(2.23) will fail. Cortes

and Vapnik adjusted for this by introducing slack variables, ξ_i, to allow for some misclassification and is known as soft margin classifier (Cortes and Vapnik, 1995). The QP problem in eq.(2.23) then becomes:

$$\begin{aligned} \underset{\boldsymbol{\omega},b,\boldsymbol{\xi}}{\text{minimise}} \quad & \frac{1}{2}\|\boldsymbol{\omega}\|_2^2 + C\sum_{i=1}^{N}\xi_i \\ \text{subject to} \quad & y_i(\boldsymbol{\omega}\cdot\boldsymbol{x}_i + b) \geq 1 - \xi_i \\ & \xi_i \geq 0 \end{aligned} \tag{2.26}$$

where C is the cost parameter which is a regularisation term used to penalise the QP problem and must be greater than zero. The second term in the objective function of eq.(2.26) is known as the loss function and controls the misclassification of samples. It can be observed from the constraints in eq.(2.26) that samples now are allowed to fall inside of the margin, $\xi_i < 1$, as well as to be misclassified, $\xi_i > 1$. The cost parameter, C, controls the flexibility where a small value introduces more slack, meaning more samples will have $\xi_i > 0$ and therefore allows for more misclassification. A large value of C on the other hand forces the slack variables to become closer to zero and classification becomes stricter. If C is set to infinity the QP problem in eq.(2.26) becomes equivalent to eq.(2.23) which appropriately is known as a hard margin classifier.

Formulation of the Lagrange dual in eq.(2.26) then becomes:

$$\begin{aligned} \underset{\boldsymbol{\alpha}}{\text{maximise}} \quad & \mathcal{L}(\boldsymbol{\alpha}) = \sum_{i=1}^{N}\alpha_i - \frac{1}{2}\sum_{i,j=1}^{N}\alpha_i\alpha_j y_i y_j \boldsymbol{x}_i\cdot\boldsymbol{x}_j \\ \text{subject to} \quad & 0 \leq \alpha_i \leq C, \qquad i = 1,\dots,N \\ & \sum_{i=1}^{N}\alpha_i y_i = 0 \end{aligned} \tag{2.27}$$

where can be observed that only the constraints for α_i has changed and now has an upper limit of C when compared to the dual of the hard margin QP problem in eq.(2.23). The solution of $\boldsymbol{\alpha}$ is obtained using the SMO algorithm.

2.3.2.3 Kernel Trick for non-linearity

For non-linear application of SVC, the so-called Kernel trick can be used to transform the samples from the original variable space to a higher dimensional feature space with the use of a Kernel function, K, according to:

$$\mathrm{K}(\boldsymbol{x}_i, \boldsymbol{x}_j) = \varphi(\boldsymbol{x}_i) \cdot \varphi(\boldsymbol{x}_j) \tag{2.28}$$

where $\varphi(\boldsymbol{x}_i) = (\varphi_1(\boldsymbol{x}_i), \varphi_2(\boldsymbol{x}_i), \dots, \varphi_L(\boldsymbol{x}_i))$ is called the feature map of $\boldsymbol{x}_i$ and L is the number of features for which $L > M$. An example of a non-linear mapping from a two-dimensional to a three-dimensional feature space is illustrated in Figure 2.5 where the classification problem becomes linearly separable.

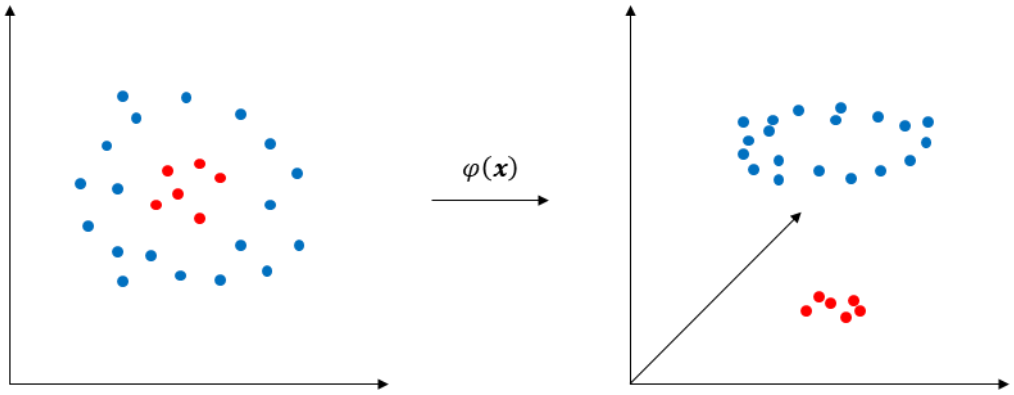

Figure 2.5. Transformation with a non-linear mapping function, $\varphi(\boldsymbol{x})$, from a two-dimensional variable space to a three-dimensional feature space where the positive samples (red) become linearly separable from the negative samples (blue).

A requirement of the Kernel function is that the corresponding gram matrix, $\boldsymbol{\Gamma}$, shown in eq.(2.29) must be symmetric, e.g. $\mathrm{K}(\boldsymbol{x}_1, \boldsymbol{x}_2) = \mathrm{K}(\boldsymbol{x}_2, \boldsymbol{x}_1)$, and positive semi-definite (Shawe-Taylor and Cristianini, 2004).

$$\boldsymbol{\Gamma} = \begin{bmatrix} \mathrm{K}(\boldsymbol{x}_1, \boldsymbol{x}_1) & \mathrm{K}(\boldsymbol{x}_1, \boldsymbol{x}_2) & \cdots & \mathrm{K}(\boldsymbol{x}_1, \boldsymbol{x}_N) \\ \mathrm{K}(\boldsymbol{x}_2, \boldsymbol{x}_1) & \mathrm{K}(\boldsymbol{x}_2, \boldsymbol{x}_2) & & \mathrm{K}(\boldsymbol{x}_2, \boldsymbol{x}_N) \\ \vdots & & \ddots & \vdots \\ \mathrm{K}(\boldsymbol{x}_N, \boldsymbol{x}_1) & \mathrm{K}(\boldsymbol{x}_N, \boldsymbol{x}_2) & \cdots & \mathrm{K}(\boldsymbol{x}_N, \boldsymbol{x}_N) \end{bmatrix} \tag{2.29}$$

Two popular kernels often used in research are the polynomial kernel in eq.(2.30) where d is the polynomial degree and the radial basis function (RBF) kernel in eq.(2.31) where σ is the peak spread. For convenience, the kernel parameter will be referred to as γ throughout this thesis.

$$\mathrm{K}(\boldsymbol{x}_i, \boldsymbol{x}_j) = (\boldsymbol{x}_i \cdot \boldsymbol{x}_j + 1)^d = \left(\sum_{l=1}^{M} x_{ik} x_{jk} + 1\right)^d \tag{2.30}$$

$$\mathrm{K}(\boldsymbol{x}_i, \boldsymbol{x}_j) = \exp\left(-\frac{\|\boldsymbol{x}_i - \boldsymbol{x}_j\|_2^2}{2\sigma^2}\right) = \exp\left(-\frac{1}{2\sigma^2}\sum_{l=1}^{M}(x_{ik} - x_{jk})^2\right) \tag{2.31}$$

Cortes and Vapnik showed in 1995 that the dot products in the dual formulations of the hard margin in eq.(2.24) and the soft margin in eq.(2.27) classifiers could effectively be replaced with a kernel function, K, in order to train the SVC algorithm (Cortes and Vapnik, 1995). The decision boundary function in eq.(2.25) can then be reformulated to include the non-linear hyper plane for classification of the samples according to:

$$D(\boldsymbol{x}) = \mathrm{sign}\left(\sum_{i=1}^{N} \alpha_i y_i \, \mathrm{K}(\boldsymbol{x}_i, \boldsymbol{x}) + b\right) \tag{2.32}$$

2.3.2.4 Applicability of SVC in this research

The main strength of SVC is that the method is robust in high-dimensional problems where the placement of the decision boundary is decided by a small subset of samples (support vectors). This results in better generalisation performance compared to that of PLS-DA (Gromski et al., 2015). However, a disadvantage of SVC is that the interpretation of important variables is difficult due to lack of supporting statistics of variable contribution to the response and can only be assessed based on the magnitude of the weights, $\boldsymbol{\omega}$. This becomes even more difficult if a non-linear kernel is applied due to the generation of extra variables and the non-linear nature of the decision boundary (Maldonado and Weber, 2009).

Multiple toolboxes exist for implementation of SVM. In a study by Steinwart and Thomann (2017), the authors compared to execution times and performances of several popular SVM toolboxes that are available for free. In this research, the LibSVM toolbox was applied, though not being the fastest, is has been extensively documented and continuously updated in order to provide more robust solutions (Chang and Lin, 2011).

Similar to that of PLS-DA, class imbalances present in the data set of interest need to be considered when using soft-margin SVC. Several strategies exist to approach this where separate cost values, C, for each class can be applied, similar to that of prior probabilities in PLS-DA discussed in Section 2.3.1.2 (Akbani et al., 2004). Alternatively, a higher loss penalties

can be assigned to the minority class samples, thus effectively changing the optimal solution to the QP problem to accept less misclassification of the minority class (Hsu et al., 2003). In this research, the former approach was used due to being similar to that of Bayes rule used in PLS-DA, thus allowing for a fairer comparison between the classification methods.

Another important consideration is the selection of the cost parameter C and potential kernel parameters which greatly affects the performance of the model. Several alternatives for optimisation of are available but where the grid search method (Hsu et al., 2003) and Bayesian optimisation (Cawley and Talbot, 2007, Czarnecki et al., 2015) are most commonly used. In the grid search approach, ranges containing several values for each of the parameters are defined to form a grid of different parameter permutations which are validated via cross-validation in order to identify the best parameters (see Section 2.5). The Bayesian optimisation on the other hand uses the information available from previous parameter evaluations as well as local gradient approximations which allows the algorithm to find a parameter solution with relatively few evaluations and thus resulting in being faster than the grid search approach (Snoek et al., 2012). However, due to the fact that the solution space of the parameters is often non-convex, the Bayesian optimisation approach is at risk of selecting a local solution. The grid search approach was therefore used in this research due to being more robust and extensive in evaluation of parameter permutations (Hsu et al., 2003).

2.3.3 Multiclass Classification Problems

Many classification problems usually consist of more than two classes which need to be separated. However, many classification techniques, including SVC, will only work for binary classification problems. To circumvent this problem, two approaches referred to as "One versus Rest" (OvR) and "One versus One" (OvO) are often applied in research (Statnikov et al., 2004, Galar et al., 2011).

In the OvO strategy, illustrated in Figure 2.6a, an individual classification model is developed for each unique class-pair. This results in a total of $\frac{1}{2}c(c-1)$ models where c is the number of classes in the data set. Class assignment of samples is decided by the number of times a class has been chosen in the developed models. This method tends to work best with an odd number of classes due to a lower risk of a sample being unassigned if the sample proves difficult to classify.

In the OvR strategy, illustrated in Figure 2.6b, an individual model is developed for each class with the remaining classes pooled together which results in a total of c models being developed. Class assignment can be performed using the intrinsic properties of the used classification

method. For PLS-DA, class assignment can be performed using the generated posterior probabilities which will be closer to one in the model representing the class of interest while being closer to zero in the remaining models. In SVC, class assignment can be performed using the generated decision values which will be positive in the model representing the class of interest while having negative values in the remaining models.

In a study performed by Hsu and Lin (2002), both OvR and OvO were extensively tested on several different data set with SVC. It was observed that both strategies had comparable performance thus making it difficult to identify the superior strategy. In this research, the OvR strategy was selected due to two reasons: 1) Each class is represented by an individual model, thus making the evaluation of the individual classes simpler due to that none of the samples will be unassigned a class. 2) There is less risk of over-fitting of the model due to lack of samples (see Section 2.5).

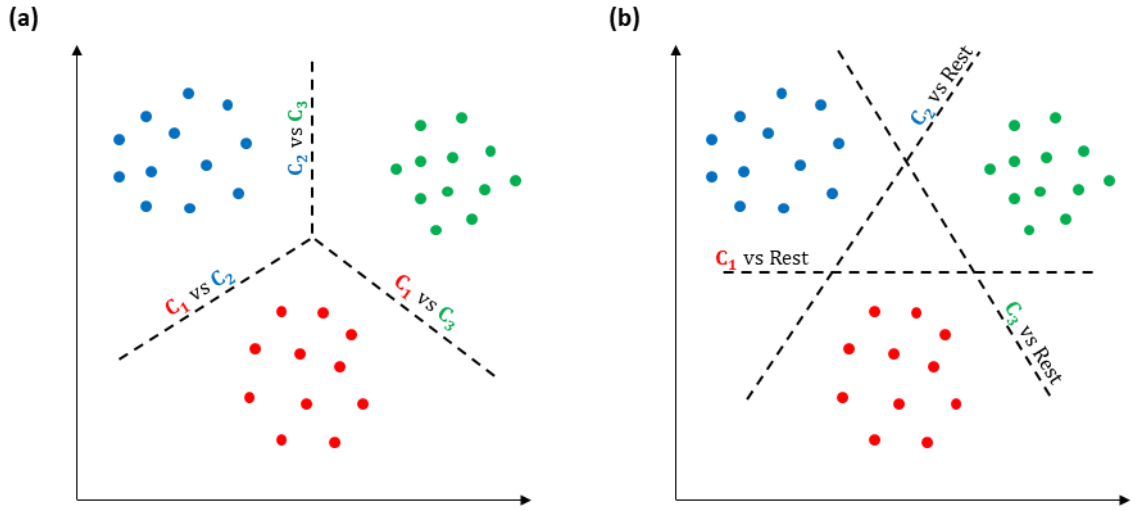

Figure 2.6. Classification strategies for multiclass problems with **(a)** One versus One and **(b)** One versus Rest. Decision boundaries are shown as dashed black lines (adapted from Statnikov et al. (2004)).

2.4 Regression

QSAR model development linking the measurements of the selected response data to the structural descriptors of mAbs was performed with dedicated regression methods. In this research, the theory of PLS and SVR have been covered and their applicability to QSAR modelling have been reviewed.

2.4.1 Partial Least Square Regression

PLS is one of the most widely used regression tools in the field of chemometrics due to its simplicity and strong diagnostic capabilities. PLS was first introduced by Wold as a method to model the relationship between $\boldsymbol{X}$ and $\boldsymbol{Y}$ through matrix decomposition similar to that of PCA (Wold et al., 1984). Unlike Multiple Linear Regression (MLR), PLS will still work even if the

variables are more numerous than the samples (N > M), the variables are correlated and noisy. The PLS algorithm is also able to model several response (dependent) variables in $\boldsymbol{Y}$ (D > 1) simultaneously (Wold et al., 2001). Two common algorithms used to perform PLS modelling are NIPALS (Geladi and Kowalski, 1986) and SIMPLS (De Jong, 1993). In this section, PLS implementation will be explained according to the NIPALS algorithm.

2.4.1.1 Theory

Like PCA, PLS will find a set of new variables which are linear combinations of the original variables in $\boldsymbol{X}$ and the response variables in $\boldsymbol{Y}$ according to eq.(2.33) and eq.(2.34), respectively. These new variables are called Latent Variables (LVs) but will be referred to as components throughout this section.

$$\boldsymbol{X} = \boldsymbol{T}\boldsymbol{P}^T + \boldsymbol{E} = \sum_{r=1}^{R} \boldsymbol{t}_r \boldsymbol{p}_r^T + \boldsymbol{E} \tag{2.33}$$

$$\boldsymbol{Y} = \boldsymbol{U}\boldsymbol{Q}^T + \boldsymbol{H} = \sum_{r=1}^{R} \boldsymbol{u}_r \boldsymbol{q}_r^T + \boldsymbol{H} \tag{2.34}$$

where $\boldsymbol{T}$ (N x R) and $\boldsymbol{U}$ (N x R) are the score matrices of $\boldsymbol{X}$ and $\boldsymbol{Y}$, respectively, and where $\boldsymbol{t}_r$ (N x 1) and $\boldsymbol{u}_r$ (N x 1) are the individual scores for component r, $\boldsymbol{P}$ (M x R) and $\boldsymbol{Q}$ (D x R) are the loading matrices of $\boldsymbol{X}$ and $\boldsymbol{Y}$, respectively, where $\boldsymbol{p}_r$ (M x 1) and $\boldsymbol{q}_r$ (D x 1) are the individual loadings for component r. $\boldsymbol{E}$ (N x M) and $\boldsymbol{H}$ (N x D) are the residual matrices of $\boldsymbol{X}$ and $\boldsymbol{Y}$, respectively. In order to have good prediction of $\boldsymbol{Y}$, the corresponding components in the score matrices, $\boldsymbol{T}$ and $\boldsymbol{U}$, needs to be calculated in such a way so that the relationship between them becomes linear and is illustrated in Figure 2.7 for the first component.

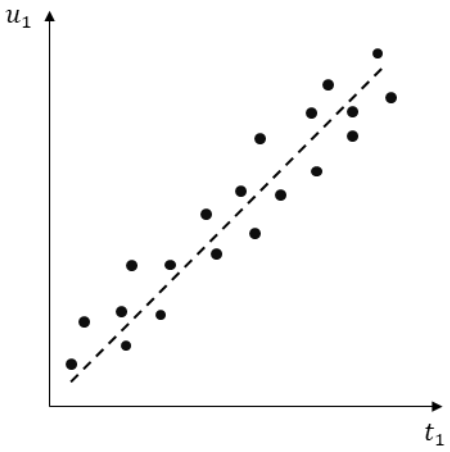

Figure 2.7. Correlation of scores of the first component from the decomposed $\boldsymbol{X}$ and $\boldsymbol{Y}$ blocks with PLS.

Eq.(2.34) can then be reformulated according to:

$$\boldsymbol{Y} = \boldsymbol{T}\boldsymbol{Q}^T + \boldsymbol{F} = \sum_{r=1}^{R} \boldsymbol{t}_r \boldsymbol{q}_r^T + \boldsymbol{F} \tag{2.35}$$

$$\boldsymbol{T} \neq \boldsymbol{X}\boldsymbol{P} \tag{2.36}$$

where $\boldsymbol{F}$ (N x D) is the new residual matrix of $\boldsymbol{Y}$. This means that the X-loadings, $\boldsymbol{p}_r$ and the Y-loadings, $\boldsymbol{q}_r$, of a component r needs to be calculated so that the captured variation in $\boldsymbol{X}$ is correlated to the captured variation in $\boldsymbol{Y}$. Thus, $\boldsymbol{T}$ cannot be calculated in the same was as in PCA eq.(2.36). Instead, PLS introduces a new variable, $\boldsymbol{W}$ (M x R), which are known as weights that describes the relationship between $\boldsymbol{X}$ and $\boldsymbol{Y}$. The weights of the first component, $\boldsymbol{w}_1$, are calculated as the first eigenvector, $\boldsymbol{v}_1$, from $\boldsymbol{X}^T\boldsymbol{Y}\boldsymbol{Y}^T\boldsymbol{X}$ which is proportional to the product of the combined covariance matrix, $\boldsymbol{\Sigma}_{XY}$ (M x D) according to:

$$\boldsymbol{\Sigma}_{XY}\boldsymbol{\Sigma}_{XY}^T = \frac{1}{(N-1)^2}\boldsymbol{X}^T\boldsymbol{Y}\boldsymbol{Y}^T\boldsymbol{X} \propto \boldsymbol{X}^T\boldsymbol{Y}\boldsymbol{Y}^T\boldsymbol{X} \tag{2.37}$$

Eq.(2.37) is only valid if both $\boldsymbol{X}$ and $\boldsymbol{Y}$ have been centred prior to the calculation (see Section 2.7). For more information on eigenvectors, refer to Appendix D.1. It can be shown that the calculation of $\boldsymbol{w}_1$ can be simplified by using $\boldsymbol{\Sigma}_{XY}$ directly according to:

$$\boldsymbol{w}_1 = \frac{\boldsymbol{X}^T\boldsymbol{Y}_f}{\left\|\boldsymbol{X}^T\boldsymbol{Y}_f\right\|_2} \tag{2.38}$$

where $\boldsymbol{Y}_f$ is the response variable with the largest magnitude when D > 1. If only one response variable is available (D = 1), then $\boldsymbol{Y}_f = \boldsymbol{Y}$. The X-scores, $\boldsymbol{t}_1$, can be calculated once $\boldsymbol{w}_1$ according to eq.(2.39). The X-loadings can then be acquired by projecting $\boldsymbol{X}$ onto $\boldsymbol{t}_1$ according to (2.40).

$$\boldsymbol{t}_1 = \boldsymbol{X}\boldsymbol{w}_1 \tag{2.39}$$

$$\boldsymbol{p}_1 = \frac{\boldsymbol{X}^T\boldsymbol{t}_1}{\boldsymbol{t}_1^T\boldsymbol{t}_1} \tag{2.40}$$

Trough substitution of eq.(2.39) into eq.(2.35), the Y-loadings and Y-scores can be calculated by projection of $\boldsymbol{Y}$ onto $\boldsymbol{t}_1$ and $\boldsymbol{q}_1$ according to expression (2.41) and (2.42), respectively.

$$\boldsymbol{q}_1 = \frac{\boldsymbol{Y}^T\boldsymbol{t}_1}{\boldsymbol{t}_1^T\boldsymbol{t}_1} \tag{2.41}$$

$$\boldsymbol{u}_1 = \frac{\boldsymbol{Y}^T\boldsymbol{q}_1}{\boldsymbol{q}_1^T\boldsymbol{q}_1} \tag{2.42}$$

$\boldsymbol{X}$ and $\boldsymbol{Y}$ are then deflated in order to calculate following components according to eq.(2.43) and eq.(2.44), respectively.

$$\boldsymbol{E}_1 = \boldsymbol{X} - \boldsymbol{t}_1\boldsymbol{p}_1^T \tag{2.43}$$

$$\boldsymbol{F}_1 = \boldsymbol{Y} - \boldsymbol{u}_1\boldsymbol{q}_1^T \tag{2.44}$$

Where $\boldsymbol{E}_1$ and $\boldsymbol{F}_1$ are the residual matrices of $\boldsymbol{X}$ and $\boldsymbol{Y}$, respectively after deflation with the first component. The weights for the second component are then calculated according to eq.(2.45) where $\boldsymbol{t}_2, \boldsymbol{p}_2, \boldsymbol{q}_2$ and $\boldsymbol{c}_2$ are calculated as previously shown with regards to $\boldsymbol{E}_1$ and $\boldsymbol{F}_1$ instead of $\boldsymbol{X}$ and $\boldsymbol{Y}$.

$$\boldsymbol{w}_2 = \frac{\boldsymbol{E}_1^T\boldsymbol{F}_1}{\|\boldsymbol{E}_1^T\boldsymbol{F}_1\|_2} \tag{2.45}$$

However, due to the deflation of $\boldsymbol{X}$, the individual component weights, $\boldsymbol{w}_r$, will not be directly related to $\boldsymbol{X}$ but instead related to the corresponding residual matrix from the previous component, $\boldsymbol{E}_{r-1}$. The weights can however be transformed to directly relate to $\boldsymbol{X}$ according to:

$$\boldsymbol{W}^* = \boldsymbol{W}(\boldsymbol{P}^T\boldsymbol{W})^{-1} \tag{2.46}$$

where $\boldsymbol{W}^*$ (M x R) is directly related to $\boldsymbol{X}$. The X-scores in expression (2.39) can then be reformulated to:

$$\boldsymbol{T} = \boldsymbol{X}\boldsymbol{W}^* = \boldsymbol{X}\boldsymbol{W}(\boldsymbol{P}^T\boldsymbol{W})^{-1} \tag{2.47}$$

The prediction of $\boldsymbol{Y}$ in eq.(2.35) can then be rewritten to the more formal expression:

$$\boldsymbol{Y} = \boldsymbol{X}\boldsymbol{B} + \boldsymbol{F} \tag{2.48}$$

where the regression coefficients, $\boldsymbol{B}$, are estimated according to:

$$\boldsymbol{B} = \boldsymbol{W}(\boldsymbol{P}^T\boldsymbol{W})^{-1}\boldsymbol{Q}^T \tag{2.49}$$

2.4.1.2 Applicability of PLS in this research

The main strength of PLS is its simplicity and diagnostic capabilities. Due to being a decomposition method, the diagnostic capabilities that are inherent in the PCA are also a feature of PLS (Bro and Smilde, 2014). This greatly aids in identification of outliers and samples that need to be further investigated. Contribution of variables to the prediction can be directly assessed in the PLS model with Variable Importance in Projection (VIP) and Selective Ratio (SR) (Farres et al., 2015). It is, however important to remember that both VIP and SR are linked to the performance of the model and therefore if low, the resulting VIP and SR values will be meaningless (Andersen and Bro, 2010). Alternatively, the contributions from individual components can be explored based on the corrected weights, $\boldsymbol{W}^*$, as they represent the linear combinations of variables related to the scores, $\boldsymbol{T}$.

A common problem when PLS is used in QSAR applications is the sheer number of independent variables that are used as input. This can be potentially detrimental and PLS

models can become over-fitted due to chance-correlation between redundant or noisy descriptors in $\boldsymbol{X}$ and the response, $\boldsymbol{Y}$ (Faber and Rajko, 2007). Therefore, in many QSAR instances, variable selection strategies become necessary in order to reduce the number of redundant or noisy variables (see Section 2.9). Bauer et al. (2017)applied PLS for prediction of protein diffusion coefficients used to understand protein-protein interactions based on independent variables generated from protein crystal structures. The authors used the VIP Scores to select highly contributing descriptors in order to increase model performance to a R^2 value of 0.9, thus indicating high correlation between $\boldsymbol{X}$ and $\boldsymbol{Y}$ (refer to Section 2.6.1 for more information on R^2). In another study, Mazza et al. (2001) applied PLS for prediction of retention times in ion-exchange chromatography based on independent variables generated from protein crystal structures (Mazza et al., 2001). The authors applied Genetic Algorithm to reduce the number of noisy independent variables which resulted in a model performance of R^2 value around 0.94. Application of PLS in this research was therefore performed with variable reduction (see Section 2.8) and variable selection (see Section 2.9) in order to reduce noise and redundancy able to affect model performance.

2.4.2 Support Vector Machines for Regression

SVM for regression (SVR) is an extension of SVC which was first introduced by Drucker et al. (1997). This method applies the same fundamental principles that were used in SVC and does not depend on the variable dimensionality but only on the samples that are presented to the algorithm.

2.4.2.1 Theory

The theory for SVR is very similar to that of SVC (see Section 2.3.2.1). The main difference is that instead of defining the largest margin used to separate the samples, SVR will define a tube in which the majority of the samples will be located. The tube is defined by the two constraints shown in eq.(2.50) and eq.(2.51) and illustrated in Figure 2.8 as the dashed blue line and the dashed red line, respectively.

$$y_i - \boldsymbol{\omega}^T \boldsymbol{x}_i - b \leq \epsilon \tag{2.50}$$

$$\boldsymbol{\omega}^T \boldsymbol{x}_i + b - y_i \leq \epsilon \tag{2.51}$$

ϵ is called the insensitive loss where $\epsilon > 0$ and is set be the user. As can be observed in Figure 2.8, the width of the tube is defined by the insensitive loss and will be equal to 2ϵ. In SVR,

slack variables (ξ_i^* and ξ_i) are commonly introduced due to noise normally being present in both $\boldsymbol{X}$ and $\boldsymbol{Y}$ which can be difficult for a hard margin regressor to fit.

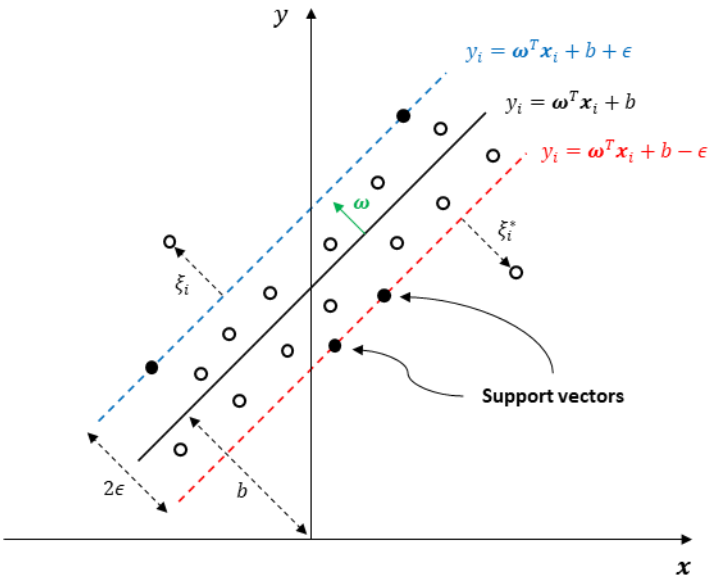

Figure 2.8. Placement of regression tube in SVR defined by two constraints (red and blue dashed lines) that encompasses the majority of the samples and where samples falling outside of the tube are penalised by the slack variables ξ_i^* and ξ_i. Support vectors are indicated as the filled black circles and the green vector perpendicular to the black regression line represents the support vector weights, $\boldsymbol{\omega}$ (adapted from Drucker et al. (1997)).

A QP problem can then be formulated according to eq.(2.52) which is very similar to the QP problem stated in eq.(2.26) for SVC. The only difference is the addition of an extra constraint in order to penalise samples on either side of the tube.

$$\begin{aligned} \underset{\boldsymbol{\omega},b,\boldsymbol{\xi}}{\text{minimise}} \quad & \frac{1}{2}\|\boldsymbol{\omega}\|_2^2 + C\sum_{i=1}^{N}(\xi_i + \xi_i^*) \\ \text{subject to} \quad & \boldsymbol{\omega}^T\boldsymbol{x}_i + b - y_i \leq \epsilon + \xi_i \\ & y_i - \boldsymbol{\omega}^T\boldsymbol{x}_i - b \leq \epsilon + \xi_i^* \\ & \xi_i, \xi_i^* \geq 0 \end{aligned} \tag{2.52}$$

For samples that are placed above or below the tube the slack variables ξ_i and ξ_i^* respectively, will become non-zero. For samples placed inside of the tube, ξ_i and ξ_i^* will equal zero and thus not affect the loss and is known as hinge or l_1-loss (Rosasco et al., 2004). The Lagrange dual to eq.(2.52) then becomes:

$$\begin{aligned}
\underset{\boldsymbol{\alpha},\boldsymbol{\alpha}^*}{\text{maximise}} \quad & W(\boldsymbol{\alpha},\boldsymbol{\alpha}^*) = -\epsilon\sum_{i=1}^{N}(\alpha_i^* + \alpha_i) + \sum_{i=1}^{N} y_i(\alpha_i^* + \alpha_i) \\
& \qquad -\frac{1}{2}\sum_{i,j=1}^{N}(\alpha_i^* + \alpha_i)(\alpha_i^* + \alpha_i)\boldsymbol{x}_i \cdot \boldsymbol{x}_j \qquad (2.53) \\
\text{subject to} \quad & 0 \le \alpha_i, \alpha_i^* \le C, \qquad i = 1, \dots, N \\
& \sum_{i=1}^{N}\alpha_i = \sum_{i=1}^{N}\alpha_i^*
\end{aligned}$$

where α_i and α_i^* are the Lagrange multipliers to the constraints in eq.(2.50) and eq.(2.51), respectively, and will both consist of N elements. For more information on Lagrange Multipliers, refer to Appendix D.3. The SMO algorithm is commonly used to solve for $\boldsymbol{\alpha}$ and $\boldsymbol{\alpha}^*$ due to being a QP problem (Platt, 1998). Similar to SVC, samples with non-zero values in α_i or α_i^* in the solution will be support vectors and used to define $\boldsymbol{\omega}$ and b. Prediction of an unknown sample, $\boldsymbol{x}_u$, can then be performed according to eq.(2.54) for linear regression.

$$f(\boldsymbol{x}_u) = \boldsymbol{\omega}^T\boldsymbol{x}_u + b = \sum_{i=1}^{N}(\alpha_i^* + \alpha_i)\boldsymbol{x}_i \cdot \boldsymbol{x}_u + b \qquad (2.54)$$

Or according to (2.55) for non-linear regression with a Kernel (see Section 2.3.2.3).

$$f(\boldsymbol{x}_u) = \boldsymbol{\omega}^T\varphi(\boldsymbol{x}_u) + b = \sum_{i=1}^{N}(\alpha_i^* + \alpha_i)\,\mathrm{K}(\boldsymbol{x}_i, \boldsymbol{x}_u) + b \qquad (2.55)$$

2.4.2.2 Applicability of SVR in this research

Many of the listed strengths and caveats presented for SVC will apply to SVR. This means that SVR has a high generalisation performance due to the selection of a small subset of samples that act as support vectors which also makes the method robust in high-dimensional problems. This makes SVR a popular choice in QSAR applications and it has been used extensively for prediction of chromatographic column performance (Robinson et al., 2017, Ladiwala et al., 2006, Chen et al., 2008, Woo et al., 2015a, Woo et al., 2015b, Chung et al., 2010). However, the authors highlighted that an initial variable selection step is necessary in order to reduce the number of non-correlated descriptors in order to increase performance.

Like the PLS method, the performance of SVR will suffer if too many redundant variables are present in data set, thus masking the independent variables that are correlated to the response. It has therefore been suggested to use variable selection techniques in order to reduce the number of redundant variables in high-dimensional data when using Support Vector Machine based methods (Zhang et al., 2016).

Determination of model parameters (C, γ and ϵ) in SVR can be performed through grid search with predefined ranges just as described in Section 2.3.2.4 for SVC. However, defining the range for ϵ is more complex due to being related to the intrinsic variation in the data. This is easier understood when observing the width of the tube in Figure 2.8 where the majority of samples are placed within the tube. More intuitively, this requires knowledge about the distribution of the residual values, ε_i, pertaining to any given prediction according to eq.(2.56) and should conform to $\varepsilon_i \sim N(0, \sigma_\varepsilon)$.

$$y_i = \hat{y}_i + \varepsilon_i \tag{2.56}$$

Cherkassky and Ma (2004) proposed that a linear model could be fitted to the data prior to applying SVR in order to investigate the distribution of the residuals (Cherkassky and Ma, 2004).

2.5 Cross Validation

Larson (1931) discovered that when training a model through "resubstitution" where all samples in a data set are used for both training and performance validation, the resulting model became heavily biased due to memorising the noise present in the data which led to extremely poor predictions of future samples. In order to circumvent this issue, cross-validation was introduced which provided a framework to train and validate models more robustly. Cross-validation has two main goals to achieve (Raschka, 2018):

1. Estimation of the generalisation error, i.e. the predictive performance of the model on future (unseen) data.
2. Model selection or tuning of the model complexity to increase model performance. This refers to the number of components to use in PCA, PLS and PLS-DA as well as selection of C, ϵ and kernel parameters in SVC and SVR to achieve optimal model performance. In literature, model complexity is also commonly referred to as the model hyperparameters. However, throughout this thesis the term model complexity will be used.

The core philosophy of cross validation (CV) lies in the practise of splitting the available data in order to train and validate a model. The core concepts will therefore first be explained with regards to the generalisation error and then how CV can be used to select model complexity.

2.5.1 Generalisation Error

One of the simplest and most commonly used technique to estimate the generalisation error of a model is the hold-out method. The method effectively splits the available data set into two parts where one is used to train the model and the other is used for validation. These will be referred to as the calibration set and test set illustrated in Figure 2.9 and will contain N_{Cal} and N_{Test} samples, respectively.

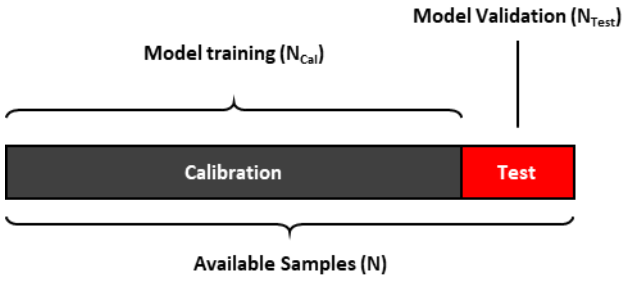

Figure 2.9. Splitting of all available samples in a data set into a calibration set for training (dark box) and a test set for model validation (red box) (adapted from Raschka (2018)).

Generally, the generalisation error can be estimated as the mean squared error (MSE) for regression problems which is presented in expression eq.(2.57) and illustrated as the red line in Figure 2.10a.

$$MSE_{Test} = \frac{1}{N_{Test}} \sum_{i=1}^{N_{Test}} (y_i - \hat{y}_i)^2 \qquad (2.57)$$

In eq.(2.57), $\hat{y}_i = f(\boldsymbol{x}_i)$, and is the predicted value of y_i based on a defined function such as one generated from PLS or SVR. For a classification problem, the generalisation error can be estimated based on the error rate presented in eq.(2.62) in Section 2.6.2 for methods such as PLS-DA and SVC. Similarly, the calibration error can be estimated by using the calibration samples instead and is shown as the black line in Figure 2.10a. As can be observed, the error of the test set will be large if the model complexity is to low which in turn also results in high calibration error. This usually occurs when the model fails to capture the correlation between $\boldsymbol{X}$ and $\boldsymbol{Y}$. Alternatively, the error of the test set will be high when the model is fitted to noise or redundant variables in the calibration samples, thus generating a small calibration error.

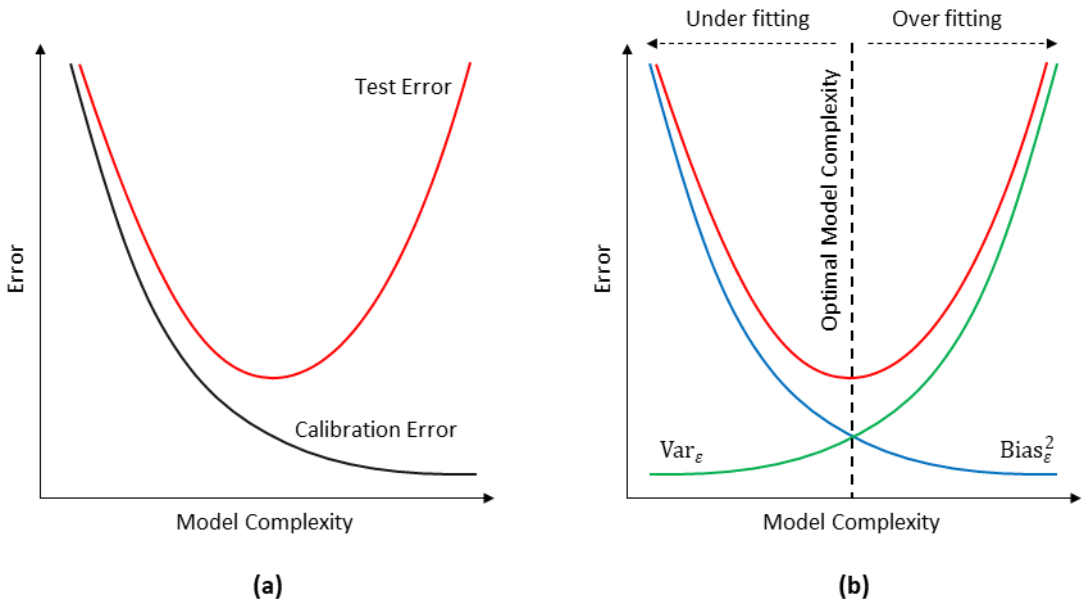

Figure 2.10. (a) Behaviour of the test or generalisation error (red line) compared to the fitted model error (black line) with regards to increasing model complexity. **(b)** Decomposition of the generalisation error (red line) into the two components model variance (green line) and model bias (blue line) (adapted from Hastie et al. (2009a)).

Eq.(2.57) can be further decomposed into the irreducible error (σ_{irr}^2), the variance of the error (Var_ε) and the bias of the error ($\mathrm{Bias}_\varepsilon$) according to:

$$\mathrm{Error}_{\mathrm{Test}} = \sigma_{irr}^2 + \mathrm{Var}_\varepsilon + \mathrm{Bias}_\varepsilon^2 \tag{2.58}$$

The irreducible error is inherent to the available data and cannot be removed from the model whereas the variance and bias are dependent on the model complexity as is illustrated in Figure 2.10b. More specifically, the bias is directly related to the fit of the model where a high bias means that the model fails to capture the relation between $\boldsymbol{X}$ and $\boldsymbol{Y}$ and the model becomes under-fitted. The variance, on the other hand, gives an estimation of the error related to fluctuations in samples where a high variance means that the model has been fitted to random noise and is therefore over-fitted. When selecting the model complexity, both the variance and bias should be as low as possible which is usually indicated as the minimum value of the error versus the model complexity illustrated as the red line in Figure 2.10b. This is more specifically referred to as the variance-bias trade-off and implies that a model cannot be trained perfectly and will always include some bias and variance (Hastie et al., 2009a).

It should be noted that the generalisation error is heavily dependent on the samples in the test as well as the sample sizes of the calibration and test sets. This is better understood when considering the resubstitution method investigated by Larson in 1931 where the model became

heavily biased due to being trained and validated with the same samples. If most of the samples are kept for model training, the test set might no longer be representative of the full sample population which might cause the model to become over-fitted. This is more commonly referred to as optimistic bias. Alternatively, if the majority of samples is placed in the test set for validation, then the model training might be negatively impacted due to lack of variability as the calibration set no longer represents the full sample population. This is more commonly referred to as pessimistic bias. The number of samples to use in the test and calibration set is widely discussed but a usual rule of thumb is to keep the majority of samples in the calibration set, thereby including most of the data variability for training. Usual calibration/test splits are 70/30 and 80/20 (Raschka, 2018).

In classification problems, it is important to consider the class distributions in the test and calibration sets which preferably should be conserved in the test and calibration sets when compared to the full sample set. This is known as sample stratification which ensures that class distributions are conserved in the test and calibration set. Not using sample stratification can have a negative impact on the model performance due to misrepresentation of available classes which becomes especially critical in unbalanced data sets where big difference in sample sizes can be present between specific classes. In the worst case, this might mean that a class is left out entirely from the test set and model validation based on the generalisation error becomes biased (Shahrokh and Dougherty, 2013).

Several strategies exist for splitting the available samples into calibration and test sets (Martin et al., 2012). One of the most common methods is random splitting where samples for the calibration and test sets are selected at random and only the number of samples belonging to each set needs to be specified. For the purposes of this research, the structured splitting approach of the Kennard-Stone algorithm (CADEX) has been applied due to being better suited to QSAR modelling problems compared to random splitting (Kennard and Stone, 1969, Martin et al., 2012). The CADEX algorithm selects samples based on the Euclidean distance between pairs of samples over the variable space of $\boldsymbol{X}$. Pair-wise samples with high distances are placed in the calibration set while pair-wise samples that have a short distance will have one sample placed in the test set and the other in calibration set. Thus, the CADEX algorithm ensures that most of the variability in the variable space is presented to the model during training as well as that selected test samples are represented by similar samples in the calibration set (Kennard and Stone, 1969).

2.5.2 Selection of Model Complexity

As mentioned previously, the calibration set is used to train the model. This means that selected calibration samples are explicitly used to tune the model complexity. This has an added benefit of model tuning being separate from the estimation of the generalization error and thus having lower risk of generating a biased model. Similar to the splitting of the full data set into a calibration and test set, the calibration set is further divided into smaller subsets or splits which are used to train the model and is known as re-sampling. An example of re-sampling for model training based on the K-fold method is presented in Figure 2.11. As can be observed the available samples in the calibration set is split into K smaller subsets. A sub-model is generated on all subsets except one (shown in red in Figure 2.11) which instead is used to validate the sub-model in the same way as the test set is used to estimate the generalization error described previously. This is repeated until all subsets have been used for validation once, thus resulting in K sub-models and K error estimations. The described repletion of sub-model development and validation is usually referred to as the inner cross validation loop. An average is usually calculated from the sub-model errors and represents the model performance for a specific selection of model complexity. The estimated error will behave similarly to the generalisation error illustrated in Figure 2.10a and Figure 2.10b and can be decomposed in the same way as shown in eq.(2.58). This means that both the bias and variance can be controlled explicitly through choice of the model complexity where the optimal model parameter set will have the lowest error illustrated in Figure 2.10b as the red line. It is important to note, however, that the minimum of the test error and the minimum of the cross-validation error is not guaranteed to overlap with each other with regards to the model complexity. This is a complex problem which is very dependent on the splitting of samples into calibration and test sets as well as the re-sampling method used for training the model.

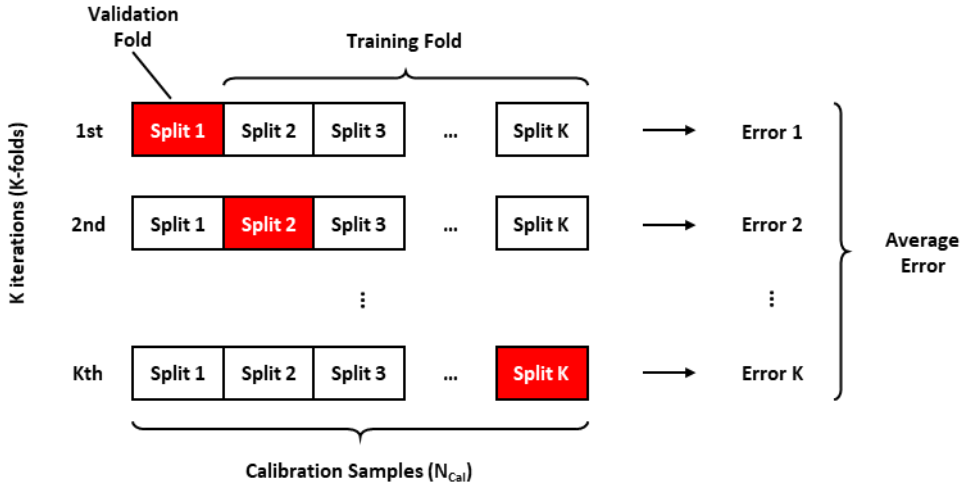

Figure 2.11. K-fold cross-validation resampling of the calibration samples for model training (adapted from Raschka (2018)).

Several strategies for the inner cross validation loop exist where some of the most commonly used are Leave-One-Out (LOO), K-fold and repeated K-fold (Wong, 2015).

2.6 Model Validation Metrics

In order to accurately evaluate trained models, several metrics for both regression and classification have been presented below.

2.6.1 Regression Metrics

The root mean squared error (RMSE) represents the variation of the error observed between the measured and predicted responses and is shown in eq.(2.59). The RMSE is commonly used to assess the model complexity due to direct evaluation of the differences between measured and predicted values.

$$RMSE = (MSE)^{\frac{1}{2}} = \left(\frac{1}{N}\sum_{i}(y_i - \hat{y}_i)^2\right)^{\frac{1}{2}} \tag{2.59}$$

The squared Pearson Correlation coefficient (R^2) provides a measure of the correlation between the measured and predicted responses and is presented in eq.(2.60). The R^2 metric can take on values between zero and one where a value closer to zero represents low correlation and poor model fit while a zero closer to one indicates strong correlation and a good model fit.

$$R^2 = \left(\frac{\sum_i \left(y_i - E(y)\right)\left(\hat{y}_i - E(\hat{y})\right)}{\sqrt{\left(\sum_i y_i^2 - E(y)^2\right)}\sqrt{\left(\sum_i \hat{y}_i^2 - E(\hat{y})^2\right)}} \right)^2 \tag{2.60}$$

$$\text{where} \quad E(y) = \frac{1}{N}\sum_{i=1}^{N} y_i$$

$$\text{and} \quad E(\hat{y}) = \frac{1}{N}\sum_{i=1}^{N} \hat{y}_i$$

The coefficient of determination (Q^2) provides a measure of well the model is able to explain the variation in the response vector and has been presented in eq.(2.61). Q^2 can attain negative values which is an indication that the model performs worse than if all responses would have been predicted as the mean of the measured responses, in which case the Q^2 would attain a value of zero. A value closer to one indicates good model fit and that high correlation between $\boldsymbol{X}$ and $\boldsymbol{Y}$.

$$Q^2 = 1 - \frac{SS_{res}}{SS_{tot}} = 1 - \frac{\sum_{i=1}^{N}(y_i - \hat{y}_i)^2}{\sum_{i=1}^{N}\left(y_i - E(y)\right)^2} \tag{2.61}$$

2.6.2 Classification Metrics

Validation of classification models are fundamentally different from regression models where instead the performance is evaluated based on the number of correctly classified and misclassified samples. In a binary classification problem, the classes are usually referred to as positive and negative. The predictions can therefore be categorised according to four definition depending on the true class of the samples: True positives (TP) are the number of positive samples that were correctly classified, False positives (FP) are the number of negative samples incorrectly classified as positive, True negatives (TN) are the number of negative samples correctly classified as positive and False negatives (FN) are the number of positive samples incorrectly classified as negative. These four values lie at the core of all model evaluation for classification problem and is usually presented in the form of a confusion matrix. For evaluation of a multiple classification problems, the OvR strategy can be implemented in order to generate a confusion matrix for each class. An example of this is presented in Figure 2.12a in which the predictions of three classes have been presented in a confusion matrix. By defining Class 1 as

the positive class and the negative class as Class 2 and Class 3, a binary representation for the predictions of class 1 can be evaluated which is illustrated in Figure 2.12b.

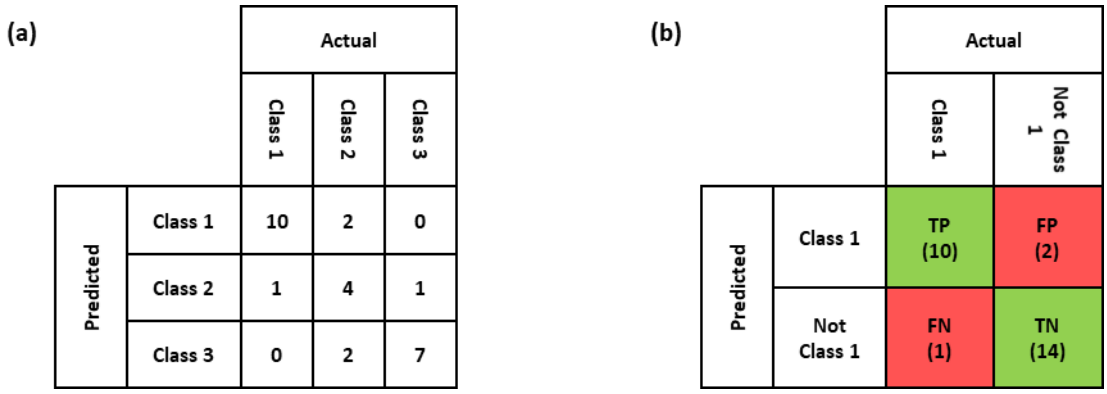

Figure 2.12. Representation of a confusion matrix as an overview of model performance for **(a)** multiple classes of **(b)** two classes (adapted from Fawcett (2006)).

A common classification metric used in research is the Error rate (ER) which represents the proportion of samples which were incorrectly classified and can take a value between 0 (all samples misclassified) and 1 (all samples correctly classified). Calculation of ER was performed according to eq.(2.62).

$$\text{ER} = \frac{FP + FN}{TP + TN + FP + FN} \tag{2.62}$$

The Sensitivity (Sen) represents the proportion of positive cases that were correctly identified and can take a value between 0 (all samples misclassified) and 1 (all samples correctly classified). Calculation of Sen was performed according to eq.(2.63).

$$\text{Sen} = \frac{TP}{TP + FN} \tag{2.63}$$

The Specificity (Spec) represents the proportion of negatives cases that were classified correctly and can take a value between one (all samples correctly classified) and zero (all samples misclassified). Calculation of Spec was performed according to eq.(2.64).

$$\text{Spec} = \frac{TN}{TN + FP} \tag{2.64}$$

The Matthews Correlation coefficient (MCC) considers all aspects of the confusion matrix (TP, TN, FP and FN) and is regarded as a balanced measure that can be used even if the sample sizes of the different classes are very different (Jurman et al., 2012, Gorodkin, 2004). MCC can take a value between -1 and 1 where a value of 1 means that all samples have been correctly classified and a value between -1 to 0 means that all samples have been misclassified. For a binary confusion matrix, the MCC was calculated according to eq.(2.65).

$$\mathrm{MCC} = \frac{TP * TN - FP * FN}{\sqrt{(TP + FP)(TP + FN)}\sqrt{(TN + FP)(TN + FN)}} \qquad (2.65)$$

The MCC metric can be extended for use on multiple classes according to eq.(2.66).

$$MCC = \frac{\sum_{k,l,m}^{c} C_{kk}C_{ml} - C_{lk}C_{km}}{\sqrt{\sum_{k=1}^{c}\left[\left(\sum_{l=1}^{c} C_{lk}\right)\left(\sum_{f,g=1|f\neq k}^{c} C_{gf}\right)\right]}\sqrt{\sum_{k=1}^{c}\left[\left(\sum_{l=1}^{c} C_{kl}\right)\left(\sum_{f,g=1|f\neq k}^{c} C_{fg}\right)\right]}} \qquad (2.66)$$

Individual class performances were also evaluated with receiver operating characteristics (ROC) curves which explores the separation of the classes according to the predicted class distributions. More specifically, the “area under the curve” (AUC) can be used as a performs metric of the class separation where a value of one indicates perfect classification and a value of 0.5 which indicates that no separation of the classes have been observed (Fawcett, 2006). In PLS-DA, the class distributions can be defined based on the calculated posterior probabilities in eq.(2.18) while in SVC, the distributions can be defined according to the calculated decision values in eq.(2.25). The ROC curve is calculated by sliding a threshold boundary over the class distributions thus allowing for the TP, TN, FP and FP which results in differing values of the sensitivity and specificity depending on the threshold value. For classes that are well separated as illustrated in Figure 2.13a, the resulting ROC curve will take on a shape as illustrated Figure 2.13b where the AUC value is close to one. In cases where class distributions are harder to separate as illustrated in Figure 2.13c, the resulting ROC curve will be closer the dashed black line indicating a AUC value closer to 0.5 which is illustrated in Figure 2.13d.

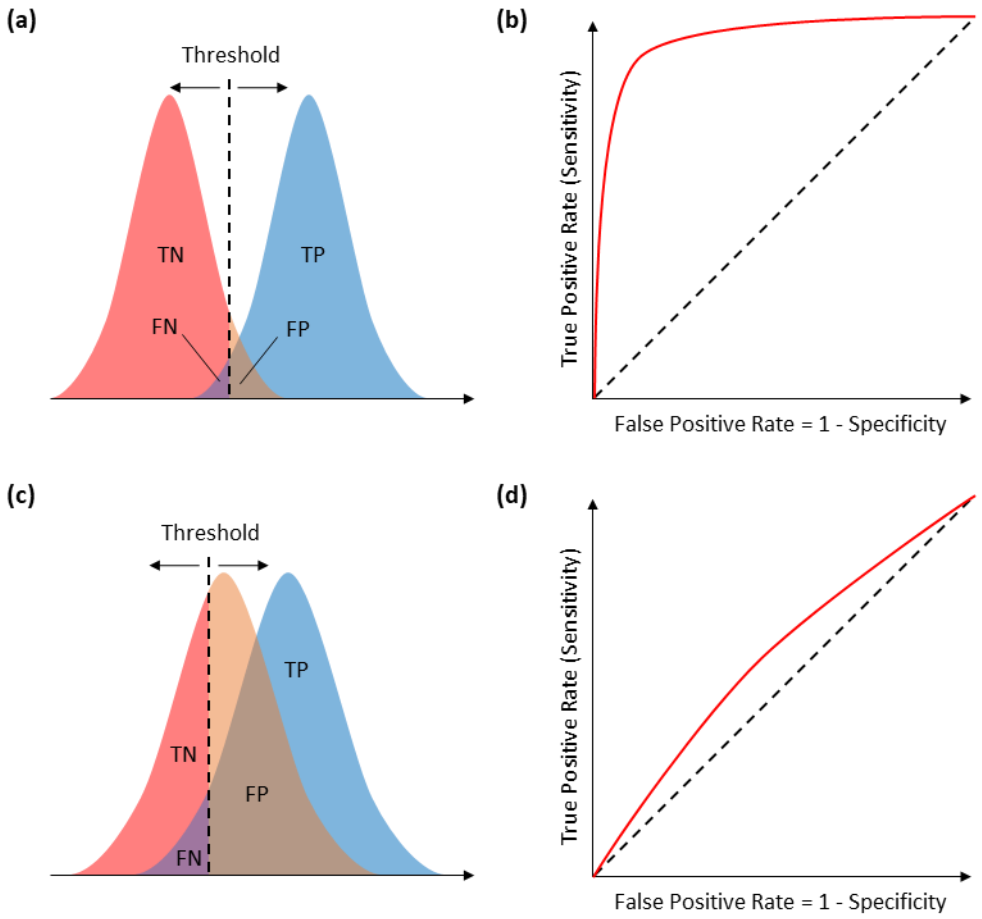

Figure 2.13. ROC curve development for two classes. The number of TP, TN, FP and FN changes depending on to the placement of the threshold which is less drastic in a problem with **(a)** well-separated class distributions compared to a problem with **(b)** overlapping class distributions. ROC curves from **(b)** well separated class distributions and **(d)** overlapping class distributions where the black dashed line represents the AUC value of 0.5 (adapted from Marini (2017)).

2.6.3 Y-Randomisation

Due to the large number of descriptors often used in QSAR modelling, it is important to evaluate if the correlation between $\boldsymbol{X}$ and $\boldsymbol{Y}$ captured by the model is related to the true underlying pattern or if it was caused by chance correlation of noisy descriptors. Y-Randomisation is a tool used in validation of QSAR models which compares the performance of models trained with randomised response vectors to that of a model trained with an unaltered response vector (Rücker et al., 2007). A number of randomised models are usually developed and the performance metric of interest is then averaged. If the averaged performance metric shows good performance, the trained model was likely fitted to noisy and redundant descriptors and can therefore not be used. For regression the metrics Q^2 and R^2 are often used while in classification the metrics ER of MCC can be used. In this research 50 models were developed on individually randomised response vectors where the metric of interest was then averaged.

2.7 Data Pre-treatment

As previously mentioned in the theory of PCA and PLS, it is important to mean-centre $\boldsymbol{X}$ and $\boldsymbol{Y}$ prior to developing the model in order for these methods to work. More generally, an action that modifies the data prior to model development is called pre-treatment or pre-processing and is used to increase the interpretation of the data sets (van den Berg et al., 2006). This is more simply understood when considering the influence of the variables in model development. As an example, when evaluating untreated data set each individual variable will conform to some specific distribution (normal distribution was used in this example) where $\boldsymbol{x}_k \sim N(\mu_k, \sigma_k^2)$ where $\mu_1 \neq \mu_2 \neq \cdots \neq \mu_M$ and $\sigma_1^2 \neq \sigma_2^2 \neq \cdots \neq \sigma_M^2$ which is illustrated in Figure 2.14a. For PCA and PLS, mean centring is a required step due to that the methods being dependent on the calculation of the covariance, which assumes that the data is centred around the origin. If models are developed on an uncentred data set with PCA or PLS, the first component will always be placed so it points from the origin to the centre of the data in the variable space in order to correct for the offset (Bro and Smilde, 2014). The effect will not be as pronounced for SVC or SVR which can adjust for uncentred data by correcting with the offset variable, b, of the hyperplane or the tube, respectively. An example of a set of the mean centred variables is illustrated in and Figure 2.14b where the distribution of each variable now conforms to $\boldsymbol{x}_k \sim N(0, \sigma_k^2)$.

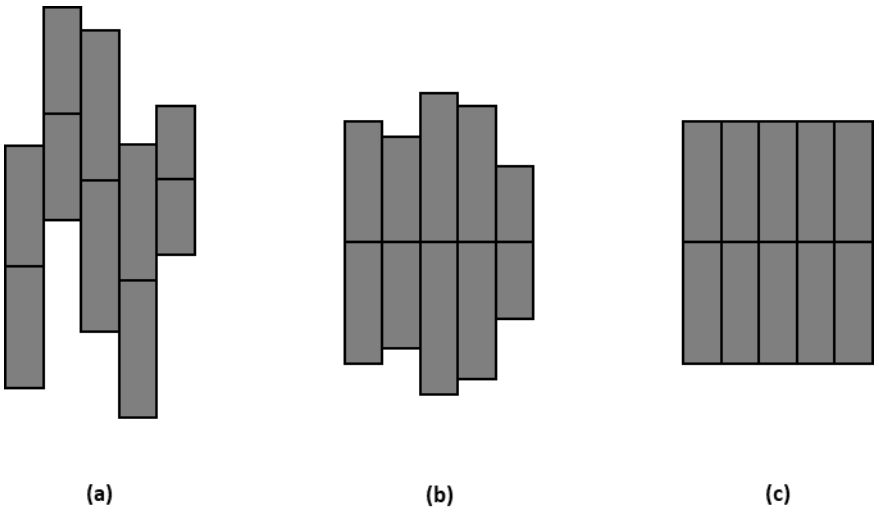

Figure 2.14. The effect of pre-treatment on variables on a data set. **(a)** Raw or untreated data set. **(b)** Mean centred data set. **(c)** Mean centred and scaled data set (adapted from van den Berg et al. (2006)).

Another important factor is the scaling of the descriptors. Commonly in many data sets, the ranges in the variables will be very different when compared to each other. This gives variables with a larger variation a bigger chance to influence the model compared to variables with a much smaller variation (Bro and Smilde, 2014). Thus, all variables are commonly scaled to

have equal variation or range in order for them to equally impact the model structure. In this research, the autoscaling method was used for pre-treatment of all data except class labels. The method both mean centres all variables as well as scales them according to the standard deviation of each variable according to eq.(2.67). This means that all variables in the data set will conform to $\boldsymbol{x}_k \sim N(0,1)$.

$$x_{ik}^{(auto)} = \frac{x_{ik} - \bar{x}_k}{\sigma_k} = \frac{x_{ik} - \bar{x}_k}{\sqrt{\frac{1}{N-1}\sum_{i=1}^{N}(x_{ik} - \bar{x}_k)^2}} \tag{2.67}$$

In eq.(2.67), $x_{ik}^{(auto)}$ is an auto-scaled element in $\boldsymbol{X}$, $\bar{x}_k$ and σ_k are the mean and the standard deviation of variable k. An example of autoscaled variables is presented in Figure 2.14c.

2.8 Variable Reduction

Due to the large number of variables (descriptors) that are generated in QSAR modelling, it is often beneficial to use unsupervised methods to remove collinear variables prior to further variable selection or model development. The V-WSP algorithm was applied to the $\boldsymbol{X}$ block in order to select a representative set of variables. This V-WSP algorithm works by replacing a group of variables with high multi-collinearity with a single variable from the group if the correlation between the variables is larger than a predefined threshold (Ballabio et al., 2014). The Procrustes index was used to evaluate the loss of information between the non-reduced and the reduced $\boldsymbol{X}$ block. The Procrustes index takes on values between zero and one where a value of zero indicates that no information loss has occurred while a value closer to one indicates that the majority of information in $\boldsymbol{X}$ has been lost (Peres-Neto and Jackson, 2001).

2.9 Variable Selection

Supervised variable selection methods were applied in this research to further reduce the number of variables in order to increase correlation between $\boldsymbol{X}$ and $\boldsymbol{Y}$. Three different methods were applied for which short descriptions have been given below.

2.9.1 Recursive Partial Least Squares

The Recursive Partial Least Squares (rPLS) is a variable selection method which iteratively reweights the variables in $\boldsymbol{X}$ through multiplication with a matrix $\boldsymbol{A}$ in which the diagonal elements $a_{kk} = |b_k|$ from the regression coefficients vector $\boldsymbol{B}$ generated from the PLS model. A new PLS model is developed on reweighted $\boldsymbol{X}$ and this is repeated until a minimum in the cross-validation error has been reached. By iteratively updating $\boldsymbol{B}$ and $\boldsymbol{X}$ as described, the

regression coefficients of variables with small contributions to the predictions will be forced to zero whereas those for variables with high contribution become larger. The stopping criterion in rPLS is based on the calculated cross-validation error at each iteration which will be forced to stop once the error start rising (Rinnan et al., 2014).

The method is however reliant on the model performance prior to variable selection. This means that if the model performance is poor prior to selection, the rPLS algorithm will not be able to select the correct variables. This is similar to that of variable evaluation with VIP and SR in PLS (Andersen and Bro, 2010).

2.9.2 Genetic Algorithm

The genetic algorithm (GA) is based on the evolutionary principle of "survival of the fittest" (Leardi, 2007). GA works by generating subsets of variables where each subset usually contains between 30-50% of all available variables in the data set. Such a subset can be seen as a logical vector consisting of *M* elements, identical to that of the number of variables, where an element value of one or zero indicates inclusion or exclusion, respectively, of the variable in the subset. Each subset is often referred to as chromosome or individual and all the generated subsets is referred to as a population. An individual model is trained on each chromosome and evaluated according to the cross-validation error as an estimation of the fitness. A new population (generation) is then produced through crossover illustrated in Figure 2.15 where two chromosomes (parents) are used to generate two new chromosomes (children). Many methods for selecting the parent chromosomes exist but where the Roulette Wheel is one of the most commonly used. The parent chromosomes are selected at random but where chromosomes with a better fit have a higher chance of being selected (Pandey et al., 2014). The parent selection and crossover are repeated until the number of children equals that of the original population size. New models are trained on the children chromosomes and the full process is iterated.

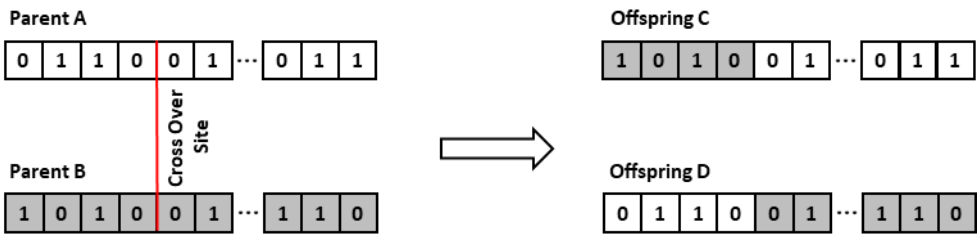

Figure 2.15. Crossover of variables between two parent chromosomes A and B resulting in two new variable permutations in the form of child C and D. The red line indicates the crossover site which is selected at random by the GA method (adapted from Pandey et al. (2014)).

One of the main strengths of GA is the ability to test many different variable permutations and select variables highly correlated to the response. However, one of the biggest drawbacks with

the method is the low reproducibility of generated results due to many aspects of the algorithm is based on random selection. A common method to increase reproducibility is to repeat the GA for several iterations in order to find variables that are most commonly selected. It has also been suggested that no more than 200 variables should be used in GA due to potential over-fitting (Leardi, 2000). Another drawback with the method is defining the many parameters such as: population size, single or double crossover, mutation rate and number of variables to include in the initial chromosome to mention a few.

The modelling method used in GA is commonly referred to as the fitness function which is not restricted to any particular method and can be either a classification or regression method. However, the fitness function should be sufficiently fast to train due to the numerous models that needs to be developed in order for GA to not become to computationally intensive (Niazi and Leardi, 2012).

2.9.3 Sparse L1-SVR

L1-SVR or more commonly referred to as LASSO-SVR is based on similar theory to that of SVR discussed in Section 2.4.2. The main difference is that the minimisation problem in eq.(2.52) uses the L1-norm, $\|\boldsymbol{\omega}\|_1$, instead of the squared L2-norm, $\|\boldsymbol{\omega}\|_2^2$. This, however, has a significant effect on the normal vector, $\boldsymbol{\omega}$, which will become sparse. Meaning that many elements in $\boldsymbol{\omega}$ will attain a value of zero. This is easier understood using Figure 2.16 for a regression problem with two variables. The red ellipses illustrated in the figure indicate the loss function or the error between the predicted and measured responses. First, considering the L2-norm illustrated in Figure 2.16a, the possible solutions for $\boldsymbol{\omega}$ will take the shape of a circle seen in green, the radius of which is determined by the constraints and the value of C. It can be observed that the optimal solution consists of non-zero values in $\boldsymbol{\omega}$, meaning that both variables will contribute to the prediction. In the case of the L1-norm, the solutions for will take the shape of a diamond illustrated as the green area in Figure 2.16b. Because of this shape, the optimal solution with the smallest error will be where ω_2 is non-zero and ω_1 is equal to zero (Zhu et al., 2004).

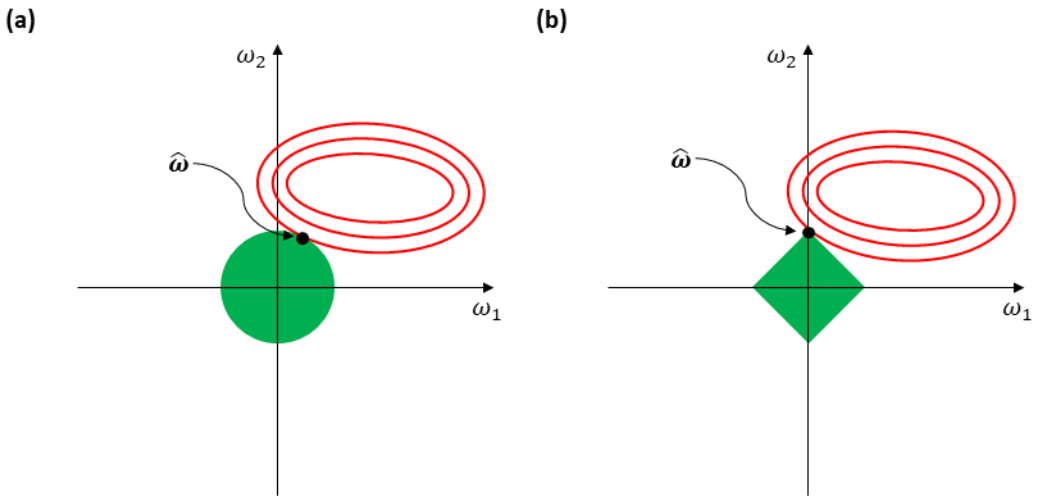

Figure 2.16. Comparison of solutions for **(a)** L2-norm and **(b)** L1-norm. The red ellipses represent the error between the predicted and measured responses in the samples set while the green areas represent the allowed solutions for $\boldsymbol{\omega}$ (adapted from Zhu et al. (2004)).

It is important to remember when using LASSO that the so-called "irrepresentable condition" must hold true which indicates that correlation between redundant and important variables must be low (Zhao and Yu, 2006).

2.10 Summary

This chapter laid the foundation of the multivariate methods and techniques used in this thesis. From the literature review of the methods in this chapter, it is apparent that each method has associated advantages and limitations. However, considerations regarding their application, training and validation have been made in order to increase the chance for successful implementation.

As discussed, the classification methods were selected to better handle uneven class balances that were present in the data set from Jain et al (2017). For this purpose, PLS-DA with Bayes decision rule and SVC with defined cost function values for each class were selected. The two methods are also complementary to each other, where PLS-DA can provide insight to potential outliers and have higher transparency in regards to variable contribution to the response whereas SVC usually have higher generalisation performance due to only using a subset of samples as support vectors.

Similarly, all regression methods in this chapter were reviewed and evaluated in order to conform to QSAR modelling. The two methods, PLS and SVR were selected due to having been applied successfully in similar QSAR implementations as have been demonstrated in literature. The methods are also complementary to each other where PLS have higher transparency in regards to sample and variable contribution and SVR a higher generalisation performance.

Due to the large number of descriptors needed to capture the structural information of the mAb structures, it became clear that variable reduction and selection techniques had to be applied. The unsupervised reduction method V-WSP was reviewed and included model development process in order to reduce the number of highly correlated descriptors. In addition, three variable selection methods: rPLS, GA and LASSO were reviewed, and their strengths and weaknesses listed. These methods were selected due to being slightly different in how they select variables. The rPLS and LASSO algorithms are highly dependent on the number of redundant variables in the descriptor set which can greatly decrease their performance if to many redundant variables are present. The GA algorithm instead selects variables based on a brute-force approach were multiple variable subsets are tested and evaluated.

Chapter 3

Primary sequence-based descriptors

In order to develop predictive models that can aid in mAb process development, structural descriptors need to be generated in order to compare the different mAbs. In this chapter the general structure of mAbs and common sources of structural variations that might impact the descriptors are highlighted and discussed. Four novel strategies have been developed for primary sequence preparation and descriptor calculation which are discussed in detail.

3.1 The Antibody Structure

There are five main heavy chain classes of antibodies: IgA, IgD, IgE, IgG and IgM where IgG have the highest occurrence in the human body with around ~75% of all antibodies found in the human serum (Schroeder and Cavacini, 2010). In this research, an extensive search was performed using the IMGT database to investigate the diversity of different antibody classes in clinical phases as well as manufacturing. The search criteria were specified to find all full-length IgA, IgD, IgE, IgG and IgM antibodies while excluding fusion proteins and fragments. Of the total 555 antibodies that met the search requirements, 543 were of the IgG class (~98%). Due to these findings, IgG antibodies are the focus of this dissertation. The IgG class can be further divided into four subclasses or so-called isotypes: IgG1, IgG2, IgG3 and IgG4. Of these, the IgG1, IgG2 and IgG4 isotypes are further investigated in this chapter due to being the most common according to the IMGT search with 74% being IgG1, 12% being IgG2 and 13% being IgG4 out of all IgG antibodies.

Figure 3.1 represents the structure of an IgG1 antibody. In general, the IgG antibody consists of four amino acid chains, of which two are heavy chains (50kDa and ~450 residues long each) and two are light chains (25 kDa and ~230 residues long each). The heavy chain can be divided into the four domains: the variable region (V_H), first constant domain (C_H1), second constant domain (C_H2) and third constant domain (C_H3) where a Hinge region connects the C_H1 and C_H2

domains of the heavy chain. The light chain can be divided in a similar manner into two domains: the light chain variable domain (V_L) and a constant domain (C_L). Like the heavy chain, the light chain has two naturally occurring isotypes: kappa and lambda. Each of the mentioned domains in the antibody contains ~110 residues whereas the hinge has 15 residues in the IgG1 isotype compared to 12 residues in the IgG2 and IgG4 isotypes (Janeway Jr et al., 2001).

3.1.1 The Fab region structure and function

The V_H and CH_1 domains of the heavy chain together with the V_L and C_L domains of the light chain make up the Fab region of the antibody. This is also known as the binding region of the antibody that binds to a specific target protein (antigen) e.g. a membrane protein on a pathogen. The binding occurs specifically in the variable domains V_H and V_L which contain six sequence loops (three for each variable domain) called Complementarity-determining regions (CDRs) that bind to a specific antigen. Antibodies can be grouped into so called idiotypes based on a group of antibodies that bind to a specific antigen and share similar structural characteristics in the variable domains and CDRs.

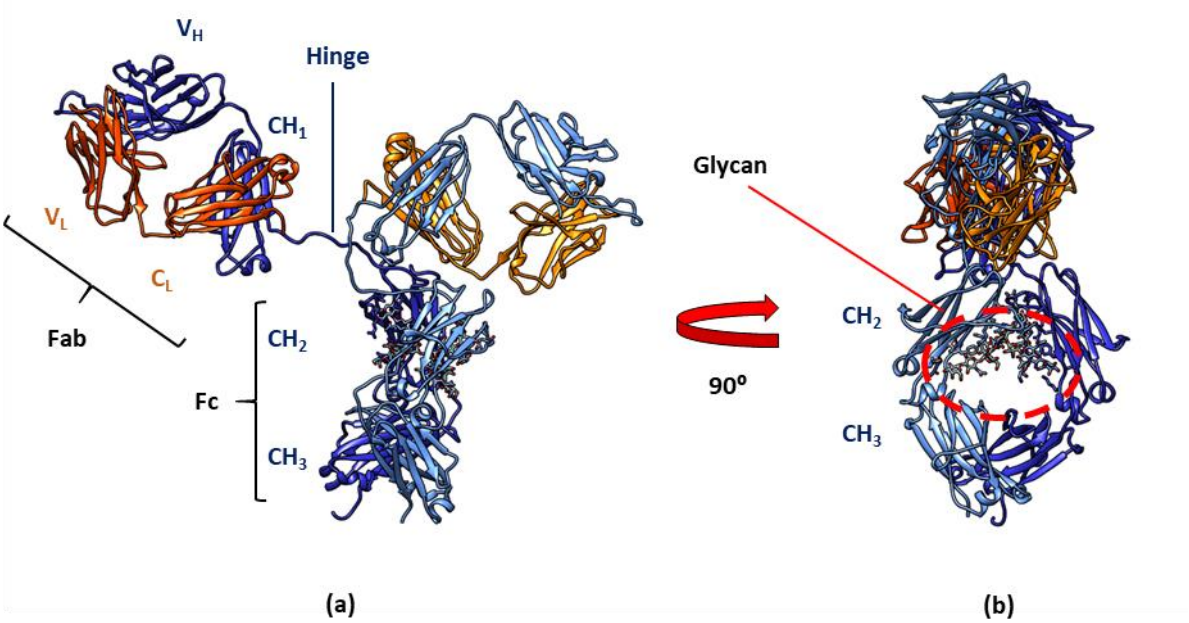

Figure 3.1. General structure of an IgG1 antibody. **(a)** Front view of the antibody showing the separate domains of the heavy chain (V_H, C_H1, Hinge, C_H2 and C_H3) depicted in blue as well as the separate domains of the light chain (V_L and C_L) depicted in orange. **(b)** Side view of the antibody structure with the two glycan structures highlighted with a red circle. Each glycan connects to Asn297 of each heavy chain (adapted from Vidarsson et al. (2014)).

3.1.2 The Fc region structure and function

The C_H2 and C_H3 domains of both heavy chains are called the Fc region of the antibody. The Fc region determines the type of response that is triggered in the immune system, the so-called Fc effector function, and has been covered elsewhere (Rajpal et al., 2014, Kizhedath et al.,

2017). An important part of this region is asparagine 297, which is strictly conserved in all IgG isotypes. It serves as an attachment point for glycans in the C_H2 domain of each heavy chain (see Figure 3.1b). The glycan structures have been shown to increase the overall stability of the IgG (Zheng et al., 2011) as well as playing an integral part in the activity of the antibody (Ferrara et al., 2011).

3.1.3 Sequence variability in constant domains

Most of the sequence variability between antibodies is found in the variable domains V_H and V_L. The variability is caused mainly by the unique structure of the CDR loops which gives them their high specificity to different antigens. Variability in sequences is also encountered in the constant domains when comparing the different isotypes in the heavy and light chain separately (see Figure 3.2). However, the extent of the variability is not as pronounced as when comparing sequences of the variable domains between antibodies. The amino acid differences between the isotypes in the heavy chain are illustrated in Figure 3.2a. EU numbering has been used to illustrate each of the residue positions in the sequence alignment (Edelman et al., 1969). The positions highlighted with red boxes are positions that play a vital role in the Fc effector function (Kizhedath et al., 2017). Positions coloured in red and underlined mark the positions of amino acids that vary between different allotypes and are slightly different in the sequence that can be found between different populations (Vidarsson et al., 2014). A more extensive view of allotypes occurring in the heavy chain isotypes is illustrated in Figure 3.2b. In total, including the allotypes, only 44 residues of a total of ~340 residues from the constant domains and hinge are different in the heavy chain between isotypes.

In addition to the variations caused by the allotypes in the heavy chain, a common modification in design of IgG4 antibodies is the mutation of the wildtype hinge residue Serine 228 to a Proline. The mutation stabilises the hinge region which becomes more rigid and more similar to that of the IgG1 hinge (Aalberse and Schuurman, 2002). This also has the effect of increasing the efficacy of the IgG4 antibodies by preventing Fab arm exchange with other IgG4 antibodies (Silva et al., 2015).

The sequence variability between kappa and lambda is however more pronounced with 74 residues being different out of the total ~110 residues in the C_L domain, with reported allotypes positions marked as red an underlined (see Figure 3.2c). No allotypes have been reported for kappa and lambda but residue variability is present between different light chain isotypes which is illustrated in Figure 3.2d. All information related to the allotypes in the heavy and light chain were acquired from the IMGT database (Lefranc and Lefranc, 2012).

3.1.4 Disulphide bonds

The heavy and light chains are linked with a single disulphide bond between the C_L and C_H1 domains that prevents the two chains from separating. In addition, the two heavy chains are also connected by disulphide bonds in the region surrounding the hinge. In IgG1 and IgG4 the heavy chains are linked with two disulphide bonds whereas IgG2 antibodies have a total of four disulphide bonds linking the two heavy chains (Liu and May, 2012). The structural differences and the sequence variability of the constant domains in the heavy and light chain are summarised in Table 3.1.

Table 3.1. Summary of structural differences of the constant domains in the heavy and light chains (adapted from Lefranc et al. (2005) and Liu and May (2012))

Heavy Chain	**IgG1**	**IgG2**	**IgG4**
C_H1 residues	98	98	98
Hinge residues	15	12	12
C_H2 residues	110	109	110
C_H3 residues	~110	~110	~110
Allotypes	7	4	3
Disulphide bonds in hinge	2	4	2
Light chain	**kappa**	**lambda**	
C_L residues	~107	~106	
Allotypes	3	5	

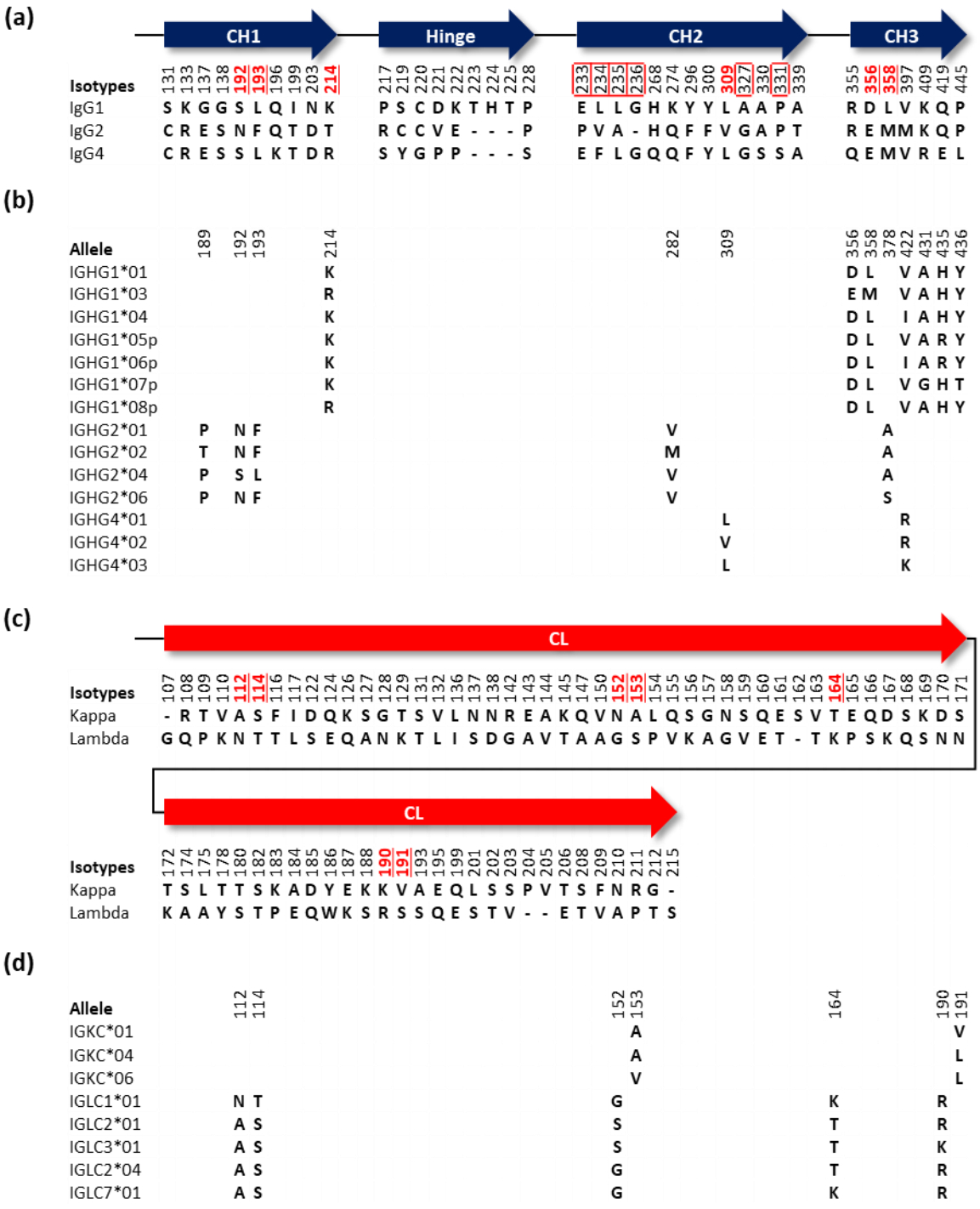

Figure 3.2. Heavy and light chain isotypes and allotypes. **(a)** Sequence alignment of the constant domains C_H1, Hinge, C_H2 and C_H3 in the heavy chain showing all structural differences between the isotypes IgG1, IgG2 and IgG4. Sequence numbering follows the EU numbering scheme and positions marked as bold, underlined and coloured red are positions with varying residues originating from different allotypes. Positions marked with red boxes highlight residues that are important in the Fc effector function **(b)** Comparison of the common allotypes with the positions in the primary sequence isolated to illustrate the varying residues based on given alleles. Allele names containing IGHG1 refer to IgG1, IGHG2 to IgG2 and IGHG4 to IgG4 **(c)** Sequence alignment of the constant domain C_L in the light chain illustrating the structural differences between the isotypes kappa and lambda. Positions with varying residues in the sequences of known allotypes are marked as bold, underlined and coloured red. **(d)** Comparison of most common isotypes of the C_L domain where only positions with varying residues are illustrated. Allele names containing IGKC refer to the kappa isotypes while allele names containing IGLC refer to the lambda isotypes (adapted from Lefranc and Lefranc (2012)).

3.1.5 Sequence variation from humanisation

Many antibodies are produced by using animal models such as house mouse. In this process antibodies are developed as part of the animal's immune system when presented with an antigen of interest. B cells expressing antibodies specific to the antigen are harvested and antibodies with high specificity are retained for further evaluation (see Figure 3.3a) (Laffleur et al., 2012). However, these antibodies cannot be used due to slight differences in the structure of the Fc region which will cause undesired binding when presented in a human environment and thereby causing adverse effects (Hansel et al., 2010). Often in order to be able to use the antibodies clinically they first need to be modified to become more human-like. Boulianne et al (1984) circumvented this problem by replacing the constant domains (C_H1, hinge, C_H2, C_H3 and C_L) of a mouse antibody with those of human counterparts and thereby producing a chimeric antibody (see Figure 3.3b) with high specificity and lowered immunogenicity (Boulianne et al., 1984). An improvement of this was made by Jones et al (1986) where instead of retaining the full variable domains of the animal antibody, a humanised antibody (see Figure 3.3c) could be produced by retaining only the CDRs which were grafted onto the framework regions of human variable domains (Jones et al., 1986). This has the effect of lowering the immunogenicity further by reducing the animal components that can cause adverse effects, but can also lower the specificity towards the antigen (Hwang and Foote, 2005). Fully human antibodies (see Figure 3.3d) can be expressed through the use of transgenic animals which have been modified to express human antibodies upon immunisation (Green et al., 1994, Mompo and Gonzalez-Fernandez, 2014).

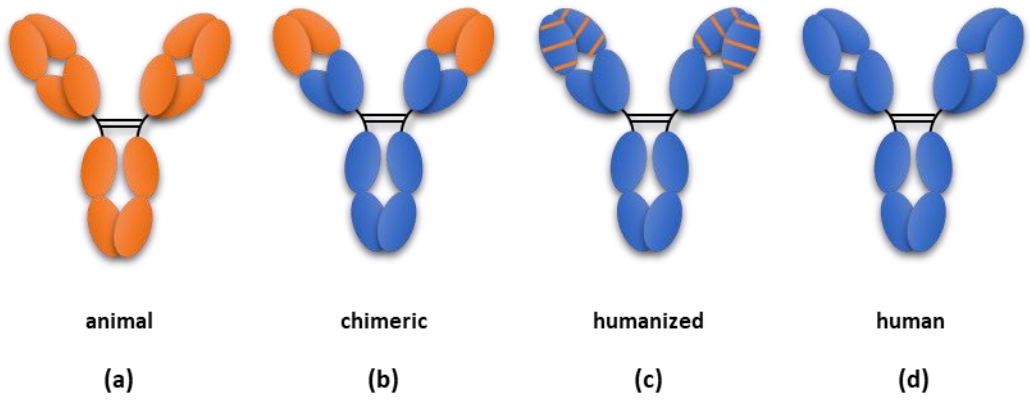

Figure 3.3. Representation of antibody modification where orange domains are expressed domains from the animal model and blue domains are expressed from human genome. Level of modification is presented in increasing order from fully animal **(a)**, to chimeric **(b)**, to humanised **(c)** and finally to fully human **(d)** (adapted from Absolute Antibody (2018)).

The humanisation of antibodies introduces an interesting artefact in the sequence variability of the variable domains which originates from the modification used to design the antibody

(animal, chimeric, humanised and human). In this dissertation, only antibodies with human constant domains will be used in order to decrease sources of variability. However, for chimeric antibodies there will be an effect originating from the species used to express the variable domains compared to that of humanised and human antibodies. As mentioned above, just as the chimeric antibodies can cause adverse effects through unwanted binding, it might also impact on the performance in operational units in a bioprocess e.g. binding in chromatographic columns.

3.2 Descriptor generation

All antibody sequences that were used in modelling in the subsequent chapters were obtained from the IMGT database unless another means of acquisition is specified. Figure 3.4 illustrates an overview of the applied workflow for the generation of descriptors. An initial isotype classification of the sequences was performed by using recognition sequences for each isotype based on the human hinge region and the beginning of the human constant C_L domain to identify the isotype of the heavy and light chain, respectively. For IgG4, an additional recognition sequence was added to incorporate the Ser228Pro mutation.

Descriptors were generated by either using 1) software to estimate protein properties with FASTA as input format or 2) conversion of each selected residue into numerical values with so called amino acid scales illustrated in Figure 3.4b. Prior to the descriptor generation, a sequence preparation step was performed in order to generate four different data sets illustrated in Figure 3.4a which is explained further in Section 3.3. Explanation of the descriptor generation is given first in order to facilitate the comparison of the different sequence preparation strategies.

3.2.1 Software based descriptors

In order to generate meaningful descriptors from the sequences to be used in modelling, dedicated software was used. In this dissertation, ProtDCal 3.5 (Ruiz-Blanco et al., 2015) and a standalone version of EMBOSS Pepstats 6.5 (McWilliam et al., 2013) were considered and used to generate the descriptors presented in Table 3.2.

Table 3.2. List of generated descriptors from ProtDCal and EMBOSS Pepstats. The stars in the second and third columns represent which software was used for generation of each descriptor.

Descriptor	ProtDCal	Pepstats	Type	Description
$G_W(U)$	●		Folding energy	Index of the contribution to the free energy from the entropy of the first shell of water molecules in an unfolded state
$G_s(U)$	●		Folding energy	Index of the interfacial free energy of an unfolded state
$W(U)$	●		Folding energy	Number of water molecules close to a residue in an unfolded state
M_W		●	Physiochemical	Molecular weight of the protein
HP	●		Physiochemical	Hydrophobicity by the Kyte-Doolittle scale
IP		●	Physiochemical	Isoelectric point of the protein
ΔH_f	●		Physiochemical	Heat of Formation
ECI	●		Physiochemical	Electronic Charge Index
ISA	●		Physiochemical	Isotropic Surface Area
A_{polar}	●		Physiochemical	Polar area of each amino acid in unfolded state
$Charge$		●	Physiochemical	The sum of all charges in sequence
AR_W		●	Physiochemical	Average residue weight
$Residues$		●	Physiochemical	Number of residues in sequence

ProtDCal is a freely available tool specifically designed to generate descriptors for multivariate modelling of proteins by using either the primary sequences in FASTA format or 3D structures in PDB format. It has been applied successfully in machine learning environments for the identification of functional protein residues (Corral-Corral et al., 2017) and prediction of N-glycosylation sites on proteins (Ruiz-Blanco et al., 2017) to mention a few**.** ProtDCal allows for generation of a variety of descriptors ranging from thermodynamic, topological (only for 3D structures) to physiochemical properties. For the purposes of this research however, descriptors were selected focusing on properties present on the surface such as charge and polarity as well as descriptors for protein stability such as folding energies and hydrophobicity due to the interest in developing models can accurately predict external behaviour of mAbs such as chromatographic column performance (Gagnon, 1996b) or self-association (Li et al., 2016).

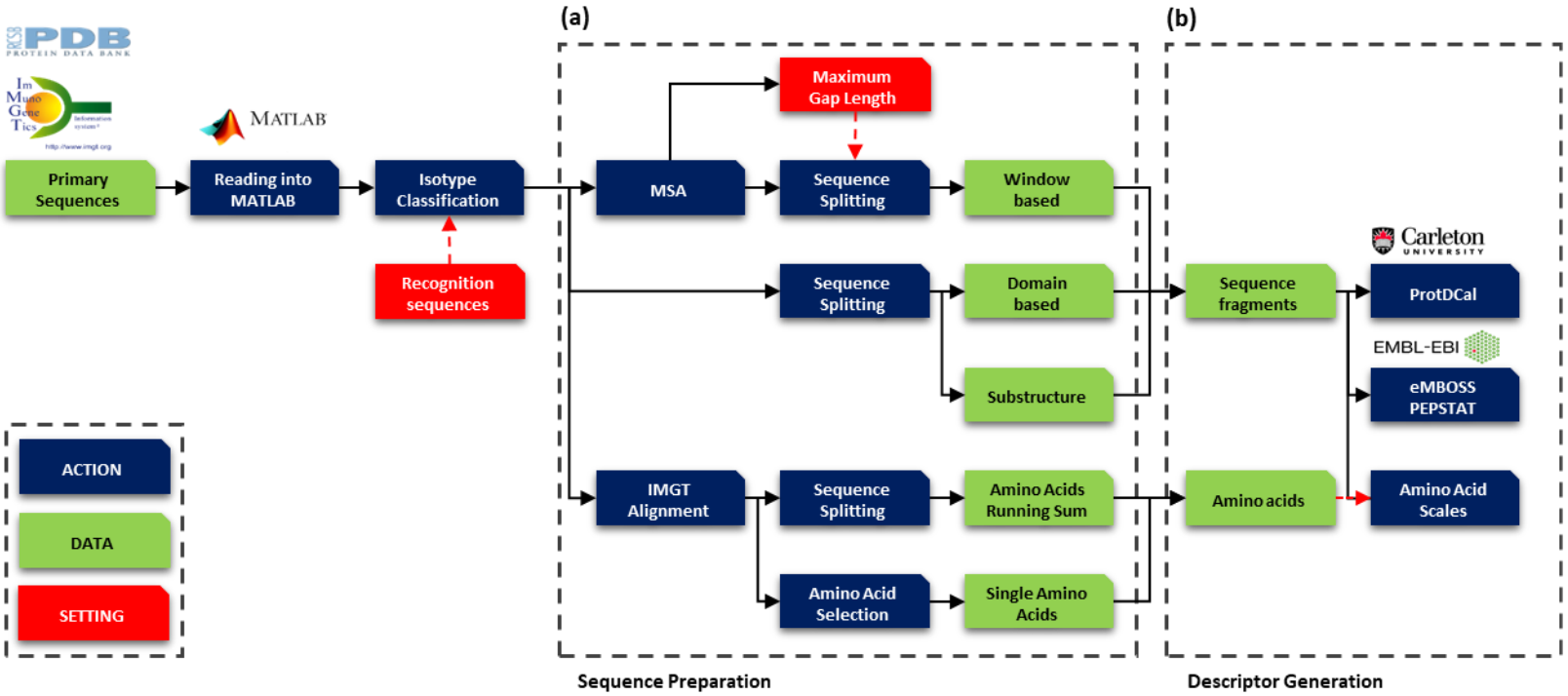

Figure 3.4. Descriptor generation workflow. **a)** Sequence alignment and splitting was performed to prepare sequence fragments and amino acids for descriptor generation of the five data blocks: Domain based, Window based, Substructure based, Running Sum based and Single Amino Acid based. **b)** Descriptors for the Domain based, Window based and Substructure based approaches were generated from the prepared fragments with ProtDCal, eMBOSS PEPSTAT and amino acid scales. As for the Single Amino Acid based and Running Sum based, only the amino acids scales were used to generate the descriptors (dashed red line).

It is important to note that ProtDCal will calculate physiochemical descriptors based on indexed values for each residue when using the primary sequences as input. This means that no assumptions are made in ProtDCal regarding environmental factors in the solution surrounding the protein. For calculation of full protein descriptors, ProtDCal provides different calculation modes or so-called aggregation techniques which determines how the descriptors are put together based the indexed residue values (Ruiz-Blanco et al., 2015). In this research considerations were given to two such methods: the sum and the Euclidean distance of the generated indices. The Manhattan distance was selected due to the descriptors being additive in nature, meaning that an approximation of a descriptor for the full protein is that of the summation of the individual amino acids. The Euclidean distance was used in addition to give more information of the magnitude of the descriptors when multiple residues are used for descriptor generation. Specifics on when the different aggregation methods were applied can be found in Section 3.3 below. The calculation of the folding energy descriptors in ProtDCal, on the other hand, is based on empirical equations which are dependent on adjacent residues as well as the temperature (Ruiz-Blanco et al., 2013). In this research, the default value of 25 ºC (298.15 ºK) was used.

In addition, ProtDCal is also able to generate descriptors for specified groups of amino acids seen in Table 3.3. These groups are based on amino acid composition of secondary structure (Otaki et al., 2010) and classical amino acid classification according to the side chain polarity, charge, aromatic structure and so on (Taylor, 1986). By generating the ProtDCal descriptors in Table 3.2 based on selected amino acids specified in a group, greater utilisation of the input sequence is achieved as specific properties can be quantified more easily e.g. calculation of descriptor based only on polar residues (PLR). All 12 presented groups in Table 3.3 were used to generate descriptors from ProtDCal thus resulting in 120 unique descriptors (10 descriptors per group) for each sequence input.

Table 3.3. Amino acid groups available in ProtDCal. RTR, BSR and AHR are based on common residues found in secondary structure. ALR, ARM, NPR, PLR, PCR, NCR and UCR are groups that conform to the classical amino acid classification. PRT represents the full sequence (adapted from Ruiz-Blanco et al. (2015))

Amino acid group	Description		Residues
RTR	Common residues in reverse turn structure	Secondary structure	Asn, Asp, Gly, Pro and Ser
BSR	Common residues in Beta Sheet structure	Secondary structure	Ile, Phe, Thr, Trp, Tyr and Val
AHR	Common residues in Alfa Helix structures	Secondary structure	Ala, Cys, Gln, Glu, His, Leu, Lys and Met
ALR	Aliphatic residues	Residue classes	Ala, Gly, Ile, Leu and Val
ARM	Aromatic residues	Residue classes	His, Phe, Trp and Tyr
NPR	Non-polar residues	Residue classes	Ala, Gly, Ile, Leu, Met, Phe, Pro, Trp and Val
PLR	Polar residues	Residue classes	Arg, Asn, Asp, Cys, Gln, Glu, His, Lys, Ser, Thr and Tyr.
PCR	Positively charged residues	Residue classes	Arg, His and Lys
NCR	Negatively charged residues	Residue classes	Asp and Glu
UCR	Uncharged polar residues	Residue classes	Asn, Cys, Gln, Ser,Thr,Tyr
UFR	Unfolding residues	Residue classes	Gly and Pro
PRT	Whole protein	Whole protein	All residues

EMBOSS Pepstats was used to provide additional descriptors to the data set. Though not as extensive as ProtDCal, the total charge, the average residue weight and the number of residues in the sequence was calculated by Pepstats. In Pepstats, the molecular weight of the sequence was calculated with the assumption of no N- or C-terminal modifications being present in the sequence whereas the isoelectric point (pI) and charge were calculated based on the physiological pH of 7.4.

3.2.2 Amino acid scale descriptors

Many advancements have been made in developing new informative descriptors to be used in the QSAR modelling framework. For modelling of proteins and peptides, so called amino acid scales were first developed and introduced by Sneath in order to numerically convert the residues into meaningful values (Sneath, 1966). A large number of physiochemical descriptors were generated for the 20 naturally occurring amino acids. These were then reduced into four vectors (components) using PCA (see Section 2.2.1) for dimensionality reduction and thus allowing the components to capture the overall differences and similarities between the amino acids based on the used descriptors. This led to a reduction in the number of descriptors that were used in QSAR modelling due to a large number of descriptors being replaced by unique

values for each amino acid in the sequences. Many new and specialised amino acid scales have since been developed to capture different properties of the amino acids. A comparison of 13 different scales was performed by van Westen et al (2013) in order to find complementary scales to be used in modelling (van Westen et al., 2013b, van Westen et al., 2013a). Based on these findings and for the purposes of this dissertation, the Z-scale (Hellberg et al., 1986, Hellberg et al., 1987b), the T-scale (Tian et al., 2007) and the MSWHIM scale (Zaliani and Gancia, 1999) were chosen to be used for numerical conversion of sequence residues as they capture physiochemical, topological and electrostatic properties, respectively (see Table 3.4). In total, 11 descriptors based on the three chosen amino acid scales were used for numerical conversion of each residue.

Table 3.4. Amino acid scales used for descriptor generation and details on captured information of the individual components

Scale	Description	Method	Number of Components	Component	Component descriptions
Z-Scale	Physiochemical	PCA	3	Z1	Contains information related to the hydrophobicity
				Z2	Contains information related to size, hydrophobicity and hydrophilicity
				Z3	Contains information related to pH and NMR values
T-scale	Topological	PCA	5	T1	No information given
				T2	No information given
				T3	No information given
				T4	No information given
				T5	No information given
MSWHIM	Electrostatic potential	PCA	3	MS1	Contains information related to the charge and size
				MS2	Contains information for further separation of positively charged residues
				MS3	Contains information for further separation of negatively charged residues

3.3 Sequence preparation and conversion

Normally, in any given problem statement where protein descriptors are used to develop a model with the goal of being able to predict some process related performance metric e.g. aggregation, retention time etc, a subset of specific structural features in the protein will be directly related to that output. Using the full antibody sequence to generate descriptors in such cases would confound the information due to the majority of the residues being redundant and more likely to introduce noise in the descriptors. Therefore, prior to the generation of the

descriptors, five novel preparation strategies were considered in order to address this issue of resolution: Domain based, Window based, Single Amino Acid based and Running Sum based strategies which are illustrated in Figure 3.4a. These five strategies were developed and considered in order to reduce the noise from the redundant residues and enhance the information from the residues related to an output of interest.

3.3.1 Domain based

In the Domain based approach, all sequences were split into smaller fragments corresponding to the antibody domains (V_H, C_H1, Hinge, C_H2, C_H3, V_L and C_L). The start and the end positions for each domain were generated based on the initial isotype classification, thus finding the positions of the hinge and the start of the constant domain C_L and then using the specific domain lengths specified in Table 3.1.

Descriptors were generated using both software and amino acid scales, see Figure 3.4b. In ProtDcal, descriptors were generated based on the 12 amino acid groups presented in Table 3.3 resulting in 120 unique descriptors. This to further extract more information from the domains but also capture the slight differences in the amino acid compositions in the domains. Global versions of the amino acid scale descriptor were generated by summing the individual component values of all residues. This was as all components are orthogonal to each other in each of the amino acid scales due to have been generated from PCA (Bro and Smilde, 2014). This therefore allows each component to be additive without influencing the other components. In total 136 descriptor for each domain was generated for the Domain based approach (5 from EMBOSS Pepstats, 120 from ProtDCal and 11 from the amino acid scales).

3.3.2 Window based

In the Window based approach, a multiple sequence alignment (MSA) was first performed with all sequences used in a study of interest in order to overlap regions with high similarity between antibodies. BLOSUM80 was used as the amino acid substitution matrix due to the antibodies sharing high sequence similarity (Henikoff and Henikoff, 1992). When aligning antibodies, longer consecutive gaps are expected in the variable regions due to the unique structure and differences in length of the CDR loops. However, in order to avoid misalignment of more conserved regions in the variables domains, control checks were implemented to ensure that that conserved cysteine and tryptophan residues were aligned in the variable regions which are illustrated in Figure 3.5 (Lefranc et al., 2003). From the resulting alignment, a window was defined based the longest consecutive gap region plus two additional residues, one on either side of the gap region. The full sequence was then divided based on the specified window, thus

generating smaller fragments of sequences equal in size to the specified window. As an example, if the window was specified to 25 residues, the first fragment would contain residues 1 to 25, the second fragment residues 26 to 50 and so on. The addition of the two extra residues to the window ensures that no single fragment would contain only gaps.

Similar to the Domain based approach, descriptors were generated using both the software and amino acid scales. However, due to the sequence fragments being much smaller than the domain sequences only the PRT options from the amino acid groups was used to generating descriptors. Instead, both Manhattan distance and Euclidean distance were used as aggregation methods to generate descriptor in ProtDCal resulting in 16 unique descriptors. In total 32 descriptors were generated for each sequence fragment that was created in the Window based approach (5 from EMBOSS Pepstats, 16 from ProtDCal and 11 from the amino acid scales).

3.3.3 Substructure Based

In the Substructure based approach the identified domains were further broken down into smaller substructures which are consistent across all full chain IgG antibodies. For the variable domains, the CDR loops and frameworks (FRs) were identified by utilising highly conserved residues present in these domains as well as applying specified rules for CDR loop identification presented in (Lefranc et al., 2003). A breakdown of the substructures in the variable domains is illustrated in Figure 3.5 showing the IMGT numbering and usual residue length for each substructure as well as conserved cysteines and aromatic residues.

In a similar manner, the identification of the substructural components in the constant domains were identified by using the IMGT numbering scheme presented in (Lefranc et al., 2005). The sequence splitting of the constant domains is more straight forward to implement due to amino acid composition and domain lengths being highly conserved in these domains. This resulted in 43 unique primary sequence fragments from a full-length mAb where 14 originated from the variables domains (V_H and V_L), 28 from the constant domains (C_H1, C_H2, C_H3 and C_L) and one from the hinge region.

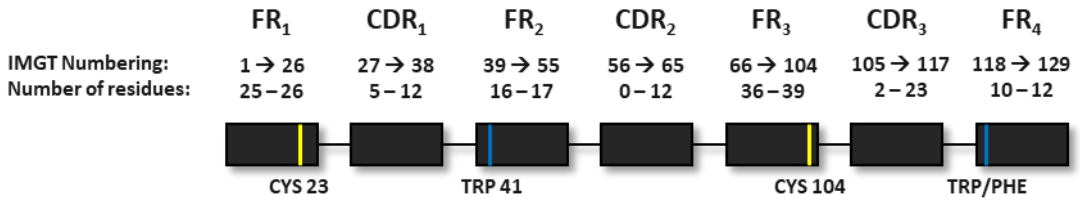

Figure 3.5. Breakdown of the variable domains into the smaller framework (FR) and CDR substructures. Conserved cysteines are represented as a yellow line while conserved aromatic residues are represented as blue lines (adapted from Lefranc et al. (2003)).

The descriptor generation in the Substructure based approach was identical to that of the Window based approach where a total of 36 descriptor were generated for each substructure sequence (5 from EMBOSS Pepstats, 20 from ProtDCal and 11 from the amino acid scales).

3.3.4 Running Sum based

In the Running Sum based approach, an alignment was first carried out by using the IMGT numbering scheme. To properly align the CDR loops, gaps was introduced in order to convert all corresponding CDRs to be of equal length. This was performed by assigning a constant maximum length to each CDR substructure and introducing gaps in sequences if the CDR sequence was shorter than the specified maximum length for the specific CDR loop. The lengths assigned were 15 residues for CDR1, 15 residues for CDR2 and 25 residues for CDR3. These lengths were based on the maximum observed CDR lengths of 297 mAb sequences taken from the IMGT mAb database where a maximum of 12, 12 and 23 residues were observed in CDR1, CDR2 and CDR3 loops, respectively. The lengths were rounded upwards to the closest whole five in order to account for future samples that might have longer CDR gaps.

In comparison, the difference in the lengths of the framework substructures is caused by systematic addition/elimination of residues whose locations in the sequence are known (Lefranc et al., 2003). For sequences that were shorter than the maximum length of a framework substructure, gaps were systematically introduced in these positions thus conforming all sequences for a specified framework substructure to the same length.

A window was defined similar to that of the Window based approach. The width of the window was set to 13 residues to be about half of the longest defined CDR loop of 25 residues. The window was then used to generate smaller fragments by sliding it upstream in the sequence one residue at a time from the beginning to the end of the alignments. As an example, the first fragment will contain residues 1 to 13, the second fragment will contain residues 2 to 14 and so on.

In this approach, only the amino acid scales were used to generate descriptors for the antibodies. Each component from the individual amino acid scales was summed based on the amino acid composition of the input fragment as described in Section 3.3.1.

3.3.5 Single Amino Acid based

Similar to the Running Sum based approach all sequences were aligned by using the IMGT numbering scheme prior to extracting any information. In the Single Amino Acid based approach however, positions of individual residues that varied between mAb samples were identified in the resulting alignment and used for descriptor generation. To include positions

with gaps, smaller sequence fragments were generated in order to avoid information loss. For positions with systematic gaps such as in the variable domain frameworks and in the constant domains, fragments were generated by adding one residue before and after the start and end of the gap, respectively. The CDR loops was used directly without modification due to their high sequence variability and length.

Similar to the Running Sum based approach, only the amino acid scales were used to generate descriptors. All identified positions with varying residues in the IMGT alignment were directly converted into numerical values using the amino acid scales. Generated fragments containing gaps and the CDR loops were converted using Manhattan distance to sum the up the individual components.

3.3.6 Differences between strategies

In the Domain based, Window based and Substructure based approaches descriptors were generated by using both software and amino acid scales Figure 3.4b due to the treatment of longer sequence fragments. Because of the long sequence fragments used in the Domain based approached there was a high probability that information from critical residues, important to the model output, would be confounded by redundant residues. The Window based approach was considered to improve the Domain based approach in order to reduce the amount of noise introduced by calculating the descriptors with fewer residues in each fragment e.g. 25 compared to that of the Domain based where the full domain, e.g. ~110 residues, was used to calculate descriptors. In this way, a data set with higher resolution of the impact from each residue could generated. However, a big disadvantage with the Window based approach is that the descriptors generated become unique to the samples in the data set which is caused by the multiple sequence alignment (MSA). More specifically, the MSA algorithm (BLOSUM80) will try to align provided sequences and maximise the alignment score by increasing residue matches and decreasing residue mismatches between sequences. This alignment becomes unique to the samples that were provided and will not necessarily be identical when new samples are added. This means the generated fragments from the Window based approach and the descriptors generated from these will be highly dependent on the form the alignment takes. This creates problems if descriptors for future samples need to be generated as these might not fit in in the previous alignment due to longer or shorter sequence regions and a manual alignment of these samples would be required. Due to this disadvantage, the Window based approach was discarded. Instead, the Substructure based approach was considered as an alternative to address this issue. By identifying and using the smaller substructures that make up the domains to generate descriptors, the resolution could be improved due to fewer residues being used

compared to the Domain based approach. This also ensures that comparable descriptors for future samples can be generated due the same substructures existing in all antibodies that are of the same conformation.

The two remaining approaches Running Sum and Single AA were developed to investigate the impact of individual residues in the sequence. The use of the IMGT numbering scheme instead of MSA ensured that corresponding residues in different sequences would be aligned correctly and be reproducible. The Running Sum based approach can be considered as an alternative to the Substructure based approach due to larger fragments still being handled. The biggest difference however is that each residue was represented multiple times in slightly different sequence variations thus allowing important residues to have an increased impact in the model development. The Single AA based approach is fundamentally different from the previously mentioned strategies as only residues that varied between antibodies in the alignment were used for descriptor generation. This was to investigate if only the varying regions in the primary sequence were the only information necessary in order to produce models with high fit and accuracy.

The impact of the sequence splitting on the number of descriptors per mAb can be observed in Table 3.5 for the different approaches. Table 3.5 also provides estimates of the potential number of descriptors per mAb based on which domains of the mAb are used for descriptor generation (V_H/V_L, Fab and Full length). It is important to note that, though higher resolution can be attained by reducing the length of the sequence fragments, the total number of descriptors increases in turn as a result of increased number of fragments which occurs in the higher resolution descriptor sets. The largest increase in descriptors can be seen in the Running sum due to more sequence fragments being generated in both the heavy and the light chains. This is more easily understood if considering descriptor generation for a full structure mAb with ~450 residues in the heavy chains and ~230 residues in the light chains. This would generate closer to 700 unique fragments when including gaps introduced by the IMGT sequence alignment. Therefore, in this approach, only the amino acid scales were used to generate descriptors in order to avoid generating an excessive number of descriptors.

Table 3.5. Representation of the expected number of descriptors generated for each mAb when using the Domain based, Window based, Substructure based, Single AA based and Running Sum based approaches to generate descriptors. A full-length mAb with 450 residues in the heavy chain and 230 residues in the light chain was considered in this case. The number of sequence fragments (Domain, Window, Substructure and Running Sum) or sequence positions (Single AA) are listed in the parenthesis

Method	**V_H/V_L**	**Fab**	**Full length**	**Input type**	**Descriptors per input**
Domain	272 (2)	544 (4)	952 (7) [4]	Domain	136
Window [1]	320 (10)	640 (20)	896 (28)	Fragment	32
Substructure	448 (14)	896 (28)	1376 (43)	Substructure	32
Running Sum [2]	2486 (226)	4686 (426)	7216 (656)	Fragment	11
Single AA [3]	1452 (132)	1540 (140)	1628 (148)	Position	11

(1) Calculated with a window width of 25 residues

(2) Calculated with a window width of 13 residues and without gaps in the sequence

(3) Calculated based on 80% similarity between mAbs with the majority of the variability in the variable domains

(4) 136 descriptors are generated for the Hinge which was treated as a domain

3.4 Summary

From the proposed methods able to generate descriptors described in this chapter it is clear that each strategy has its advantages and disadvantages. However, specific sequence preparation strategies might be better suited for different purposes as "no one size fits all". This makes the proposed descriptor generation highly customisable and can be adapted to specific needs in the model development. The described workflow for descriptor generation using the primary sequence of mAbs has been applied as described in Chapter 4 where the intrinsic variation originating from the mAb isotypes and species origins has been explored. The suitability if these descriptors for prediction of HIC retention times and mAb yields is addressed in Chapter 5.

Chapter 4

Impact of mAb isotypes and species origins on primary sequence-based descriptors

In this chapter, the potential structural variations in the generated primary sequence-based descriptors presented in the previous chapter was investigated with regards to the mAb isotypes and species origins. Due to many residues being conserved in individual isotypes based on the sequence alignment in the previous chapter, it was expected that descriptors generated from the constant domains of the heavy or light chain would impact on the generated descriptors. This was more uncertain in the case of the species origins due to the variable domains containing the majority of the sequence variability in the mAb primary sequence and therefore critical residues were likely to be confounded. Exploration was performed with PCA to characterise the impact of the heavy and light chain isotypes while more dedicated classification methods such as PLS-DA and SVC were used to establish potential correlation between the sequence structure and the species origins.

4.1 Material and Methods

4.1.1 Sequence gathering

Primary sequences of therapeutic based mAbs were collected from the IMGT database accessed in March 2017. Only sequences of full chain mAbs were collected where mixed heavy chain isotypes, such as IgG2/4, and mixed species origins, such as chimeric-humanised samples, were excluded. In total, 273 mAb sequences were collected and stored in a database along with key information pertaining to the heavy and light chain isotypes as well as the species origin (see Table A.2 in Appendix A). Table 4.1 lists the number of mAbs out of the collected 273 belonging to a specific isotype or species origin.

Table 4.1. Summary of isotype and species origin diversity of the 273 gathered mAb sequences from the IMGT database.

Chain/Species	Isotype/Origin	Number of Samples
HC	IgG1	197
	IgG2	35
	IgG4	41
LC	kappa	242
	lambda	31
Species	chimeric	35
	human	122
	humanised	116

4.1.2 Descriptor Generation

Structural descriptors for the ***X*** block were generated using the methodology presented in Section 3.2 with four unique primary sequence-based descriptor (PSD) sets prepared: Domain based (PSD1), Substructure based (PSD2), Single AA based (PSD3) and Running Sum based (PSD4).

4.1.3 Modelling Methods

4.1.3.1 Principal Component Analysis

Principal Component Analysis (PCA) was used as an exploratory analysis tool to investigate the four descriptor sets and the relationship between descriptors and different chain isotypes and species origins. Each model was selected to contain 90% of the total variation contained in the descriptor set of interest. PCA implementation was performed using the PLS Toolbox version 8.6.1 (Eigenvector Research, Inc). For more details on PCA, see Section 2.2.1.

4.1.3.2 Partial Least Square Discriminant Analysis

The NIPALS algorithm was used to develop a PLS regression model for predicting the dummy variables generated from the class information pertaining to the species origin of the mAbs. Discriminant Analysis (DA) was then applied to create decision thresholds in order to classify the predictions of the developed PLS model. For more information on PLS-DA, refer to Section 2.3.1.

4.1.3.3 Support Vector Machines for Classification

The LibSVM toolbox was used and implemented in MATLAB 2016a for SVC model development (Chang and Lin, 2011). The C-SVM function in LibSVM uses by default the One-vs-One (OvO) strategy for multiclass classification problems. A shell script was developed to

implement the One-vs-Rest (OvR) classification strategy instead in order to reliably compare SVC to PLS-DA and this is presented in Appendix B.1. Optimisation of the model parameter C was performed using a grid search approach on defined points over specified ranges for each parameter (for details on parameters see Section 2.3.2). The grid points used for C was [10^{-5}, 10^{-4}, 10^{-3}, 10^{-2}, 10^{-1}, 10^{0}, 10^{1}, 10^{2}, 10^{3}, 10^{4}].

4.1.4 Data Curation and Pre-treatment

All descriptor sets were first curated by removing columns containing null values, coded as -999. Furthermore, descriptors with a standard deviation below 0.0001 were also removed as they did not contain sufficient variation for the model development. The standard deviation for a descriptor, k, was calculated according to equation 4.1 where N is the number of samples in the dataset and $\bar{x}_k$ is the average value of the descriptor k. All data blocks were auto-scaled before being used in model development in order to centre the data around zero as well as to scale all descriptors to unit variance (see Section 2.7).

$$\sigma_k = \sqrt{\frac{1}{N-1}\sum_{i=1}^{N}(x_{ik} - \bar{x}_k)^2} \tag{4.1}$$

4.1.5 Model Training and Validation

4.1.5.1 Structured data splitting

Prior to model development with PLS-DA and SVC the data set was split into a calibration set and an external test set to represent future samples. The Kennard-Stone (CADEX) algorithm was used for this purpose which divides the samples according to structural similarity, in the form of Euclidean distance, between samples in the descriptor space (see Section 2.5.1 for more details). 80% of the samples were retained for model calibration and the remaining 20% were kept for external testing and model validation.

4.1.5.2 Cross Validation

A repeated k-fold cross validation scheme was applied for model development for PLS-DA and SVC where k was chosen to be five in order to get an 80/20 sample split ratio between training and validation samples, respectively. 20 iterations were performed to better utilise the data set and decrease the potential impact of outliers in the data on the cross validation.

4.1.5.3 Model Validation

Validation PLS-DA and SVC models were performed using the overall error rate (ER) in eq.(2.62) and the Matthews Correlation Coefficient (MCC) in eq.(2.66) based on the confusion matrices of the developed models. Model parameters in PLS-DA and SVC were selected based on the minimum ER value observed in the cross validation.

4.2 Results and Discussion

4.2.1 Domain based selection of descriptors

Exploratory analyses of the HC and LC isotypes as well as the species origin were performed by first selecting descriptors that were known to be closely related to the investigated response in question based on sequence difference between isotypes described in Section 3.1.3. Figure 4.1 illustrates the selection of descriptors based on their domain of origin. For the HC isotypes, only the heavy chain domains: V_H, C_H1, C_H2 and C_H3 were used and are marked in red illustrated in Figure 4.1a. Similarly, investigation of the LC isotypes was performed with descriptors from the light chain domains: V_L and C_L (see Figure 4.1b). For the Species origins, only the V_H and V_L were used, (see Figure 4.1c), due to these structural differences being present only in the variable domain due to the humanisation of the mAbs (Kim et al., 2005).

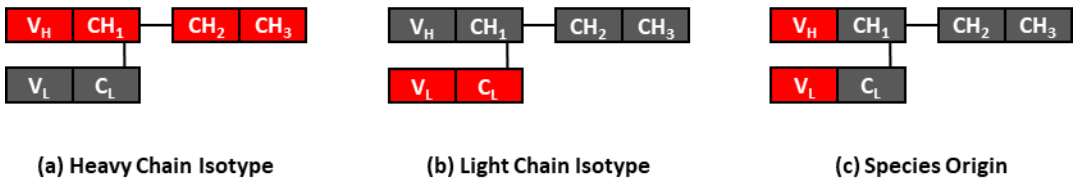

Figure 4.1. Descriptor selection based on the structural origin of investigated response for **(a)** heavy chain isotypes, **(b)** light chain isotypes and **(c)** species origin. Descriptors from the mAb domains used in structural exploration are coloured red while excluded domains are coloured grey in the three presented cases.

PCA was used as an exploratory tool to capture and visualise the information contained in the generated descriptor sets presented in Section 3.2. As PCA is scale dependent, the descriptors were auto-scaled before analysis (Bro and Smilde, 2014). The PCA models were built to capture approximately 90% of all variations contained in the individual descriptor sets. A summary of the PCA models is presented in Table 4.2 and list exploration of both heavy and light chain descriptors separately.

Table 4.2. PCA model summary of heavy chain (HC) descriptors and light chain descriptors (LC) according to the four descriptor resolutions PSD1, PSD2, PSD3 and PSD4. Models were developed to capture approximately 90% of the total variation present in the individual descriptor sets.

Chain	Descriptor Set	Number of Descriptors	Principal Components	Explained Variation (%)
HC	PSD1	543	19	89.96
	PSD2	817	27	90.14
	PSD3	1625	68	90.02
	PSD4	4367	41	90.02
LC	PSD1	272	12	90.20
	PSD2	490	20	90.19
	PSD3	1601	43	90.06
	PSD4	2387	26	89.92

4.2.2 Exploration of HC Isotypes

In the case of the heavy chain, all samples formed three clearly defined groups when analysing the scores from the PCA models. The PCA results of PSD1 is illustrated in Figure 4.2 where the scores and loadings of the two first components were enough to characterise the structural difference between the heavy chain isotypes. It can be observed that IgG1 samples are separated from IgG2 and IgG4 samples in the first PC which explains 34.34% of the total data variation in the descriptor set illustrated in Figure 4.2a. The second component further separates IgG2 from IgG4 samples and explained an additional 17.03% of the total data variation in the PSD1 descriptor set. The subsequent components showed no further separation of the heavy chain isotypes but instead captured varying degrees of variation linked to the sequence variability of the variable domain, V_H (data not shown). From the loadings of the first and second PCs illustrated in Figure 4.2b and Figure 4.2c it can be observed that the constant domains: C_H1, C_H2 and C_H3 contribute more significantly to the separation observed in the score plot while the loadings of the descriptors in the variable domain V_H remain close to zero. This phenomenon is explained by investigating the VDJ gene recombination responsible for expressing the heavy and light chain of the mAbs. All genes encoding for the full heavy chain are located on chromosome 14 in the human genome where the VDJ region codes for the diversity of the V_H domain. Genes encoding for constant domains are located further downstream and contain information for encoding all heavy chain isotypes (Jung and Alt, 2004, Schroeder and Cavacini, 2010). This means the primary sequence of the V_H domain cannot be used to infer the isotype of the heavy chain due to being shared between IgG1, IgG2 and IgG4

and it is therefore the reason for the low contribution of the V_H domain in the loadings plots illustrated in Figure 4.2b and Figure 4.2c.

Identical observations were made for the other descriptor sets: PSD2 (see Figure C.1a and Figure C.1b), PSD3 (see Figure C.1c and Figure C.1d) and PSD4 (see Figure C.1e and Figure C.1f) presented in Appendix C, where the structural differences between the HC isotypes formed distinct groups in the score plots. Some differences in explained data variation was however observed. When using PSD1, PSD2 and PSD4, the first two PCs explained between 35-50% of the total data variation. In the PSD3 descriptor set however, PC1 and PC4 contained the information for heavy chain isotype separation which also had a lower cumulative explained variation of 17.08% of the total data variation. PC2 and PC3 described variation pertaining to the sequence variability in the variable domain, V_H (data not shown). The primary reason for the lower explained variation in PSD3 compared to the other descriptor sets was due to the high resolution where each amino acid is represented individually. This led to a higher exclusion of descriptors from the constant domains during the data curation with more static descriptors being removed in PSD3 compared to the descriptor sets PSD1, PSD2 and PSD4. In the latter descriptor sets all descriptors are a sum of multiple residues and therefore contain more variation. A summary of the PCA analysis of the four descriptor sets exploring the components involved in the separation of the HC isotypes is presented in Table 4.3.

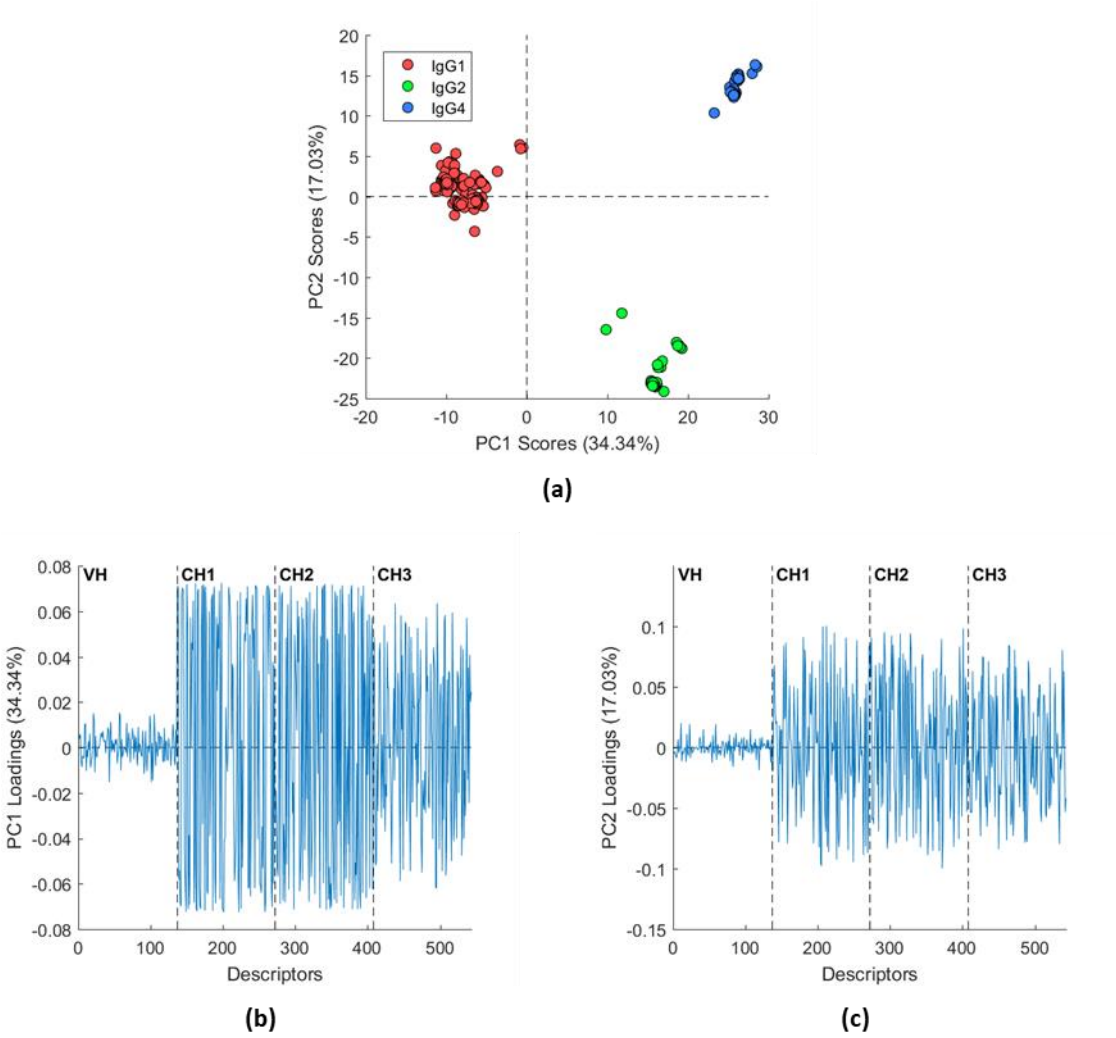

Figure 4.2. PCA exploration of V_H, C_H1, C_H2 and C_H3 descriptors from PSD1. **(a)** Score plot of the first two principal components (PCs). The isotypes IgG1 are coloured red, IgG2 coloured green and IgG4 coloured blue. **(b)** Loadings of the first PC. **(c)** Loadings of the second PC.

Table 4.3. Summary of PCA analysis listing the principal components used to observe separation of HC and LC isotypes together with the corresponding explained data variation for each descriptor set. The last column shows the percentage of descriptors generated from the constant domains.

Chain	Descriptor Set	Principal Components	Explained Variation (%)	Number of Descriptors	Constant Domain Descriptors (%)
HC	PSD1	1, 2	51.37	543	74.95
	PSD2	1, 2	42.93	817	70.13
	PSD3	1, 4	17.08	1625	45.17
	PSD4	1, 2	35.57	4367	68.26
LC	PSD1	1	52.23	272	50.00
	PSD2	1	54.29	490	50.20
	PSD3	1	49.81	1601	47.09
	PSD4	1	52.61	2387	47.47

4.2.3 Exploration of LC Isotypes

Similarly to the heavy chain, a very clear separation of the light chain isotypes, kappa and lambda, was observed in the first PC for the PSD1 descriptor set seen in Figure 4.3a which explained 52.23% of the data variation. However, contributions to the separation were not only caused by the constant domain C_L but the variable domain V_L also contributed to the separation of kappa and lambda seen in Figure 4.3b. Identical trends of PCA scores and loadings were also observed in the other three descriptor sets: PSD2 (see Figure C.2a and Figure C.2b), PSD3 (see Figure C.2c and Figure C.2d) and PSD4 (see Figure C.2e and Figure C.2f) presented in Appendix C where the first principal component explained 54.29%, 49.81% and 52.61% of the data variation, respectively. The contribution of the V_H domain to the separation is due to the fact that the VJ gene recombination of the light chain occurs at two separate chromosomes where lambda is encoded on chromosome 2 and kappa on chromosome 22. Both chromosomes have an individual VJ region for encoding the V_L domain whose primary sequence thus becomes dependent on the isotype that is expressed (Jung and Alt, 2004, Schroeder and Cavacini, 2010). It therefore becomes possible to infer the light chain isotype based on the primary sequence of the V_L domain alone. This is further supported by the fact that the explained variation of the first PC in all descriptor sets is larger than the percentage of descriptors originating from the constant domain C_L as presented in Table 4.3.

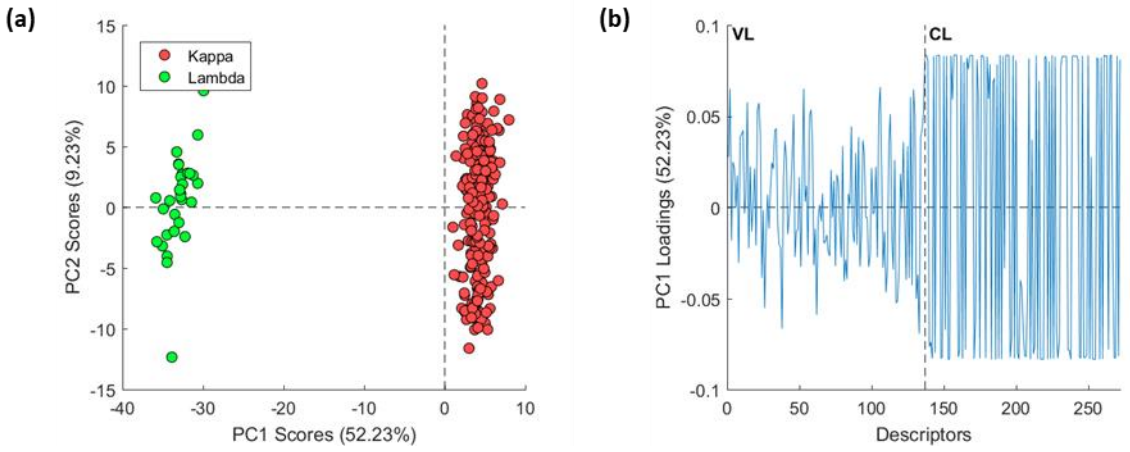

Figure 4.3. PCA analysis of V_L and C_L descriptors from the PSD1 descriptor set. **(a)** Score plot of the first two principal components (PCs). The isotype kappa is coloured red and lambda is coloured green. **(b)** Loadings of the first PC.

4.2.4 Exploration of species origin

Compared to previous observations on HC and LC isotype analysis, the PCA analysis of the V_H and V_L domain descriptors did not yield a clear separation between chimeric, human and humanised samples as can be observed for the PSD1 descriptor set in Figure 4.4a. Instead,

structural features related to the LC isotypes had a big influence on the captured data variation and this was a driving force in the separation of samples as can be observed in Figure 4.4b for descriptor set PSD1. Similar observations were made for the three other descriptors sets and are presented in Appendix C for PSD2 (see Figure C.3a and Figure C.3b), PSD3 (see Figure C.3c and Figure C.3d) and PSD4 (see Figure C.3e and Figure C.3f). This was not unexpected however due to the contribution of the V_L domain descriptors observed in Figure 4.3b and that the expression of kappa and lambda light chain occurs at different Chromosomes. Another impacting factor is the high diversity of the CDR regions in the variable domains which are the main source of data variation in the four descriptor sets and therefore makes it difficult to observe any species origin related separation with PCA. Even when exploring principal components of higher order, no defined separation of the species origins can be observed in the descriptor sets. Therefore, PLS-DA was used for classification in order to explore the extent of data variation related to the species origins. SVC was also applied as an additional classification method to evaluate the effect of the descriptor sets on model performance and accuracy between methods.

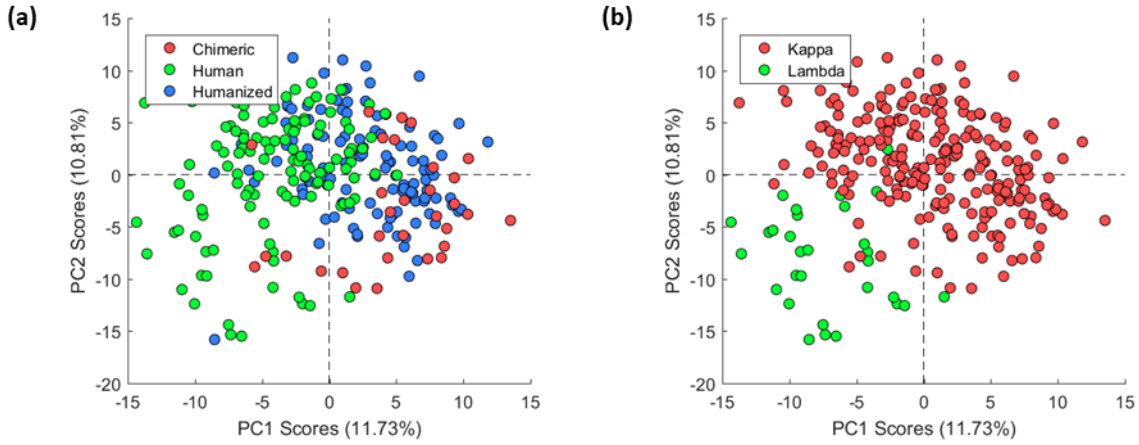

Figure 4.4. PCA scores of the first and second principal components (PCs) from V_H and V_L domain descriptors of PSD1. **(a)** chimeric (red), human (green) and humanised (blue) samples. **(b)** I LC isotypes kappa (red) and lambda (green)

4.2.5 Species origin classification

To evaluate developed supervised models, the sample set was split into a calibration and test sets with an 80/20 ratio using the CADEX algorithm in order to retain the majority of samples and data variation for training. Using the CADEX algorithm also assured that samples in the test set would be structurally similar to the samples in in the calibration set with regards to the descriptor space. Table 4.4 lists the splits of the four descriptor sets with regards to the species origins. It can be observed that the ratio of test set samples was retained at around 0.2 for the

three individual species origins in the four descriptor sets thus retaining representation in the test set.

Table 4.4. Sample split with CADEX of the descriptor sets: PSD1, PSD2, PSD3 and PSD4. The number of samples belonging to each individual species origin is listed for both the calibration and test sets.

Descriptor Set	Number of Descriptors	Species Origin	Calibration	Test Set	Sample Ratio (Test)
PSD1	272	chimeric	28	7	0.20
		human	95	27	0.22
		humanised	95	21	0.18
PSD2	488	chimeric	26	9	0.26
		human	98	24	0.21
		humanised	94	22	0.19
PSD3	1738	chimeric	28	7	0.20
		human	92	30	0.25
		humanised	98	18	0.16
PSD4	2640	chimeric	29	6	0.17
		human	93	29	0.24
		humanised	96	20	0.17

A summary of the performance of the developed PLS-DA and SVC models is shown in Table 4.5 for each of the four descriptor sets. In general, models developed with SVC showed a little higher performance compared to PLS-DA in both the cross-validation and test set, thus indicating slightly better generalisation which was most pronounced in the PSD1 and PSD2 descriptor sets. A potential reason for this may be due to the fact that all samples impact on the on the regression prediction in PLS-DA model and therefore it is more likely to be influenced by noisy samples. On the other hand, SVC models are developed only on an optimal subset of the samples (support vectors) used for defining the decision boundary which thereby reduces the influence of noisy samples on the model performance. Notwithstanding this, all models had excellent performance in the external test set with MCC values well above 0.7 except for the PLS-DA model developed using PSD1. Due to the differences in sample sizes between chimeric, human and humanised samples, the MCC metric is preferred as it gives fair representation of all classes regardless of samples size (Jurman et al., 2012). The high MCC values are therefore an indication of strong correlation between the structural descriptors of the V_H and V_L domains and the species origin. As no descriptor reduction or selection has been performed on the descriptor sets prior to model development, a strong correlation between the primary sequence and the species origin can be assumed.

In addition, the developed PLS-DA models also give an indication of the extent of the data variation in the V_H and V_L domain descriptors that are correlated to the species origin. From Table 4.5 it can be observed that roughly a quarter of the total data variation in PSD2, PSD3 and PSD4 is used for class prediction by the models whereas the variation used inPSD1 is slightly higher with 35.93%. Thus, an estimation of the structural variation from the V_H and V_L domains correlated to species origin can be inferred based on the used data variation by the developed PLS-DA models.

Table 4.5. Summary of model performance of PLS-DA and SVC developed on the descriptor sets: PSD1, PSD2, PSD3 and PSD4. Performance metrics for calibration (Cal), cross-validation (CV) and the external test (Test) set are provided.

Method	Descriptor Set	Explained *X* Variation (%)	Cal		CV		Test	
			MCC	ER	MCC	ER	MCC	ER
PLS-DA	PSD1	35.93	0.82	0.11	0.68	0.19	0.68	0.20
	PSD2	22.21	0.77	0.14	0.62	0.23	0.79	0.13
	PSD3	28.70	0.95	0.03	0.75	0.15	0.96	0.04
	PSD4	24.41	0.88	0.07	0.71	0.18	0.91	0.05
SVC	PSD1	-	0.92	0.05	0.72	0.17	0.85	0.09
	PSD2	-	0.93	0.04	0.72	0.17	0.94	0.04
	PSD3	-	0.99	0.01	0.74	0.15	0.94	0.04
	PSD4	-	0.95	0.03	0.79	0.13	0.94	0.04

In addition, individual classification performance in relation to the chimeric, human and humanised samples was assessed with receiver operating characteristics (ROC) curves on the cross-validation results in order to understand the slightly lower MCC values compared to those in the calibration and test set. More specifically, the area under the curve (AUC) was used as a performance metric with a value of 0.5 indicating poor classification accuracy and a value of one indicating perfect classification (Fawcett, 2006). The AUC values obtained from the cross-validation on PLS-DA model developed using PSD3 data set are illustrated in Figure 4.5a and the equivalent SVC model in Figure 4.5b. The black dashed line represents the AUC value of 0.5 thus indicating a reference border where no discrimination between classes are possible (see Section 2.6.2). Clearly these were all above 0.9 thus indicating high accuracy. It can be observed that most of the misclassification occurs in the humanised samples (blue line) whose AUC values are lower compared to those of the chimeric and human samples. This is the cause for the lower MCC values in the cross-validation compared to the calibration and external test set, where the misclassification of humanised samples was lower (data not shown). This trend was also observed in the cross-validation results of PLS-DA and SVC ROC curves for the remaining three descriptor sets of PSD1, PSD2 and PSD4, illustrated in Figure C.4 in Appendix C. A

closer inspection of the resulting confusion matrices from the cross-validation of the four descriptor sets showed that the misclassified humanized samples were classified as a mix of chimeric and human (data not shown). Therefore, no particular preference was observed of the misclassified samples that leaned more towards the chimeric class or the human class. A potential reason for this could be due to the mix of chimeric CDRs and the human framework regions which in unique instances, have a higher resemblance to that of fully chimeric or fully human sequences.

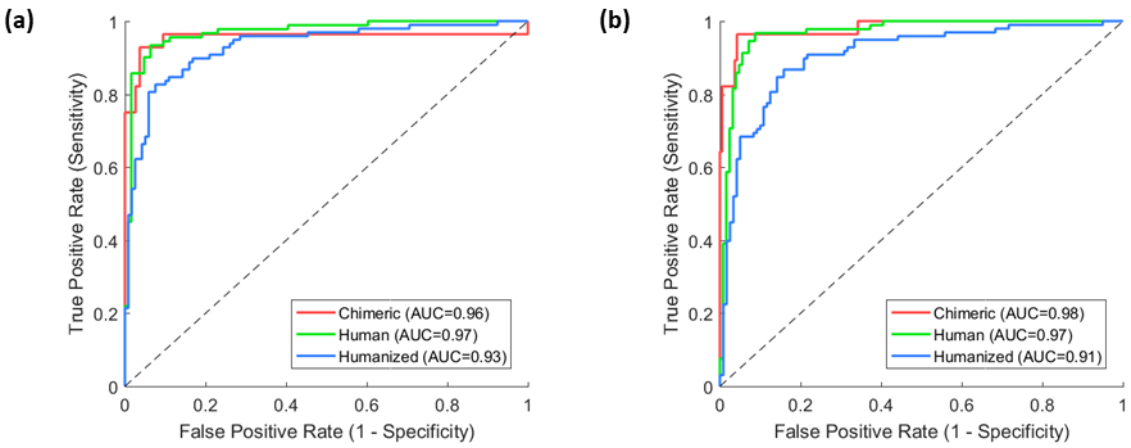

Figure 4.5. ROC curves and AUC for chimeric (red line), human (green line) and humanised (blue line) samples developed on prediction data from the cross-validation of PSD3 in **(a)** PLS-DA and **(b)** SVC. The black dashed line represents the AUC value of 0.5 where no discrimination between classes can be made.

4.3 Summary

Based on the results presented in this chapter, the developed primary sequence-based descriptors from Chapter 3 work well for identifying more apparent structural differences such as the HC and LC isotypes through exploration techniques such as PCA. More advanced supervised methods had to be used, however, to successfully separate and classify the species origin of the used samples in order to reach higher accuracy. These exploration and classification results were not unexpected based on the evident differences in the primary sequence of the constant domains and the structural variation originating from humanisation of mAbs presented in Section 3.1.5 (see Figure 3.2). Instead, the descriptor sets applicability to these problems indicates that the developed descriptors reflect the underlying biological features and thus the development of more advanced predictive models can be attempted. The next logical step would be to try to develop models for prediction of mAb behaviour in more complex experimental environments where the structural correlation to the response might be more elusive.

The second important finding in this chapter is the characterisation of sources of structural variation correlated to mAb isotypes and species origins that greatly impact the descriptors. The described workflow in this chapter can therefore be used to determine sources of systematic variation that is present in the mAb structure. Characterisation of such variation becomes vital in model development as it can negatively impact model performance if the variation is unrelated to the response which is explored in the next chapter.

Chapter 5

QSAR Model development: Primary sequence-based descriptors

In Chapter 3, a novel workflow was presented for the generation of descriptor sets, capturing varying sequence resolutions, were developed from the primary sequences of mAbs. In this chapter the four primary sequence-based descriptor sets were investigated and applied in the prediction of HIC retention times and mAb yields. These were chosen as response vectors for model development due to being important parameters in pharmaceutical industries for the assessment of productivity and product stability, respectively. The structural variation related to the heavy and light chain isotypes as well as species origins present in the primary sequence-based descriptor sets observed in Chapter 4 were further explored with regards to the chosen responses. A benchmarking scheme for sequential improvement and comparison of the models with regards to descriptor reduction and selection is also developed and presented in this chapter.

5.1 Material and Methods

5.1.1 Response Data

In this research, the quantitative process data published by Jain et al. (2017) was used to develop predictive models (Jain et al., 2017). It is important to note that all constant domains in the heavy chain were expressed as IgG1 for the heavy chain with allele IGHG1*01. The original isotype of the light chain was retained in the explored samples where two alleles were used for expressing either kappa (IGKC*01) or lambda (IGLC1*01) conformation.

The diversity of the of Jain dataset is illustrated in Figure 5.1 which shows the distribution of Kappa and Lambda mAbs (Figure 5.1a), the distribution of human, humanized and chimeric

mAbs (Figure 5.1a) as well as the distribution of mAbs in the different clinical phases: phase II, phase III and phase IV (approved) (Figure 5.1c).

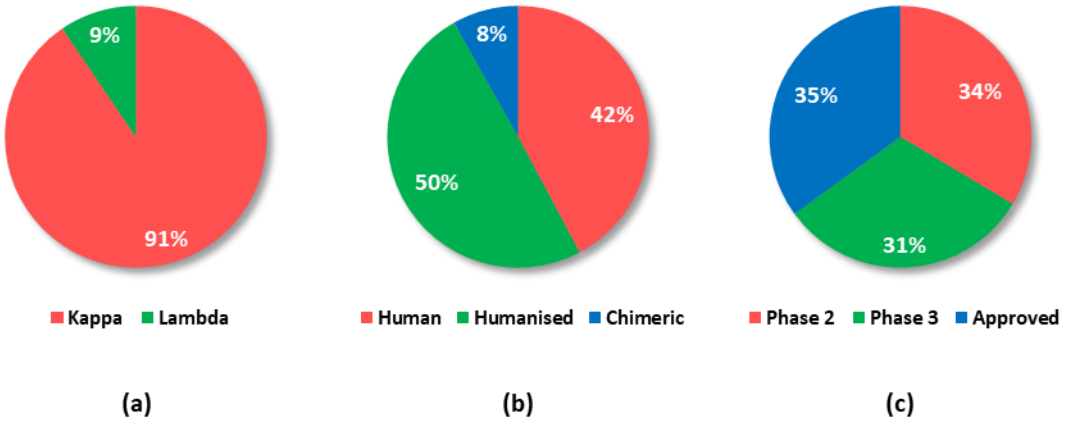

Figure 5.1. General summary of mAbs in the dataset from Jain et al. (2017) according to **(a)** the light chain isotypes, **(b)** species origins and **(c)** clinical phase distribution.

Out of the 12 characterised biophysical properties available in the publication of Jain et al. (2017), the mAb yields from the HEK cell line cultivations and the HIC retention times were selected as model responses as discussed in Section 1.5. A brief description of the experimental setup for both responses is explained below according to the description provided by the authors. No triplicates were given for either for mAb yield or HIC retention times for the 137 mAb.

5.1.1.1 mAb expression and extraction

The 137 mAbs were expressed in HEK293 cells under identical cultivation conditions. After 6 d of growth, the cell culture supernatant was harvested by centrifugation and passed over Protein A agarose (MabSelect SuRe from GE Healthcare Life Sciences). The bound mAbs were then washed with PBS and eluted with buffer (200 mM acetic acid/50 mM NaCl, pH 3.5) into 1/8 volume 2 M Hepes, pH 8.0. The final products were buffer-exchanged into 25 mM Hepes and 150 mM sodium chloride at pH 7.3.

5.1.1.2 HIC

5 µg of IgG samples (1 mg/mL) were mixed with a mobile phase A solution (1.8 M ammonium sulphate and 0.1 M sodium phosphate at pH 6.5) to achieve a final ammonium sulphate concentration of about 1 M before analysis. A Sepax Proteomix HIC butyl-NP5 column was used with a linear gradient of mobile phase A and mobile phase B solution (0.1 M sodium phosphate, pH 6.5) over 20 min at a flow rate of 1 mL/min with UV absorbance monitoring at 280 nm.

5.1.1.3 Exclusion of samples

Out of the 137 available mAbs in the data set, 6 mAbs were excluded based on one of the following reasons:

1) Original mAb was not of IgG class e.g. IgM
2) Original mAb was of a hybrid conformation e.g. IgG2/4
3) Experimental data for mAb was not available

This resulted in 131 mAbs being selected for further evaluation and are listed in Appendix A, Table A.3 with corresponding experimental measurements for HIC retention times and mAb yields.

5.1.2 Descriptor Data Generation

Structural descriptors for the $\boldsymbol{X}$ block were generated based on the methodology presented in Chapter 3 where four unique descriptor sets were attained: Domain based (PSD1), Substructure based (PSD2), Single AA based (PSD3) and Running Sum based (PSD4) where PSD is short for "Primary sequence-based descriptors". All sequences for the variable domains V_H and V_L were provided as supplementary information in the study from Jain et al (2017). Final heavy chain sequences for descriptor generation were prepared by attaching the allele sequence IGHG1*01 representing IgG1 isotype to the V_H domains. The allele sequences IGLK1*01 and IGLC1*01 were used and attached to V_L domains of kappa and lambda isotype, respectively.

5.1.3 Modelling Methods

5.1.3.1 PLS

Partial Least Squares regression was performed using the NIPALS algorithm. The first 20 latent variables were calculated to allow for a majority of the data variation in $\boldsymbol{X}$ and $\boldsymbol{Y}$ to be captured. A higher number of latent variables is usually not recommended as they commonly only improve fitting of individual samples, thus causing over-fitting (Wold et al., 2001). For more information on PLS, refer to Section 2.4.1.

5.1.3.2 SVR

Optimisation of the model parameters C and ϵ was performed by using a grid search approach on defined points over specified ranges for each parameter (for details on parameters see Section 2.4.2). The grid points used for C were [10^{-5}, 10^{-4}, 10^{-3}, 10^{-2}, 10^{-1}, 10^{0}, 10^{1}, 10^{2}, 10^{3}, 10^{4}] whereas the grid points used for ϵ were [10^{-3}, $10^{-2.5}$, 10^{-2}, $10^{-1.5}$, 10^{-1}, $10^{-0.5}$, 10^{0}, $10^{0.5}$, 10^{1}]. This resulted in 90 different parameter permutations that were evaluated in the cross validation.

5.1.4 Model Training and Validation

5.1.4.1 Structured data splitting

Prior to model development the data set was split into a calibration set and an external test set to represent future samples. The Kennard-Stone (CADEX) algorithm was used to divide the samples according to structural similarity in the form of Euclidean distance between samples in the descriptor space (see Section 2.5.1 for more details). 80% of the samples were retained for model calibration where the remaining 20% was kept for external testing and model validation.

5.1.4.2 Cross-Validation scheme

A repeated k-fold cross validation scheme was applied for model development where k was chosen to be five in order to get an 80/20 sample split ratio between training and validation samples, respectively. 20 iterations were performed to better utilise the data set and decrease potential impacts of outliers in the data on the cross validation. For more information, see Section 2.5.2.

5.1.4.3 Model Validation

All models were validated adhering to the OECD guidelines for R^2 and Q^2 in QSAR/QSPR models (Veerasamy et al., 2011, Alexander et al., 2015). The guidelines state that R^2 and Q^2 should be greater than 0.5 and 0.6 in the cross-validation and external prediction, respectively. The thresholds for R^2 and Q^2 in the OECD guidelines are intended to be used for early model development to explore potential correlation of factors and descriptors related to the modelled responses. Once characterised, additional descriptor development and adjustments can be performed to further improve model performance. For more information on R^2 and Q^2, refer to Section 2.6.1.

5.1.4.4 Y-Randomisation

Y-randomisation was used to evaluate the presence of random correlation between a descriptor set and a randomised response vector. The response vector was randomised 50 times and an individual model was developed on each permutation. Calculated R^2 and Q^2 values from the 50 models were then averaged. If no chance correlation is present in the descriptor set both the averaged R^2 and Q^2 values will be low. For more details on Y-randomisation, refer to Section 2.6.3.

5.1.5 Descriptor reduction and selection

The placement of the unsupervised V-WSP reduction algorithm in the model development pipeline needed to be considered in order to generate an unbiased test set, as discussed in Section 2.5.1. Two approaches were considered where the first scenario places the V-WSP reduction prior to the structured data splitting using CADEX illustrated in Figure 5.2a. This sequence however, introduces a bias due to collinearity reduction of descriptors with all available samples in the data set. This means, that even after splitting the data set into a calibration set (black box) and a test set (red box), the selection of the test set samples might have been affected by the descriptor reduction of all samples. The descriptor reduction is thus influenced by all samples and therefore becomes biased. Instead, the second scenario illustrated in Figure 5.2b has the V-WSP reduction placed after the data splitting which ensures that only selected calibration samples influence the descriptor reduction. This approach is thus unbiased as it keeps the external test set samples separate throughout the model development pipeline where descriptor reduction and selection were performed only on the calibration set. For these reasons, development of all models in this chapter was performed adhering to the workflow illustrated in Figure 5.2b.

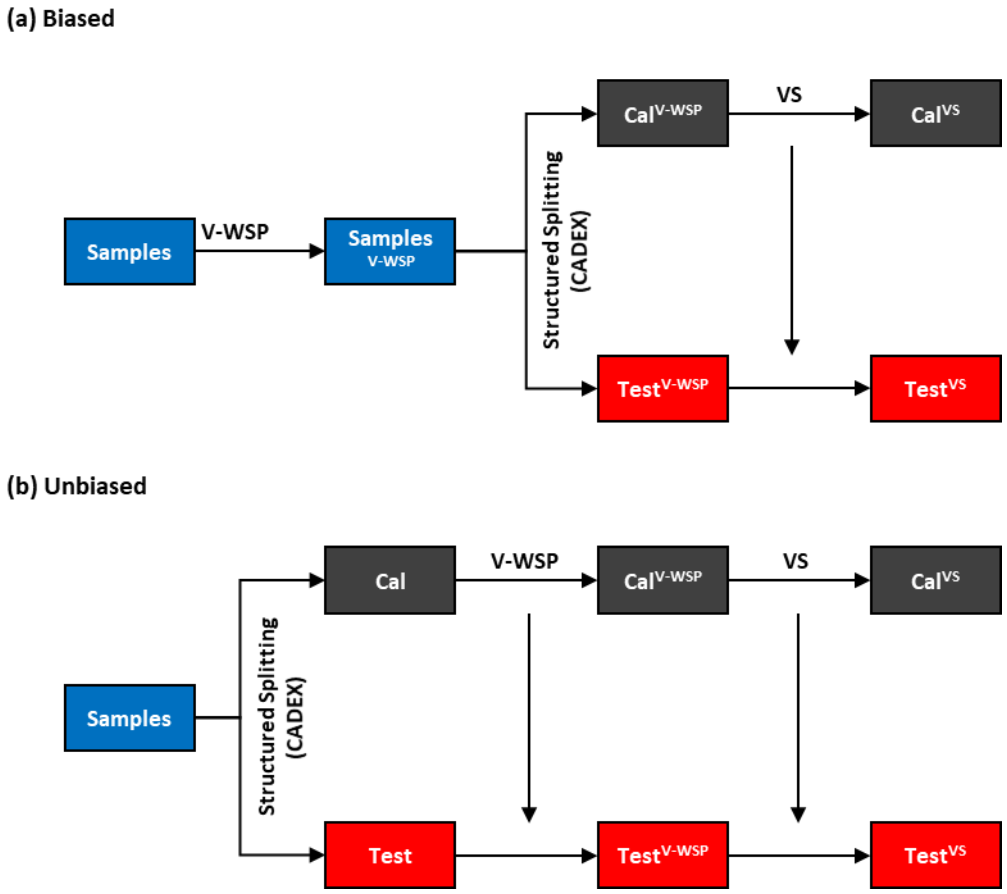

Figure 5.2. Overview and placement consideration of the V-WSP algorithm in regards to the data splitting and the variable selection (VS). **(a)** Placement of V-WSP reduction prior to structured sample splitting results in a biased selection of descriptors due to influence from all samples. **(b)** Structured splitting performed before V-WSP reduction results in an unbiased selection of descriptors due to being independent from the test set samples. Vertical arrows represent selection of descriptors in the test set to match the calibration set.

5.1.5.1 V-WSP

The V-WSP algorithm was applied as an unsupervised reduction method to reduce the number of descriptors in the ***X*** block by only keeping descriptors with low correlation between them (Ballabio et al., 2014). Procrustes goodness of fit was used as a metric to investigate how much of the information between the original and reduced data was retained after the variable reduction with the V-WSP algorithm (Peres-Neto and Jackson, 2001, Kendall, 1989). A Procrustes value of zero means that the information in the data sets is identical and a value of one means that the data sets a completely dissimilar. In the absence of any published acceptable correlation thresholds, the thresholds for each domain were selected by empirically testing all values from 0.5 to 0.99 with increments of 0.01. The correlation threshold was chosen based on guidelines from Ballabio et al. (2014) where the goal of the reduction is the elimination of redundant information and not the preservation of the data structure.

To this end, the correlation thresholds were chosen on a case by case basis for each individual group of descriptors defined by the domains in PSD1 or the substructures in PSD2, PSD3 and

PSD4 therefore corresponding to inherent structural blocks in the mAbs. This was done in order to preserve vital information present in each individual structural block of the mAb structure and at the same time reduce the number of redundant descriptors. Reduction with V-WSP was performed prior to any supervised variable selection method used in this research according to Figure 5.2b.

5.1.5.2 rPLS

Supervised variable selection with rPLS was performed with PLS Toolbox 8.6.1 (Eigenvector Research Inc) together with MATLAB 2016a (Mathworks®). An initial PLS model was developed with selected descriptors from V-WSP reduction and the latent variable with the smallest RMSECV was selected as a starting point for the rPLS selection. For more information on rPLS, refer to Section 2.9.1.

5.1.5.3 GA

Supervised variable selection with Genetic Algorithm (GA) was performed using PLS Toolbox 8.6.1 (Eigenvector Research Inc) together with MATLAB 2016a (Mathworks®) and PLS as the fitness function. A population size of 100 was used and the maximum number of generations was set to 100. The convergence for the GA algorithm was set to 50%. Default values for the mutation rate and the ratio of kept variables in the initial models was kept as 0.5% and 30%, respectively. For more information on the GA algorithm, refer to Section 2.9.2.

5.1.5.4 LASSO

Supervised variable selection with L1-norm regularisation (LASSO) with SVR was applied using the function *fitrlinear* in MATLAB 2016a (Mathworks®) where SVR was set as the learner and lasso set as the regularisation method. A grid search was performed similar to that of SVR method in Section 5.1.3.2 above in order to optimise the parameter selection. The *fitrlinear* function uses λ according to eq.(5.1) instead of C as a regularisation term as previously described in Section 2.4.2.1.

$$\min_{\boldsymbol{w},b,\boldsymbol{\xi},\boldsymbol{\xi}^*} \lambda\|\boldsymbol{w}\|_1 + \frac{1}{n}\sum_{i=1}^{n}(\xi_i + \xi_i^*)^2 \qquad (5.1)$$

The relationship between C and λ is described in eq.(5.2) where n is the number of samples (Rifkin, 2002). The relationship was used to convert the previously used C values to that of λ instead.

$$C = \frac{1}{2\lambda n} \tag{5.2}$$

For more details on the LASSO method, refer to Section 2.9.3.

5.1.6 Model Benchmarking

In this research, descriptor reduction and selection were performed and evaluated in subsequent steps (Figure 5.3) in order to better investigate their impact on the model performance. For each descriptor set, the CADEX algorithm was applied to split the available samples into a calibration set for training (80%) and a test set for model validation (20%). Following the outline in Figure 5.3, an initial model was developed with all descriptors in the descriptor set of interest. A second model was then developed after V-WSP reduction had been performed on the descriptor set. A final model was then developed after variable selection with either rPLS, LASSO or GA had been performed on the V-WSP reduced descriptor set. The performance metrics of R^2 and Q^2 of the cross-validation and the test set from each of the three model were then compared to evaluate the effect of the descriptor reduction and selection methods. This process was repeated for each of the four descriptor sets: PSD1, PSD2, PSD3 and PSD4 when using either PLS or SVR as modelling method.

In total, 32 models were developed in order to compare the performance of different permutations of the presented methods. It is important to note that LASSO was only applied when SVR was used as modelling method whereas rPLS was only applied when PLS was used as modelling method.

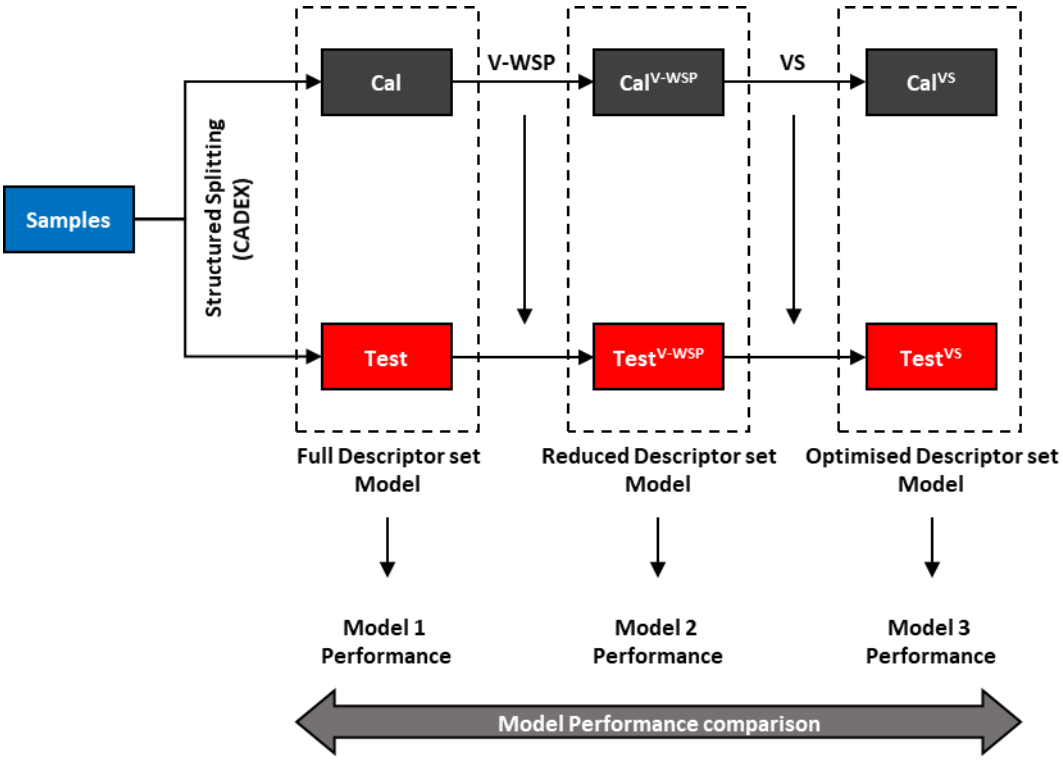

Figure 5.3. Sequential model development and evaluation for investigation of changes in performance with descriptor reduction and selection methods. Three models are developed on 1) all available descriptors, 2) the V-WSP reduced descriptor set and 3) the descriptor set after supervised variable selection (VS).

5.1.7 Statistical testing

In Chapter 4, strong correlations were observed between the individual chains and their corresponding isotypes based on exploratory analysis with PCA (see Section 4.2.2 for the heavy chain and Section 4.2.3 for the light chain). A strong correlation was also observed between the variable domains and the species origin when explored with PLS-DA and SVC (see Section 4.2.5). Statistical models were therefore used to establish if any significant differences were present between groups (statistical factors) of responses. In this research the factors were defined as the heavy chain, the light chain and the species origin of the mAbs. The heavy chain factor consisted of three levels being: IgG1, IgG2 or IgG4. The light chain factor consisted of two levels being: kappa or lambda. Finally, the species factor consisted of three levels being: chimeric, human or humanised. Figure 5.4 illustrates a decision tree for choosing an appropriate test depending on the normality and the available number of levels in the investigated factor.

Normality was tested using the Anderson-Darling test with a significance level of 0.05 (Anderson and Darling, 1952). H_0 is the hypothesis that the data is normally distributed whereas H_1 is the alternative hypothesis that the data follows another distribution.

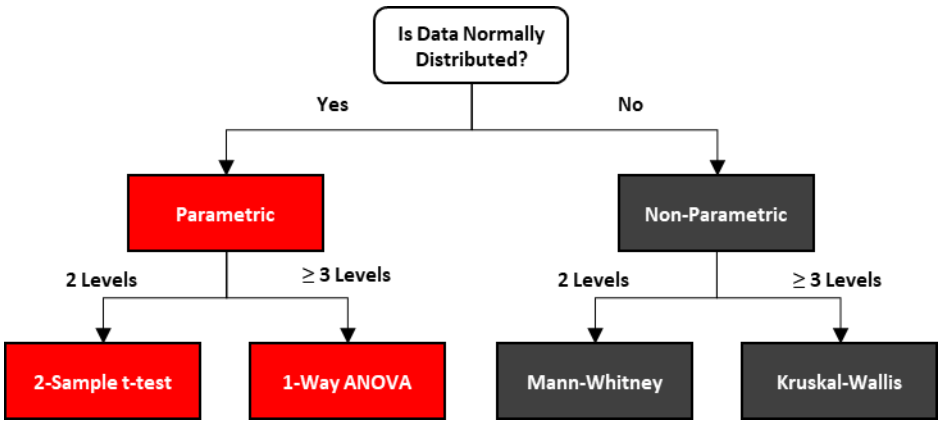

Figure 5.4. Decision tree for statistical testing of response data based on normality and number of available levels for the investigated factor.

5.1.7.1 Parametric methods

Two different parametric tests were used for data that conformed to a normal distribution where the number of available levels in the factor of interest determined which test to use. If two levels were available, a 2-sample t-test was used to test for any significant differences between the group means whereas if three levels were available, a 1-way Analysis of Variance (ANOVA) was used (Krzywinski and Altman, 2014a).

5.1.7.2 Non-parametric methods

Non-parametric tests were used if the data did not conform to a normal distribution. Similar to the parametric methods, the number of available levels in the factor of interest determined which statistical test would be performed. A Mann-Whitney rank test was performed for factors with two levels and a Kruskal-Wallis test was performed for factors with three levels (Krzywinski and Altman, 2014b).

5.1.7.3 Multiple comparison

Two statistical tests were performed for each individual response, one for testing the significant difference between the heavy chain isotypes and the other to test the significant differences between the light chain isotypes. However, performing multiple inferences on the same data set can cause Type I error (incorrectly rejecting H_0). This is due to that fact that when the number of statistical tests increases, the probability of any one of them being significant increases. To adjust for this, the Bonferroni correction was used to modify the significance level according to eq.(5.3) which gives the effective significance level for which each test needs to be tested against (Sedgwick, 2014).

$$\alpha_{(per\ comparison)} = \frac{\alpha}{m} \tag{5.3}$$

where α is the desired significance level, m is the number of performed tests and $\alpha_{(per\ comparison)}$ is the effective significance level.

5.2 Results and discussion

5.2.1 Selection of samples for model development

From Chapter 4 it was observed that much of the data variation in the descriptors had a strong relationship to the heavy chain and light chain isotypes according to the PCA score plots illustrated in Figure 4.2 and Figure 4.3, respectively. This variation is systematic and originates from the unique structure and amino acid composition found in the individual mAb isotypes illustrated in Figure 3.2 in Chapter 3. This is of importance as systematic variation in the $\boldsymbol{X}$ block that is unrelated to the responses can have a negative impact on the developed models and cause large prediction errors (Wold et al., 1998, Trygg and Wold, 2002). Therefore, prior to model development a statistical analysis was performed to test if a significant difference was present between response measurements related to different isotypes of the heavy and light chain. Due to the lack of samples in the IgG2-lambda and IgG4-lambda permutations (two samples in each group), two-factor hypothesis testing methods such as the parametric two-way ANOVA (Fisher, 1992) or its non-parametric equivalent, the Schreier-Ray-Hare test (Sokal and Rohlf, 1969) could not be reliably used. The unequal samples sizes can lead to a decrease in statistical power, meaning that it becomes increasingly difficult to correctly reject H_0 and thus causing a Type II error (Rusticus and Lovato, 2014). Instead, multiple comparisons of single factors (heavy or light chain) were performed in order to increase the sample sizes in each factor level. Appropriate statistical tests were chosen according to the decision tree illustrated in Figure 5.4.

Normality testing was performed for all mAb isotypes groups (kappa, lambda, IgG1, IgG2 and IgG4) for both the HIC retention times and the mAb yields with the results presented in Table 5.1. For the HIC retention times data, normality could not be assumed for the IgG1 and IgG2 isotypes in the heavy chain as well as the kappa isotype in the light chain due to $p < 0.05$. Due to the lack of normality, non-parametric statistical methods were applied were a Kruskal-Wallis test and a Mann-Whitney test were used for significance testing of the heavy chain isotypes and the light chain isotypes, respectively. For the mAb yield data, normality could be assumed in all isotypes and thus parametric statistical methods were applied in these instances. A one-way ANOVA and a two-Sample t-test were used for significance testing of the heavy chain isotypes and the light chain isotypes, respectively.

Table 5.1. Hypothesis testing of heavy and light chain isotypes using Anderson-Darling Normality Test with a significance level of 0.05. H_0 is the hypothesis that the data follows a normal distribution.

Factor (Chain)	Level (Isotype)	Samples	HIC		Yield	
			p	Decision	p	Decision
LC	kappa	119	0.0005	Reject H_0	0.4310	Keep H_0
	lambda	12	0.1498	Keep H_0	0.0648	Keep H_0
HC	IgG1	89	0.0005	Reject H_0	0.1709	Keep H_0
	IgG2	20	0.0097	Reject H_0	0.8839	Keep H_0
	IgG4	22	0.1990	Keep H_0	0.9414	Keep H_0

Results of the statistical tests are presented in Table 5.2. The effective significance level for each test was set to 0.025 according to the Bonferroni correction due to two multiple comparison being performed for each response. The analysis showed that the isotype had no significant impact on the measured responses for either the HIC retention times or the mAb yields. Due to these findings only IgG1-kappa samples were kept for model development due to being the most numerous in the present data set. In addition, this is also the predominantly preferred conformation of new mAbs in clinical trials according to the IMGT database search in Chapter 3. This resulted in 81 samples being selected from the 131 samples in the original data set.

Table 5.2. Hypothesis testing of with a significance level of 0.025 according to the Bonferroni correction for multiple comparisons. H_0 is the hypothesis that there is no significant difference between means of different isotypes. Non-parametric tests are referred to as NP and parametric test as P.

Response	Factor (Chain)	Levels (Isotypes)	Type	Test	Equal Variance	p	Decision
HIC	HC	3	NP	Kruskal-Wallis	-	0.1201	Keep H_0
	LC	2	NP	Mann-Whitney	-	0.0721	Keep H_0
Yield	HC	3	P	1-Way ANOVA	Yes (p=0.2270)	0.8532	Keep H_0
	LC	2	P	2-Sample T-test	Yes (p=0.8052)	0.6326	Keep H_0

It is important to remember that the heavy chain constant domains in all mAbs in the study of Jain et al (2017) were expressed as IgG1, which introduces a bias in the statistical testing of the heavy chain isotypes. As for the light chain, as the original isotypes were kept mostly intact through expression with one allele for kappa and another for lambda, the impact of the light chain isotypes on the measurements becomes more representative. As the statistical testing above was performed through the partitioning of mAbs according to their original isotype, the lack of significance might not hold true if identical experiments were to be performed with unaltered mAbs. The selection of IgG1-kappa mAb samples in this case therefore ensures that

the measurements are more representative in terms of the original mAb structures due to less sequence alteration.

In retrospect, even though the alteration of the original mAbs introduced a bias in the statistical testing of the heavy chain, it gives an alternative approach for investigation of potential variation when combined with exploratory analysis methods such as PCA, PLS-DA or SVC. This to better control the introduction of potential systematic variation in the $\boldsymbol{X}$ block prior to use in model development in order to improve the prediction accuracy of the resulting models. This becomes more relevant in environments such as industrial or clinical settings where the original mAb structures are kept intact in order to infer information.

5.2.2 Impact of species origin

Multiple models were developed on the retained 81 IgG1-kappa samples according to the benchmarking scheme presented in Section 5.1.6 which resulted in unique 32 models. The model performance of each individual model is presented in Table C.4a and Table C.5a in Appendix C for the HIC retention times and mAb yields, respectively. As can be observed, models developed from the full descriptor set or the V-WSP reduced descriptor sets resulted in a poor fit in terms of the cross validation R^2 (0.04 – 0.22) and Q^2 (-0.06 – 0.15) suggesting that the models were unable to capture the underlying correlation within the data. Adequate improvements were first seen after a variable selection step had been performed with the GA selection proving to be superior compared to that of rPLS and L1-SVR variable selection in both PLS and SVR generated models. A concern, however, is the poor R^2 and Q^2 values of the external test set, which never reached satisfactory levels for models with adequate cross validation metrics. All developed models therefore failed the OECD criteria of having a R^2 and $Q^2 > 0.5$ in the cross validation as well as a R^2 and $Q^2 > 0.6$ in the external test set.

5.2.2.1 Behaviour of species origins in PLS models

PLS was used as a diagnostic tool to further investigate the cause of the poor validation in the test set. It was observed that initial of models for HIC retention time prediction developed on the V-WSP reduced descriptor sets only had one component. From the error plots generated by PLS, it was observed that the lowest RMSE value was attained with one component which otherwise increased with higher model complexity for PSD1 (Figure 5.5a), PSD2 (Figure 5.5b), PSD3 (Figure 5.5c) and PSD4 (Figure 5.5d). The same trends in the error was also observed for PLS models developed for prediction of mAb yields and is presented in Figure C.5 in Appendix C.

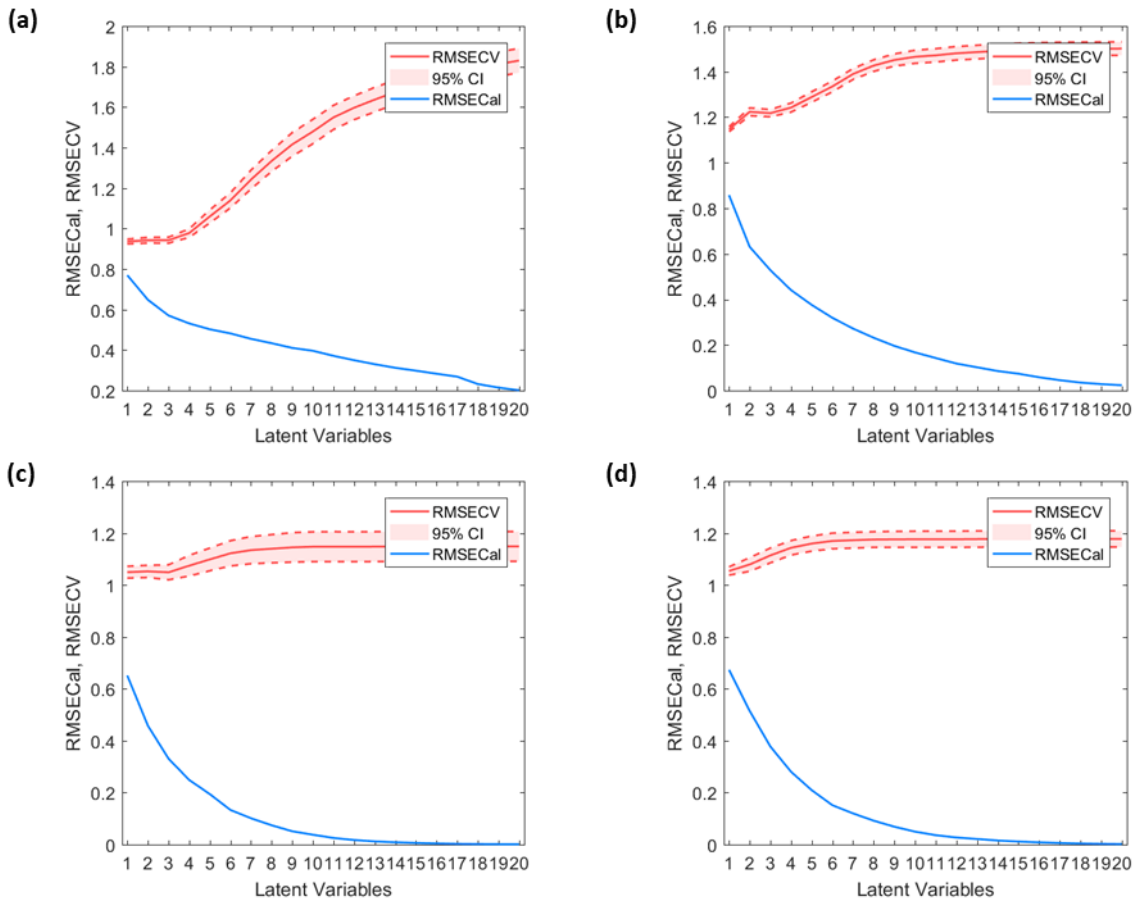

Figure 5.5. PLS error for prediction of HIC retention times in the calibration (blue line) and the cross-validation (red line) with regards to the number of latent variables developed from the V-WSP reduced descriptor sets of (**a**) PSD1, (**b**) PSD2, (**c**) PSD3 and (**d**) PSD4.

Further investigation was performed where a PLS models with two components were developed for each descriptor set in order to closer investigate the samples residuals and scores. This showed that the residuals and PLS scores were greatly affected by the species origin of the mAbs which is illustrated in Figure 5.6 for the HIC retention times. Models used in the Figure 5.6 were developed after V-WSP reduction had been performed and they show the impact of the species origin for the individual descriptor sets. From the influence plots for PSD1 (Figure 5.6a), PSD2 (Figure 5.6c), PSD3 (Figure 5.6e) and PSD4 (Figure 5.6g) it can be observed that the chimeric samples tend to have higher residual values compared to humanised and human samples. This becomes increasingly apparent with higher primary sequence resolution illustrated in PSD2 (Figure 5.6c), PSD3 (Figure 5.6e) and PSD4 (Figure 5.6g) where the chimeric samples are further removed from the humanised and human samples compared to PSD1 (Figure 5.6a). As discussed in Section 3.1.5, this variation originates from the species origin that was used to design the mAbs where mAbs originating from mouse will differ slightly in amino acid composition compared to human mAbs in the framework regions of the variable domains. The retained data variation from the descriptor sets used in the trained PLS models is also affected by the systematic variation caused by the different species origins. This is

illustrated as score plots for PSD1 (Figure 5.6b), PSD2 (Figure 5.6d), PSD3 (Figure 5.6f) and PSD4 (Figure 5.6h). The same trends in the residuals and PLS scores were also observed for PLS models developed for the prediction of the mAb yield measurements where the chimeric samples separated from the human and humanised samples which is presented in Figure C.6 in Appendix C.

The PLS scores ($\boldsymbol{T}$) were used in this analysis as they provide better insight into the rotation of the Latent variables e.g. what is captured by the model with respect to the PLS loadings ($\boldsymbol{W}^*$) in the descriptor space according to the relationship $\boldsymbol{T} = \boldsymbol{X}\boldsymbol{W}^*$ (Wold et al., 2001).The PLS algorithm tries to maximise the co-variance between $\boldsymbol{X}$ and $\boldsymbol{Y}$ but can become confused if there is a systematic variation in $\boldsymbol{X}$ unrelated to $\boldsymbol{Y}$ (Trygg and Wold, 2002). A separation of chimeric samples can be observed through groupings in the lower right quadrant which is most evident in PSD3 and PSD4 with the highest sequence resolution. This illustrates that the PLS model becomes influenced by the different species origins and tries to separate the samples accordingly.

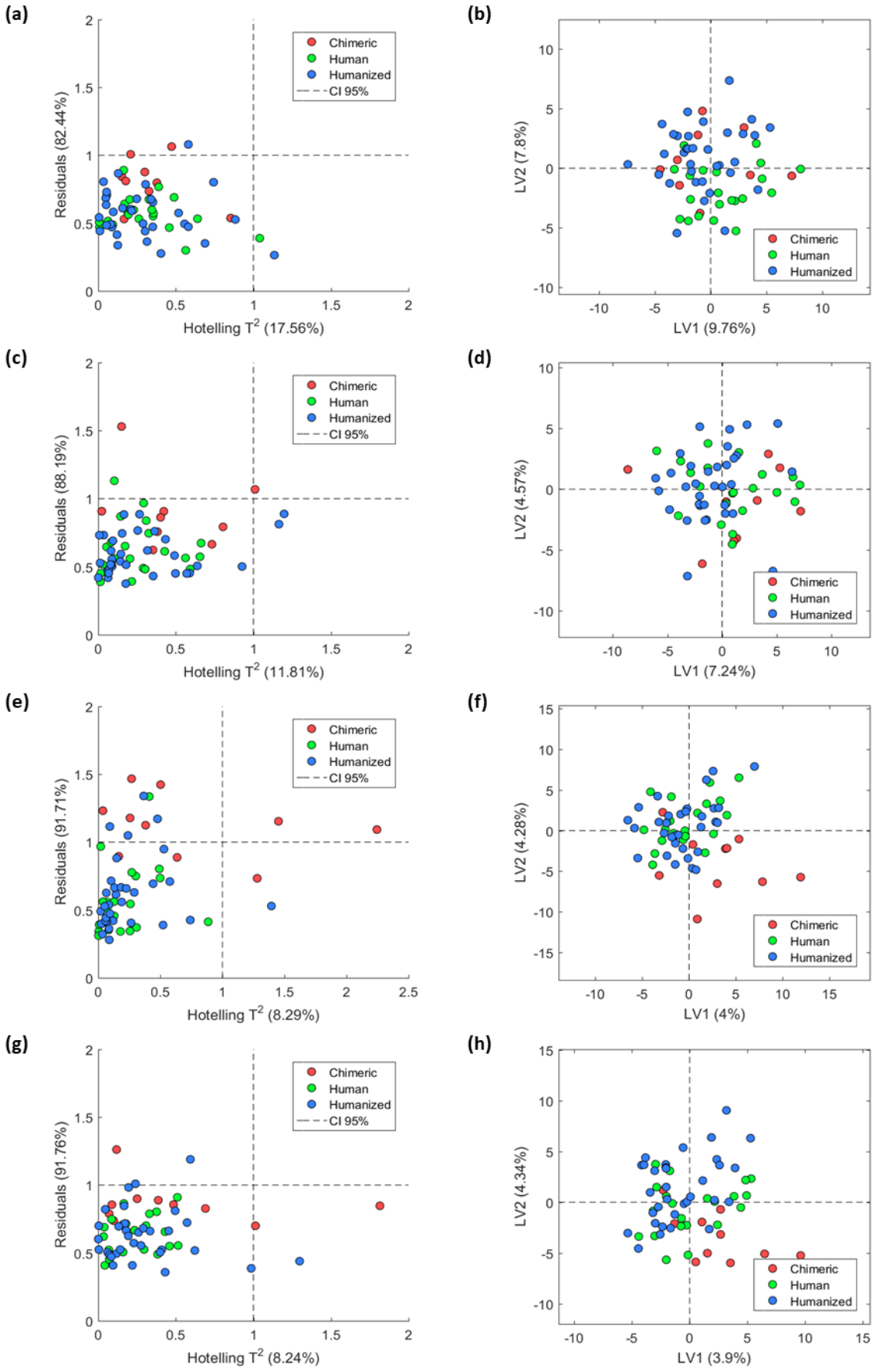

Figure 5.6. Impact of species on PLS models developed using the HIC retention times as the modelled response where chimeric samples are coloured red, human samples in green and humanised in blue. PLS Influence plots for PSD1 **(a)**, PSD2 **(c)**, PSD3 **(e)** and PSD4 **(g)**. PLS scores (T) for the individual samples for PSD1 **(b)**, PSD2 **(d)**, PSD3 **(f)** and PSD4 **(h)**.

5.2.2.2 Significance of species origins

As the variable domains were kept unaltered in the study of Jain et al (2017), additional significance testing according to the species origins was performed to investigate potential differences in the responses between chimeric, human and humanised samples. The study was performed in the same way as described previously in Section 5.2.1 and is therefore only covered briefly here. From the study, it was shown that no significant difference between the HIC retention time means of mAbs from various species origins was observed (Table C.2 in Appendix C) whereas a significant difference ($p = 0.0093 < 0.0133$) was observed between chimeric and humanised samples for the mAb yield measurements (Table C.3 in Appendix C).

In Section 4.2.5 it was shown that classification of the chimeric, human and humanised samples was possible with PLS-DA and SVC due to systematic structural differences in the primary sequences of the V_H and V_L domains. Therefore, combined with the supporting evidence from the diagnostic PLS models in Section 5.2.2.1 and the statistical significance testing of the species origins, an additional sample selection was performed. For the development of models with the HIC retentions time measurements only the humanised samples were retained ($N = 45$). For model development the mAb yield measurements, only chimeric and humanised samples were retained ($N = 55$).

5.2.3 HIC model development on humanised samples

The cross validation and test set validation for all developed models for the HIC retention time prediction is presented in Table C.4b in Appendix C. Models developed with PLS and SVR using the full and V-WSP reduced descriptor sets still show a poor fit in the Cross-validation with values around or below 0.3 and 0.2 for R^2 and Q^2, respectively, for all descriptor sets. Adequate Cross-validation performance was first observed after variable selection where GA especially performed well with both PLS and SVR according to the OECD guidelines (Veerasamy et al., 2011, Alexander et al., 2015). The SVR models developed after variable selection with LASSO never attained good cross-validation performance in any of the data sets. A potential cause to this might be due to that the descriptor sets contains redundant descriptors with differing levels of collinearity toward response correlated descriptors. For the LASSO algorithm to work properly, only a small degree of collinearity can exist between redundant and response correlated descriptors in order for appropiate selection to be performed which is known as the "*Irrepresentable Condition*" (Meinshausen and Yu, 2009).

Out of the four benchmarked descriptor sets, only the PLS and SVR models developed using PSD1 (Domain based) and PSD4 (Running sum) passed the OECD criteria for both cross

validation (R^2 and $Q^2 > 0.5$) and external testing (R^2 and $Q^2 > 0.6$). Due to similar model performance between the PLS and SVR, model selection was based on diagnostic capabilities where the PLS models are preferred due to easier evaluation of residuals and descriptor contribution towards $\boldsymbol{Y}$. PSD1 was selected as the preferred descriptor set due to two reasons:

1. The interpretability of descriptors in PSD1 is higher due to most of them being physiochemical in nature. The PSD4 descriptor set in comparison consists entirely of descriptors generated from three amino acid scales (Z-scale, T-scale and MS-WHIM). Each descriptor represents a score generated from PCA on a set of physiochemical (Z-scale), topological (T-scale) or electrostatic (MS-WHIM) properties and is thus a linear combination of larger descriptor sets (see Section 3.2.2 for more details).
2. The PLS model developed on PSD1 had a lower model complexity compared to the PLS model developed on PSD4 based on the selection of Latent variables (LVs) from the cross validation. Three LVs were selected for the PLS model developed on PSD1 compared to 12 LVs for the PLS model developed on PSD4. This makes interpretability of the contribution from the individual LVs more difficult in the case of PSD4 due to the fact that deflation of $\boldsymbol{X}$ and $\boldsymbol{Y}$ occurs each time a LV is extracted in the PLS algorithm and models with lower complexity are preferred (Wold et al., 2001).

From the original 272 descriptors present in the full PSD1 descriptor set, 51 were retained from the V-WSP reduction thus effectively reducing the number of descriptors by ~80%. Procrustes index was used to evaluate the loss of information when comparing the full and V-WSP reduced PSD1 descriptor sets. A value of 0.1434 was obtained, thus indicating that only a small portion of the information was lost in the reduction step (Ballabio et al., 2014). This can also be observed in Table C.4b in Appendix C for PSD1 where the of R^2 and Q^2 values in the cross validation and the test set remained mostly unchanged after the reduction. Out of the 51 remaining descriptors, GA selected a subset of 17 descriptors used to develop the final PLS model. Model predictions of the calibration and test set samples are shown in Figure 5.7a as a measured vs predicted plot. The test samples are further illustrated in Figure 5.7b as a bar plot for easier comparison of the measured and predicted values. The model performance is summarised in Table 5.3. The PLS regression coefficients for the selected descriptors are illustrated in Figure 5.8.

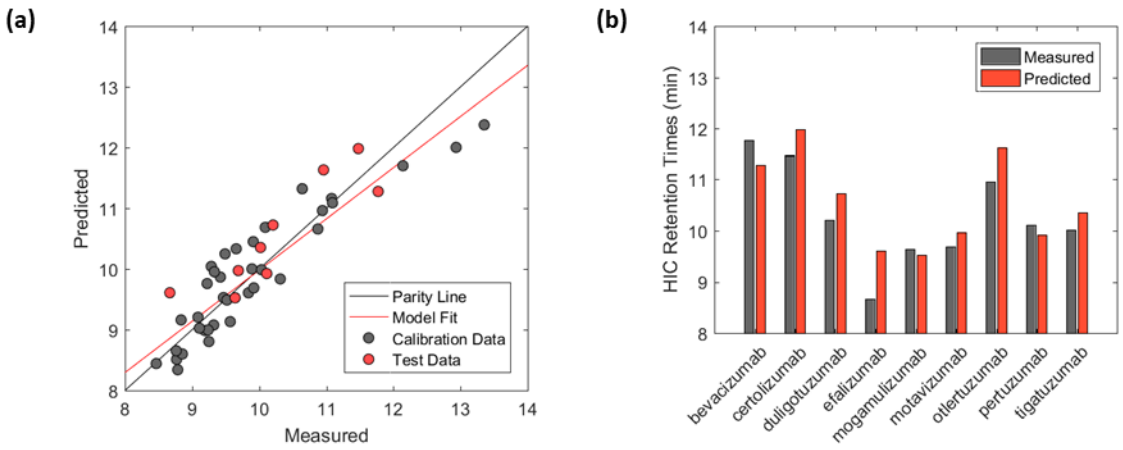

Figure 5.7. HIC retention time predictions of 45 IgG1-kappa humanised mAbs with PLS model (3 LVs) developed on the PSD1 descriptor set after reduction with V-WSP and selection with GA. **(a)** Measured versus predicted plot with calibration (grey) and test (red) samples. **(b)** Predicted and measured HIC retention times of test set samples.

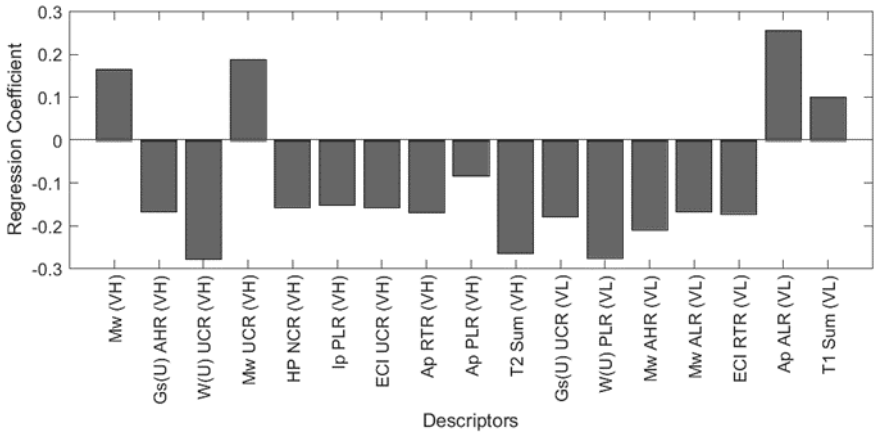

Figure 5.8. Regression coefficients of the PLS model (3 LVs) developed on the PSD1 descriptor set after reduction with V-WSP and selection with GA.

Table 5.3. PLS model summary developed for HIC retention time prediction using the PSD1 descriptor set. Root Mean Square Error (RMSE), R^2, Q^2 and model bias are listed for Calibration, Cross validation, Test set and Y-randomisation

	PLS			
	RMSE	**R^2**	**Q^2**	**Bias**
Calibration	0.47	0.84	0.84	0.00
Cross Validation	0.67	0.63	0.62	0.01
Test	0.51	0.78	0.69	-0.27
Y-scrambled (Average)	1.42	0.05	-0.63	0.01

Many of the test set samples were slightly over predicted which resulted in a negative bias (-0.27). The reason for this is not known but could be a slight indication of over-fitting of the calibration samples due to the difference in bias between the cross-validation and test set (Hastie et al., 2009a).

A general trend observed in the descriptors showed that residue groups consisting mainly of polar and charged residues such as AHR (common residues in alfa helix), NCR (negatively charged residues) UCR (uncharged residues), PLR (polar residues), and RTR (common residues in reverse turn/loops) had a negative contribution on the prediction, thus indicating that mAbs with a high number of polar residues tend to have lower retention times. This is illustrated by the negative coefficients values of the isoelectric point (Ip), charge (ECI), and hydrophobicity (HP) where lower values in these descriptors increases the predicted retention time. This is supported by literature where higher concentrations of salts are required to neutralise the protein polarity in order to expose hydrophobic patches that can bind to the HIC column (Gagnon, 1996a).

The summed molecular weight of the residues in the UCR group in the V_H chain had a positive contribution to the HIC retention time. The UCR group contains tyrosine which has the highest weight among all the group constituents and is also the only residue with a benzene ring, thus making it slightly hydrophobic. This indicates that with increasing number of tyrosine residues, the HIC retention time will increase. This is supported by the descriptor describing the theoretical number of water molecules surrounding a residue, W(U), for the UCR residues in the V_H chain where more polar residues tended to have more surrounding water molecules compared to tyrosine. W(U) was also shown to have a strong negative correlation to the retention time in both the V_H and V_L chain for polar residues further indicating a correlation between hydrophobic residues and longer retention times, which is supported by literature (Kennedy, 1990).

The polar area of residues (Ap) was also shown to be an important factor where larger areas contributed to lower retention times for RTR and PLR residues due to these groups containing mostly polar residues (see Table 3.3 in Section 3.2.1). The opposite was observed in the V_L chain where the polar area of aliphatic residues (ALR) contributed to higher retention times. Glycine has the highest indexed polar area value in ProtDCal of all residues in the ALR group (see Table 3.3 in Section 3.2.1) which indicates that a higher number of glycine residues in the V_L chain contributes to a higher retention time. Glycine and proline are known as unfolding residues which indicates that a higher number of glycine residues aids in decreasing the protein stability and thus increase binding in HIC due to exposure of the hydrophobic patches. This is supported by literature where glycine was shown to have a negative impact on alfa helix stability when introduced (Scott et al., 2007). This is further supported by the model where the molecular weight (M_w) of ALR residues in the V_L chain has a negative correlation to the retention time indicating that other residues besides glycine contribute to lower retention times.

Also, a potential reason for the higher performance achieved with PSD1 compared to higher resolution datasets, such as PSD2 (substructure based) and PSD3 (single amino acid based), could be due to the introduction of more redundant descriptors in PSD2 and PSD3 which has been shown to negatively impact model performance and descriptor selection algorithms (Donoho, 2000, Fan and Lv, 2010). This is especially true for descriptors generated based on the amino acid composition of the sequence where each residue in the mAb structure equally impacts the resulting descriptors. Therefore, through generation of descriptors based on the individual domains, a reduction of the number of redundant descriptors present in the datasets can be achieved compared to descriptor generation for each substructure (PSD2) or each amino acid in the sequence (PSD3).

Y-Randomisation (or Y-Scrambling) was used as a final validation step to evaluate the selection of the descriptors (Rücker et al., 2007). A PLS model was trained on a randomised (scrambled) HIC response vector while the sample order in the PSD1 descriptor set was kept unchanged. This was repeated 50 times and the average of R^2 and Q^2 for the cross validation was calculated. A R^2 value of 0.05 and a Q^2 value of -0.63 was obtained. This indicates that no chance correlation is present and that the selected descriptors are important to describe the relationship between the structure of the mAbs and HIC responses. Results are summarised in Table 5.3.

In order to appropriately evaluate if a mAb can cause potential problems in processing, a threshold needs to be defined based on the mAb HIC retention times. In the research of Jain et al (2017) the authors defined an upper threshold for the HIC retention time as a confidence interval of 11.7 ± 0.6 minutes which was based on the retention times of 48 approved mAbs in their full data set of 137 mAbs. The remaining 89 mAbs in the data set are all pending in clinical phase II or phase III. Thus, any mAbs with a predicted HIC retention time falling above the lower confidence limit (11.1 minutes) could be flagged due to potential risk of being problematic in process development while mAbs falling below can be considered well-behaved. When applying the threshold on the predictions from the PLS-GA model developed on the PSD1 descriptor set, eight mAbs were flagged due to above the lower confidence limit: atezolizumab, bevacizumab, certolizumab, enokizumab, obinutuzumab, otlertuzumab, ranibizumab and tildrakizumab. Five of these mAbs have been approved while three are still in clinical trials. However, this does not necessarily indicate that predictions falling inside or above the threshold confidence interval will definitely fail in process development as there are a number of factors involved that are not accounted for in this evaluation. However, historical data in this context from approved products can be used to develop predictive models that would

allow for risk evaluation in early process development and thereby reduce the load on the bioprocess pipeline.

5.2.4 mAb yield model development on humanised samples

The cross validation and test set validation for all developed models for the prediction of the mAb yields are presented in Figure C.5b in Appendix C. The developed models behaved similarly to the models for the prediction of the HIC retention times, where adequate performance in the cross validation was only achieved after variable selection had been performed. GA selection and rPLS achieved good performance for all descriptor sets while LASSO selection suffered due to collinearity between redundant and response-correlated descriptors explained in Section 2.9.3.

Unfortunately, no model performed well on the external test set. PLS-GA model developed using PSD3 had a high R^2 value of 0.69 but a Q^2 value of 0.35 in the test set thus indicating a high offset of the predictions compared to the measured values. The difference between R^2 and Q^2 is also greater than 0.3 thus failing the OECD criteria of $|R^2 - Q^2| < 0.3$ (Veerasamy et al., 2011). PLS-GA model developed using PSD4 had similar R^2 and Q^2 values of around 0.5 in the test set, but this is below the desired value of 0.6 according to the OECD guidelines. Predictions of PLS-GA model developed using PSD4 are illustrated in Figure 5.9a. It can be observed that all calibration samples fall directly on the parity line whereas the predictions of the test set samples have large differences between predicted and measured values as illustrated in Figure 5.9b. This is usually an indication of the model being overfitted where the model fits the random pattern in the noisy variables of the calibration data set (Lever et al., 2016). The model performance is summarised in Table 5.4.

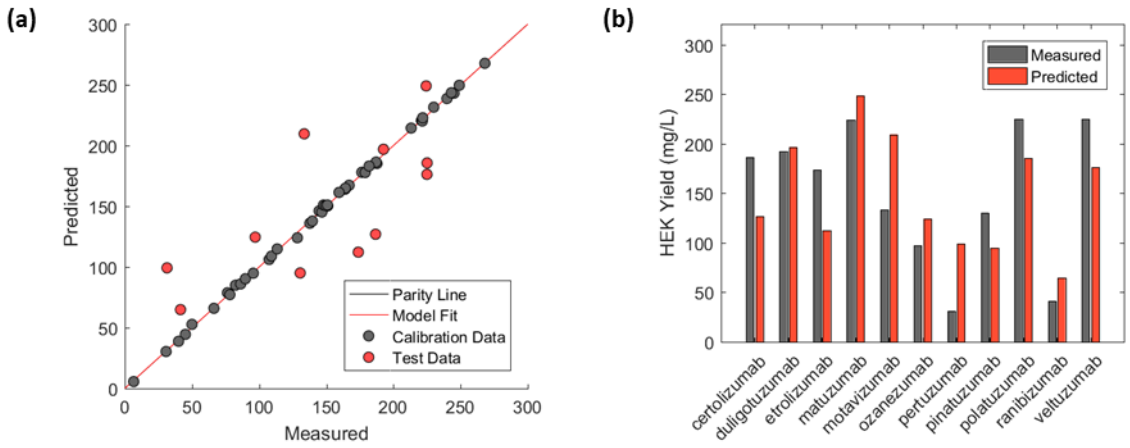

Figure 5.9. mAb yield predictions of 55 IgG1-kappa humanised and chimeric mAbs with PLS model (3 LVs) developed on the PSD4 descriptor set after reduction with V-WSP and selection with GA. **(a)** Measured versus predicted plot with calibration (grey) and test (red) samples. **(b)** Prediction and measured HIC retention times of test set samples.

Table 5.4. PLS-GA model summary developed for mAb yield prediction using the PSD4 descriptor set. Root Mean Square Error (RMSE), R^2, Q^2 and model bias are listed for Calibration, Cross validation and Test set.

	PLS			
	RMSE	**R^2**	**Q^2**	**Bias**
Calibration	1.51	1.00	1.00	0.00
Cross Validation	15.58	0.95	0.94	-0.68
Test	47.56	0.51	0.50	1.90

Several factors might impact the model development. All mAbs were expressed recombinantly using mammalian expression vectors where the heavy and light chain were expressed from individual cassettes (Jain et al, 2017). It has been shown that excess expression of the LC chain compared to the expression of the HC chain facilitates higher cell productivity and mAb yield (Bayat et al., 2018, Bhoskar et al., 2013). However, due to the unique structure of the variable domains in the mAbs, differences in folding efficiency in the endoplasmic reticulum might prevent an excess expression of the LC chain (Braakman and Bulleid, 2011). This is especially important in the model development which assumes that all measured yields had identical experimental setup which probably does not hold true as the HC:LC expression ratios will be different between mAbs. The HC:LC ratio might therefore be an important measurement needed for the improved model performance and can be used either as an extra input in the ***X*** block along with the structural descriptors or, used as an additional dependent variable along with the mAb yields.

Another potential cause for the poor performance in the test set might be the lack of necessary variation in the data. In the case of the ***X*** block, by using the primary sequence to generate structural descriptors, no information can be gained regarding higher order structural

information such as secondary or tertiary structure and potential intra-protein interactions. More samples might also be needed to better represent the range of ***Y*** responses, but also to introduce more structural variation in the ***X*** block. Noise and descriptor collinearity are also influencing factors in the model development where the descriptor selection methods can suffer and the wrong descriptors are thus selected (Fan and Lv, 2010).

5.3 Summary

The regulatory and quality assurance requirements for the process development of therapeutic mAbs are becoming more stringent to ensure high product specificity and clinical safety. This has in turn led to an increase in the number of experiments needed to characterise the design space of a process in order to investigate the impact of process parameters on the product quality. Today, platform approaches are becoming increasingly popular for process development of therapeutic mAbs which limits the number of operational units that needs to be characterised (Shukla et al., 2017). However, even with platform approaches the number of experiments needed for process characterisation is still cumbersome and costly. This is especially true in early process development where uncertainty is high with regards to the manufacturability of the mAb and where the effective processing routes might not be clear.

Over recent years, the QSAR framework for *in silico* model development has become increasingly popular for end point predictions of aggregation (Obrezanova et al., 2015) as well as downstream applications (Robinson et al., 2017, Woo et al., 2015a). This makes the QSAR framework a potentially valuable tool that can aid risk assessment in early process development to better direct experimental designs and thus reduce costs (Karlberg et al., 2018). The use of *in silico* approaches allows for more informed estimates of the potential behaviour of an mAb in different unit operations of the process. This becomes possible by efficiently making use of historic process data from previously established mAb manufacturing processes and therefore constructing an expert system.

In this Chapter the importance of exploring systematic variations as a source of noise in QSAR model development has been shown and should be considered as a critical step in the model development. A combination of PLS and statistical testing of the responses was performed to decrease the impact of systematic variation originating from the chain isotypes and species origin. This had a beneficial effect on the model performance in both the cross validation and external test set prediction after sample reduction with regards to the species origin. However, due to the alteration of the constant domains in the original mAb structures, no conclusive results could be drawn regarding the impact of systematic variation related to the heavy chain isotypes IgG2 and IgG4 and the light chain isotype lambda. The workflow presented in this

Chapter, however, provides a structured approach for selecting samples and reducing systematic variation that could negatively impact the model performance. In the work of Andersen and Bro (2010), the authors stated that removal of outliers is a vital step prior to variable selection due to the high sensitivity these methods have towards outliers. Thus, the removal of samples with systematic variation uncorrelated to the response greatly aids variable selection and reduces the risk of potential selection of uncorrelated variables.

Further, an efficient benchmarking scheme is presented here to validate several modelling methods, descriptor sets and incremental descriptor reduction and selection. A model was successfully developed for predicting HIC retention times and conformed to the model validation scheme presented in the OECD guidelines for cross-validation (R^2 and $Q^2 > 0.5$) and the test set (R^2 and $Q^2 > 0.5$). Though not all variation has been explained by the model, the presented workflow is intended as an early model development step to evaluate useful descriptors and factors affecting model performance. Additional descriptor generation and modification might therefore help in improving model accuracy further. Based on the defined confidence interval of 11.7 ± 0.6 from Jain et al (2017), sample predictions can easier be assessed as potentially problematic if the prediction falls above the lower confidence limit (11.1 minutes). This however does not indicate that they are certain to fail but that caution should be exercised and further studies are needed to characterise potential problems.

Unfortunately, no satisfactory model could be developed for the prediction of mAb yields as indicated by the signs of overfitting evidenced by the poor test set results. A potential cause could be the simplicity of the descriptor generation based on the primary sequence which does not take into account higher ordered structure and stability. This is investigated further in Chapter 7, where 3D structure descriptors will be evaluated in model development.

Chapter 6

3D Structure Descriptors

In this chapter descriptor generation with regards to the protein structure and dynamics is assessed as an alternative to the primary sequence descriptors generated in Chapter 3. An overview of protein structure model development is presented and key aspects such as the linkage of cysteines to form disulphide bridges and structure evaluation are assessed. The generated protein structures were used as inputs to molecular dynamics simulations in order to relax the protein structure as well as to capture conformational dynamics of the mAbs. The theory and implementation of molecular dynamics has been assessed in detail in order to create a wide knowledge base to produce more realistic simulations of the mAb structures that were used in this research but as well for future applications. In addition, strategies for modification of protein charges with regards to the pH as well as addition of co-solvents to the simulation system has been proposed.

The methodology for generating 3D structure descriptors follows the same approach as in Section 3.3 in order to generate descriptor set of different resolutions. Three resolutions were generated for the 3D structure descriptors based on the full chains, the individual domains and the substructures. ProtDCal was implemented to generate the 3D structure descriptors but were modified with the solvent accessible surface area of the superficial residues in order to represent the surface properties of the mAbs.

6.1 Structure Generation

In order to generate meaningful descriptors for model development, structures need to be available. Usually structure determination of proteins is performed by using either X-ray crystallography or Nuclear Magnetic Resonance (NMR) which both can give a very high atomistic resolution of the structure. Another method called Cryogenic-Electron Microscopy (Cryo-EM) has been making its impact within this area as well due to the many improvements

that has been made over the years to the method and the analytical software to refine the atomistic resolution (Carroni and Saibil, 2016, Merk et al., 2016). These methods are however very time consuming and expensive due to the specific requirements of the methods and are not always guaranteed to succeed (Krishnan and Rupp, 2012). Instead, the use of *in silico* methods provides an alternative to estimate the protein structure and has therefore become popular in structure determination.

6.1.1 Background on in silico methods

In silico structure prediction can roughly be divided into two schools:

1. *Ab initio* methods where the secondary and tertiary structure is predicted directly from the primary sequence
2. Comparative or homology modelling where templates of existing structures are used to predict the structure of proteins of interest.

Due to the high complexity in protein folding, pure *ab initio* methods do exist today but have low accuracy and are limited to smaller proteins (< 120 residues). Extremely high computational resources are also required in order to predict the protein folding with *ab initio* methods (Lee et al., 2017). More recently, a new method based on deep learning called AlphaFold has shown promising results and predicts likely distances between residues as well as potential angles between chemical bonds (Evans et al., 2018).

Instead, homology modelling has been shown to offer good prediction accuracy when protein templates exist and can be used. The high structural accuracy in homology modelling is based on the principle that high primary sequences similarity results in high tertiary structure similarity (Venclovas, 2011).

6.2 Homology Modelling

The approach for predicting structures in homology modelling can be broken down into five individual steps (Marti-Renom et al., 2000):

1. Identification of evolutionary related proteins to a target protein that can be used as templates (also known as homologs).
2. Alignment of the target protein sequence to the template.
3. Model building of target protein structure based on available structural information in the template.
4. Error estimation of target model structure.
5. Scoring of models for comparison

Step one and two can usually be done in parallel where many different techniques exist to find templates. Depending on the sequence identity that can be achieved between the target protein and template however, alternative approaches need to be considered. When the sequence identity is greater than 40% which is also known as the daylight zone (Rost, 1999), the search and selection of templates can be performed using pairwise sequence alignment tools such as Basic Local Alignment Search Tool (BLAST) (Johnson et al., 2008) or FASTA (Pearson, 1998) from the National Centre for Biotechnology Information (NCBI). At lower sequence identity (25-40%, also known as the twilight zone), methods such as position-specific iterated BLAST (PSI-BLAST) (Altschul et al., 1997) or Hidden Markov Models (HMMs) (Eddy, 1998) can be used instead for more sensitive searches to find homologs.

Different approaches exist to build the target model from the templates in step three. Commonly used approaches are modelling by assembly of rigid bodies (Sutcliffe et al., 1987), modelling by segment matching or coordinate reconstruction (Levitt, 1992) and modelling by satisfaction of spatial restraints (Sali, 1995).

An initial error estimation of the produced model can usually be carried out by inspecting the differences between the target protein sequence and that of the template. It is commonly known that when the similarities in the alignment between the template and the target protein decrease, the errors in the model will increase in turn. These errors originate from five sources (Fiser, 2010) related to:

1. Side-chain packing
2. Structural prediction of regions in the target protein that has shifted but otherwise correctly aligned with the template structure
3. Structural prediction of regions in the target protein that does not have an alignment
4. Structural prediction of regions in the target protein that are misaligned in the template structure
5. Structural prediction of target protein with wrong templates

As mentioned, the error is highly dependent on the sequence identity of the target protein and the template. If the sequence similarity is greater than 40%, approximately 75-90% of the predicted model structure will overlap, with an offset error of the peptide chain atoms of roughly 1 Å from their true positions. If sequence similarity goes lies in between 30-40%, the structure overlap decreases in turn and drops to 50-75% with an offset of 3 Å in the peptide chain atoms (Sanchez and Sali, 1998). This therefore shows the importance of appropriate selection of good templates to be used in homology modelling. It has also been shown that the model accuracy

increases by using multiple templates to estimate the target protein structure (Fernandez-Fuentes et al., 2007).

Table 6.1 lists some of the most commonly used software for model generation for mAbs. This list is by no means exhaustive of all the different web services and stand-alone software used for homology modelling.

Table 6.1. Commonly used homology modelling software for structure prediction of mAbs.

Software	Description	Reference
Web Antibody Modelling (WAM)	Canonical modelling of CDR loops L1-3 and H1-2 and template search for H3. CDRs are grafted onto template frameworks	(Whitelegg and Rees, 2000)
Prediction of ImmunoGlobulin Structure (PIGS)	Canonical modelling of all CDR loops and grafted onto template frameworks.	(Marcatili et al., 2014)
Rosetta Antibody	Grafts selected CDR templates onto template framework regions and energy optimises all residues in model. Further refinement of resulting model is performed using Monte Carlo minimisation.	(Sircar et al., 2009)
Molecular Operating Environment (MOE) Antibody Modeller	Grafts selected CDR templates onto framework templates. Energy minimisation with AMBER99 forcefields is performed to relax structure and resolve steric clashes in grafted regions.	(Almagro et al., 2011)
Modeller	One or more templates used to represent the full structure. Imposes conformational and sterically restraints in the target model according to the templates.	(Webb and Sali, 2014)

All software packages in Table 6.1, except Modeller, are specialised model generation for mAbs and perform a separate template search for the individual framework regions and CDRs. Both WAM and PIGS are very similar in execution when generating a target model as both methods use canonical structure prediction of the CDR loops. This means that the CDR loops can only assume a limited number of conformations based on the length of the loop and on the identity of specific residues at key positions (Chothia and Lesk, 1987). The PIGS web service is, however, more preferable as its reference database and canonical structure definitions are frequently updated (Marcatili et al., 2014). Compared to the canonical approaches, Rosetta Antibody focuses on resolving steric clashes in the target model that arises from the grafting of the CDR loops onto the framework regions as well as residue overlap caused by the use different templates (Sivasubramanian et al., 2009). The MOE Antibody Modeller is similar to that of Rosetta Antibody, but does not perform such an extensive refinement and focuses mostly on the regions where the CDRs were grafted onto the framework regions.

Research published in Almagro et al. (2011) benchmarked four antibody structure prediction tools where PIGS, Rosetta Antibody and MOE Antibody Modeller were included and tested on nine F_v antibody structures (V_H and V_L). The authors showed that accurate predictions could be generated for most of the structure except for the H3 loop, which was distinctly different compared to the experimental structures. It was also shown that Rosetta Antibody produced models with fewer steric clashes compared to PIGS and MOE Antibody Modeller.

In this research, Modeller (version 9.20) was selected to generate structures for the mAbs due to the in-house expertise available in the School of Natural and Environmental Sciences at Newcastle University. Modeller can also be locally installed and prediction of structures can be performed without connecting to the web server. This is usually desirable for Contract Manufacturing Organisations (CMOs) that deal with third party sequences and therefore face restrictions in the use of web services. Though the use of PIGS and Rosetta Antibody may have been preferred for better accuracy in the structures of the CDR loops, these methods were excluded due to being web services. However, further molecular dynamics simulations were performed of the generated structures to minimise the structure energy and resolved steric and conformational clashes (see Section 6.4).

6.2.1 Antibody Template Selection

To simplify the structure generation, it was decided to only model the Fab regions (V_H, C_H1, V_L and C_L domains) of the mAbs due to two reasons:

1. The mAb data sets used in this research were modified and expressed with selected allotypes (see Section 5.1.1). The heavy chain was expressed as IgG1 with allotype IGHG1*01 whereas in the light chain the allotypes IGKC*01 and IGLC2*01 were used, respectively, for kappa and lambda chains (Jain et al., 2017). Thus, except for the sequence variability originating from the C_L, the main source of variability originated from the variable domains V_H and V_L.
2. Structure preparation of full-length mAbs is much more complex due to consisting of four individual chains and two glycans attached in the Fc region. Information about the glycan profiles is also extremely limited.

The template search was performed using BLAST where homologs with high sequence identity and existing structures in the Protein Data Bank (PDB) (Berman et al., 2000) were identified. Individual searches of the heavy and light chain of the Fab fragments always yielded template candidates with more than 80% sequence identity. Based on this, it was decided to select a single template for each isotype permutation of the Fab fragments for simplicity and due to

further simulations to be performed. Quality assessment of the templates was based on their R-factor value which is a measurement of similarity between the crystal structure and experimental X-ray diffraction data. A value of zero indicates a perfect fit while a value of 0.6 or higher is obtained if a random structure is used. For larger proteins such as mAbs, values around 0.2 or below are a good indication of well-defined structures (International Union of Crystallography, 2017). The resulting templates are displayed in Table 6.2 where 2FGW and 7FAB were the only structures used in this research due to the mAbs being expressed as IgG1. The sequence identity listed as SeqID remained high with greater than 70% identity when aligned with the mAbs in the data sets. 5SX4 and 5DK3 are listed as potential candidates, respectively, for IgG2 and IgG4.

Table 6.2. List of templates PDB structures to be used as templates for different isotype permutations.

PDB	HC	LC	Resolution	R-factor	Modifications	SeqID
2FGW	IgG1	kappa	3 Å	0.176	Loop refinement (H3: 101-108)	>70%
7FAB	IgG1	lambda	2 Å	0.169	None	>70%
5SX4	IgG2	kappa	2.8 Å	0.223	Ligand and solutes removed	-
5DK3	IgG4	kappa	2.28	0.184	Solutes, Fc and one of Fab region removed	-

6.2.2 Pairwise Cysteine Distance Restraints

Five naturally occurring disulphide bonds will always be present in the Fab region of the mAb with two in the light chain, two in the heavy chain and one interchain bridge between the heavy and light chains. MODELLER by default will not restrain the distances between cysteines involved in disulphide bridges and can be observed in Figure 6.1a where distance between the sulphur atoms are more than 15 Å. By adding individual restraint for pairwise cysteines in the homology model the positions of the sulphur atoms can be adjusted to form the disulphide bonds as sown in Figure 6.1b. Figures were generated in UCSF Chimera (version 1.13) (Pettersen et al., 2004).

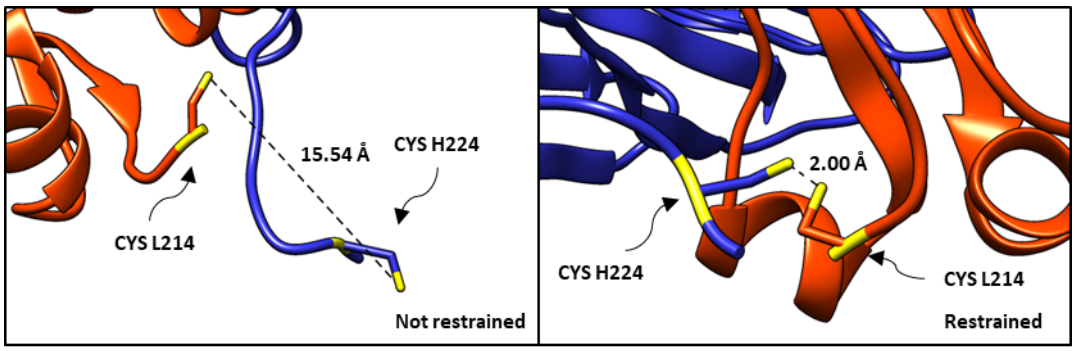

Figure 6.1. Distance restraint of cysteines in adalimumab generated. Structure coloured as orange depicts the light chain and structure coloured as blue depicts the heavy chain **(a)** Homology model without added distance restraints to the interchain cysteines. **(b)** Homology model with restraint between the interchain cysteines.

6.2.3 Model Assessment

Due to the difference in the amino acid composition and the length between the template and the mAb sequences used in this research, direct comparison with root mean square deviation (RMSD) of atom positions is not possible. Instead initial model assessment was performed with the inherent metric Discrete Optimised Protein Energy (DOPE) in Modeller (Shen and Sali, 2006) which is used to assess the energy of a structure or the residues in a structure. It is often used to select a model or structure from several predictions where a lower DOPE value relates to a more stable structure.

Figure 6.2 illustrates the normalised DOPE profiles for the template 2FGW (green line) and adalimumab (orange line) for the heavy and light chain. As can be observed, the DOPE profiles of the template and predicted structure overlap in most regions. The largest differences between the template and predicted model can be observed in the regions containing the CDR loops (H1, H2, H3 and L3) which have the highest deviation from template and thus are structurally different. This is, however, expected due to differing amino acid compositions in the CDR regions between adalimumab and the template. To date, accurate prediction of the CDR loops with homology modelling is still very difficult, especially in the case of the H3 loop which has the highest degree of varying amino acid composition and length when compared between mAbs (Almagro et al., 2011). In comparison, the structure of the constant domains C_L and C_H1 overlaps in Figure 6.2a and Figure 6.2b, respectively, due to a higher sequence identity between the template and protein target. The trends observed between the generated structure of adalimumab and the templates were also broadly observed in all generated mAb structures in this research.

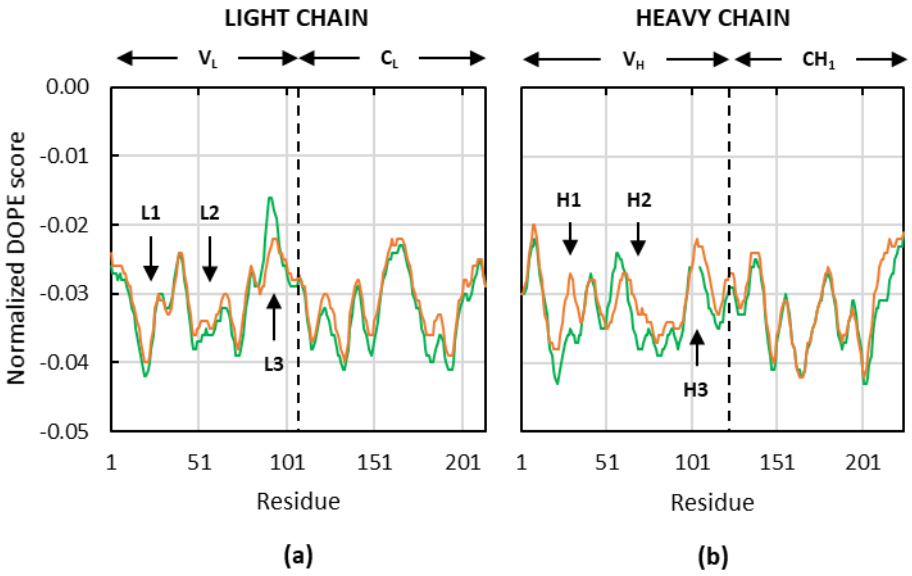

Figure 6.2. DOPE score for generated model (orange line) and template (green line) for the light chain **(a)** and heavy chain **(b)** for the aligned residues. Positions of CDR loops regions are marked by name and arrows in both the heavy and light chain.

6.2.4 Structure considerations

It is possible to use the generated homology structures of the mAbs to generate structural descriptors. However, four key considerations of the generated structured needed to be addressed before doing so:

1. Origin of the templates
2. The structure is biased towards the template
3. The structure is not completely relaxed
4. Residue states in the structure might not be accurately represented

The first point involves faults or assumptions that are present in the acquired experimental structures which might not necessarily represent reality. In the case of X-ray crystallography, the mAbs are never naturally packed in close proximity to each other in a physiological environment. The close proximity as a result of the crystallisation might introduce structural artefacts in the generated 3D structures and therefore may not be completely accurate. In the case of NMR, the structures are determined in a dynamic system where the proteins have less self-interaction. However, the acquired 3D structures will be heavily biased towards the environment in which the structure determination was performed e.g. pH, temperature, molality etc.

Point two and three originate from structure generation in Modeller which estimates the target protein structure based on the used template. Compared to specialised software, such as Rosetta Antibody and PIGS which use unique templates for individual framework regions and CDR

loops in the mAbs, Modeller was used to predict the mAb structure with a single template. This constrains the structure towards the used template and might not necessarily represent the true structure, especially of the CDR loops. It can also cause the structure to not be in a non-relaxed state, especially in regions where a difference in length exists between the target protein and template. Caution thus needs to be exercised as these differences might have an impact on the generated descriptors if the homology model if used directly for descriptor generation.

The fourth point relates to the impact of the environmental factors that can change structural conformation and dynamics of the mAbs. In mAb manufacturing, drastic changes in the environment are common in many operational units in the downstream process. The pH and molality are common process factors that are changed to enhance binding and elution of mAbs in different chromatographic columns that can drastically impact the conformation of the protein structure.

6.3 Protein dynamics

Proteins have since long ago been described as being static structures with a specific function. The reality however is that proteins are dynamic in nature with small structural fluctuations over time. This is highly related to the folding energy landscape of a protein, where at a stable conformation, many structurally similar states exist separated by small thermodynamic free energy barriers (Bryngelson et al., 1995). Figure 6.3a illustrates a simplified example of the energy landscape of a protein. As can be observed, fluctuations between the different states depends heavily on the magnitude of the free energy barrier where transitions to similar state are more frequent due to a smaller energy barrier (ΔG_{Local}) whereas larger conformational changes require more energy (ΔG_{Global}). The magnitude of time is also an important factor that needs to be considered where transition between larger conformational states takes longer due to the cumulative kinetic energy required to overcome the large energy barriers. Figure 6.3b illustrates changes in structural states related to the different timescale and was adapted from the work of Henzler-Wildman and Kern (2007) as well as the work of Adcock and McCammon (2006). It can be observed that smaller changes, such as bond vibrations and methyl rotations, occurs at shorter timescales whereas rotation of larger solvent accessible side-chains and loop motions lies on a timescale of nanoseconds due to larger energy differences in the barriers. Changes in environmental factors, such as temperature, pH and molality to name a few, are also important to consider, as they will inevitably result in a change of the energy landscape of the protein which is illustrated as a shift from its original conformation (green line) to that new conformation (orange line) in Figure 6.3a**.** This can also have an effect on the protein function

that is active in the original environment and inactive in the changed environment due to conformational change.

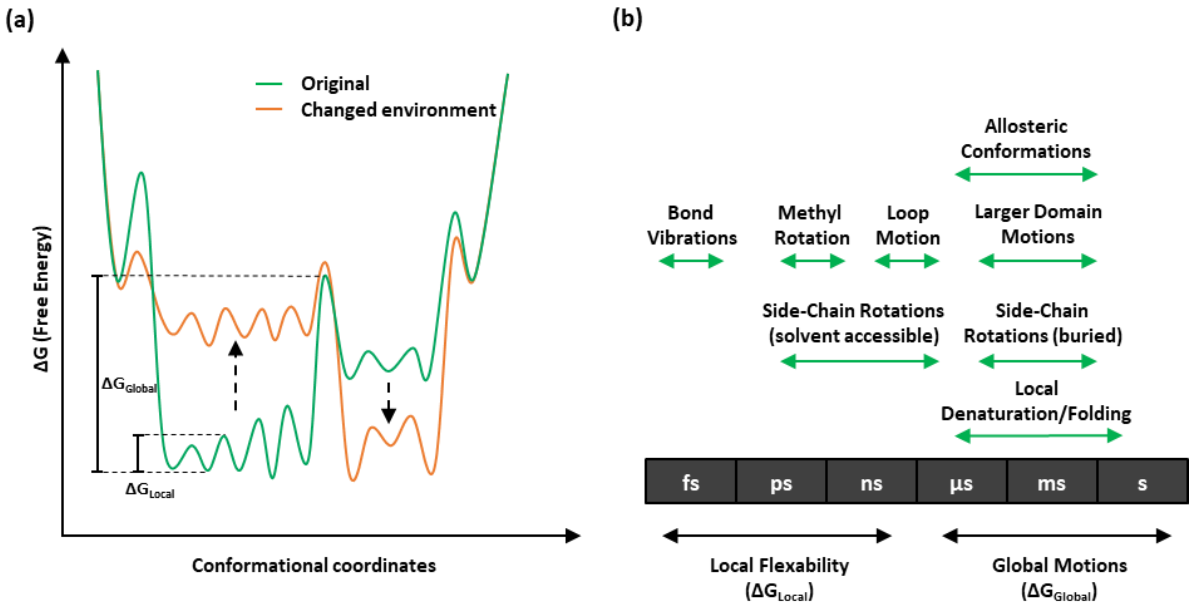

Figure 6.3. Potential dynamics of a protein. **(a)** A simplified energy landscape for an arbitrary protein. Environmental changes can drastically change the landscape as shown in the shift from the green line to the orange line with a different conformation occupying the energy minima. **(b)** The time scale needed to observe local as well as global conformational changes in a protein (adapted from Henzler-Wildman and Kern (2007) and Adcock and McCammon (2006)).

6.3.1 Describing the system dynamics

Accurate insight into the protein dynamics can today be gained through the use of computational simulations. The complexity of the simulations can usually be divided into four levels of resolutions to observe a system where a short description on each has been given below.

Quantum mechanics

The atom nuclei and electrons of a system can be described by solving the time-dependent Schrödinger equation (TDSE) for a single particle.

$$\hat{\mathrm{H}}\psi(\boldsymbol{r},t) = \left\{-\frac{\hbar^2}{2m}\nabla^2 + V\right\}\psi(\boldsymbol{r},t) = i\hbar\frac{\partial\psi(\boldsymbol{r},t)}{dt} \qquad (6.1)$$

$$where\ \nabla^2 = \left(\frac{\partial^2}{\partial x^2} + \frac{\partial^2}{\partial y^2} + \frac{\partial^2}{\partial z^2}\right)$$

where Ĥ is the Hamiltonian operator which corresponds to the total energy of the system, ψ the wave function, $\boldsymbol{r}$ the position vector of the particle ($\boldsymbol{r} = x\boldsymbol{i} + y\boldsymbol{j} + z\boldsymbol{k}$), t the time, ħ the reduced Planck constant, m the mass of the particle, V the potential energy and i the imaginary number. However, the TDSE is not practical for describing structure dynamics due to being computationally intensive and it is more commonly applied for studies of faster phenomena such a light emission absorption and emission. Instead, the time-independent form is more commonly used to describe structure dynamics according to:

$$\left\{-\frac{\hbar^2}{2m}\nabla^2 + V\right\}\psi(\boldsymbol{r}) = E\psi(\boldsymbol{r}) \tag{6.2}$$

The quantum mechanics (QM) simulations provide highly detailed information about the dynamics of the system but are also able to incorporate chemical reactions due to the approximations of the electron orbitals. However, only smaller systems with a few atoms can be simulated with QM due to the high complexity and computationally cumbersome calculations (Leach, 2001d).

Classical/Molecular mechanics

Simulate the atomistic positions and movement in space by solving Newtons equations of motion for individual particles in the system:

$$\boldsymbol{F}_i = m_i\boldsymbol{a}_i = m_i\frac{d^2\boldsymbol{r}_i}{dt^2} \tag{6.3}$$

where $\boldsymbol{F}$ is the force, m the mass of the atom, and $\boldsymbol{a}$ the acceleration of the particle. The atomistic interactions are approximated by using empirical force fields that describe the potential energies of the system (see Section 6.4.1). This allows for longer simulation times up to the scale of microseconds and even milliseconds when coarse-grained force fields are used. A drawback with molecular mechanics (MM) is its inability to break or create covalent bonds (Adcock and McCammon, 2006). Molecular mechanics simulations are also referred to as Molecular Dynamics (MD).

Hybrid QM/MM

Can be used to simulate systems that are too computational expensive for standard QM but where chemical reactions are important such as enzymatic reactions. The protein structure or system is divided into two parts where a smaller part is simulated with QM which encloses the

structure responsible for the chemical reaction whereas the larger part is simulated with MM (Liu et al., 2001).

Monte Carlo

Instead of using a deterministic system such as MD which is reliant on a time component, Markov Chain Monte Carlo (MCMC) is a statistical approach that samples the conformation space by randomly moving the system atoms. This means that the atom movement in a MCMC simulation is only dependent on its immediate predecessor and therefore no temporal relationship exists between the trials (Leach, 2001e). A drawback with MCMC is that the simulation can become computationally expensive with increased number of atoms in the systems due to the exponential increase in degrees of freedoms in the system if not properly restrained.

Selection of simulation resolution

Information gained through computational molecular simulations can answer many questions regarding the protein dynamics due to the high level of detail captured. Most commonly used are the MD simulations which allows for longer simulation times and the ability to follow conformational events due to being deterministic. In this research, the focus has been placed on MD simulations due to being faster and that chemical reactions are not required for the descriptor generation.

6.4 Molecular Dynamics

Many advancements have been made over the years to MD simulations such as theoretical improvements with new empirical force fields as well as practical improvements of simulation speed and increase the system size (Rauscher et al., 2015). One such advancement is the incorporation of Graphical Processing Units (GPUs). State-of-the art graphics cards contains thousands of cores which can be used to divide the molecular system into smaller parts which can be run in parallel. This shifts the workload from the Central Processing Unit (CPU) to the GPU which calculates the forces on the atoms whereas the CPU is free to allocate data and combine the results of the smaller parts (Loukatou et al., 2014).

Improvements in simulation time can also be gained through simplification of the system with a so-called coarse-grained approach. Instead of representing all atoms in the system (referred to as all-atom or atomistic), a coarse-grained simulation may represent each amino acid side-chain as a single cluster with their corresponding force fields. This drastically reduces the degrees of freedom in the system (see Section 7.2.2.1) which in turn decreases the necessary

number of calculations that needs to be performed (Kmiecik et al., 2016). One of the most commonly used coarse-grained force fields is MARTINI which has been shown to achieve simulation results close to that of atomistic simulations (May et al., 2013). Figure 6.4 illustrates the applicability domains of atomistic and coarse-grained models with regards to the system size and simulation time (adapted from Kmiecik et al (2016)).

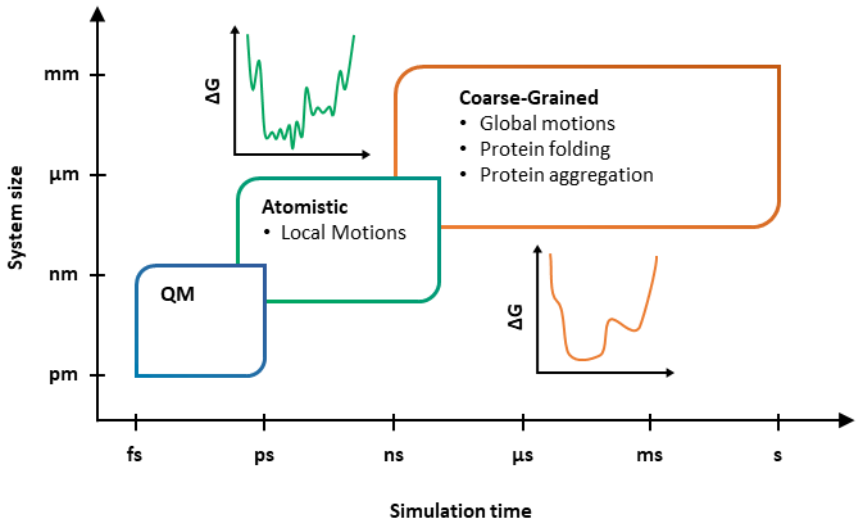

Figure 6.4. The relationship between the system size and possible simulation times for QM, atomistic and coarse-grained simulations. Loss of information is inevitable when moving to simplified estimation of the system such as atomistic and coarse-grained representation which are illustrated by the green and orange graphs, respectively (adapted from Kmiecik et al. (2016)).

As shown, larger systems and longer simulation times become possible when moving from more computationally intensive QM calculations towards system approximations with MM calculations. With further decrease in degree of freedoms in a system resulting from the move from an atomistic to a coarse-grained setup, the system size and simulation times can be increased even further. However, caution needs to be exercised as a system simplification step inevitably leads to a loss of information of protein dynamics which will no longer be captured in the simulations. This can easily be visualised when comparing the energy landscapes of an atomistic model to those of a coarse-grained model represented as the green and orange energy graphs in Figure 6.4, respectively. In the atomistic model, the rotations of the side chains and bond vibrations will more or less be intact resulting in many local conformational minima in the energy landscape. In a coarse-grained model however, side-chains are treated as a single cluster and therefore lack many of the local motions. The energy landscape of a coarse-grained will therefore be smoother but will follow the general trend of an atomistic model. Therefore, it is advised to choose the simulation resolution based on the area of investigation where an atomistic model is recommended to capture local motions and a coarse-grained model recommended to capture global motions.

A popular approach to increase the resolution is to use multiscale modelling where major events are first captured with a coarse-grained model. Events of interest can be further modelled by reconstructing the coarse-grained model to atomistic resolution at specified time points (Heath et al., 2007). This allows for more detailed information about the system to be captured and avoids the need of performing longer atomistic simulations in the beginning.

A list of commonly used MD software packages is presented in Table 6.3. For the purpose of this research, GROMACS (version 5.1.4) was selected due to the in-house expertise available at Newcastle University. In addition, GROMACS is able to incorporate the MARTINI force field used for coarse-grained modelling. This is of added benefit due to the increasing popularity of MARTINI and the many advancements made to the force field which have increased the model accuracy to almost rival that of atomistic (Marrink and Tieleman, 2013).

Table 6.3. Non-exhaustive list of popular MD simulation software.

Software	Atomistic	Coarse-Grained	GPU support	OS	Availability	Reference
AMBER	YES	NO	YES	Window, Linux	Commercial	(Salomon-Ferrer et al., 2013)
CHARMM	YES	NO	YES	Linux	Commercial (1)	(Brooks et al., 2009)
GROMACS	YES	YES (2)	YES	Linux	Free	(Van Der Spoel et al., 2005)
MOE	YES	NO	YES	Windows, Linux	Commercial	(MOE, 2018)
NAMD	YES	YES (2)	YES	Windows, Linux	Free	(Phillips et al., 2005)

(1) A reduced version of CHARMM can be acquired for free.

(2) Uses the MARTINI force fields

6.4.1 Force Fields

In order to calculate the forces acting in a system, the potential energy, $U(\boldsymbol{r}^N)$, for each atom needs to be defined where $\boldsymbol{r}^N = (\boldsymbol{r}_1, \boldsymbol{r}_2, \dots, \boldsymbol{r}_N)$ are the Cartesian coordinates for the N atoms in the system. The molecular interactions can be approximated with mathematical expressions to represent different interactions of the system. An equation for approximation of the total potential energy in a system can be written as (Leach, 2001b):

$$U(\boldsymbol{r}^N) = U_{bonds} + U_{angles} + U_{torsions} + U_{columb} + U_{vdw} \qquad (6.4)$$

As shown, the interactions can be divided into two categories of bonded (green solid lines) and non-bonded (red and black dashed lines) interactions shown in Figure 6.5a and Figure 6.5b, respectively.

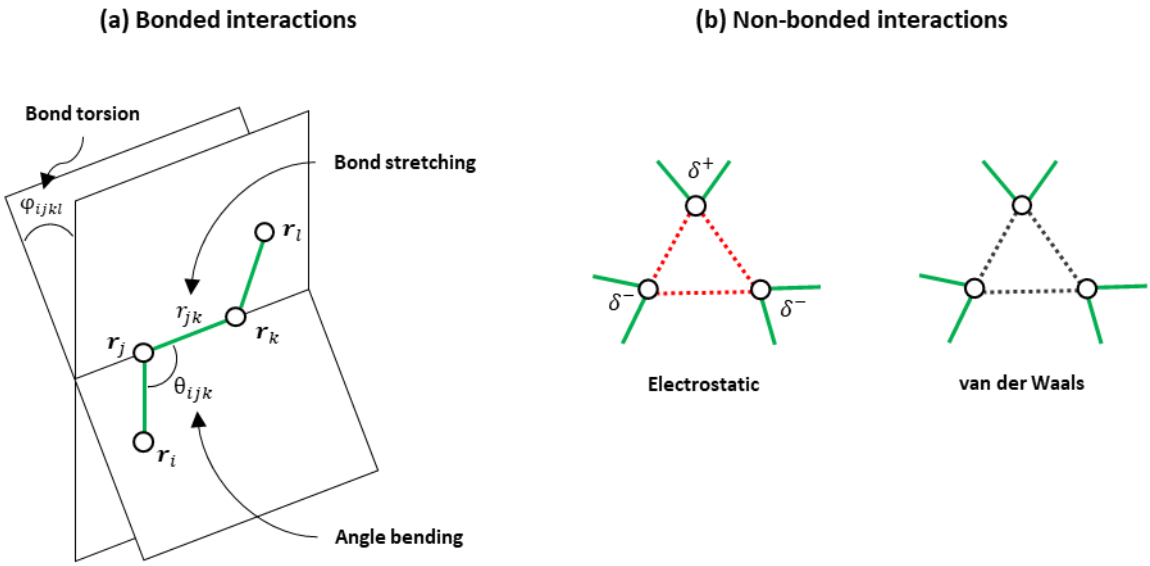

Figure 6.5. **(a)** The bonded interactions originating from bond stretching, angle bending and bond torsion (rotation). **(b)** The non-bonded interactions originating from electrostatic and van der Waals potentials (adapted from Allen (2004) and Leach (2001b)).

The bonded interactions represent the potential energies originating from the covalent bonds and steric conformation of the structure in the form of bond stretching, angle bending and torsion from bond rotations. Resulting potential energies from the bonded interactions are shown in Figure 6.6 and were adapted from the GROMACS manual 5.1.4 (Abraham et al., 2016).

The potential from the bond stretching between two atoms is approximated using Hooke's law for harmonic potentials (see Figure 6.6a) to define the potential well:

$$U_{bonds}(r_{ij}) = \frac{1}{2} k_{ij}^{b} (r_{ij} - r_{eq})^2 \tag{6.5}$$

where $r_{ij} = |\boldsymbol{r}_{ij}|$ and $\boldsymbol{r}_{ij} = \boldsymbol{r}_i - \boldsymbol{r}_j$

which in turn takes on the following expression for the force:

$$\boldsymbol{F}_{bonds}^{i}(\boldsymbol{r}_{ij}) = -k_{ij}^{b}(r_{ij} - r_{eq})\frac{\boldsymbol{r}_{ij}}{r_{ij}} \tag{6.6}$$

The constant k_{ij}^{b} is the spring constant where a higher value prevents greater bond stretching. The variable $\boldsymbol{r}_{ij}$ is the bond vector between two atom positions with the magnitude or bond length r_{ij}. The constant r_{eq} is usually referred to the natural bond length where the potential energy is at its lowest.

The potential energy from angle bending (see Figure 6.6b) is also frequently described using Hooke's law but uses the angle between two bonds instead of the bond length:

$$U_{angles}(\theta_{ijk}) = \frac{1}{2} k_{ijk}^{\theta}(\theta_{ijk} - \theta_{eq})^2 \tag{6.7}$$

The potential energy of the angle bending takes on the following expression for the force:

$$\begin{aligned} \boldsymbol{F}_{angles}^{i}(\theta_{ijk}) &= -\frac{dU_{angles}(\theta_{ijk})}{d\boldsymbol{r}_i} \\ \boldsymbol{F}_{angles}^{k}(\theta_{ijk}) &= -\frac{dU_{angles}(\theta_{ijk})}{d\boldsymbol{r}_k} \\ \boldsymbol{F}_{angles}^{j}(\theta_{ijk}) &= -\boldsymbol{F}_{angle}^{i} - \boldsymbol{F}_{angle}^{k} \end{aligned} \tag{6.8}$$

$$\text{where} \quad \theta_{ijk} = \arccos\left(\frac{\boldsymbol{r}_{ij} \cdot \boldsymbol{r}_{kj}}{r_{ij} r_{kj}}\right)$$

The constant k_{ijk}^{θ} is the spring constant where higher values prevent bending making the structure more rigid. The variable θ_{ijk} is the angle between two connecting bonds from three atomic positions. The constant θ_{eq} represents the natural angle based on the atom types of the three atoms.

The torsion potential is almost always expressed as a cosine Fourier series expansion with $\mathrm{m} = 1,2,\ldots,\mathrm{M}$ (Leach, 2001b). The torsion is defined by three connecting bonds and therefore involves four atomic coordinates (see Figure 6.5a) according to:

$$U_{torsions}(\varphi_{ijkl}) = \frac{1}{2} \sum_{m} k_{ijkl}^{\varphi,m}(1 - \cos(m\varphi_{ijkl} - \gamma_m)) \tag{6.9}$$

The expression for the resulting torsion force is not shown due to being much more extensive than previous forces. The constant $k_{ijkl}^{\Phi,m}$ is the magnitude of the torsion potential, m represents

the which series in the series expansion, the variable φ_{ijkl} is the torsion angle and γ_m is the phase factor which describes at which angle the potential energy is at its lowest. Figure 6.6c shows the potential energy from the torsion of an arbitrary molecule bond where the energy is at its lowest when with less steric clashes occurs (staggered conformation) and at its highest when more steric clashes occurs (eclipsed conformation).

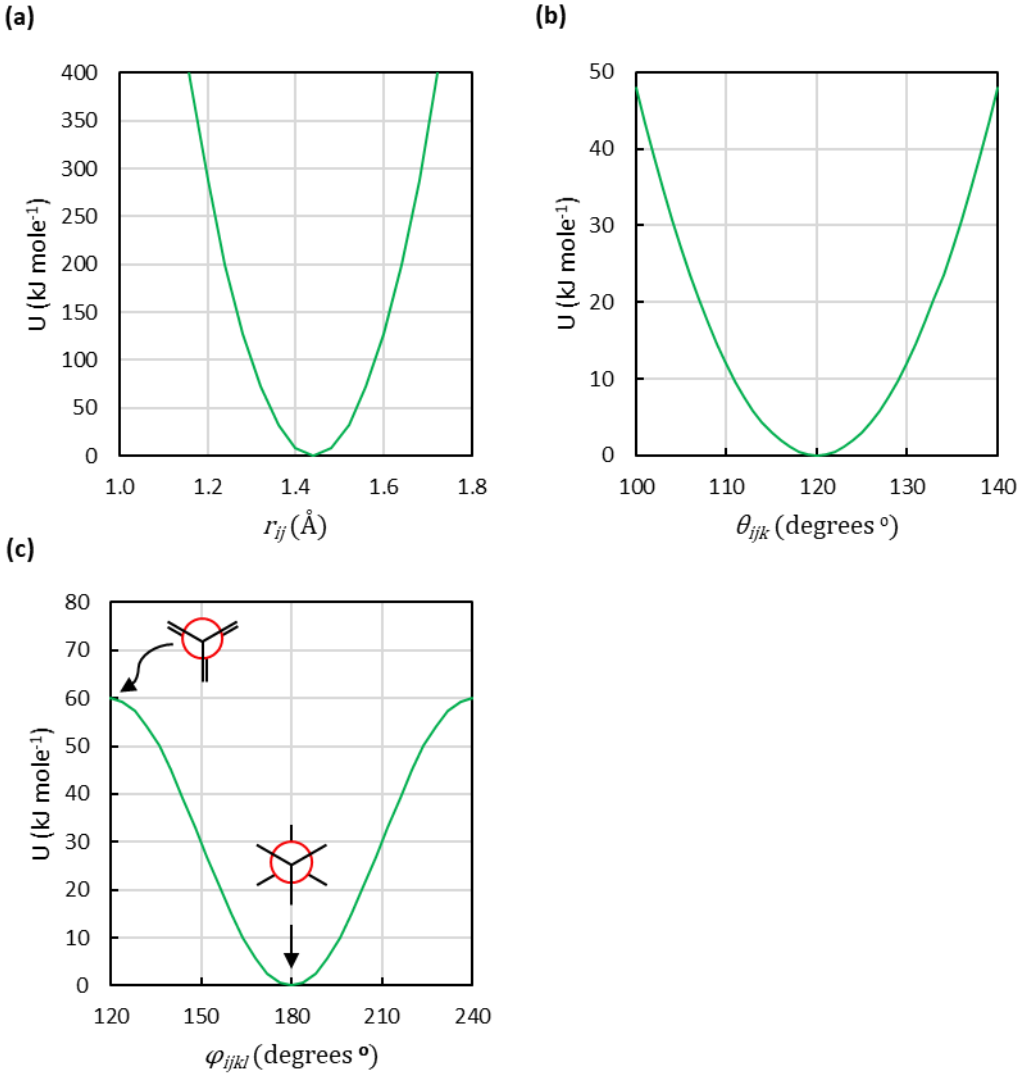

Figure 6.6. Potential energy of bonded interactions. **(a)** An approximation of the potential energy in the bond stretching using Hooke's law as a function of the distance between two bonded atoms. **(b)** The potential energy from angle bending as a function of the angle between two connecting bonds and approximated with Hooke's law. **(c)** Approximation of the potential energy from bond torsion as a function of the bond angle. Highest potential is observed in eclipsed conformation and lowest in staggered conformation (adapted from the GROMACS manual 5.1.4).

The non-bonded interactions represent the potential energies originating from electrostatic and van der Waals interactions. These include both internal interactions in the protein as well as external interactions from the solvate. Resulting potential energies from the non-bonded

interactions are shown in Figure 6.7 and were adapted from the GROMACS manual (Abraham et al., 2016).

Potential energies originating from van der Waals interactions are commonly described by using the Lennard-Jones (Jones, 1924) equation:

$$U_{vdw}(r_{ij}) = 4\varepsilon\left[\left(\frac{\sigma}{r_{ij}}\right)^{12} - \left(\frac{\sigma}{r_{ij}}\right)^{6}\right] \tag{6.10}$$

The potential energy takes on the following form for the resulting force:

$$\boldsymbol{F}^{i}_{vdw}(r_{ij}) = 4\varepsilon\left[12\frac{\sigma^{12}}{r_{ij}^{13}} - 6\frac{\sigma^{6}}{r_{ij}^{7}}\right]\frac{\boldsymbol{r}_{ij}}{r_{ij}} \tag{6.11}$$

The constant ε defines the depth of the potential well whereas the constant σ defines the distance between two atoms when the potential is at a minimum. It can be observed in Figure 6.7b that an arbitrary attraction occurs when the distance is 3 Å between two atoms, this is similar to that of the Morse potential seen in Figure 6.6a but lacks a physical bond. The magnitude of the Lennard-Jones potential is also much lower compared to that of the Morse potential.

The electrostatic potential energy between two charged atoms in the system can be described by using the following expression:

$$U_{columb}(r_{ij}) = \frac{1}{4\pi\varepsilon_0}\frac{q_i q_j}{r_{ij}} \tag{6.12}$$

The electrical potential takes on the familiar expression of coulombs law when converted into the resulting force:

$$\boldsymbol{F}^{i}_{columb}(\boldsymbol{r}_{ij}) = \frac{1}{4\pi\varepsilon_0}\frac{q_i q_j}{r_{ij}^{2}}\frac{\boldsymbol{r}_{ij}}{r_{ij}} \tag{6.13}$$

The variable q is the charge of the atom and ε_0 is known as the permittivity constant. It can be observed through Figure 6.7b that the potential energy increases with shorter distance between charges. When of same charge the atoms will repel each other while different charges will attract each other.

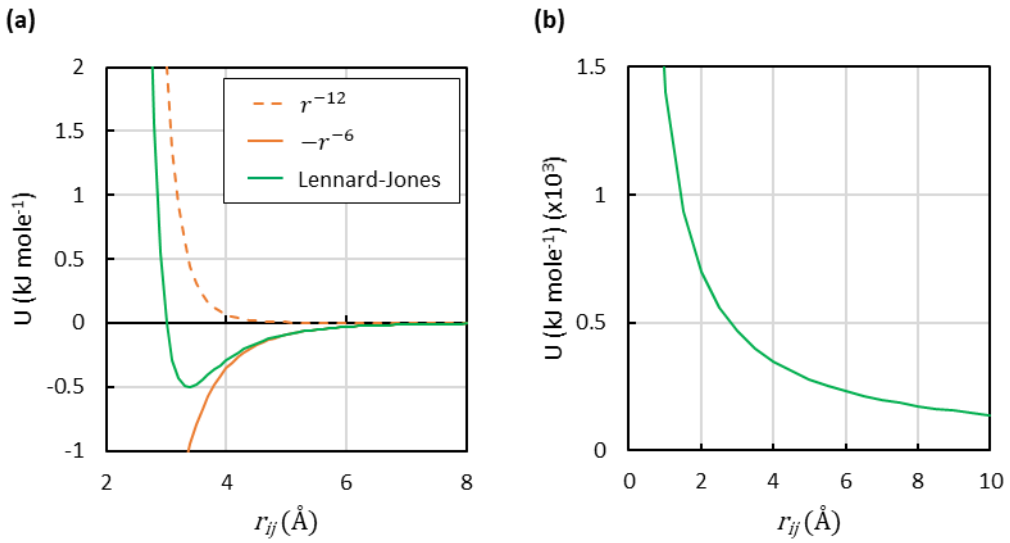

Figure 6.7. Potential energy of non-bonded interactions. **(a)** The electric potential as a function of distance between two charged points. **(b)** The van der Waals potential approximated with Lennard-Jones potential (green line) as a function of the distance between two non-bonded atoms. Consists of one repulsion (orange dashed line) and one attraction (orange full line) component (adapted from the GROMACS manual 5.1.4).

It should be mentioned that the hydrogen bond, which is a common non-bonded interaction in proteins, is not treated as a separate bond type in the force fields but rather as a combination of Lennard-Jones and electrostatic potential instead.

In comparison to the bonded interactions, the number of non-bonded interactions that needs to be evaluated in a system increases with the order of N^2 due to the fact, that any pair of atoms in the system can interact. To avoid time-consuming simulations or, in worst cases, system crashes, cut-off schemes are used to reduce the number of potential long-range calculations that needs to be performed. Commonly applied is Particle Mesh Ewald (PME) summations which consists of short-range contributions and long-range contributions. Short-range interactions are determined by a predefined cut-off radius (commonly 1 nm) to identify neighbouring atoms to the atom of interest. If the distance is less than the defined cut-off radius, the atom is included in the force calculation and a so-called neighbours list is created that specifies the neighbouring atoms to the atom of interest which was first proposed by Verlet (1968). Long-range interactions are atoms with distances exceeding the defined cut-off radius from the atom of interest and are instead calculated with Fourier transform from the real space to the reciprocal space which allows for faster computation.

As can be observed, equations (7.5), (7.7), (7.9), (7.10) and (7.12) contain parameters for optimal bond lengths, angles, potential wells, force constants etc that needs to be specified. Put in simple terms, a force field is a list of parameter values for different atom types with corresponding equations that are used to calculate the potential energy of the system (Allen,

2004). Ii is important to note that an atom type should not be confused with an element from the periodic table. The definition of an atom type here involves the hybridisation state and/or the charge of the atom as well as the type of connected atoms. For example, carbon will have several atom types which describe different hybridisation states and surroundings. This in turn means that they will behave slightly different from each other and therefore need to be described with a unique set of parameters for each atom type. This also makes the number of atom types listed in the force fields much more numerous than the number of elements in the periodic system.

Table 6.4 gives a non-exhaustive list of popular force fields that are used in MD simulations currently where several different versions of the AMBER, CHARMM and GROMOS force fields exists. Only slight variations exist between the different force fields which include differences in parameter values or slight differences in the potential energy equations, usually in the non-bonded interactions (Allen, 2004). The estimation of the parameters for different atom types are almost always carried out with QM calculations or taken from experimental measurements (Kmiecik et al., 2016).

Table 6.4. Non-exhaustive list of popular force fields.

Force Field	Parameter determination	Reference
AMBER	Multi-purpose force field widely used for proteins and DNA simulations	(Cornell et al., 1995)
CHARMM	Multi-purpose force field widely used for both small and macromolecule simulations	(Brooks et al., 1983)
GROMOS	First developed for simulations of protein or DNA in hydrophobic solvent. Now the force field is multi-purpose.	(Oostenbrink et al., 2004)
OPLS-AA	Multi-purpose force field	(Jorgensen et al., 1996)

In this research, the atomistic amber99sb-ILDN force field was used to simulate the dynamics of the antibody Fab fragments. The authors Lindorff-Larsen et al. (2010) modified the original amber99sb force field to more accurately describe side chain torsions in a protein.

6.4.2 The MD Algorithm and Time Integration

The global MD algorithm is shown in Figure 6.8 and consists of four steps (adapted from the GROMACS User Manual 5.1.4 (Abraham et al., 2016)).

In the initial step of any MD simulation, the positions and velocities for each atom in the system need to be specified. Atom positions can be acquired through PDB files from either experimental data or a predicted structure (see Section 6.2). Usually no velocities are available when starting a new simulation project unless it is a continuation of a previous simulation. In

these cases, the Maxwell-Boltzmann distribution can be used to randomly assign initial velocities to all atoms in the system at a given temperature T.

$$p(v_i) = \sqrt{\frac{m_i}{2\pi kT}} \exp\left(-\frac{m_i v_i^2}{2kT}\right) \tag{6.14}$$

Lastly, a force field needs to be selected to describe the potential energy function and interactions in the system and will not be changed throughout the simulation.

The forces in the system are then calculated from the potential energy of the system in step two. The resulting force on each atom is calculated as a vector sum based on all interactions from surrounding atoms (see Section 6.4.1). This step also involves all corrections applied to the system in order to maintain or change the thermodynamic macrostate by controlling the system volume, temperature and pressure. This is further explained in Section 6.4.4.

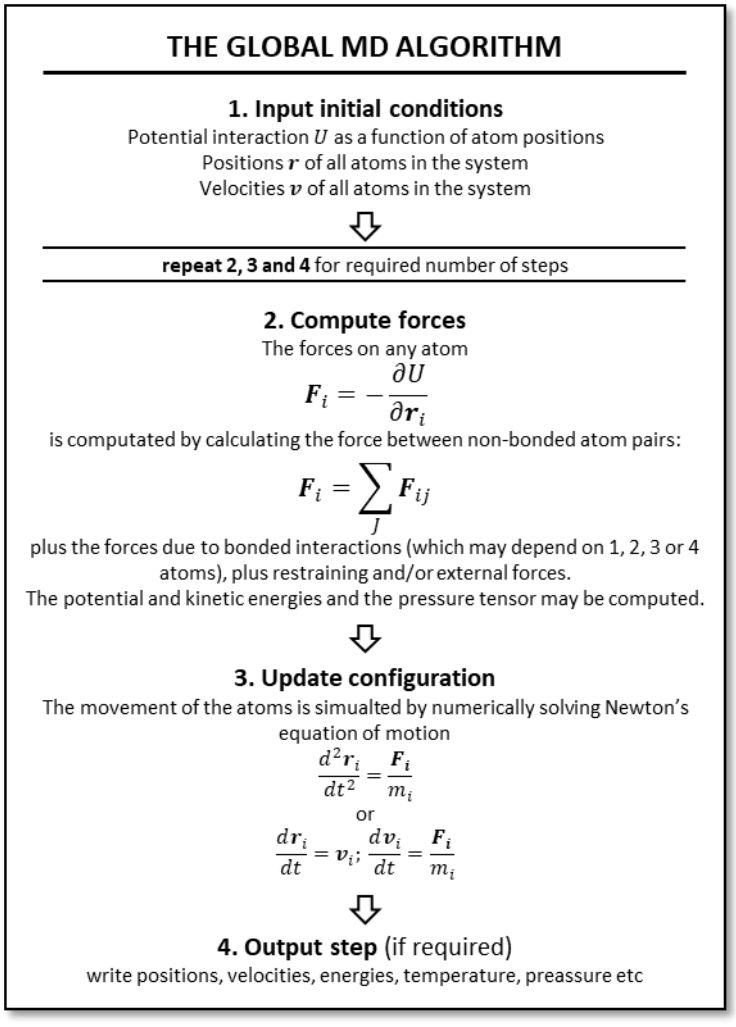

Figure 6.8. Four steps of the global MD algorithm. **Step 1)** Positions and initial velocities are assigned and a force field chosen. **Step 2)** Calculation of resulting forces on all atoms in the system. **Step 3)** Updates the positions and

velocities of all atoms in the system. **Step 4)** Saves specified information to a log file (adapted from the GROMACS User Manual 5.1.4).

The third step in the MD algorithm updates the positions of all atoms in the system based on the calculated forces in step two. This is done by numerical integration in order to approximate the resulting velocities and positions of the atoms in the system. Two popular approaches that commonly used to perform the integration are the Verlet velocity algorithm (Swope et al., 1982) and the Verlet leapfrog algorithm (Hockney and Eastwood, 1988) where the later will be investigated more thoroughly. The leapfrog algorithm updates the atom position and velocity according to:

$$\boldsymbol{v}_i\left(t+\frac{1}{2}\Delta t\right)=\boldsymbol{v}_i\left(t-\frac{1}{2}\Delta t\right)+\frac{\boldsymbol{F}_i(t)}{m_i}\Delta t \tag{6.15}$$

$$\boldsymbol{r}_i(t+\Delta t)=\boldsymbol{r}_i(t)+\ \boldsymbol{v}_i\left(t+\frac{1}{2}\Delta t\right)\Delta t \tag{6.16}$$

where $\boldsymbol{v}_i$ and $\boldsymbol{r}_i$ are the velocity and the position of atom i and Δt is the timestep used in the numerical integration. In the leapfrog algorithm, positions are updated at each full time-step $(t+\Delta t)$ (6.15) while the velocities are updated at each half time-step $(t+\Delta t/2)$ (6.16) thus making the atomic position and velocity jumping over each other like two leaping frogs. This allows for more accurate calculations of the velocities as compared to if the positions and velocities would have been synchronised.

In MD simulations, the time step Δt needs to be sufficiently large in order to efficiently simulate the protein dynamics without unnecessary resampling of the conformational space. However, if a too big a time step is selected it can cause instability and inaccuracies when the subsequent atom positions are calculated resulting in unfavourable conformations and high potential energies. A rule of thumb is to adapt the time step to the smallest local motion in the system in order to avoid this problem. Usually, a default time step of 2 fs is used in MD simulations today. It is important to note that the vibration period of the hydrogen bonds is shorter than the timestep of 2 fs and therefore cannot be accurately sampled. In order to avoid instability, the hydrogen bonds are constrained with the LINCS algorithm which keeps the length of the hydrogen bond constant throughout the simulation.

6.4.3 Periodic Boundary Conditions

Even with advancement of computational power the actual size of the system to be simulated is extremely small compared to a real-world setting. This also means that the surface to volume

ratio in the simulation is much higher compared to a real experimental setup which can introduce artefact caused by surface effects. Unless this is the aim with the simulation, a way to avoid this problem is to use so called Periodic Boundary Conditions (PBCs). In the event where a molecule exits the simulation box it will automatically re-enter the system on the opposite side with its trajectory preserved as can be seen in Figure 6.9a. This effectively means that the system has been enlarged by infinity. Caution needs to be exercised in order to avoid self-interaction of example a protein. This is commonly avoided by making sure that the distance between the protein to the edge of the simulation box is at least three solvation layers wide which roughly translates to 0.9 – 1.0 nm (González, 2011). This concept is shown in Figure 6.9b where the cut-off radius is illustrated as the dashed red circles surrounding a particle of interest. The system size is adequately chosen in this case where the particle of interest will not self-interact as well as overlap between the circles have been avoided thus making sure that potential water molecules in the systems are not affected by the particle from adjacent boundary cells (adapted from (González, 2011)).

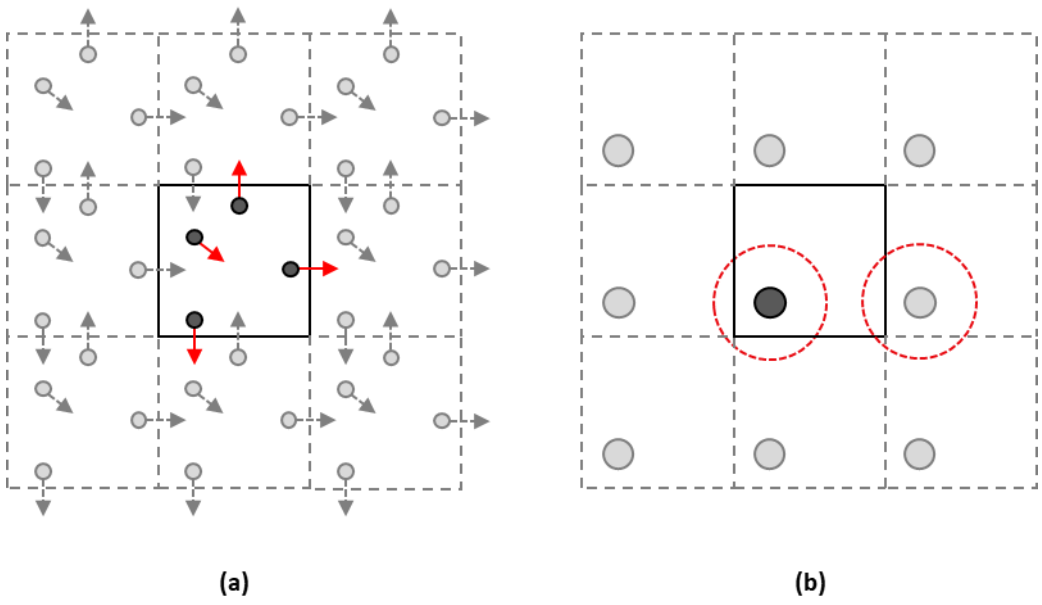

Figure 6.9. The application of the periodic boundary condition in a simulation. **(a)** Movement of particles out of the simulation box will enter the opposite. **(b)** Depicts the cut-off radius for long-range interactions as the dashed red circle and the importance of choosing a proper box size in order to avoid overlap and self-interaction (adapted from González (2011)).

The shape of the PBC can also be changed in order to optimise the simulation if a rectangular box introduces too many water molecules into the system when solvated. Preferably, the shape of the PBC should be chosen so it reflects the underlaying geometry of the macromolecule e.g. a Truncated Octahedron or a Rhombic Dodecahedron can be used for simulation of globular

proteins whereas a hexagonal prism can be used for simulation of a rod like protein or DNA (Leach, 2001a).

6.4.4 Thermodynamic macro and microstates

In order to properly simulate a system, it is important to make sure that the simulation accurately captures its thermodynamic properties. So far, the main discussion has been about atom interactions and motions in a system of interest. The positions and velocities of the atoms are commonly referred to as thermodynamic microstate variables, which in turn define the thermodynamic macrostate properties of volume, pressure and temperature in a system. It is important to remember that a macrostate with a set volume, temperature and pressure can be described by several different microstates whereas the opposite is not possible where instead one microstate will have single corresponding macrostate. This is easier understood when considering a smaller system containing a few atoms with defined positions and velocities. If two of the atoms were to swap velocity directions and magnitudes, the microstate of the system would change due to the change in the microstates variables whereas the macrostate will still be conserved.

This is an important aspect that needs to be considered in order to correctly simulate a real-world experiment where a specific temperature, volume and pressure are used. The absolute temperature of a system can be calculated by using the total kinetic energy shown in (6.17) below.

$$E_{Kin} = \frac{1}{2}\sum_{i=1}^{N} m_i v_i^2 = \frac{k_B T}{2}(3N - N_C) \tag{6.17}$$

$k_B$is Boltzmann's constant, N_C is the number of constraints applied on the system and $3N - N_C$ is the total number of degrees of freedom in the system. The pressure, p, can be calculated by using the total kinetic energy and the virial of the system shown in (6.18) below.

$$p = \frac{2}{3V}(E_{Kin} - \langle T \rangle) \tag{6.18}$$

$$\langle T \rangle = -\frac{1}{2}\sum_{i}^{N}\sum_{j>i}^{N}\langle F_{ij} r_{ij} \rangle \tag{6.19}$$

V is the system volume and $\langle T \rangle$ is the virial or the expected value of the sum of products between atom coordinates and the forces acting on them (Berendsen et al., 1984). The brackets represent the average value over time.

When performing a MD simulation, several different simulation ensembles are available that that restrains the system by keeping some of the thermodynamic properties constant while allowing other to fluctuate. The choice of which ensemble to use depends heavily on how the system should behave and the aim of investigation. Three commonly used ensembles are NVE, NVT and NPT where all ensembles have a constrained number of atoms (N). The NVE ensemble is a so-called micro-canonical ensemble with constrained volume (V) and energy (E) and is most often used to study the conformational energy landscape. The NVE ensemble should never be used to equilibrate a system as the desired temperature can never be reached when the energy is conserved. The NVT ensemble is a canonical ensemble and thus in thermal equilibrium with constrained volume and temperature (T). This type of ensemble is often used to simulate biological reactions. The NPT ensemble is an isothermal–isobaric ensemble with constrained pressure (p) and temperature and is commonly used to simulate chemical reactions in environments where the pressure is maintained such as open atmosphere reactions. Both the NVT and NPT ensembles are commonly used for system equilibration to reach specified temperature and pressure in order to replicate experimental environments. More detailed descriptions on the different ensembles are reviewed elsewhere (Brown and Clarke, 1984).

In order to maintain the desired thermodynamic parameters of a system in a simulation, the use of so-called coupling schemes becomes necessary in order to control parameters of interest such as the temperature and pressure of the system.

The temperature can be controlled by using thermostats. The Berendsen (Berendsen et al., 1984) and Velocity-rescaling thermostats (Bussi et al., 2007) controls the temperature by directly scaling the velocities of the atoms in the system through first-order decay. The Berendsen and Velocity-rescaling thermostats are known as coupling methods. Alternatively, the Nosé-Hoover thermostat (Nosé, 1984, Hoover, 1985) can be used and works by adding an extra correction term to the Newton's equation of motion seen in Figure 6.8 which subtracts or adds to the atom velocities in the system if the temperature is too warm or too cold, respectively. The Nosé-Hoover thermostat is a so-called extended system dynamics method. The three listed thermostats are virtually linked to a heat bath with constant temperature through which heat is exchanged as illustrated in Figure 6.10. This also means that the energy will no longer be conserved in the system and will change depending on the temperature difference between the heat bath and the system of interest.

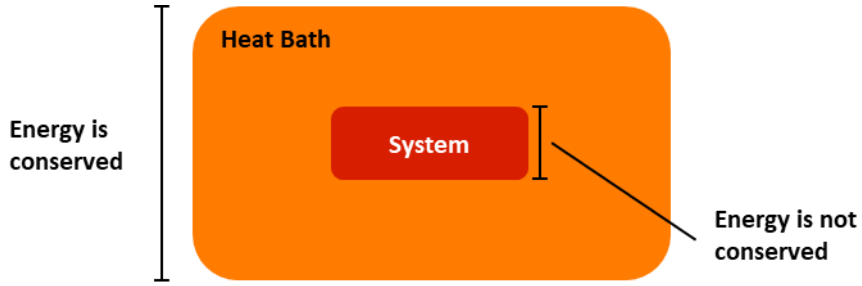

Figure 6.10. A system coupled to a virtual heating bath illustrating the heat exchange between the heat bath and the system of interest (adapted from Ghiringhelli (2014)).

The pressure, similarly to the temperature, is controlled by using barostats. A commonly used weak coupling method is the Berendsen barostat (Berendsen et al., 1984) which is similar to the Berendsen thermostat but instead scales the dimensions of the system in order to achieve the desired reference pressure. Alternatively, the Parrinello-Rahman barostat is an extended system dynamics method similar to that of the Nosé-Hoover thermostat where the volume becomes and extra variable (Parrinello and Rahman, 1981). This allows the system size to vary, thus contracting or expanding the system if the pressure is too low or too high, respectively, compared to the desired reference pressure.

6.4.5 GROMACS System Equilibration

In this research, the GROMACS guidelines for system equilibration were used prior to any production runs in order to emulate real-world experimental conditions (Abraham, 2014). Four equilibration steps were performed with a final production run at the end according to the steps below:

1. Solvation of the system
2. Energy minimisation (EM)
3. Temperature increase to target value through NVT ensemble
4. Adjustment of pressure to target value through NPT ensemble
5. MD production run

The first step involves specifying the periodic boundary conditions to define the simulation box and then filling the empty space with water molecules and counter ions to buffer the system. A common practice is to add chloride and sodium ions to counter the charges of the protein to get a system with a net charge of zero.

The EM is a crucial step that prevents the system from “blowing up” when equilibrated due to potential close proximities and steric clashes between atoms which can result in large forces. These clashes originate partly from the protein structure that, if predicted, might not be

completely relaxed and therefore structurally unfavourable (see Section 6.2.4). Another source is clashes originating from the addition of the solvate to the system where potentially some water molecules might have been placed too close to the protein. The energy minimisation conformationally resolves these clashes by relaxing the system through rotational and directional motions of the clashing atoms, thus lowering the energy of the system (Leach, 2001c). Several methods exist to perform the EM where derivative minimisation methods are most commonly used. First-order methods such as steepest descent and conjugate gradient are fast methods that use the first derivative or gradient to find the energy minima but with the drawback that they can get stuck in local minima. Second-order derivative methods, such as quasi-Newton and L-BFGS, include information about the energy curvature and are less likely to get stuck at local minima but are more computationally intensive due to the need to calculate the Hessian matrix (second derivative matrix). For more detailed information on the listed minimisation methods, refer to the following work (Schlick, 1992). The steepest descent minimisation was used in all simulations due to its speed compared to quasi-Newton and L-BFGS.

In the third equilibration step, an NVT ensemble was used to raise the temperature of the system to a desired target value. Initial velocities in the system were assigned with the Maxwell-Boltzmann distribution presented in eq.(6.14) according to a target temperature of 300 ºK. Position restraints were added to the backbone of the proteins in order to avoid structural collapse due to the rapid heating of the system. The restraints added followed Hooke's law where a virtual spring was attached between the backbone atoms and their original position in space as described by eq.(6.6). A high value was used for the spring constant to keep the backbone rigid. This allowed for further relaxation of the protein side-chains and solvent molecules while the system is heated as well as avoids large conformational changes of the protein structure caused by rapid heating. The ensemble was allowed to run until the temperature of the system had reached the desired target value with little fluctuation. This step was performed using the Velocity-rescaling thermostats in all simulations.

Due to the volume being kept constant in the NVT ensemble, the resulting pressure will be offset compared to the desired target value at the end the NVT run. Therefore, in the fourth equilibration step, a NPT ensemble was used to adjust the pressure in the system to 1 bar with the Parrinello-Rahman barostat. The system temperature was kept constant through continued use with the Velocity-rescaling thermostat. By correcting the pressure, the volume of the system will inevitably change and will no longer conform to the initially defined dimensions. This however is of little consequence as the goal is to emulate the temperature and pressure in a real-

world experiment. Additionally, similar to the previous step the backbone was kept restrained in order to avoid structural collapse while equilibrating the pressure.

In the fifth and final step, a production run was performed as a continued NPT ensemble with a temperature of 300 ºK and a pressure of 1 bar. The backbone constraints on the proteins were removed to allow the protein to adjust to the environment. In order to capture the dynamics of the system a simulation time of 50 ns was used.

6.5 Modifications of protein structure and solvent

In addition to steps described in Section 6.4.5, two more considerations were made to increase the fidelity of the performed simulations.

6.5.1 Co-solvent preparation

The standard simulations in GROMACS are performed in water together with the counter ions sodium and chloride. Real experiments however will usually have additional ions and molecules that are added to either influence the stability of the protein or due to being necessary in particular experiments/process steps. A workflow depicting the preparation of small molecule co-solvents is illustrated in Figure 6.11a. In this research the ChemSpider database was used to find structural information of co-solvents of interest (Pence and Williams, 2010). ChemSpider provides the SMILE format for all listed small molecules which describes the connectivity properties between the atoms in the compound. The Build Structure feature in USCF Chimera (version 1.13) was then used to convert the SMILE format into a MOL2 format which in addition to describing the connectivity have generated space coordinates for the atoms in the compound (Pettersen et al., 2004). Alternatively, OpenBabel can be used instead of Chimera which is more specialised and allows for conversion of nearly all the chemical formats for small molecules (O'Boyle et al., 2011).

In GROMACS when reading in a protein structure, the software will generate a corresponding structure file (e.g. protein.gro) as well as a topology file (topol.top). The structure file will contain the coordinates for all atoms in the system, including all atoms in the protein, solvate and co-solvents. If a previous simulation of the system has been performed such as EM, NVT or NPT, the structure file will also contain the initial velocities for each atom in the system that will be used for the next chronological simulation. The topology file on the other hand is a list that describes the properties of all the atoms in the system such as the atom types, masses and charges. The topology file also lists the connectivity of the atoms in the system to describe all pair-wise bonds (two atoms), angles (three atoms) and torsions (four atoms) with corresponding force field parameters. These are used to perform the calculations of the potential energies

described in Section 6.4.1. Any additions to the simulation system in the form of solvents or other particles will also be included in the topology file and their properties described. For proteins that consist of multiple chains that are connected with disulphide bonds such as mAbs, all chains can be merged into a single structure. This allows for cysteines between chains to be connected and is necessary in order to properly represent the mAb structure. This in turn will generate a single topology file for the merged structure. Alternatively, multiple chains can be represented by using multiple topology files that describe the individual chains. However, interchain disulphide bonds cannot be defined if used, thus increasing the risk of system instability.

In the last step when adding a custom co-solvent, the AnteChamber PYthon Parser interface (ACPYPE) was used in order to generate additional structure and topology files for the co-solvent that could be used in the simulation (Sousa da Silva and Vranken, 2012). For the purposes of this research the topologies were generated using the General Amber Force Field (GAFF) for small molecules with AM1-BCC calculations for estimation of charges (Wang et al., 2004). The co-solvent topology file was then referenced in the protein topology file in order for GROMACS to be able to use the new co-solvent.

To acquire the correct concentration of co-solvent in the simulation there was a need to calculate the number of molecules to be added to the simulation box. This was based on the total number of water molecules present in the simulation box and calculated according to stoichiometric formula in (6.20) below.

$$N_{cs} = \frac{N_{water} M_{water}}{\rho_{water}} C_{cs} \tag{6.20}$$

N_{cs} is the total number of co-solvent molecules, N_{water} is the total number of water molecules, M_{water} is molar mass of water (18.0153 g/mol), ρ_{water} is the water density at 300 ºK (997 g/l) and C_{cs} is the target concentration of the co-solvent (mol/l). The calculated number of molecules were then added to the simulation box by using the insert-molecule function in GROMACS with the generated co-solvent structure file from ACPYPE as input.

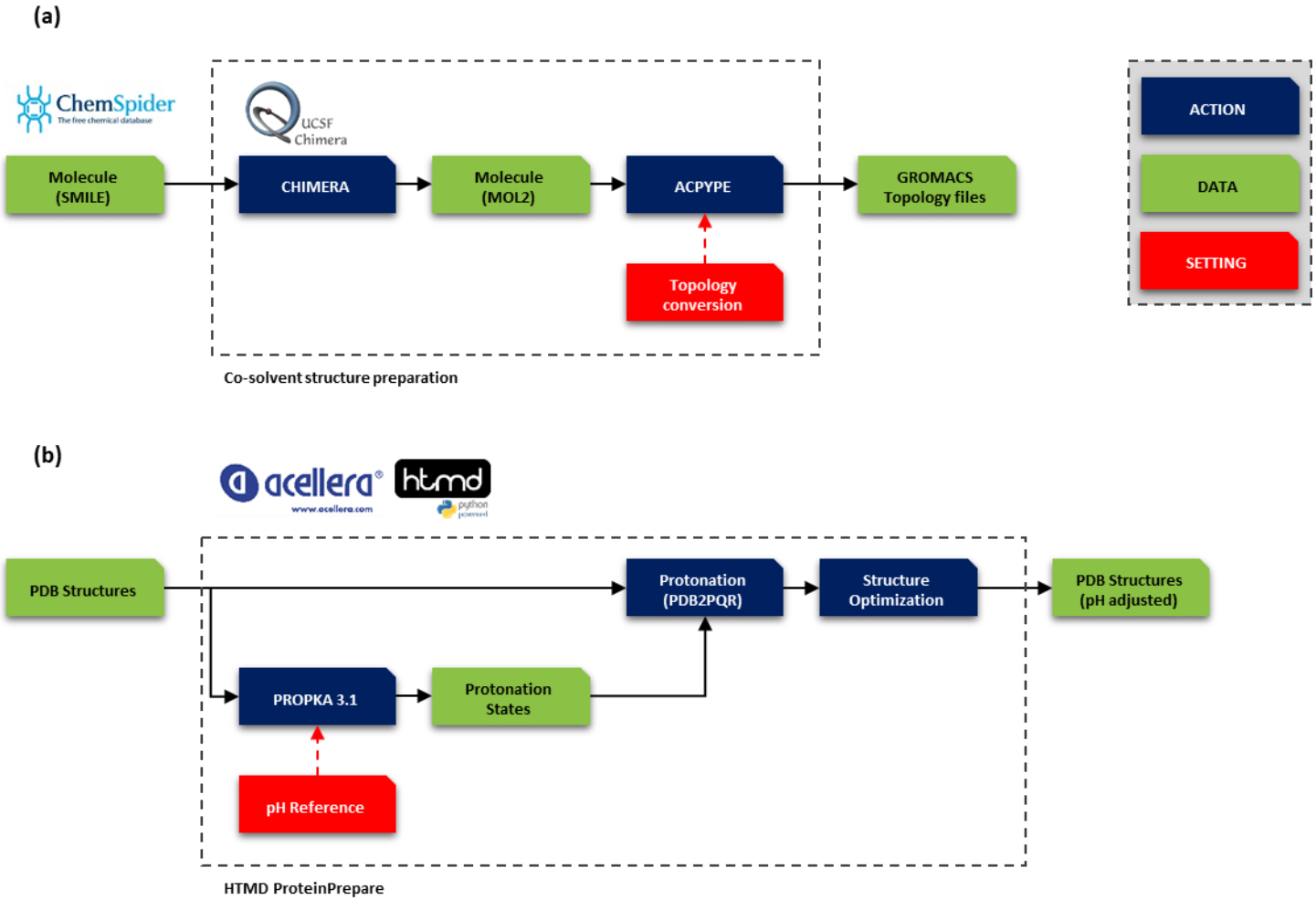

Figure 6.11. Workflows for modification of environment and protein structure. **(a)** Preparation workflow of a co-solvent compound from a SMILE structure to resulting coordinate and topology files that can be used in GROMACS with the use of USCF Chimera and ACPYPE. **(b)** PDB structure modification of pH dependent residues with htmd ProteinPrepare from Acellera. Residue protonation states were predicted with PROPKA3.1 according to a target pH and then assigned with the PDB2PQR function. A structural optimization is performed to relax the structure prior to conversion to a PDB format

6.5.2 Modification of residue protonation states

Another parameter that is often likely to change is different experimental setups and operational units in industrial processes is the pH which affects the protonation states of ionisable residues. Most often when running a MD simulation, the default protonation states in the acquired structure are used. This might not, however, represent the true protein structure due to differences between the protonation states in an experiment and that of the simulation. This can have a negative impact on the dynamics due to wrong assumptions are made in the electrostatic interactions.

The workflow illustrated in Figure 6.11b was used to modify the protein structure to better conform to a specific pH. In this research, a local installation of the ProteinPrepare suite which is part of the High-Throughput Molecular Dynamics (HTMD) environment (Acellera Ltd) was used to modify the protonation states of acidic and basic residues in the protein structures prior to simulations (Martinez-Rosell et al., 2017). More specifically, ProteinPrepare makes use of PROPKA (version 3.1) to predict the pK_a values of any acidic and basic residues that are present in the protein (Olsson et al., 2011, Sondergaard et al., 2011). The PROPKA tool takes into consideration the locations of the acid/base residues as well as surrounding residues that can impact on the pK_a. For buried residues the pK_a value is adjusted in order to drive charged residue to become more neutral. Buried negatively charged residues (acids) have increased pK_a values while buried positively charged residues (bases) have their pK_a value lowered. This is also impacted by proximity of other ionisable residues which further modifies the pK_a values of the residues. ProteinPrepare then compares the predicted pKa values towards that of a target pH value in order to assign the protonation states of the residues. Table 6.5 lists all ionisable residues together with the three-letter code for the different protonation states.

Table 6.5. List of residue protonation states

Amino acid	**Type**	**Protonation states**		
		Positive	Neutral	Negative
Aspartic acid	Acid	-	ASH	ASP
Cysteine [(1)]	Acid	-	CYS/CYX	CYM
Glutamic acid	Acid	-	GLH	GLU
Tyrosine [(2)]	Acid	-	TYR	TYM
Arginine [(3)]	Base	ARG	AR0	-
Histidine	Base	HIP	HID/HIE	-
Lysine [(3)]	Base	LYS	LYN	-

[(1)] Cysteines involved in disulphide bridges are coded as CYX while free cysteine is coded as CYS.

[(2)] Does not naturally occur as negatively charged which requires very high pH values

[(3)] Does not naturally occur as neutral which requires very high pH values

If two cysteines are in close proximity then ProteinPrepare will assign them as CYX, meaning that they are involved in a disulphide bridge. The software will assign a pK_a value of 99 to all CYX residues in order to avoid deprotonation in the event when a high target pH is used. Caution should be exercised as well when a high target pH value is used that drives tyrosine to become charged as well as arginine and lysine to become neutral. The resulting structure will not be useable in any MD simulation due to that the topologies for these protonation states will not exist in any force field.

Protonation of residues according to the predictions from PROKPKA were performed with PDB2PQR (version 2.1) inside of ProteinPrepare (Dolinsky et al., 2004, Dolinsky et al., 2007). As a final step, PDB2PQR performed an energy minimisation of the structure by rotating and flipping the side-chains to allow the structure to become more relaxed where the AMBER99 force field was used. The final structure was then exported as a PDB file.

The effect of assigning different environmental pH values is illustrated in Figure 6.12 where the electrostatic surface of adalimumab Fab fragment is shown with positive charges depicted in blue, neutral in white and negative charges in red. When the pH is low (=2) the negatively charged residues (acids) become neutral due to becoming protonated resulting in a highly positively charged surface. Through incremental increase of the pH it can be observed the negatively charged residues and positively charged residues (bases) become deprotonated resulting in a more negatively charged surface.

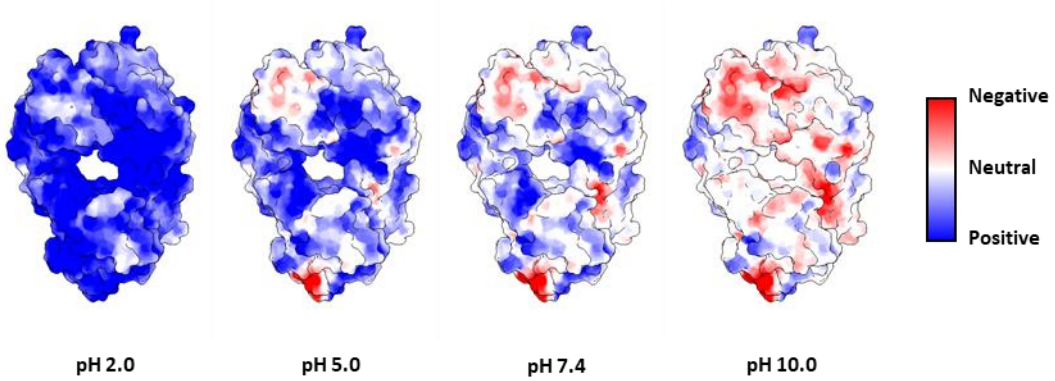

Figure 6.12. Impact of pH on the electrostatic surface of adalimumab Fab fragment. At a pH of 2 the surface is predominately positively charged (blue) and shift to become more negatively charged (red) with increasing pH. The figure was generated from surface renderings using USCF Chimera (version 1.13).

The structure optimisation step with PDB2PQR is not necessarily needed due to the energy minimisation that is performed when equilibrating the system in GROMACS. An alternative approach would be to use PROPKA3.1 to predict the pKa values for the residues and manually

assign the protonation states of the residues according to a target pH by using the optional inputs in the pdb2gmx function in GROMACS.

6.6 Descriptor Generation

A summary of the software packages that have been used in this research for the preparation and the simulation of proteins structures and dynamics is listed in Table 6.6. A general overview of the protein preparation and simulation is also illustrated in Figure 6.13 which shows the protein structure prediction with MODELLER, the protein dynamic simulation with GROMACS as well as the descriptor generation from the resulting output from GROMACS.

In order to generate meaningful descriptors, it was necessary to first extract a structure from the production run simulations that were in conformational equilibrium. This section describes in detail how the final structure was acquired from the GROMACS simulations as well as how 3D structure descriptors were generated.

Table 6.6. List of software packages used in this research to prepare and simulate the protein structure and dynamics.

Software	Version	Description
MODELLER	9.20	Used for structure prediction from primary sequence with the help of PDB templates. Implemented to restrain distances between cysteines involved in disulphide bridges.
GROMACS	5.1.4	Simulation software to estimate the protein dynamics of a target protein structure in a defined environment.
CHIMERA	1.13	Visualisation and analysis software. Useful for editing structure and fill in missing loops.
VMD	1.9.2	Visualisation and analysis software. Useful for calculation of protein RMSD and RMSF as well as visualising the dynamic of the protein through a playback function of the trajectories.
ACPYPE	0.1.0	Software that simplifies the generation of small molecule topologies and parameters that are compatible with many existing forcefields such as AMBER and CHARMM.
PROPKA	3.1	Software for the prediction of pK_a values of acidic and basic residues in a protein structure. PROPKA takes into account if the residue is buried or accessible on the surface in order to perform more accurate calculations.
PDB2PQR	2.1	Fills in any missing heavy atoms and adds hydrogen atoms according to protonation states computed from PROPKA. Also optimises structure by resolving residues involved in steric clashes.

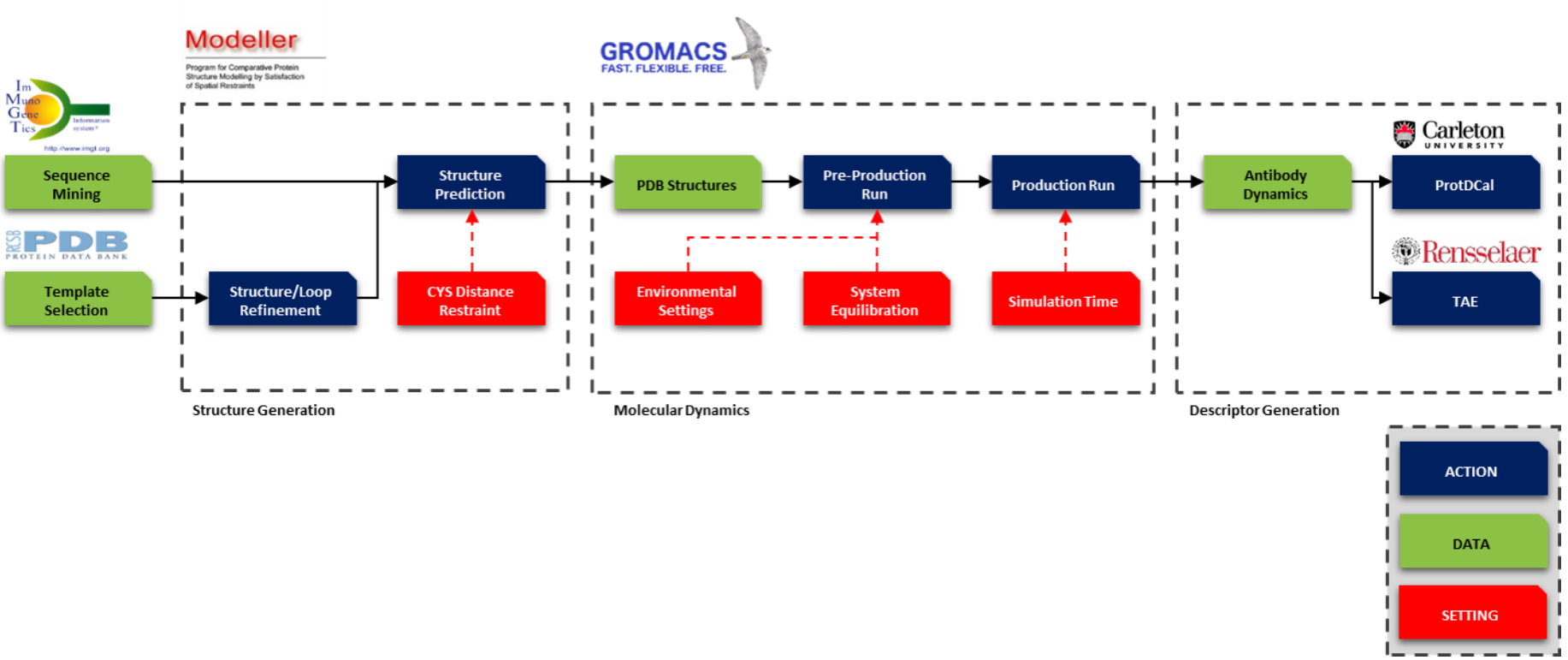

Figure 6.13. Outline of protein structure prediction, protein dynamics simulation and descriptor generation. Structure was predicted with MODELLER and distance restraints for cysteines involved in disulphide bridges. MD simulations were performed with GROMACS where environmental factors such as pH and co-solvents could be added. Descriptor generation was performed with ProtDCal and TAE calculations which modified with individual residue SASA values obtained from GROMACS.

6.6.1 Time frame selection

Due to the constraints placed on the backbone in production run, relaxation of the structures occurred in the beginning of the simulation for each mAb. This is illustrated in Figure 6.14 which shows the conformational change of adalimumab simulated in water. It can be observed in Figure 6.14a that a conformational shift occurs from its original conformation (t=0) to a more relaxed conformation (t=5) which is then retained throughout the rest of the simulation indicating that an equilibrium has been reached. The RMSD used in the figure is a measurement of atomistic deviation over time from a reference structure where the constrained structure from the previous NPT equilibration was used. This conforms to the idea of the energy landscape illustrated in Figure 6.3a where the protein structure will strive to attain as low conformational energy as possible. It also illustrates the structure bias from MODELLER where the predicted structure is biased towards the template and not necessarily in a relaxed state.

Further analysis showed that the smaller fluctuations (vibrations) observed in Figure 6.14a were due to local motions of the loops and turns in the mAb and are illustrated as the peaks in Figure 6.14b and Figure 6.14c for the light chain and heavy chain, respectively. The RMSF values used in the figures are temporal averages of the atomic trajectories (i.e. motions) in space of the residues, thus capturing the residue fluctuation over time. The RMSF values in the figures were calculated from the protein motions acquired after equilibrium had been reached until the end of the simulation.

Based on these facts, the extraction of the structure was therefore performed by selecting a time frame located in the equilibrium interval of the simulations. The timeframe was selected towards the end of each simulation in order to allow the structures to relax and reach conformational stability. This was due to the fact that relaxation times between mAbs varied, thus introducing uncertainty of conformational stability if earlier timeframes were used. This is covered more in detail in Section 7.1.2 which discusses the simulation results for the 137 mAbs in the publication of Jain et al. (2017).

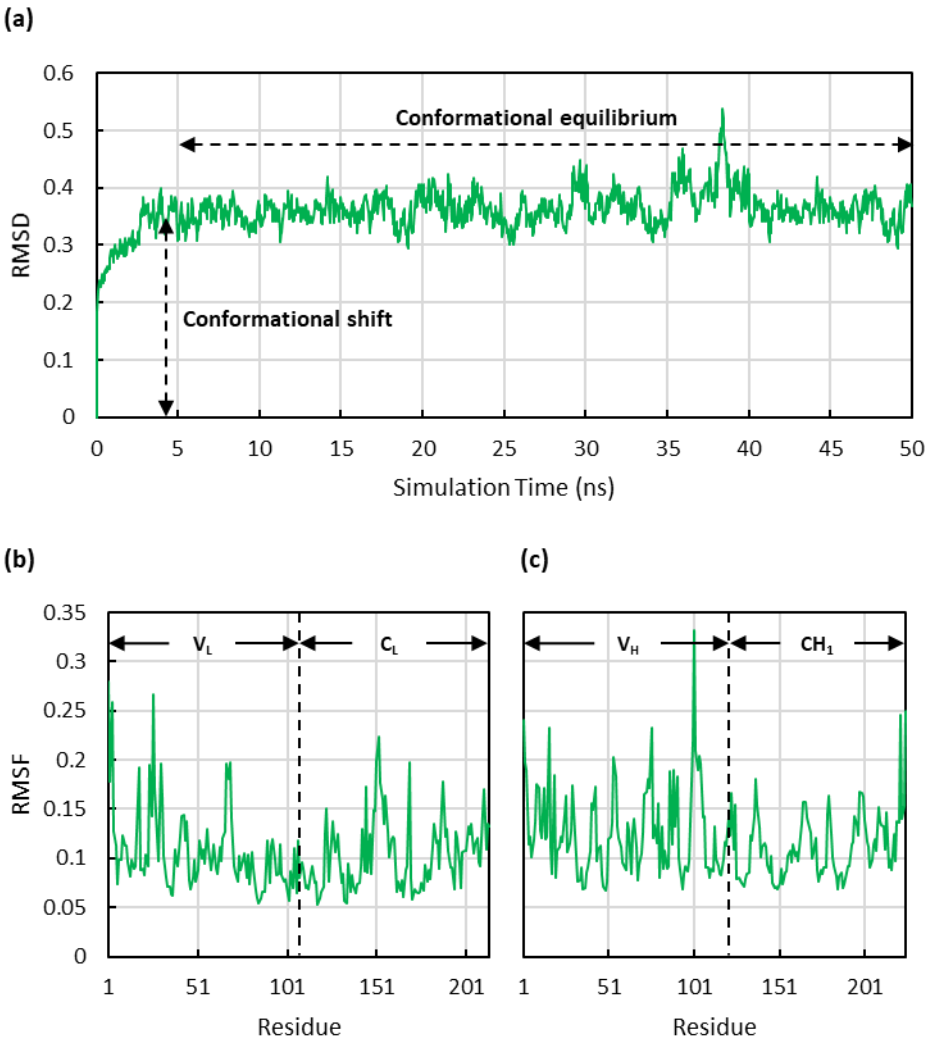

Figure 6.14. MD simulation result for adalimumab. (a) The conformational change of adalimumab evolving over time in the production run. **(b)** The average fluctuations of the individual residues in the light chain between t=5 ns and t=50 ns. **(c)** The average fluctuations of the individual residues in the heavy chain between t=5 ns and t=50 ns.

6.6.2 Descriptor software and calculations

Similar to the primary sequence-based descriptors, ProtDCal was used for generation of 3D structure descriptor by using the acquired PDB structures from the MD simulations as input (Ruiz-Blanco et al., 2015). GROMACS was used to generate the solvent accessible surface area (SASA) for the residues in the mAbs which were used as basis or modification of many of the generated descriptors. Table 6.7 lists the descriptors. Focus was placed on descriptors pertaining to the surface, shape and energies that were impossible to capture when using the primary sequence.

Table 6.7. List of energy and topological descriptors used to describe the protein structure

Descriptor	ProtDCal	GROMACS	Type	Description
$G_c(F)$	•		Energy	Contribution to the free energy from the conformational entropy in a folded state
$G_W(F)$	•		Energy	Contribution to the free energy from the entropy of the first shell of water molecules in a folded state
$G_s(F)$	•		Energy	Interfacial free energy of a folded state
$W(F)$	•		Energy	Number of water molecules close to a residue in a folded state
HBd	•		Energy	Number of hydrogen bond in the backbone of the protein
ΔG_s	•		Energy	Variation of the interfacial free energy between folded and unfolded states
ΔG_W	•		Energy	Contribution to the folding free energy of the first shell off water molecules
ΔG_{el}	•		Energy	Free energy contribution of the charge distribution within the protein
ΔG_{LJ}	•		Energy	Contribution of the Van der Waals interaction to the folding free energy
ΔG_{tors}	•		Energy	Contribution of the dihedral torsion potential to the folding free energy
$SASA_{polar}$		•	Topological	The total solvent accessible surface area from the polar residues
S_{polar}		•	Topological	The effective surface polarity from the charged and polar residues
$SASA_{non-polar}$		•	Topological	The total solvent accessible surface area from the non-polar residues
$S_{non-polar}$		•	Topological	The effective surface hydrophobicity from the non-polar residues
$ln(FD)$	•		Topological	Logarithm of the folding degree

In addition, 37 Transferable Atom Equivalent (TAE) descriptors were used in order to describe electron and charge densities of the mAbs. TAE is in simple terms a library of empirical atomic charge density components that are used to construct electron densities able to describe the protein surface of individual amino acids (Breneman and Rhem, 1997).

The TAE descriptors used in this research were available in ProtDCal as listed value for each amino acid. This meant that the generated TAE descriptors were based on the amino acid composition in ProtDCal rather than feature of the protein and therefore no different from using the primary sequence as input. In order to conform these descriptors to represent the surface of the mAb the generated SASA values from GROMACS were used according to eq.(6.21). The equation calculates the fraction of each amino acid that is accessible to solvent and is known as

the relative surface area (RSA) and ranges from zero (the residue is completely buried) to one (maximum exposure).

$$TAE_k^{Surface} = \sum_i \frac{SASA_i}{MaxASA_i} TAE_{ik} = \sum_i RSA_i \cdot TAE_{ik} \qquad (6.21)$$

$TAE_k^{Surface}$ is the resulting kth TAE descriptor for the surface, $SASA_i$ is the solvent accessible surface area of residue i, $MaxASA_i$ is the maximum accessible surface area of a residue i, TAE_{ik} it the kth listed TAE descriptor for residue i and RSA_i is the relative surface area of residue i. The $MaxASA$ value is defined as the accessible surface area of an amino acid X in a Gly-X-Gly tripeptide conformation. Published empirical values from Tien et al. (2013) were used to calculate the descriptor in this research.

In a similar fashion, descriptors for describing the hydrophobicity, eq.(6.22), and the polarity, eq.(6.23), of the surface were generated by using the Kyte-Doolittle scale. Specifically, the hydrophobicity of the surface was calculated by using the nine in the NPR amino acid group in Table 3.3 in Chapter 3 and the polarity was calculated using the 11 residues in the PLR amino acid group.

$$S_{non-polar} = \sum_{i \in NPRp} \frac{SASA_i}{MaxASA_i} k_i^{KD} \qquad (6.22)$$

$$S_{polar} = \sum_{i \in PLRp} \frac{SASA_i}{MaxASA_i} k_i^{KD} \qquad (6.23)$$

$S_{non-polar}$is the surface descriptor describing the hydrophobicity, $S_{polar}$is the surface descriptor describing the surface polarity and k_i^{KD} is the Kyte-Doolittle value for residue i.

No treatment was needed for the generated energy descriptors from ProtDCal as these are calculated based on the surrounding environment.

6.6.3 Descriptor resolution

Similar to the primary sequence-based descriptor, strategies for defining the descriptor resolution was used where selection of residues to use were based on the intrinsic structural features of all mAbs (see Section 3.3). Three different resolutions were considered when

generating 3D structure descriptors: Chain, Domain and Substructure. Table 6.8 lists the number of generated descriptors for the three resolution in a V_H/V_L and a Fab configuration.

Table 6.8. Number of generated descriptors based on resolution type and size of the mAb.

Method	**V_H/V_L**	**Fab**	**Input type**	**Descriptors per input**
Chain	Skipped [(1)]	104 (2)	Chain	52
Domain	104 (2)	208 (4)	Domain	52
Substructure	728 (14)	1456 (28)	Substructure	52

[(1)] Is identical to the domain resolution when V_H/V_L is used

6.7 Summary

In this chapter a workflow for generating and simulating mAb structures has been presented. Due to the high structural similarities shared between mAbs and availability of structure templates, the homology modelling approach with MODELLER was selected for initial prediction of the mAb structure. However, due to the high sequence dissimilarity in the variable regions between the predicted structure and the template it was assumed that predicted structures would have an unfavourable energetic state and therefore not be relaxed. MD simulations with GROMACS was therefore performed as a subsequent step after the homology modelling in order to relax the predicted structures.

Descriptor were then generated with ProtDCal but modified with residue SASA values from GROMACS in order to only capture the surface properties. Generated descriptors presented in this chapter has been applied and assessed on prediction of HIC retention times and mAb yields in Chapter 7.

Chapter 7

QSAR Model Development: 3D Structure Descriptors

In Chapter 6, a workflow for the generation of novel 3D structure descriptors was presented which provided an alternative approach to describe the mAb structure compared to the previously explored descriptors generated from the primary sequences described in Chapter 3. The 3D structure descriptors were designed to represent the surface properties as well as the stability properties of the mAbs. Three different 3D structure descriptor resolutions were investigated which were generated based on the full chains, the individual domains and the individual substructures present in the mAb structure (from the lowest to the highest resolution).

The new 3D structure descriptors were first evaluated for potential systematic variation originating from the unique structure of the light chain isotypes with the use of PCA. In addition, the potential variation originating from the species origins was also explored with classification methods such as PLS-DA and SVC. These were important factors in the development of the predictive models presented in Chapter 5 where the primary sequence-based descriptors contained systematic variation uncorrelated to the investigated responses.

HIC retention times and mAb yields were chosen as response vectors for model development due to being important parameters in pharmaceutical industries for the assessment of productivity and product stability, respectively. All models were developed according to the benchmarking scheme first presented in Chapter 5. PLS and SVR were used as modelling methods. Model optimisation was performed in incremental steps where V-WSP was used for initial variable reduction. rPLS, LASSO and GA was then applied for subsequent variable selection on the V-WSP reduced descriptor set in order to increase correlation between descriptors and responses.

7.1 Material and Methods

7.1.1 Response Data

In this research quantitative process data published by Jain et al (2017) was used to develop predictive models for HIC retention times and mAb yields. For more details on the dataset and experimental setup of the mAb yield and HIC, refer to Section 5.1.1. Out of the 137 available mAbs in the data set, 131 were retained based on the reasoning discussed in Section 5.1.1.3.

7.1.2 Descriptor Data Generation

Fab fragments of the mAbs were prepared for simulation using the available sequences of the variable domains V_H and V_L provided as supplementary information in the study of Jain et al (2017). The heavy chain was prepared by attaching an IgG1 C_H1 sequence obtained from allele sequence IGHG1*01 to the provided V_H domains. Similarly, the light chain was prepared by attaching a C_L domain sequence to the provided V_L domains obtained from either allele sequence IGLK1*01 (kappa) or IGLC1*01 (lambda).

Homology models were generated using MODELLER version 2.17 (Webb and Sali, 2014) with a single template where PDB 2FGW and 7FAB were used for Fab fragments of kappa and lambda isotypes, respectively (see Table 6.2 in Chapter 6). Pair-wise cysteines involved in disulphide bridges were restrained where the sulphur atoms were placed at a distance of 2 Å from each other in order to properly connect the cysteine residues. Two mAbs (muromonab and teplizumab) were excluded in this process due to having cysteines in the CDR regions which caused MODELLER to form incorrect disulphide bridges, thus misrepresenting the structure.

Atomistic simulations of the Fab fragments were performed with GROMACS (version 5.1.4) and simulated in water with a concentration of 0.1 M NaCl in order to stabilise surface charges. Prior to the production run, the system was equilibrated to a temperature of 25 ^oC and pressure of 1 bar. In this research, the high-performance computing (HPC) service ROCKET at Newcastle University was used run the production simulation. Each Fab fragment was simulated for a total of 50 ns to allow structure to reach conformational equilibrium described in Section 6.6.1. Atezolizumab was excluded in this process due to causing critical failures in the simulation. Several attempts were performed to re-simulate atezolizumab but all failed due to high system instability.

Structural descriptors for the remaining mAbs were generated based on the methodology presented in Section 6.6 where three unique descriptor sets were obtained: Chain based (MSD1), Domain based (MSD2) and Substructure based (MSD3) where MSD is short for “Molecular Structure Descriptors”. In total, this resulted in 128 mAbs being selected for further

evaluation as listed in Table A.3 in Appendix A with corresponding experimental measurements for HIC retention times and mAb yields.

7.1.3 Modelling Methods

7.1.3.1 PCA

PCA was used as an exploratory analysis tool to investigate the three descriptor sets and the relationship between descriptors and the light chain isotypes as well as the species origins. PCA implementation was performed using the PLS Toolbox version 8.6.1 (Eigenvector Research, Inc). For more details on PCA, see Section 2.2.1.

7.1.3.2 PLS-DA

The NIPALS algorithm was used to develop a PLS regression model for predicting the dummy variables generated from the class information pertaining to the species origin of the mAbs. Discriminant Analysis (DA) was then applied to create decision thresholds in order to classify the predictions of the developed PLS model. For more details on PLS-DA, see Section 2.3.1.

7.1.3.3 SVC

The LibSVM toolbox was used and implemented in MATLAB 2016a for SVC model development (Chang and Lin, 2011). The C-SVM function in LibSVM was used for multiclass classification problems. A shell script was developed to implement the OvR multiclass strategy in SVC instead of using the default OvO strategy in LibSVM in order to reliably compare SVC to PLS-DA. The shell scripts for model fitting and prediction are presented in Appendix B, Code B.1 and Code B.2, respectively. Optimisation of the model parameter C was performed using a grid search approach on defined points over specified ranges for each parameter (for details on parameters see Section 2.3.2). The grid points used for C were $[10^{-5}, 10^{-4}, 10^{-3}, 10^{-2}, 10^{-1}, 10^{0}, 10^{1}, 10^{2}, 10^{3}, 10^{4}]$.

7.1.3.4 PLS

Partial Least Squares regression was performed using the NIPALS algorithm. The first 20 latent variables were calculated to allow for a majority of the data variation in $\boldsymbol{X}$ and $\boldsymbol{Y}$ to be captured. A higher number of latent variables is often not recommended as they usually only improve fitting of individual samples, thus causing over-fitting (Wold et al., 2001). For more information on PLS, refer to Section 2.4.1.

7.1.3.5 SVR

The optimisation of the model parameters C and ϵ was performed by using a grid search approach on defined points over specified ranges for each parameter (for details on parameters, see Section 2.4.2). The grid points used for C were [10^{-5}, 10^{-4}, 10^{-3}, 10^{-2}, 10^{-1}, 10^{0}, 10^{1}, 10^{2}, 10^{3}, 10^{4}] whereas the grid points used for ϵ were [10^{-3}, $10^{-2.5}$, 10^{-2}, $10^{-1.5}$, 10^{-1}, $10^{-0.5}$, 10^{0}, $10^{0.5}$, 10^{1}]. This resulted in 90 different model parameter permutations that were evaluated in the model cross validation.

7.1.4 Data curation and pre-treatment

An initial data curation step was performed where descriptors with a standard deviation lower than 0.0001 were removed as they were considered to be static and thus not contributing informational content to the model.

Both the descriptor set (***X*** block) and the response vector (***Y*** block) were autoscaled when used in regression models in order to allow the descriptors to influence the resulting model equally (see Section 2.7). In classification models, only the ***X*** block was autoscaled whereas the class labels were assigned as zero and one in PLS-DA and minus one and one in SVC.

7.1.5 Model Training and Validation

7.1.5.1 Structured data splitting

Prior to model development the data set was split into a calibration set and an external test set to represent future samples. The Kennard-Stone (CADEX) algorithm was used to divide the samples according to structural similarity based on the Euclidean distance between samples in the descriptor space (see Section 2.5.1 for more details). 80% of the samples were retained for model calibration and the remaining 20% were used for external testing and model validation.

7.1.5.2 Cross-Validation scheme

A repeated k-fold cross validation scheme was applied for model development where *k* was chosen to be five in order to get an 80/20 sample split ratio between training and validation samples, respectively. 20 iterations were performed to better utilise the data set and to decrease the potential impacts of outliers in the data on the cross validation. For more information, see Section 2.5.2.

7.1.5.3 Model Validation

The validation of PLS-DA and SVC models was performed using the overall error rate (ER) and the Matthews Correlation Coefficient (MCC) based on the confusion matrices of the

developed models. The appropriate model complexity of the PLS-DA and SVC models was determined through the selection of model complexity with the lowest ER in the cross validation. For more information on the classification metrics, refer to Section 2.6.2.

All regression models were validated using the OECD guidelines for R^2 and Q^2 for QSAR models (Veerasamy et al., 2011, Alexander et al., 2015). The guidelines state that R^2 and Q^2 should be greater than 0.5 and 0.6 in the cross-validation and external prediction, respectively. In addition, the difference between R^2 and Q^2 should not exceed 0.3. The thresholds R^2 and Q^2 in the OECD guidelines are intended to be used for early model development to explore potential correlation of factors and descriptors related to the modelled responses. Once characterised, additional descriptor development and adjustments can be performed to further improve model performance. For more information on the regression metrics, refer to Section 2.6.1.

7.1.5.4 Y-Randomisation

Y-randomisation was used to evaluate the presence of random correlation between a descriptor set and a randomised response vector. The response vector was randomised 50 times and an individual model was developed on each permutation. Calculated R^2 and Q^2 values from the 50 models were then averaged. If no chance correlation is present in the descriptor set, both the averaged R^2 and Q^2 values will be low. For more details on Y-randomisation, refer to Section 2.6.3.

7.1.6 Variable reduction and Selection

7.1.6.1 V-WSP

The V-WSP algorithm was applied as an unsupervised variable reduction method to remove collinear descriptors present in the $\boldsymbol{X}$ block. Implementation of V-WSP was performed in the same way as described in Section 5.1.5.1.

In order to avoid removal of collinear descriptors belonging to different chains, domains or substructure, the V-WSP reduction was performed on groups of descriptors defined by the resolution of the descriptor set. In MSD1, the groups were defined as individual chains. In MSD2, the groups were defined as individual domains. In MSD3, the groups were defined as individual substructures. This was done in order to avoid excessive information loss and to represent each group individually. Reduction with V-WSP was performed prior to any supervised variable selection method.

7.1.6.2 rPLS

Supervised variable selection with rPLS was performed using PLS Toolbox 8.6.1 (Eigenvector Research Inc) together with MATLAB 2016a (Mathworks®). An initial PLS model was developed with selected descriptors from V-WSP reduction and the latent variable with the smallest RMSECV was selected as a starting point for the rPLS selection. For more information on rPLS, refer to Section 2.9.1.

7.1.6.3 GA

Supervised variable selection with Genetic Algorithm (GA) was performed using PLS Toolbox 8.6.1 (Eigenvector Research Inc) together with MATLAB 2016a (Mathworks®) and PLS as the fitness function. A population size of 100 was used and the maximum number of generations was set to 100. The convergence for the GA algorithm was set to 50%. Default values for the mutation rate and the ratio of kept variables in the initial models was kept as 0.5% and 30%, respectively. For more information on GA, refer to Section 2.9.2.

7.1.6.4 LASSO

The LASSO algorithm was implemented using the function *fitrlinear* in MATLAB 2016a (Mathworks®) where SVR was set as the learner and LASSO selected as the regularisation method. A grid search was performed in the same fashion to that of SVR described in Section 5.1.5.4 in order to optimise the parameter selection.

7.2 Results and Discussion

7.2.1 Analysis of protein dynamics

The evaluation of the simulations was performed by observing the generated RMSD plots for the 128 mAb simulations which are shown in Figure 7.1. The majority of the mAb structures reached conformational stability after 15 ns which can be observed as the plateaus in Figure 7.1a. However, four mAb structures failed to reach conformational stability during the simulation where the RMSD value instead kept increasing as illustrated in Figure 7.1b. Interestingly, three of these mAbs: briakinumab, fezakinumab and tralokinumab are of lambda conformation whereas eldelumab is of kappa conformation. It has been shown in research that light chains of the lambda isotype in general are more unstable than kappa which might explain why conformational stability were not reached in the simulations (Rouet et al., 2014).

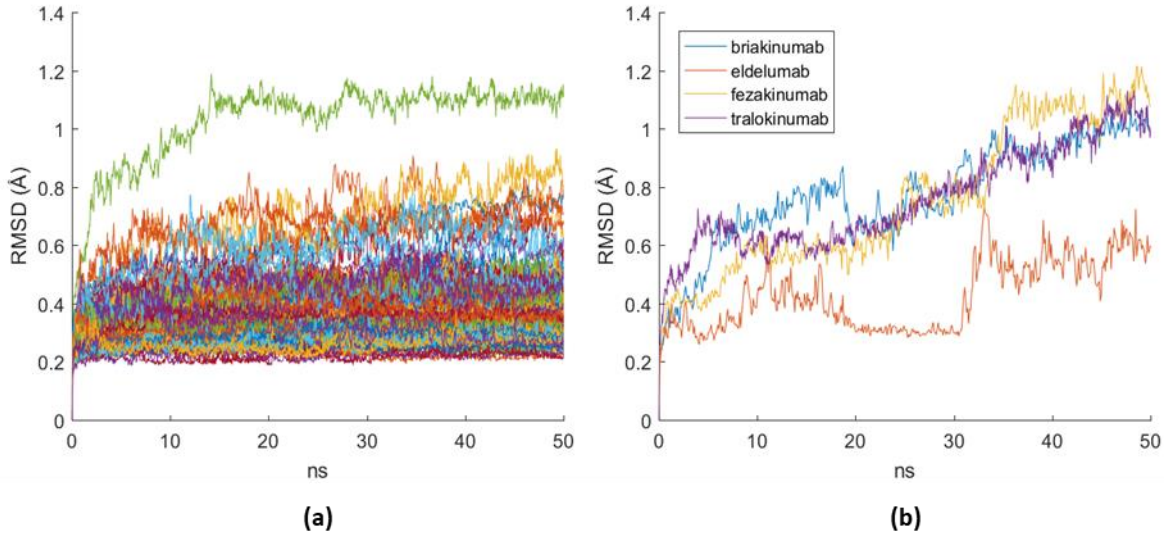

Figure 7.1. RMSD plots of GROMACS simulations where **(a)** mAbs have reached conformational stability and **(b)** mAbs that have not reached conformational stability.

In addition to the plots, the standard deviation of the RMSD, σ_{RMSD}, was calculated from the snapshots obtained between 15 ns and 50 ns in the simulations according to equation (7.1).

$$\sigma_{RMSD} = \left(\frac{1}{N_{frames} - 1} \sum_{t=15\ ns}^{50\ ns} \left(RMSD_t - E(RMSD) \right)^2 \right)^{\frac{1}{2}} \qquad (7.1)$$

where N_{frames} is the number of snapshots between 15 ns and 50 ns, $RMSD_t$ is the RMSD value at time t and $E(RMSD)$ is the expected value or average of the RMSD according to equation (7.2).

$$E(RMSD) = \frac{1}{N_{frames}} \sum_{t=15\ ns}^{50\ ns} RMSD_t \qquad (7.2)$$

The σ_{RMSD} value thus represents the variability of the RMSD curve in the simulation interval between 15 ns and 50 ns where stability had been reached for the majority of mAb structures. Therefore, in a more indirect manner, the σ_{RMSD} value can be used to infer conformational stability of a protein where a low value represents a stable conformation whereas a high value represents conformational change. The four mAb structures: briakinumab, fezakinumab, tralokinumab and eldelumab illustrated in Figure 7.1b had σ_{RMSD} values above 0.12 with the highest value of 0.21 (fezakinumab). The mAb structures that were considered stable all had values below 0.07, thus having less conformational variation occurring after the structure had been relaxed (data not shown). Further inspection of eldelumab was performed in order to

investigate the second plateau illustrated in Figure 7.1b between 30 ns and 50 ns of the simulation. It was observed that the rise in RMSD occurring at 30 ns was caused by the V_H domain slightly twisting upwards in the Fab fragment as illustrated in Figure 7.2 where Figure 7.2a and Figure 7.2b are snapshots taken at the 25 ns and 35 ns timeframes of the simulation respectively. The new structural conformation of eldelumab illustrated in Figure 7.2b then remained stable throughout the rest of the simulation. In the case of briakinumab, fezakinumab and tralokinumab, twisting occurred in all domains where the V_H and V_L domains packed closer to the C_L and C_H1 domains respectively, thus resulting in a more compact and spherical structure (data not shown). The observed conformational change of the structures were gradual throughout the simulations which also explains the continued increase of the RMSD values for briakinumab, fezakinumab and tralokinumab.

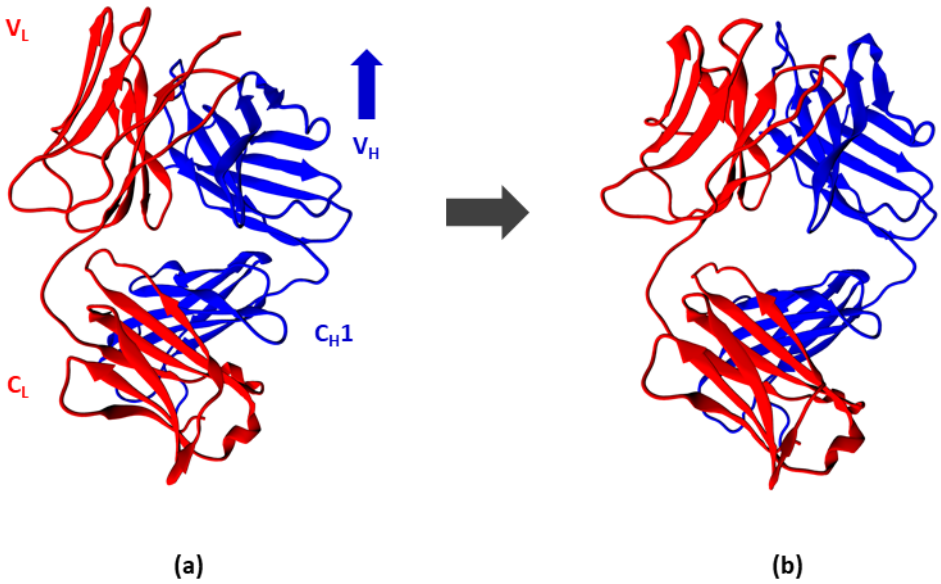

Figure 7.2. Displacement of the V_H domain (blue arrow) in the simulation of eldelumab from the domains original position captured at **(a)** 25 ns to its new placement captured at **(b)** 35 ns. The heavy chain is coloured blue while the light chain is coloured red.

For all simulations except briakinumab, eldelumab, fezakinumab and tralokinumab, the structures remained stable throughout the simulation and no conformational changes occurred. The last timeframe in each of these simulations was therefore used to generate a PDB structure from which descriptors were later generated (see Section 6.6). For eldelumab, the last timeframe was used due to that the second plateau remained stable from 30 ns until the end of the simulation. Preferably, continued simulation of briakinumab, fezakinumab and tralokinumab would be desirable in order to allow the structures to converge to a stable conformation. However, due to time constraints within the project, the last timeframe in the simulations (50 ns) were used to generate the descriptors. Though it introduces some uncertainty regarding

briakinumab, fezakinumab and tralokinumab structural stability, it was believed that if the simulations were allowed to run further, they would converge to a stable conformation. Therefore by selecting the last timeframe in the simulation, it could be assumed that the structures would be closer to the stable conformations than they were prior to the simulations.

7.2.2 Impact of the light chain isotypes

Similar to the exploratory analysis performed in Chapter 4 on the 273 mAb sequences obtained from the IMGT database, the impact of the light chain isotypes, kappa and lambda, on the generated 3D structure descriptors described in Chapter 6 was explored with PCA. Only descriptors generated from the light chain were used in this exploratory analysis because no structural information relating to the heavy chain isotype were present in the structures due to all mAbs being expressed as IgG1. The number of principal components (PCs) was incrementally increased until approximately 90% of the data variation in the descriptors sets had been explained. This was done due to the light chain isotype being expected to have a strong impact on the generated descriptors in a similar fashion as was observed in Chapter 4 for the primary sequence-based descriptors.

A clear diagonal separation of kappa and lambda could be observed in the first and second PCs in MSD1 (Figure 7.3a), MSD2 (Figure 7.3b) and MSD3 (Figure 7.3c) with an explained variation of 81.18%, 72.0.3% and 42.45%, respectively. However, not all of the explained variation of the first two PCs can be attributed entirely to the separation of the isotypes which also separates the individual samples from each other due to their unique surface properties. It is difficult to estimate to what extent the V_L and C_L domains influence the separation. However, a clear contribution from both domains could be observed when investigating the loadings of PC1 and PC2, as illustrated in Figure C.7 in Appendix C. The remaining PCs showed no further separation of the light chain isotypes and were therefore assumed to capture variation related to individual samples instead (data not shown). A short summary of the PCA results is presented in Table 7.1.

The statistical analysis on the response vectors of the HIC retention time and mAb yield performed in Section 5.2.2 is still valid due to being independent from the generated descriptors and only investigates the behaviour of the responses according to the isotypes. Just as with the primary sequence-based descriptors, a strong impact of the isotypes on the generated 3D structure descriptors was evident (see Figure 7.3). This can potentially act as a systematic variation that is uncorrelated to the response and can have a negative impact on the performance of developed regression models (Wold et al., 1998). It is important to remember that the heavy chain was modified by Jain et al (2017) where all heavy chain constant domains were expressed

as IgG1 regardless of their original conformation. Therefore, no conclusions can be drawn with regards to the impact of the original heavy chain isotypes on the responses. For these reasons, only IgG1-kappa samples were used for further model development, resulting in 79 samples being retained from the previously 128 selected samples.

As previously described in Chapter 4, the amino acid composition of the primary sequence in the V_L domain will be different between kappa and lambda due to being expressed from separate genes in the VJ recombination (Jung and Alt, 2004). This had a significant impact on the generated 3D structure descriptors from the V_L domain which had high contributions to the loadings of the PC1 and PC2 (see Figure C.7 in Appendix C). This indicates that a fraction of residues directly related to the light chain isotype are present on the surface and it further highlights the need for an appropriate selection of samples in order to avoid introduction of uncorrelated systematic variation prior to model development.

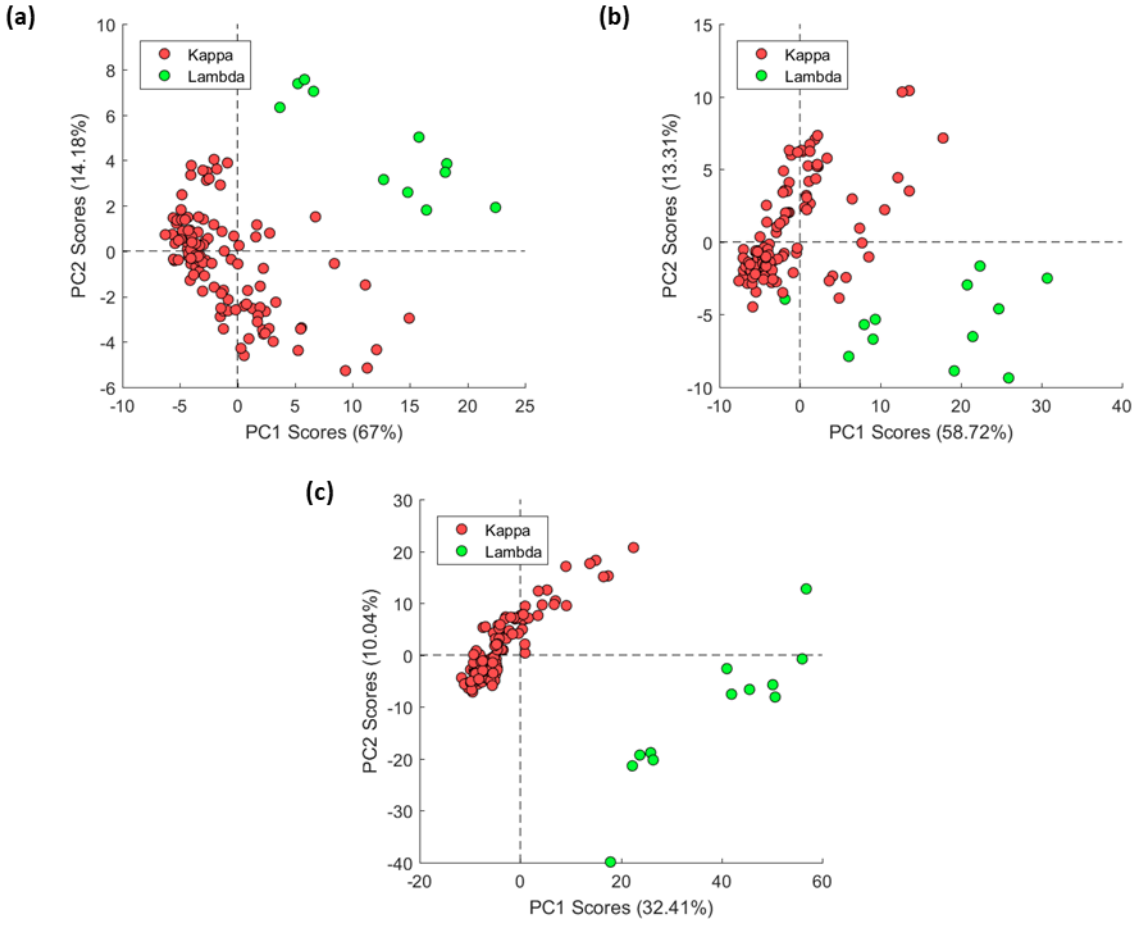

Figure 7.3. PCA score plots of the first two components calculated from the light chain descriptors from MSD1 **(a)**, MSD2 **(b)** and MSD3 **(c)** where kappa and lambda samples are coloured red and green, respectively.

Table 7.1. PCA exploration summary of light chain descriptors from MSD1, MSD2 and MSD3 where each model was developed to capture approximately 90% of the total data variation. The last two columns show information of PCs related to the LC isotype separation and the cumulative explained variation of those PCs.

Descriptor Set	Number of Descriptors	Principal Components	Explained Variation (%)	LC Isotype separating components	Explained Variation (%) by selected component
MSD1	50	4	90.04	1 and 2	81.18
MSD2	100	6	90.24	1 and 2	72.03
MSD3	632	26	90.12	1 and 2	42.45

7.2.3 Impact of species origin

To explore the potential impact of the species origin, classification methods such as PLS-DA and SVC were applied to the 79 selected IgG1-kappa samples. All 100 descriptors in MSD1 were used in the model development due to having been calculated on the full heavy or light chains where separation of constant and variable domains is not possible (see Section 6.6.3). As for MSD2 and MSD3, only descriptors belonging to the variable domains V_H and V_L were used which resulted in 100 and 644 descriptors being used, respectively. The CADEX algorithm was used to split the data into 80/20 for calibration and test, respectively, according to the structural information contained in the individual descriptor sets MSD1, MSD2 and MSD3. When CADEX was used directly, the algorithm produced a skewed split of species origins in the calibration and test sets in all individual descriptor sets. This was especially pronounced for the chimeric species origin where only one sample was placed in the test set for MSD2 and MSD3 while no samples were placed in the test set for MSD1. Instead, a sample stratification strategy was implemented to ensure that all species origins were appropriately represented in the test set (Shahrokh and Dougherty, 2013). This was performed by applying the CADEX algorithm individually on the three species origins where 80% were retained for training and 20% for model validation in the test set. A summary of the sample splitting is presented in Table C.6 in Appendix C.

A summary of the performance of the developed PLS-DA and SVC models is presented in Table 7.2 for the three descriptor sets. None of the developed models performed well in the cross-validation where the error rates were close to 0.4 regardless of modelling method or descriptor set, meaning that approximately 40% of the samples were classified incorrectly. The corresponding MCC values showed an indication of a weak correlation (0.2-0.3) between the generated descriptors and the species origin classes, thus indicating a lack of correlation in the data (Jurman et al., 2012). This is further supported through investigation of the individual AUC values of the three species origins obtained from the ROC curves illustrated in Figure C.8 in

Appendix C. For both PLS-DA and SVC models developed on the MSD1 and MSD2 descriptor sets, the AUC values tended to be placed around 0.65 for the chimeric and human species origins while the humanised species origin was around 0.75. For PLS-DA and SVC models developed on the MSD3 descriptor set, the AUC value of the chimeric species origin tended to be around 0.8 while the human and humanised classes had values around 0.7. The AUC values are considered to be relative and dependent on the data set used. However, as a rule of thumb AUC values above 0.8 can be considered as a reasonable performance while values below 0.8 can be considered poor (Fawcett, 2006). Thus, none of the developed classification models were able to identify an underlaying correlation between the generated 3D structure descriptors and the species origins.

Compared to the cross-validation, the results observed in the test set tended to vary a bit more. In general, SVC models tended to have slightly higher MCC values and lower ER values compared to PLS-DA. The best performance was observed in the SVC model developed on the MSD3 descriptor set with a MCC value of 0.75 and an ER value of 0.18. However, due to the poor performance in cross-validation this model cannot be considered to produce accurate predictions in future samples.

Table 7.2. Summary of PLS-DA and SVC model performance developed on the descriptor sets: MSD1, MSD2, and MSD3. The MCC and ER performance metrics for calibration (Cal), cross-validation (CV) and the external test (Test) set are provided as well as the explained data variation of ***X*** and ***Y*** by PLS-DA.

Method	**Descriptor Set**	**Explained *X* Variation (%)**	**Explained *Y* Variation (%)**	**Cal**		**CV**		**Test**	
				MCC	**ER**	**MCC**	**ER**	**MCC**	**ER**
PLS-DA	MSD1	86.68	62.27	0.86	0.08	0.19	0.48	0.29	0.41
	MSD2	76.59	45.97	0.72	0.16	0.20	0.48	0.07	0.53
	MSD3	26.95	57.52	0.78	0.13	0.26	0.42	0.59	0.24
SVC	MSD1	-	-	0.89	0.06	0.28	0.40	0.48	0.29
	MSD2	-	-	0.92	0.05	0.32	0.37	0.37	0.35
	MSD3	-	-	0.97	0.02	0.26	0.40	0.75	0.18

When compared to the classification results in Section 4.2.5 where primary sequence-based descriptors had a strong correlation to the species origin classes, the 3D structure descriptors investigated in this chapter could not be directly linked to the species origin. A plausible cause for this could be that the necessary information needed for a reliable classification becomes buried inside the protein structure. Compared to the primary sequence-based descriptors, where each residue in the V_H and V_L domains had equal representation, in the 3D structure descriptors the species origin related residues might no longer be represented due to having been modified to conform to the solvent accessible surface area. Thus, the systematic variation related to the

species origins observed in Section 4.2.5 becomes nearly negligible when 3D structure descriptors are used.

It is important to note that there was no significant statistical difference between the means of the HIC retention time between the three species origins whereas for the mAb yields, a significant statistical difference between the means of the chimeric and humanised samples was observed (see Section 5.2.2). However, due to the lack of systematic variation present in the 3D structure descriptors related to the species origin, all 79 IgG1-kappa samples were retained for further model development presented in Table A.3 in Appendix A.

7.2.4 HIC model development on IgG1-kappa samples

The same structured approach for model benchmarking described in Chapter 5 was applied for regression fitting with regards to the HIC retention times. The CADEX algorithm was used to divide the 79 retained IgG1-kappa samples into a calibration set for training (80%) and a test set for model validation (20%). PLS and SVR were used as modelling methods. A first set of initial models was developed on all available descriptors in MSD1, MSD2 and MSD3. A second set of models was developed with collinearity reduction using the V-WSP algorithm to reduce the number of descriptors in MSD1, DS and MSD3. Lastly, a final set of models was developed on the retained descriptors from the V-WSP reduction using rPLS, LASSO and GA for variable selection to reduce the number of descriptors even further. The model quality metrics on cross validation and test set validations for all developed models are presented in Table C.7a in Appendix C. These were benchmarked according to the OECD guidelines.

Models developed on the MSD1 never attained good performance and the cross-validation of R^2 and Q^2 remained below or around 0.2 regardless of the modelling method or the level of reduction of the descriptors. Models developed on MSD2 followed a similar trend as MSD1 but had slightly increased R^2 and Q^2 values of 0.39 and 0.34, respectively, in PLS whereas values of 0.30 and 0.29 were obtained in SVR after variable selection with GA. Adequate cross-validation performance was first observed when models were developed on MSD3 in the following cases: 1) PLS model after descriptor selection with rPLS, 2) PLS model after descriptor selection with GA and 3) SVR model after descriptor selection with GA. Out of these three, only descriptor selection with GA demonstrated satisfactory performance in the external test with a R^2 and Q^2 of 0.66 and 0.65, respectively, for PLS and a R^2 and Q^2 of 0.64 and 0.63, respectively, for SVR. Neither rPLS nor LASSO performed as well as GA for variable selection on the MSD3 descriptor set. LASSO especially had poor performance in both the cross-validation and test set whereas rPLS had acceptable performance in terms of the OECD guidelines in the cross-validation but poor performance in the test set. A potential cause to this

might be due to the descriptor sets containing redundant descriptors with differing levels of collinearity toward response correlated descriptors. Especially for the LASSO algorithm to work properly, only a small degree of collinearity can exist between redundant and response correlated descriptors in order for the appropriate selection to be performed (Meinshausen and Yu, 2009). In conclusion, only the PLS and SVR models developed using MSD3 (Substructure based) and optimised with GA fulfilled the OECD criteria for both cross validation (R^2 and $Q^2 > 0.5$) and external testing (R^2 and $Q^2 > 0.6$) (Veerasamy et al., 2011, Alexander et al., 2015). Due to similar model performance, both the PLS and SVR models can be used for the prediction of HIC retention times. However, the PLS model is preferred in an industrial setting due to being more straightforward to train where only one model parameter needs to be specified. The PLS model also have stronger diagnostic capabilities where the investigation of sample and descriptor contribution towards $\boldsymbol{Y}$ is more intuitive.

The selected model was developed initially from the original 1163 descriptors available in the full MSD3 descriptor set where 319 were retained from the V-WSP reduction, thus effectively reducing the number of descriptors by ~70%. The Procrustes index was used to evaluate the loss of information when comparing the full and V-WSP reduced MSD3 descriptor sets. A value of 0.0638 was obtained, indicating that only a small fraction of the information was lost in the reduction step (Ballabio et al., 2014). This can also be observed in benchmark table for MSD3 (see Table C3.2a in Appendix C) where the of R^2 and Q^2 values in the cross validation and the test set remained mostly unchanged after the reduction. Out of the 319 remaining descriptors, GA selected a subset of 51 descriptors used to develop the final PLS model. A full list of the selected descriptors is presented in Table C.8 in Appendix C. Model predictions of the calibration samples (dark circles) and test samples (red circles) are shown in Figure 7.4a as a measured vs predicted parity plot. The test samples from Figure 7.4a are further illustrated in Figure 7.4b as a bar plot for easier comparison of the measured and predicted values for individual mAbs. The model performance is summarised in Table 7.3.

Y-Randomisation (or Y-Scrambling) was used as a final validation step to evaluate the selection of the descriptors (Rücker et al., 2007). A PLS model was trained on a randomised (scrambled) HIC response vector while the sample order in the MSD3 descriptor set was kept unchanged. This was repeated 50 times and the average of R^2 and Q^2 for the cross validation was calculated. A resulting R^2 value of 0.03 and a Q^2 value of -3.94 was obtained. This indicates that no chance correlation is captured by the model and that the selected descriptors are important to describe the relationship between the structure of the mAbs and HIC responses. The results are summarised in Table 7.3.

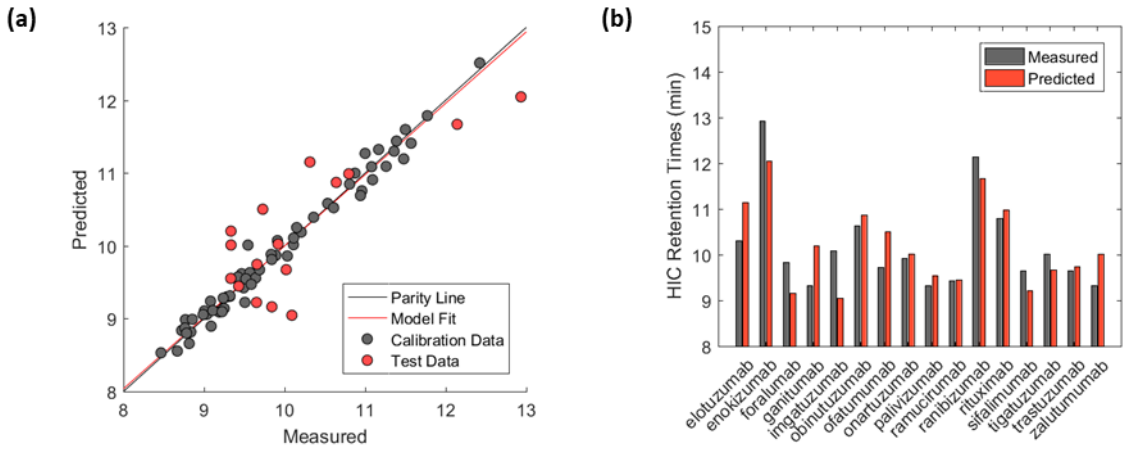

Figure 7.4. Predictions of HIC retention times with PLS-GA model developed on the MSD3 descriptor set (LVs = 9). **(a)** Measured versus predicted plot with calibration samples in black and test set samples in red. **(b)** Measured (black) and predicted (red) values of test set samples.

Table 7.3. PLS model summary developed for HIC retention time prediction using the MSD3 descriptor set. Root Mean Square Error (RMSE), R^2, Q^2 and model bias are listed for Calibration, Cross validation, Test set and Y-randomisation (Y-scrambled). The Y-randomisation metrics are the average values of 50 randomised models.

	PLS			
	RMSE	**R^2**	**Q^2**	**Bias**
Calibration	0.13	0.98	0.98	0.00
Cross Validation	0.51	0.75	0.71	0.02
Test	0.59	0.66	0.65	-0.11
Y-scrambled (Average)	2.01	0.03	-3.94	-0.01

The developed PLS model has signs of slight over-fitting when observing the calibration samples (dark) and the test set samples (red) in Figure 7.4a. The calibration samples showed a low RMSE value of 0.13 compared to the test set with an RMSE value of 0.59, which is also indicated by a greater distance of these samples from the parity line. This is an indication of over-fitting as the RMSE values between the calibration and test set should be ideally similar to each other (Lever et al., 2016). A likely reason for this is that a small number of redundant or noisy descriptors were selected by the GA algorithm to better fit the calibration samples in the cross-validation which in turn resulted in a high calibration fit with R^2 and Q^2 values of 0.98 and 0.98, respectively (Leardi, 2000). However, though not perfect, the underlaying correlation between the mAb structures and the HIC retention times has been captured by the PLS model as indicated by R^2 and Q^2 values greater than 0.6 for the test set (Veerasamy et al., 2011)

A general trend observed in the descriptors was that about 45% of all descriptor belonged to the CDR regions, 31% to the framework regions and the remaining 24% belonged to both the constant domains of C_H1 and C_L (see Table C.8 in Appendix C). This indicates the importance of the structural information contained in the variable domains. This is sensible as the CDRs are the source of the greatest sequence variability in the entire mAb structure which in turn affects surface and structure related properties of both the CDRs as well as framework regions in the variable domains (Lefranc et al., 2003). The effect will likely not be as pronounced in the constant domains of the 79 IgG1-kappa samples due to having identical primary sequence. Instead, the variability present in the 3D structure descriptors of the constant domains are likely to be related to conformational differences originating from the molecular dynamics simulations. However, it is important to note that the descriptors from the constant domains cannot be disregarded due to dynamic interactions between the constant and variable domains which in turn will affect the generated descriptors (Feige et al., 2010).

A closer inspection of the descriptors revealed that selected descriptors describing the polar surface areas (S_{polar} and $SASA_{polar}$) and non-polar surface areas ($S_{non\text{-}polar}$ and $SASA_{non\text{-}polar}$) belonged almost exclusively to the CDR regions. Representation of the volume (VOLTAE) and the electrostatic potential (SIEP) generated as part of the TAE descriptors were also commonly found belonging to the CDRs. This is consistent with published research where the CDRs have a pivotal role in binding to the HIC column resin with stronger binding usually occurring when the CDRs are long and hydrophobic (Hebditch et al., 2018).

In addition, the stability of the mAb structures played a central role for prediction of the retention times represented mostly by energy-based descriptors. 11 of the 24 GA selected energy descriptors were related to the conformational entropy $G_c(F)$, which describes the stability of the protein with regards to the hydrophobic interactions in the protein core which were selected for the CDRs, framework regions and the constant domains. Other important energy descriptors of note were the number of estimated water molecules surrounding the surface, W(F), and the interfacial free energy, ΔG_s, representing the energy contribution from interactions between polar residues and surrounding water molecules. This is supported by published literature where the protein stability has been reported to play a pivotal role in HIC binding (Beyer and Jungbauer, 2018). This is further elucidated when considering that salt is added to promote binding in HIC columns and more stable mAbs require higher concentration of salt to disrupt electrostatic forces on the surface in order to expose hydrophobic patches (Gagnon, 1996a).

In retrospect, a replacement for the TAE descriptors might help to improve model performance. This is due to the TAE descriptors consisting of static values for the individual amino acids which will be identical regardless of the environment they are in (Breneman and Rhem, 1997). Similarly, an alternative to the ProtDCal descriptors describing the energy and stability of the structure might also improve model performance due to being based on simplified empirical calculations. It was shown that they can provide a fair and often good approximation of stability energies when compared to experimental results. However, their applicability was not suited for all protein structures where large differences were observed between predicted and observed experimental energies in some cases (Ruiz-Blanco et al., 2013). A suggestion would be to perform surface properties and energy calculations directly in GROMACS or similar software as will be discussed further in Section 8.1.

7.2.5 mAb yield model development on IgG1-kappa samples

An identical benchmarking scheme as described at the start of Section 7.2.4 was performed to fit the MSD1, MSD2 and MSD3 descriptor sets to the mAb yield response. The cross validation and test set validation for all developed models are presented in Appendix C, Table C.7b. The developed models behaved similarly to the models for the prediction of the HIC retention times, where adequate performance in the cross validation was only achieved after variable selection had been performed. GA selection and rPLS achieved acceptable performance with R^2 and Q^2 greater than 0.6 for both PLS and SVR developed using MSD3 descriptor set. Selection with LASSO however suffered due to correlation between redundant and response-correlated descriptors as explained in Section 2.9.3.

Unfortunately, none of the developed models had an adequate performance in the external test set regardless of which permutation of modelling, reduction or variable selection method was used. The predictions from the PLS model developed using MSD3 and optimised with GA is illustrated in Figure 7.5a. The test samples (red circles) from Figure 7.5a are further illustrated in Figure 7.5b as a bar plot for easier comparison of the measured and predicted values for individual mAbs.It can be observed that many of the test set samples have been underpredicted which resulted in low R^2 and Q^2 values of 0.11 and -0.92, respectively. The model performance is summarised in Table 7.4.

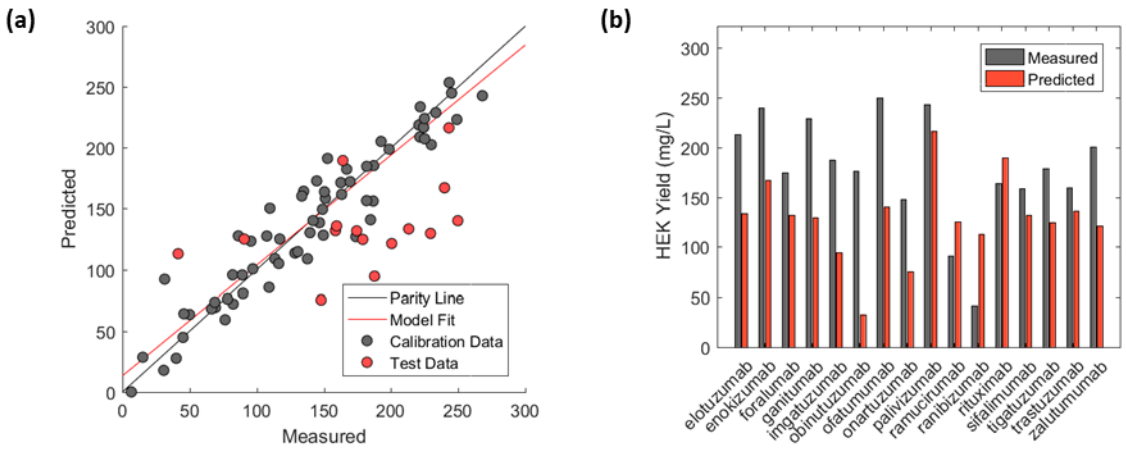

Figure 7.5. Predictions of mAb yield with a PLS-GA model developed on the MSD3 descriptor set (LVs = 3). (a) Measured versus predicted plot with calibration samples (black) and test set samples (red). (b) Measured (black) and predicted (red) values of test set samples.

Table 7.4. PLS model summary developed for mAb yield prediction using the MSD3 descriptor set. Root Mean Square Error (RMSE), R^2, Q^2 and model bias are listed for Calibration, Cross validation and Test set.

	PLS			
	RMSE	**R^2**	**Q^2**	**Bias**
Calibration	20.09	0.90	0.90	0
Cross Validation	36.42	0.69	0.68	-2.73
Test	74.25	0.11	-0.92	49.55

It is difficult to identify the true reason for the poor performance in the test set although a potential cause may be the lack of necessary variation in the data. Addition of extra samples to the data set might aid to better represent the range of ***Y*** responses, but also to introduce more structural variation in the ***X*** block. Noise and descriptor collinearity are also influencing factors in the model development where the descriptor selection methods can suffer where the wrong descriptors are selected thus leading to fitting of noise uncorrelated to the samples in the test set (Fan and Lv, 2010). A nested cross-validation approach might help in improving the model generalisation due to using all the available data but at the loss of a dedicated test set (Cawley and Talbot, 2010). Another approach would be to try ensemble techniques such as bagging or boosting where multiple models are developed on separate sample subsets which have been shown to improve model performance and generalisation (Drucker, 1997).

From a more biological perspective, transcription and translation of the heavy and light chains occurs separately within the cell which usually result in a higher concentration of light chains being expressed compared to the heavy chains. The structure of the mAbs might therefore not be directly related to the mAb yields (Bayat et al., 2018, Bhoskar et al., 2013). In Pybus et al. (2014), the authors investigated the mAb expression with regards to the corresponding mRNA

structure in CHO cells. They found that expression was significantly impacted by the stability of the mRNA structure where less stable mRNA structures resulted in lower yields. The mRNA sequence also determines which RNA codons are used during translation which has a significant impact on the expression as also reported by the authors. Optimisation of the nucleotide sequence is therefore vital in order to have an efficient expression of mAbs. The sequence variation in the variable domains has also been shown to impact expression in CHO cells which relates back to the mRNA and RNA codons (Mason et al., 2012). The sequence variation can impact the protein folding in the endoplasmic reticulum which in turn can become overloaded due to the accumulation of unfolded or misfolded proteins, thus leading to lower expression rates (Braakman and Bulleid, 2011, Stoops et al., 2012). Based on these facts, it is therefore difficult to accurately predict the yields based on the mAb structure alone, but information pertaining to the mRNA sequences would be needed as well (Pybus et al., 2014).

7.2.6 Comparison to primary sequence-based models

Initially, a model comparison for HIC retention time prediction of the developed primary sequence-based model presented in Section 5.2.3 and the developed 3D structure model presented in Section 7.2.4 was supposed to be performed with an independent external data set. Due to using CADEX, different samples were selected for the test set in the two models which meant that an unbiased evaluation using the samples from the data set provided by Jain et al. (2017) could not be performed. Instead, HIC retention times for humanised mAbs from the Advanced Manufacturing Supply Chain Initiative (AMSCI) data were supposed to be used (CPI, 2015). However, due to project time constraint and the lengthy process to draw up confidentiality agreements, the AMSCI sequences and HIC retention times could not be accessed in time and a direct comparison between the models was therefore no longer possible.

However, some conclusions regarding the applicability can be made. As was observed in Chapter 5, when all species origins were used in model development, none of the resulting models had adequate performance with regards to the OECD criteria due to poor performance in the test set (R^2 and $Q^2 < 0.6$). This was caused by the systematic variation in the primary sequence-based descriptors that originated from structural differences between the species origins which were uncorrelated to the HIC response (see Section 5.2.2). Adequate performance was not reached until only humanised samples had been selected, significantly increasing the model performance in both the cross validation and test set when primary sequence-based descriptors were used. In comparison, due to the negligible systematic variation present in the generated 3D structure descriptors from the species origins, model development could proceed with all available IgG1-kappa samples as well as achieving adequate performance in both the

cross-validation and test set (see Section 7.2.4). The use of 3D structure descriptors therefore increases the applicability of the QSAR model to the point where the species origin can be ignored. However, stronger systematic variations originating from the different mab isotypes still needs to be considered and therefore the model will only be able to predict accurately on IgG1-Kappa samples.

From the perspective of a pharmaceutical industry, neither the primary sequence-based model or the 3D structure descriptor model has adequate performance to be used as a predictive tool in QbD risk assessment as of yet. This would require a higher model performance with R^2 and Q^2 values of at least 0.8 in both the cross-validation and test set in order to decrease the offset between measured and predicted values thus increasing the confidence in the predictions. However, based on the acquired results, both the primary sequence-based descriptors and the 3D structure descriptors shows promise for further improvements. In this research, the initial descriptor sets were developed to capture a wide range of different properties and features in although the majority of these were discarded in the model optimisation with V-WSP reduction and GA selection. Further model development is therefore recommended by re-evaluating the properties of the selected descriptors in order to expand and incorporate more related structural properties and features in the descriptor sets. It is important to note that the 3D structure descriptors are more flexible than the primary sequence-based descriptors. This is due to that process related information regarding the environment e.g. temperature, pH, molality etc can be incorporated in the MD simulations and their effects on the protein structure can be approximated (see Section 6.5). This is not possible with the primary sequence-based descriptors due to being static.

7.3 Summary

In this chapter the 3D structure descriptors, developed from mAb structures simulated with GROMACS, were explored and used for the development of predictive models for the prediction of HIC retention times and mAb yields.

Exploration of the 3D structure descriptors of the light chain with PCA showed a strong correlation to the kappa and lambda isotypes which were present in all of the three generated descriptor sets. Based on previous results from the statistical hypothesis testing in Section 5.2.2, no correlation between the light chain isotypes and responses of HIC retention times as well as mAb yields could be significantly proven. As described in Section 7.1.1, modification of the heavy chain was made by Jain et al (2017) as they expressed all IgG2 and IgG4 mAbs as IgG1. If the original isotypes were preserved, though unknown, it could have potentially altered the measured experimental responses. For this reason, only IgG1 samples were selected due to the

uncertainty of the true behaviour of the IgG2 and IgG4 mAbs. Contrary to the previously explored primary sequence-based descriptors, only negligible correlation between the generated 3D structure descriptors and the species origins was observed through classification models based on PLS-DA and SVC. As a result, selection of a subset of 79 IgG1-kappa samples of all species origins from the available 128 samples was used in order to reduce harmful systematic variation uncorrelated to the response vectors as well as keeping the samples true to their original conformations.

In this chapter, it has been shown that a model for predicting the HIC retention times could be developed with 3D structure descriptors generated from the individual substructures (MSD3) of a Fab fragment. Both PLS and SVR models developed on the MSD3 descriptor set after descriptor selection with GA had similar performance, but the PLS model was selected due to more straightforward implementation. The PLS model had adequate performance in accordance with the OECD guidelines for QSAR models with a R^2 and Q^2 of 0.75 and 0.71, respectively, in the cross validation and a R^2 and Q^2 of 0.66 and 0.65, respectively, in the test set. Though not all variation was explained by the model, it provided valuable insight into important descriptors and factors affecting model performance.

No satisfactory model could be developed for the prediction of mAb yields as indicated by the signs of overfitting evidenced by the poor test set results. A potential cause could be that structural information alone might not be directly correlated to the yield and other factors related to the expression from the cell might be missing.

Unfortunately, no direct comparison could be made between the selected primary sequence-based model in Chapter 5 and the 3D structure model in this chapter for prediction of HIC retention times as explained above. However, the model developed using the 3D structure descriptors showed broader applicability due to being unconstrained in regards to the species origins. In comparison, the model developed on the primary sequence-based descriptors was trained on humanised samples only and would not be able to reliably predict retention times for chimeric and human samples. Further improvement of the developed models is still necessary in order to increase prediction accuracy prior to application in risk assessment.

Chapter 8

Conclusions and Future Work

In this project the QbD framework was reviewed due to being commonly used in process development for mAbs and provides a systematic approach to increases process understanding through characterisation of process parameters and their effect on the product quality. However, due to the numerous process parameters that need to be characterised, the QbD framework still faces challenges in implementation. Much research has been focused in areas such as high-throughput platforms and process optimisation to reduce attrition in the process development. However, it was identified that one of the biggest challenges in QbD implementation is the lack of knowledge about both the process and product in early process development where the manufacturability of an mAb might not be possible.

In the literature review, it was shown that the QSAR framework for *in silico* model development has become increasingly popular for end point predictions of protein behaviour in different unit operations. This makes the QSAR framework a potentially valuable tool which can aid risk assessment in early process development to better direct experimental designs and thus reduce costs. The use of *in silico* approaches therefore allows for more informed estimates of the potential behaviour of a mAb in different unit operations of the process. This could become possible by efficiently making use of historic prosses data from previously established mAb manufacturing processes and constructing an expert system. The integration of QSAR into the QbD framework was therefore proposed in order to increase product understanding which is especially important in early process development.

In this research, an extensive framework was developed based on QSAR in order to address the challenges facing mAb process development. The framework can roughly be divided into three parts according to: 1) Generation of descriptors relating both to the primary sequence as well as the 3D structure of mAbs. 2) Exploration and statistical assessment of generated descriptor and responses, respectively, for elimination of detrimental systematic variation. 3) Model

development and validation coupled with descriptor reduction and selection. The implementation of such frameworks is becoming increasingly important in pharmaceutical industries in order to speed up development and lower the costs of new biopharmaceuticals. Due to the shifts toward high-throughput technology that has occurred during the recent years in both upstream and downstream of the mAb process, the increased availability of process data introduces and excellent starting point for the implementation of the presented framework.

In this research, focus was placed on the development of predictive models assessing HIC retention times and mAb yields due to these important factors for protein stability and productivity assessment in process development. The highlights from the different chapters in this thesis and potential improvements are addressed according to the following areas: 1) Descriptors, 2) Sample Selection and 3) Model Development and Assessment for easier evaluation.

8.1 Descriptors

Two different approaches for generating descriptors for development of predictive models was reviewed and implemented in this project. The first approach presented in Chapter 3, used the primary sequence of the mAbs where descriptors were produced using EMBOSS Pepstats, ProtDCal and amino acid scales. These descriptors were designed to capture structural variations based on differences in amino acid compositions between mAbs. The second approach presented in Chapter 6, was based on development of 3D structure from the primary sequences. Due to the lack of published structures, homology modelling was applied to produce approximations of the 3D structures for all mAbs used in this research. Molecular Dynamics simulations was then performed to relax the homology structures. Descriptors were then developed with GROMACS and ProtDCal and captured properties related to the surface and stability of the mAbs.

In both approaches, descriptor sets of different resolutions were generated. For the primary sequence-based descriptors, the lowest resolution was attained when descriptors were calculated from all residues in an individual domain which meant that each domain could be represented individually. The highest resolution was attained when descriptors were generated for each individual residue in the primary sequence. For the 3D structure descriptors, the lowest resolution was calculated from each individual chain while the highest was calculated from the individual substructures present in the mAb structure. By comparing the different resolutions in the developed predictive models, a trade-off could be made in order to investigate the required resolution for adequate model performance. More explicitly, a too low resolution would often confound important structural properties while to high resolution would introduce

noise in the form of redundant descriptors into the developed models where in both cases lead to poor model performance.

8.1.1 Suggestion for Improvements

One of the biggest weaknesses with the generated descriptors is the absence of data on protein modifications such as the mAb glycan structure which has a major impact on the mAb stability. Due to that the upstream environment was identical for all mAbs in data set acquired from Jain et al. (2017), it was assumed that the glycan structure would be similar between the mAbs used for model development in this research. However, this assumption cannot be made in an industrial setting where the glycan structure is likely to be different between mAbs and therefore must be considered as a source of variability and represented in the modelling data.

In this research atomistic simulations using GROMACS were performed on all mAbs in order to relax the structure and capture the structure dynamics. However, as presented in Section 7.2.1, three mAbs failed to converge to a stable conformation. It was suggested that continued simulation would be necessary in order for the structure to converge to a stable conformation. In retrospect, a longer simulation time, such as 100 ns as well as multiple runs for each structure, would be beneficial for all structures as it allows for more structural variation to be captured while at the same time minimises the risk of simulations ending at conformational transition points. However, running all simulations at atomistic resolution for 50 ns takes considerable amounts of time. An alternative would be to investigate coarse-grained simulations which will run much faster due to the protein structure being simplified thus resulting in less particles in the simulation system. A comparison would need to be made to ensure that the protein dynamics of coarse-grained simulation is representative to that of the atomistic simulation in order to not bias the resulting structure. The use of coarse-grained simulation would also allow for longer simulations to be run, thus generating a stronger foundation for understanding to structure dynamics.

3D structure descriptor in this research were generated from a PDB structure acquired from a single time-frame from the MD simulation. However, due to the structure being dynamic and changing slightly over time, only using single time-frame might not accurately represent the surface and stability of the structure. An alternative would be to generate descriptors on all available time frames from when the structure has reached conformational stability to the end of the simulation and then average the descriptors over time. This would probably result in more stable and representative descriptors due to conforming to the dynamics of the mAb structure.

As mentioned earlier in Chapter 7, the calculation of energy descriptor through ProtDCal are based on simplified empirical mathematical models which might not accurately represent the environment in which the mAbs are simulated. It is therefore proposed that stability and energy related descriptors are calculated directly in GROMACS or equivalent software which can take into consideration many different interactions between the atoms in the system. GROMACS also supports energy calculations of predefined groups of residues, thus allowing for calculation of descriptors conforming to the different descriptor set resolutions presented in Chapter 6.

Though never implemented, a workflow of modifying the titration states of residues in the mAb structure as well as adding co-solvents to the system was presented in Chapter 6. It would be interesting to see how the descriptors change in response to the change in pH and co-solvent concentration. If the HIC elution curves were available for the mAbs in Jain et al. (2017) instead of just the end point retention times, several simulations with differing salt concentrations could have been performed and linked to the cumulative elution, thus expanding the data set. Alternatively, the proposed methodology could be used on published experimental data which follows DoE experimental design.

8.2 Sample Selection

Selection of samples played a critical role in the model development in order to reduce systematic variation uncorrelated to the response vectors where a structured approach for investigating sources of variation was proposed. Two sources of variation were identified early on where the first originated from the unique structures of the heavy chain isotypes IgG1, IgG2 and IgG4 whereas the second originated from the unique structure of the light chain isotype kappa and lambda. Exploration of the primary sequence-based descriptor with PCA on the gathered 273 IMGT sequences presented in Chapter 4 revealed that both the heavy and light chain isotypes had a clear and strong separation. Further analysis showed that a significant portion of the data variation in the descriptors were used to explain the observed separations. Similar results were observed when exploring the 3D structure descriptors of the 128 samples acquired from Jain et al. (2017) presented in Chapter 7, where a clear separation of light chain isotypes kappa and lambda were observed with PCA. However, due to the alteration of the heavy chain constant domains in the original mAb structures which were all expressed as IgG1, no conclusive results could be drawn regarding isotypes IgG2 and IgG4.

The statistical analysis performed in parallel on the response vectors of HIC retention times and the mAb yields from the data set provided by Jain et al. (2017) showed that no differences could be significantly proven in either of the responses when the heavy or light chain isotypes were compared. Important to note is that the statistical analysis performed on the heavy chain

isotypes was biased due to all samples being expressed as IgG1 and was therefore not likely to show a significant difference between the isotypes. However, due to the clear separation of IgG1, IgG2 and IgG4 that was observed in Chapter 4 when exploring the primary sequence-based descriptors, it was impossible to know if the unaltered mAbs would have an effect on the responses.

A similar analysis of the species origins was performed by exploring data variation in the generated descriptor correlated to that of the species origins. These analyses were performed with classification methods such as PLS-DA and SVC instead of PCA due to higher degree of variability in the explored descriptors. A strong correlation was observed between the species origins and the primary sequence-based descriptors but not with the 3D structure descriptors.

Elimination of systematic variation uncorrelated to the responses was performed by removing groups of samples belonging to a specific isotype or species origin which were strongly correlated with the descriptors but where a difference between responses could not be significantly proven in the statistical analysis. It is important to mention that the reasoning of selecting the IgG1 in this research was based on the assumption that the experimental measurements of the response vectors might have been different for the IgG2 and IgG4 samples if they were not expressed as IgG1. The IgG1 samples were therefore selected due to their heavy chain isotype not having been altered.

8.2.1 Suggestion for Improvements

Though it was never followed up due to time constraints, the good classification performance observed when predicting the species origins in Chapter 4 might be interesting to look into. It is often assumed that there is no intrinsic difference between humanised and human samples. However, the prediction accuracy was high in both the cross-validation and the test set, thus indicating that a structural difference between human and humanised samples are present.

Homology models and MD simulations of true IgG2 and IgG4 mAbs were never performed in this research. It was shown that only a negligible correlation was present between the 3D structure descriptors and the light chain isotypes. It would therefore be interesting to observe if the performance of classification models developed on a mix of IgG1, IgG2 and IgG4 mAbs where 3D structure descriptors are used as model input would be different.

8.3 Model Development and Assessment

Model development on the significantly larger data set provided by Jain et al. (2017) allowed for more advanced testing and benchmarking. In Chapter 5 and Chapter 7, predictive models for HIC retention times and mAb yields were developed with primary sequence-based

descriptors and 3D structure descriptors, respectively. Due to the larger sample sets that were retained after samples selection a dedicated test set could be used to validate the developed models properly. A model development framework was proposed for testing different permutation of modelling methods with descriptor reduction and selection methods. In this research, an initial model was developed on the full descriptor set. The unsupervised V-WSP algorithm was then applied to decrease the number of collinear descriptors where a new model was developed on the reduced descriptor set. A subsequent descriptor selection was performed on the reduced descriptor set with supervised descriptor selection techniques such as rPLS, LASSO and GA which resulted in three new models being developed. This process was performed for all available descriptor sets in order to identify needed resolution for adequate model performance in both the cross-validation and the test set. The performance of all models was evaluated based on the OECD guidelines for QSAR models.

Predictive models for HIC retention times were successfully developed for both the primary sequence-based descriptors and the 3D structure descriptors. The model developed on the 3D structure descriptors had a larger applicability due to having been trained on all chimeric, human and humanised samples and passed the OECD criteria. The model developed on the primary sequence-based descriptors was more constrained due to having been trained solely on the humanised samples due to a poor performance of the model when different samples were included into model calibration. The reason for this was due systematic variation originating from the species origins which was much more pronounced in the primary sequence-based descriptors due to capturing all information from the primary sequence. For the 3D descriptors however, due to being buried inside of the protein structure, residue related to the species origin class did not translate over to the descriptors due to their SASA values being close to zero (see Section 6.6.2). This resulted in 79 mAbs being used to train the 3D structure-based model compared to 45 mAbs being used for training the primary sequence-based model. Much more structural variability is therefore introduced in the 3D structure based-model which increases the model's robustness when predicting retention times for future samples.

In the paper of Robinson et al. (2017), a QSAR model was developed for predicting the elution salt concentration in a HIC column where the authors developed descriptors generated from 3D structures of Fab fragments which was then trained with SVR. The authors reported that a R^2 of 0.60 was observed in the cross-validation while a R^2 of 0.44 was observed in the external test set. Both the primary sequence-based model and 3D structure-based model presented in Chapter 5 and Chapter 7, respectively in this research, attained a higher R^2 in both the cross-validation and external test set compared to Robinson et al. (2017).

8.3.1 Suggestion for Improvements

In this research much focus was placed on developing a single model by splitting all available samples once into a calibration set and a test set. However, alternative training approaches for model development exist such as nested cross-validation which consist of two validation loops: an outer loop for model validation and an inner loop for model training. The available samples are often split at random in the outer loop which can be repeated any number of times and have shown to produce models with good generalisation (Raschka, 2018). Other alternatives are ensemble techniques such as bagging and boosting which have also been shown to produce models with good generalisation capabilities. A drawback with these methods is that no dedicated test set will be available to substitute as future samples.

A recommendation from Leardi (2000) was that the GA algorithm should not be used on problems with more than 200 descriptors which can result in over-fitting which was observed in the mAb yield models. A work-around would be to modify the GA algorithm to generate random descriptor subsets based on groups instead of the individual descriptors. The descriptors used in this research can all be grouped according to the structure they were generated from e.g. chain, domain, substructure etc as well as the type of the descriptor e.g. topological, energy based etc. This would not only make GA selection faster but the importance of the individual structures of the mAb as well as the descriptor types could be assessed more efficiently.

As mentioned in this research, the V-WSP algorithm was applied to reduce the number of highly correlated descriptors. The implementation however, is very dependent on the data set where the correlation thresholds were selected in order to minimise loss of information. The resulting reduction might therefore be slightly different if performed on another data set and is therefore subjective. However, in both the primary sequence-based descriptors and 3D structure descriptors, it was observed that the constant domains generally had a lower correlation threshold applied (~0.6-0.7) resulting in less descriptors being retained, while the variable domains generally had a higher correlation threshold applied (~0.8-0.9) resulting in more descriptor being retained (data not shown). A recommendation would be to use static correlation thresholds when reducing the descriptor sets based on the observed values for the constant and variable domains. This would in turn lead to a more objective reduction of descriptors regardless of the data set used.

A common problem encountered model development is that the distribution of response data if often skewed. This if often true in experimental data of mAbs where the majority of samples are well-behaved whereas only a few are flagged as problematic. The CADEX algorithm used in this research only takes into account the structural descriptors when selecting samples for

training and validation. For a more controlled selection, a stratification strategy with regards to the response distribution could be applied in order to split the distribution in to three to four equal sample sizes in which the CADEX algorithm is applied individually.

8.4 Summary

In summary, the work presented in this thesis has provided an extensive framework for generation of structural descriptor and predictive model development that can be applied for prediction of mAb behaviour in processing. As was demonstrated, successful model development was achieved for prediction of HIC retention times. Though the model performance can be further improved, it allows for further study into development of new descriptors and approaches for which several suggestions for improvement on the defined framework have been given. The framework is therefore very promising due to that only the structural information of the mAbs is needed in order to predict chromatographic behaviour. The applied descriptor generation and modelling frameworks has therefore the potential to work in other chromatographic systems such as AIEX, CEX, etc where column binding is dependent on the structural features of the mAbs, which has also been supported by literature. Therefore, continued development and implementation of the proposed framework could be used to acquire a foundation of risk assessment tools to aid in early process development of new drug candidates and used to investigate potential processing behaviour and process route selection. This has the added value of increasing the process and product understanding which can potentially lower the number of required experiments in order to characterise the process design space and in turn lower development costs. As stated by DiMasi et al. (2016), the expected total cost from clinical phase I to market release was approximated to $1.460 billion. Even if the proposed implementation of QSAR modelling into the QbD framework only reduces cost by 1-2% at minimum, this is still a reduction of $14.6-29.2 million.

A continued development and expansion of QSAR risk assessment tools, not only in process development, but for clinical safety and biological activity as well, might allow for prediction of mAb developability (Zurdo et al., 2015). This means, that based on the potential risk of a mAb candidate to fail due to lack of clinical safety, problematic in manufacture or lack of biological activity, a more informed decision can be made to either fail or proceed with the candidate. This can therefore aid in reducing attrition as well as prevent large investments from being made on mAb candidates with low developability.

References

AALBERSE, R. C. & SCHUURMAN, J. 2002. IgG4 breaking the rules. *Immunology,* 105**,** 9-19.

ABDI, H. 2007. The eigen-decomposition: Eigenvalues and eigenvectors. *Encyclopedia of measurement and statistics***,** 304-308.

ABRAHAM, M. 2014. *Steps to Perform a Simulation* [Online]. Available: http://www.gromacs.org/Documentation/How-tos/Steps_to_Perform_a_Simulation [Accessed November 7 2017].

ABRAHAM, M., VAN DER SPOEL, D., LINDAHL, E. & HESS, B. 2016. *GROMACS User Manual version 5.1.4* [Online]. Available: www.gromacs.org [Accessed May 5 2017].

ABSOLUTE ANTIBODY. 2018. *Humanization* [Online]. Available: https://absoluteantibody.com/antibody-resources/antibody-engineering/humanisation/ 2018, February].

ACTIP. 2017, May 15. *Monoclonal Antibodies Approved by the EMA and FDA for Therapeutic Use* [Online]. Available: http://www.actip.org/products/monoclonal-antibodies-approved-by-the-ema-and-fda-for-therapeutic-use/.

ADCOCK, S. A. & MCCAMMON, J. A. 2006. Molecular dynamics: survey of methods for simulating the activity of proteins. *Chem Rev,* 106**,** 1589-615.

AKBANI, R., KWEK, S. & JAPKOWICZ, N. Applying support vector machines to imbalanced datasets. European conference on machine learning, 2004. Springer, 39-50.

ALEXANDER, D., TROPSHA, A. & WINKLER, D. A. 2015. Beware of R 2: simple, unambiguous assessment of the prediction accuracy of QSAR and QSPR models. *Journal of chemical information and modeling,* 55**,** 1316-1322.

ALLEN, M. P. 2004. Introduction to molecular dynamics simulation. *In:* ATTIG, N., BINDER, K., GRUBMULLER, H. & KREMER, K. (eds.) *Computational soft matter: from synthetic polymers to proteins.* Juelich, Germany: John von Neumann Institute for Computing (NIC).

ALMAGRO, J. C., BEAVERS, M. P., HERNANDEZ-GUZMAN, F., MAIER, J., SHAULSKY, J., BUTENHOF, K., LABUTE, P., THORSTEINSON, N., KELLY, K., TEPLYAKOV, A., LUO, J., SWEET, R. & GILLILAND, G. L. 2011. Antibody modeling assessment. *Proteins,* 79**,** 3050-66.

ALT, N., ZHANG, T. Y., MOTCHNIK, P., TATICEK, R., QUARMBY, V., SCHLOTHAUER, T., BECK, H., EMRICH, T. & HARRIS, R. J. 2016. Determination of critical quality attributes for monoclonal antibodies using quality by design principles. *Biologicals,* 44**,** 291-305.

ALTSCHUL, S. F., MADDEN, T. L., SCHAFFER, A. A., ZHANG, J., ZHANG, Z., MILLER, W. & LIPMAN, D. J. 1997. Gapped BLAST and PSI-BLAST: a new generation of protein database search programs. *Nucleic Acids Res,* 25**,** 3389-402.

ANDERSEN, C. M. & BRO, R. 2010. Variable selection in regression-a tutorial. *Journal of Chemometrics,* 24**,** 728-737.

ANDERSON, T. W. & DARLING, D. A. 1952. Asymptotic theory of certain" goodness of fit" criteria based on stochastic processes. *The annals of mathematical statistics***,** 193-212.

BALLABIO, D. & CONSONNI, V. 2013. Classification tools in chemistry. Part 1: linear models. PLS-DA. *Analytical Methods,* 5**,** 3790-3798.

BALLABIO, D., CONSONNI, V., MAURI, A., CLAEYS-BRUNO, M., SERGENT, M. & TODESCHINI, R. 2014. A novel variable reduction method adapted from space-filling designs. *Chemometrics and Intelligent Laboratory Systems,* 136**,** 147-154.

BARKER, M. & RAYENS, W. 2003. Partial least squares for discrimination. *Journal of Chemometrics: A Journal of the Chemometrics Society,* 17**,** 166-173.

BAUER, K. C., HAEMMERLING, F., KITTELMANN, J., DUERR, C., GOERLICH, F. & HUBBUCH, J. 2017. Influence of structure properties on protein–protein interactions—QSAR modeling of changes in diffusion coefficients. *Biotechnology and bioengineering,* 114**,** 821-831.

BAYAT, H., HOSSIENZADEH, S., POURMALEKI, E., AHANI, R. & RAHIMPOUR, A. 2018. Evaluation of different vector design strategies for the expression of recombinant monoclonal antibody in CHO cells. *Preparative Biochemistry and Biotechnology,* 48**,** 160-164.

BERENDSEN, H. J., POSTMA, J. V., VAN GUNSTEREN, W. F., DINOLA, A. & HAAK, J. 1984. Molecular dynamics with coupling to an external bath. *The Journal of chemical physics,* 81**,** 3684-3690.

BERMAN, H. M., WESTBROOK, J., FENG, Z., GILLILAND, G., BHAT, T. N., WEISSIG, H., SHINDYALOV, I. N. & BOURNE, P. E. 2000. The Protein Data Bank. *Nucleic Acids Res,* 28**,** 235-42.

BEYER, B. & JUNGBAUER, A. 2018. Conformational changes of antibodies upon adsorption onto hydrophobic interaction chromatography surfaces. *Journal of Chromatography A,* 1552**,** 60-66.

BHAMBURE, R., KUMAR, K. & RATHORE, A. S. 2011. High-throughput process development for biopharmaceutical drug substances. *Trends in Biotechnology,* 29**,** 127-135.

BHAMBURE, R. & RATHORE, A. S. 2013. Chromatography process development in the quality by design paradigm I: Establishing a high-throughput process development platform as a tool for estimating "characterization space" for an ion exchange chromatography step. *Biotechnol Prog,* 29**,** 403-14.

BHOSKAR, P., BELONGIA, B., SMITH, R., YOON, S., CARTER, T. & XU, J. 2013. Free light chain content in culture media reflects recombinant monoclonal antibody productivity and quality. *Biotechnology progress,* 29**,** 1131-1139.

BIANCOLILLO, A. & MARINI, F. 2018. Chemometric methods for spectroscopy-based pharmaceutical analysis. *Frontiers in chemistry,* 6.

BISHOP, C. M. 2006. Introduction. *Pattern recognition and machine learning.* Springer.

BOSER, B. E., GUYON, I. M. & VAPNIK, V. N. A training algorithm for optimal margin classifiers. Proceedings of the fifth annual workshop on Computational learning theory, 1992. ACM, 144-152.

BOULIANNE, G. L., HOZUMI, N. & SHULMAN, M. J. 1984. Production of functional chimaeric mouse/human antibody. *Nature,* 312**,** 643.

BOYD, P. N., LINES, A. C. & PATEL, A. K. 1995. The effect of the removal of sialic acid, galactose and total carbohydrate on the functional activity of Campath-1H. *Molecular Immunology,* 32**,** 1311-1318.

BRAAKMAN, I. & BULLEID, N. J. 2011. Protein folding and modification in the mammalian endoplasmic reticulum. *Annual review of biochemistry,* 80**,** 71-99.

BRANDT, J. P., PATAPOFF, T. W. & ARAGON, S. R. 2010. Construction, MD simulation, and hydrodynamic validation of an all-atom model of a monoclonal IgG antibody. *Biophys J,* 99**,** 905-13.

BRENEMAN, C. M. & RHEM, M. 1997. QSPR analysis of HPLC column capacity factors for a set of high-energy materials using electronic van der waals surface property descriptors computed by transferable atom equivalent method. *Journal of computational chemistry,* 18**,** 182-197.

BRENEMAN, C. M., SUNDLING, C. M., SUKUMAR, N., SHEN, L., KATT, W. P. & EMBRECHTS, M. J. 2003. New developments in PEST shape/property hybrid descriptors. *J Comput Aided Mol Des,* 17**,** 231-40.

BRENEMAN, C. M., THOMPSON, T. R., RHEM, M. & DUNG, M. 1995. Electron-Density Modeling of Large Systems Using the Transferable Atom Equivalent Method. *Computers & Chemistry,* 19**,** 161-&.

BRERETON, R. G. & LLOYD, G. R. 2014. Partial least squares discriminant analysis: taking the magic away. *Journal of Chemometrics,* 28**,** 213-225.

BRO, R. & SMILDE, A. K. 2014. Principal component analysis. *Analytical Methods,* 6**,** 2812-2831.

BROOKS, B. R., BROOKS, C. L., 3RD, MACKERELL, A. D., JR., NILSSON, L., PETRELLA, R. J., ROUX, B., WON, Y., ARCHONTIS, G., BARTELS, C., BORESCH, S., CAFLISCH, A., CAVES, L., CUI, Q., DINNER, A. R., FEIG, M., FISCHER, S., GAO, J., HODOSCEK, M., IM, W., KUCZERA, K., LAZARIDIS, T., MA, J., OVCHINNIKOV, V., PACI, E., PASTOR, R. W., POST, C. B., PU, J. Z., SCHAEFER, M., TIDOR, B., VENABLE, R. M., WOODCOCK, H. L., WU, X., YANG, W., YORK, D. M. & KARPLUS, M. 2009. CHARMM: the biomolecular simulation program. *J Comput Chem,* 30**,** 1545-614.

BROOKS, B. R., BRUCCOLERI, R. E., OLAFSON, B. D., STATES, D. J., SWAMINATHAN, S. A. & KARPLUS, M. 1983. CHARMM: a program for macromolecular energy, minimization, and dynamics calculations. *Journal of computational chemistry,* 4**,** 187-217.

BROWN, D. & CLARKE, J. 1984. A comparison of constant energy, constant temperature and constant pressure ensembles in molecular dynamics simulations of atomic liquids. *Molecular Physics,* 51**,** 1243-1252.

BRUHLMANN, D., JORDAN, M., HEMBERGER, J., SAUER, M., STETTLER, M. & BROLY, H. 2015. Tailoring recombinant protein quality by rational media design. *Biotechnol Prog,* 31**,** 615-29.

BRYNGELSON, J. D., ONUCHIC, J. N., SOCCI, N. D. & WOLYNES, P. G. 1995. Funnels, pathways, and the energy landscape of protein folding: a synthesis. *Proteins: Structure, Function, and Bioinformatics,* 21**,** 167-195.

BUSSI, G., DONADIO, D. & PARRINELLO, M. 2007. Canonical sampling through velocity rescaling. *The Journal of chemical physics,* 126**,** 014101.

BUYEL, J. F., WOO, J. A., CRAMER, S. M. & FISCHER, R. 2013. The use of quantitative structure-activity relationship models to develop optimized processes for the removal of tobacco host cell proteins during biopharmaceutical production. *Journal of Chromatography A,* 1322**,** 18-28.

CARRONI, M. & SAIBIL, H. R. 2016. Cryo electron microscopy to determine the structure of macromolecular complexes. *Methods,* 95**,** 78-85.

CASSS & ISPE. 2009. *A-Mab: a case study in bioprocess development* [Online]. Available: http://www.casss.org/associations/9165/files/A-Mab_Case_Study_Version_2-1.pdf [Accessed 15 November 2015].

CAWLEY, G. C. & TALBOT, N. L. 2007. Preventing over-fitting during model selection via Bayesian regularisation of the hyper-parameters. *Journal of Machine Learning Research,* 8**,** 841-861.

CAWLEY, G. C. & TALBOT, N. L. 2010. On over-fitting in model selection and subsequent selection bias in performance evaluation. *Journal of Machine Learning Research,* 11**,** 2079-2107.

CHANG, C.-C. & LIN, C.-J. 2011. LIBSVM: a library for support vector machines. *ACM transactions on intelligent systems and technology (TIST),* 2**,** 27.

CHATTERJEE, S. 2012. Design Space Considerations. QbD Works.

CHEN, H., TAN, C., LIN, Z. & WU, T. 2018. Classification and quantitation of milk powder by near-infrared spectroscopy and mutual information-based variable selection and partial least squares. *Spectrochimica Acta Part A: Molecular and Biomolecular Spectroscopy,* 189**,** 183-189.

CHEN, J., YANG, T. & CRAMER, S. M. 2008. Prediction of protein retention times in gradient hydrophobic interaction chromatographic systems. *Journal of Chromatography A,* 1177**,** 207-214.

CHEN, J., YANG, T., LUO, Q., BRENEMAN, C. M. & CRAMER, S. M. 2007. Investigation of protein retention in hydrophobic interaction chromatographic (HIC) systems using the preferential interaction theory and quantitative structure property relationship models. *Reactive and Functional Polymers,* 67**,** 1561-1569.

CHERKASSKY, V. & MA, Y. 2004. Practical selection of SVM parameters and noise estimation for SVM regression. *Neural networks,* 17**,** 113-126.

CHOTHIA, C. & LESK, A. M. 1987. Canonical structures for the hypervariable regions of immunoglobulins. *J Mol Biol,* 196**,** 901-17.

CHUNG, W. K., HOU, Y., HOLSTEIN, M., FREED, A., MAKHATADZE, G. I. & CRAMER, S. M. 2010. Investigation of protein binding affinity in multimodal chromatographic systems using a homologous protein library. *Journal of Chromatography A,* 1217**,** 191-198.

COLLANTES, E. R. & DUNN, W. J. 1995. Amino-Acid Side-Chain Descriptors for Quantitative Structure-Activity Relationship Studies of Peptide Analogs. *Journal of Medicinal Chemistry*, 38**,** 2705-2713.

COONEY, B., JONES, S. D. & LEVINE, H. L. 2016. Quality By Design for Monoclonal Antibodies, Part 1: Establishing the Foundations for Process Development. *Future*.

CORNELL, W. D., CIEPLAK, P., BAYLY, C. I., GOULD, I. R., MERZ, K. M., FERGUSON, D. M., SPELLMEYER, D. C., FOX, T., CALDWELL, J. W. & KOLLMAN, P. A. 1995. A second generation force field for the simulation of proteins, nucleic acids, and organic molecules. *Journal of the American Chemical Society*, 117**,** 5179-5197.

CORRAL-CORRAL, R., BELTRAN, J. A., BRIZUELA, C. A. & DEL RIO, G. 2017. Systematic Identification of Machine-Learning Models Aimed to Classify Critical Residues for Protein Function from Protein Structure. *Molecules*, 22.

CORTES, C. & VAPNIK, V. 1995. Support-vector networks. *Machine learning*, 20**,** 273-297.

COSTA, A. R., RODRIGUES, M. E., HENRIQUES, M., OLIVEIRA, R. & AZEREDO, J. 2014. Glycosylation: impact, control and improvement during therapeutic protein production. *Crit Rev Biotechnol*, 34**,** 281-99.

CPI. 2015. *CPI led UK Biotech consortium secures £6.2m investment* [Online]. Available: https://www.uk-cpi.com/news/cpi-led-uk-biotech-consortium-secures-6-2m-government-investment.

CZARNECKI, W. M., PODLEWSKA, S. & BOJARSKI, A. J. 2015. Robust optimization of SVM hyperparameters in the classification of bioactive compounds. *Journal of cheminformatics*, 7**,** 38.

D'AGOSTINO SR, R. B. & RUSSELL, H. K. 2005. Scree test. *Encyclopedia of Biostatistics*, 7.

DE JONG, S. 1993. SIMPLS: an alternative approach to partial least squares regression. *Chemometrics and intelligent laboratory systems*, 18**,** 251-263.

DEHMER, M., VARMUZA, K., BONCHEV, D. & EBRARY ACADEMIC COMPLETE INTERNATIONAL SUBSCRIPTION COLLECTION. 2012. Statistical modelling of molecular descriptors in QSAR/QSPR. *Quantitative and network biology v 2.* Weinheim: Wiley-Blackwell,.

DEL VAL, I. J., KONTORAVDI, C. & NAGY, J. M. 2010. Towards the implementation of quality by design to the production of therapeutic monoclonal antibodies with desired glycosylation patterns. *Biotechnol Prog*, 26**,** 1505-27.

DIMASI, J. A., GRABOWSKI, H. G. & HANSEN, R. W. 2016. Innovation in the pharmaceutical industry: new estimates of R&D costs. *Journal of health economics,* 47**,** 20-33.

DOLINSKY, T. J., CZODROWSKI, P., LI, H., NIELSEN, J. E., JENSEN, J. H., KLEBE, G. & BAKER, N. A. 2007. PDB2PQR: expanding and upgrading automated preparation of biomolecular structures for molecular simulations. *Nucleic Acids Res,* 35**,** W522-5.

DOLINSKY, T. J., NIELSEN, J. E., MCCAMMON, J. A. & BAKER, N. A. 2004. PDB2PQR: an automated pipeline for the setup of Poisson-Boltzmann electrostatics calculations. *Nucleic Acids Res,* 32**,** W665-7.

DONOHO, D. L. 2000. High-dimensional data analysis: The curses and blessings of dimensionality. *AMS Math Challenges Lecture,* 1**,** 32.

DOYTCHINOVA, I. A., WALSHE, V., BORROW, P. & FLOWER, D. R. 2005. Towards the chemometric dissection of peptide - HLA-A*0201 binding affinity: comparison of local and global QSAR models. *Journal of Computer-Aided Molecular Design,* 19**,** 203-212.

DRUCKER, H. Improving regressors using boosting techniques. ICML, 1997. 107-115.

DRUCKER, H., BURGES, C. J., KAUFMAN, L., SMOLA, A. J. & VAPNIK, V. Support vector regression machines. Advances in neural information processing systems, 1997. 155-161.

DU, Q. S., HUANG, R. B. & CHOU, K. C. 2008. Recent advances in QSAR and their applications in predicting the activities of chemical molecules, peptides and proteins for drug design. *Current Protein & Peptide Science,* 9**,** 248-259.

DUDEK, A. Z., ARODZ, T. & GALVEZ, J. 2006. Computational methods in developing quantitative structure-activity relationships (QSAR): A review. *Combinatorial Chemistry & High Throughput Screening,* 9**,** 213-228.

ECKER, D. M., JONES, S. D. & LEVINE, H. L. 2015. The therapeutic monoclonal antibody market. *mAbs,* 7**,** 9-14.

EDDY, S. R. 1998. Profile hidden Markov models. *Bioinformatics,* 14**,** 755-63.

EDELMAN, G. M., CUNNINGHAM, B. A., GALL, W. E., GOTTLIEB, P. D., RUTISHAUSER, U. & WAXDAL, M. J. 1969. The covalent structure of an entire gammaG immunoglobulin molecule. *Proc Natl Acad Sci U S A,* 63**,** 78-85.

EON-DUVAL, A., BROLY, H. & GLEIXNER, R. 2012. Quality attributes of recombinant therapeutic proteins: an assessment of impact on safety and efficacy as part of a quality by design development approach. *Biotechnol Prog,* 28**,** 608-22.

EUROPEAN MEDICINES AGENCY 2016. Guideline on development, production, characterisation and specification for monoclonal antibodies and related products. Committee for medicinal products for human use (CHMP).

EVALUATEPHARMA® 2018. *World Preview (2018) Outlook to 2024*, EvaluatePharma®.

EVANS, R., JUMPER, J., KIRKPATRICK, J., SIFRE, L., GREEN, T., QIN, C., ZIDEK, A., NELSON, A., BRIDGLAND, A. & PENEDONES, H. 2018. De Novo structure prediction with deep-learning based scoring. *Thirteenth Critical Assessment of Techniques for Protein Structure Prediction (Abstracts)*.

FABER, N. M. & RAJKO, R. 2007. How to avoid over-fitting in multivariate calibration - The conventional validation approach and an alternative. *Analytica Chimica Acta,* 595**,** 98-106.

FAN, J. & LV, J. 2010. A selective overview of variable selection in high dimensional feature space. *Statistica Sinica,* 20**,** 101.

FARID, S. S. 2007. Process economics of industrial monoclonal antibody manufacture. *Journal of Chromatography B-Analytical Technologies in the Biomedical and Life Sciences,* 848**,** 8-18.

FARRES, M., PLATIKANOV, S., TSAKOVSKI, S. & TAULER, R. 2015. Comparison of the variable importance in projection (VIP) and of the selectivity ratio (SR) methods for variable selection and interpretation. *Journal of Chemometrics,* 29**,** 528-536.

FAWCETT, T. 2006. An introduction to ROC analysis. *Pattern recognition letters,* 27**,** 861-874.

FEIGE, M. J., HENDERSHOT, L. M. & BUCHNER, J. 2010. How antibodies fold. *Trends in biochemical sciences,* 35**,** 189-198.

FERNANDEZ-FUENTES, N., RAI, B. K., MADRID-ALISTE, C. J., FAJARDO, J. E. & FISER, A. 2007. Comparative protein structure modeling by combining multiple templates and optimizing sequence-to-structure alignments. *Bioinformatics,* 23**,** 2558-65.

FERRARA, C., GRAU, S., JAGER, C., SONDERMANN, P., BRUNKER, P., WALDHAUER, I., HENNIG, M., RUF, A., RUFER, A. C., STIHLE, M., UMANA, P. & BENZ, J. 2011. Unique carbohydrate-carbohydrate interactions are required for high affinity binding between Fc gamma RIII and antibodies lacking core fucose. *Proceedings of the National Academy of Sciences of the United States of America,* 108**,** 12669-12674.

FERREIRA, A. P. & TOBYN, M. 2015. Multivariate analysis in the pharmaceutical industry: enabling process understanding and improvement in the PAT and QbD era. *Pharmaceutical development and technology,* 20**,** 513-527.

FISCHER, S., HANDRICK, R. & OTTE, K. 2015. The art of CHO cell engineering: A comprehensive retrospect and future perspectives. *Biotechnology Advances,* 33**,** 1878-1896.

FISER, A. 2010. Template-based protein structure modeling. *Methods Mol Biol,* 673**,** 73-94.

FISHER, R. A. 1992. Statistical methods for research workers. *Breakthroughs in statistics.* Springer.

GAGNON, P. 1996a. Hydrophobic Interaction Chromatography. *Purification tools for monoclonal antibodies.* (Tucson) Arizona: Validated Biosystems Inc.

GAGNON, P. 1996b. *Purification tools for monoclonal antibodies,* (Tucson) Arizona, Validated Biosystems Inc.

GALAR, M., FERNÁNDEZ, A., BARRENECHEA, E., BUSTINCE, H. & HERRERA, F. 2011. An overview of ensemble methods for binary classifiers in multi-class problems: Experimental study on one-vs-one and one-vs-all schemes. *Pattern Recognition,* 44**,** 1761-1776.

GASTEIGER, E., HOOGLAND, C., GATTIKER, A., DUVAUD, S. E., WILKINS, M. R., APPEL, R. D. & BAIROCH, A. 2005. *Protein identification and analysis tools on the ExPASy server*, Springer.

GELADI, P. & KOWALSKI, B. R. 1986. Partial least-squares regression: a tutorial. *Analytica chimica acta*, 185**,** 1-17.

GHIRINGHELLI, L. 2014. *Statistical Mechanics and Molecular Dynamics* [Online]. Institute for Pure & Applied Mathematics (IPAM) at UCLA. Available: http://helper.ipam.ucla.edu/publications/gss2014/gss2014_12140.pdf [Accessed November 2 2018].

GHOSE, S., TAO, Y., CONLEY, L. & CECCHINI, D. Purification of monoclonal antibodies by hydrophobic interaction chromatography under no-salt conditions. MAbs, 2013. Taylor & Francis, 795-800.

GLASSEY, J., GERNAEY, K. V., CLEMENS, C., SCHULZ, T. W., OLIVEIRA, R., STRIEDNER, G. & MANDENIUS, C. F. 2011. Process analytical technology (PAT) for biopharmaceuticals. *Biotechnology Journal,* 6**,** 369-377.

GLASSEY, J. & VON STOSCH, M. 2018. *Hybrid Modeling in Process Industries,* CRC Press.

GOLABGIR, A., HOCH, T., ZHARIY, M. & HERWIG, C. 2015. Observability analysis of biochemical process models as a valuable tool for the development of mechanistic soft sensors. *Biotechnol Prog,* 31**,** 1703-15.

GONZÁLEZ, M. 2011. Force fields and molecular dynamics simulations. *École thématique de la Société Française de la Neutronique,* 12**,** 169-200.

GORODKIN, J. 2004. Comparing two K-category assignments by a K-category correlation coefficient. *Computational biology and chemistry,* 28**,** 367-374.

GRAINGER, R. K. & JAMES, D. C. 2013. CHO cell line specific prediction and control of recombinant monoclonal antibody N-glycosylation. *Biotechnol Bioeng,* 110**,** 2970-83.

GREEN, A. & GLASSEY, J. 2015. Multivariate analysis of the effect of operating conditions on hybridoma cell metabolism and glycosylation of produced antibody. *Journal of Chemical Technology and Biotechnology,* 90**,** 303-313.

GREEN, L. L., HARDY, M. C., MAYNARD-CURRIE, C. E., TSUDA, H., LOUIE, D. M., MENDEZ, M. J., ABDERRAHIM, H., NOGUCHI, M., SMITH, D. H., ZENG, Y., DAVID, N. E., SASAI, H., GARZA, D., BRENNER, D. G., HALES, J. F., MCGUINNESS, R. P., CAPON, D. J., KLAPHOLZ, S. & JAKOBOVITS, A. 1994. Antigen-specific human monoclonal antibodies from mice engineered with human Ig heavy and light chain YACs. *Nat Genet,* 7**,** 13-21.

GRILO, A. L. & MANTALARIS, A. 2019. The increasingly human and profitable monoclonal antibody market. *Trends in biotechnology,* 37**,** 9-16.

GROMSKI, P. S., MUHAMADALI, H., ELLIS, D. I., XU, Y., CORREA, E., TURNER, M. L. & GOODACRE, R. 2015. A tutorial review: Metabolomics and partial least squares-discriminant analysis–a marriage of convenience or a shotgun wedding. *Analytica chimica acta,* 879**,** 10-23.

GUNTHER, J. C., SEBORG, D. E. & BACLASKI, J. 2006. Fault detection and diagnosis in industrial fed-batch fermentation. *2006 American Control Conference***,** 6.

HAMMERSCHMIDT, N., TSCHELIESSNIG, A., SOMMER, R., HELK, B. & JUNGBAUER, A. 2014. Economics of recombinant antibody production processes at various scales: Industry-standard compared to continuous precipitation. *Biotechnology Journal,* 9**,** 766-775.

HANSEL, T. T., KROPSHOFER, H., SINGER, T., MITCHELL, J. A. & GEORGE, A. J. 2010. The safety and side effects of monoclonal antibodies. *Nat Rev Drug Discov,* 9**,** 325-38.

HARMS, J., WANG, X., KIM, T., YANG, X. & RATHORE, A. S. 2008. Defining process design space for biotech products: case study of Pichia pastoris fermentation. *Biotechnol Prog,* 24**,** 655-62.

HASTIE, T., TIBSHIRANI, R. & FRIEDMAN, J. 2009a. Model assessment and selection. *The elements of statistical learning.* 2nd ed.: Springer.

HASTIE, T., TIBSHIRANI, R. & FRIEDMAN, J. 2009b. Support vector machines and flexible discriminants. *The elements of statistical learning.* 2nd ed.: Springer.

HAVERICK, M., MENGISEN, S., SHAMEEM, M. & AMBROGELLY, A. Separation of mAbs molecular variants by analytical hydrophobic interaction chromatography HPLC: overview and applications. MAbs, 2014. Taylor & Francis, 852-858.

HEATH, A. P., KAVRAKI, L. E. & CLEMENTI, C. 2007. From coarse-grain to all-atom: toward multiscale analysis of protein landscapes. *Proteins,* 68**,** 646-61.

HEBDITCH, M., ROCHE, A., CURTIS, R. A. & WARWICKER, J. 2018. Models for Antibody Behavior in Hydrophobic Interaction Chromatography and in Self-Association. *Journal of pharmaceutical sciences,* 108(4)**,** 1434-1441.

HECHINGER, M., LEONHARD, K. & MARQUARDT, W. 2012. What is Wrong with Quantitative Structure-Property Relations Models Based on Three-Dimensional Descriptors? *Journal of Chemical Information and Modeling,* 52**,** 1984-1993.

HELLBERG, S., SJOSTROM, M., SKAGERBERG, B. & WOLD, S. 1987a. Peptide Quantitative Structure-Activity-Relationships, a Multivariate Approach. *Journal of Medicinal Chemistry,* 30**,** 1126-1135.

HELLBERG, S., SJOSTROM, M., SKAGERBERG, B. & WOLD, S. 1987b. Peptide quantitative structure-activity relationships, a multivariate approach. *J Med Chem,* 30**,** 1126-35.

HELLBERG, S., SJOSTROM, M. & WOLD, S. 1986. The prediction of bradykinin potentiating potency of pentapeptides. An example of a peptide quantitative structure-activity relationship. *Acta Chem Scand B,* 40**,** 135-40.

HENIKOFF, S. & HENIKOFF, J. G. 1992. Amino acid substitution matrices from protein blocks. *Proc Natl Acad Sci U S A,* 89**,** 10915-9.

HENZLER-WILDMAN, K. & KERN, D. 2007. Dynamic personalities of proteins. *Nature,* 450**,** 964-72.

HERWIG, C., GARCIA-APONTE, O. F., GOLABGIR, A. & RATHORE, A. S. 2015. Knowledge management in the QbD paradigm: manufacturing of biotech therapeutics. *Trends Biotechnol,* 33**,** 381-7.

HOCKNEY, R. W. & EASTWOOD, J. W. 1988. *Computer simulation using particles*, CRC Press.

HOOVER, W. G. 1985. Canonical dynamics: Equilibrium phase-space distributions. *Phys Rev A Gen Phys,* 31**,** 1695-1697.

HOTELLING, H. 1933. Analysis of a complex of statistical variables into principal components. *Journal of educational psychology,* 24**,** 417.

HOU, Y., JIANG, C. P., SHUKLA, A. A. & CRAMER, S. M. 2011. Improved Process Analytical Technology for Protein A Chromatography Using Predictive Principal Component Analysis Tools. *Biotechnology and Bioengineering,* 108**,** 59-68.

HSU, C.-W., CHANG, C.-C. & LIN, C.-J. 2003. *A practical guide to support vector classification* [Online]. Department of Computer Science and Information Engineering, National Taiwan University, Taipei, Taiwan. Available: https://www.csie.ntu.edu.tw/~cjlin/papers/guide/guide.pdf.

HSU, C. W. & LIN, C. J. 2002. A comparison of methods for multiclass support vector machines. *IEEE transactions on Neural Networks,* 13**,** 415-425.

HWANG, W. Y. & FOOTE, J. 2005. Immunogenicity of engineered antibodies. *Methods,* 36**,** 3-10.

ICH HARMONISED TRIPARTITE GUIDELINE. 1997a. *General considerations for clinical trials - E8* [Online]. International Conference on Harmonization of Technical Requirements for Registration of Pharmaceuticals for Human Use. Available: https://www.ich.org/fileadmin/Public_Web_Site/ICH_Products/Guidelines/Efficacy/E8/Step4/E8_Guideline.pdf.

ICH HARMONISED TRIPARTITE GUIDELINE. 1997b. *Viral safety evaluation of biotechnology products derived from cell lines of human or animal origin - Q5A(R1)* [Online]. International Conference on Harmonization of Technical Requirements for Registration of Pharmaceuticals for Human Use. Available: http://www.gmp-compliance.org/guidemgr/files/MEDIA425.PDF.

ICH HARMONISED TRIPARTITE GUIDELINE. 2005. *Quality Risk Management - Q9* [Online]. International Conference on Harmonization of Technical Requirements for Registration of Pharmaceuticals for Human Use. Available: http://www.ich.org/fileadmin/Public_Web_Site/ICH_Products/Guidelines/Quality/Q9/Step4/Q9_Guideline.pdf.

ICH HARMONISED TRIPARTITE GUIDELINE. 2008. *Pharmaceutical Quality Systems - Q10* [Online]. International Conference on Harmonization of Technical Requirements for Registration of Pharmaceuticals for Human Use. Available: http://www.ich.org/fileadmin/Public_Web_Site/ICH_Products/Guidelines/Quality/Q10/Step4/Q10_Guideline.pdf.

ICH HARMONISED TRIPARTITE GUIDELINE. 2009. *Pharmaceutical Development - Q8(R2)* [Online]. International Conference on Harmonization of Technical Requirements for Registration of Pharmaceuticals for Human Use. Available:

http://www.ich.org/fileadmin/Public_Web_Site/ICH_Products/Guidelines/Quality/Q8_R1/Step4/Q8_R2_Guideline.pdf.

INDAHL, U. G., MARTENS, H. & NÆS, T. 2007. From dummy regression to prior probabilities in PLS-DA. *Journal of Chemometrics: A Journal of the Chemometrics Society,* 21**,** 529-536.

INSAIDOO, F. K., RAUSCHER, M. A., SMITHLINE, S. J., KAARSHOLM, N. C., FEUSTON, B. P., ORTIGOSA, A. D., LINDEN, T. O. & ROUSH, D. J. 2015. Targeted Purification Development Enabled by Computational Biophysical Modeling. *Biotechnology Progress,* 31**,** 154-164.

INTERNATIONAL UNION OF CRYSTALLOGRAPHY. 2017. *R-Factor* [Online]. International Union of Crystallography,. Available: http://reference.iucr.org/dictionary/R_factor 2018].

IVARSSON, M., NOH, H., MORBIDELLI, M. & SOOS, M. 2015. Insights into pH-induced metabolic switch by flux balance analysis. *Biotechnol Prog,* 31**,** 347-57.

JAIN, T., SUN, T., DURAND, S., HALL, A., HOUSTON, N. R., NETT, J. H., SHARKEY, B., BOBROWICZ, B., CAFFRY, I., YU, Y., CAO, Y., LYNAUGH, H., BROWN, M., BARUAH, H., GRAY, L. T., KRAULAND, E. M., XU, Y., VASQUEZ, M. & WITTRUP, K. D. 2017. Biophysical properties of the clinical-stage antibody landscape. *Proc Natl Acad Sci U S A,* 114**,** 944-949.

JANEWAY JR, C. A., TRAVERS, P., WALPORT, M. & SHLOMCHIK, M. J. 2001. The structure of a typical antibody molecule. *In:* JANEWAY JR, C. A., TRAVERS, P., WALPORT, M. & SHLOMCHIK, M. J. (eds.) *Immunobiology: The Immune System in Health and Disease.* 5 ed. New York: Garland Science.

JIANG, W. L., KIM, S., ZHANG, X. Y., LIONBERGER, R. A., DAVIT, B. M., CONNER, D. P. & YU, L. X. 2011. The role of predictive biopharmaceutical modeling and simulation in drug development and regulatory evaluation. *International Journal of Pharmaceutics,* 418**,** 151-160.

JOHNSON, M., ZARETSKAYA, I., RAYTSELIS, Y., MEREZHUK, Y., MCGINNIS, S. & MADDEN, T. L. 2008. NCBI BLAST: a better web interface. *Nucleic Acids Res,* 36**,** W5-9.

JONES, J. E. 1924. On the determination of molecular fields.—II. From the equation of state of a gas. *Proc. R. Soc. Lond. A,* 106**,** 463-477.

JONES, P. T., DEAR, P. H., FOOTE, J., NEUBERGER, M. S. & WINTER, G. 1986. Replacing the complementarity-determining regions in a human antibody with those from a mouse. *Nature,* 321**,** 522.

JORGENSEN, W. L., MAXWELL, D. S. & TIRADO-RIVES, J. 1996. Development and testing of the OPLS all-atom force field on conformational energetics and properties of organic liquids. *Journal of the American Chemical Society,* 118**,** 11225-11236.

JUNG, D. & ALT, F. W. 2004. Unraveling V(D)J recombination; insights into gene regulation. *Cell,* 116**,** 299-311.

JURMAN, G., RICCADONNA, S. & FURLANELLO, C. 2012. A comparison of MCC and CEN error measures in multi-class prediction. *PloS one,* 7**,** e41882.

KARLBERG, M., VON STOSCH, M. & GLASSEY, J. 2018. Exploiting mAb structure characteristics for a directed QbD implementation in early process development. *Critical reviews in biotechnology,* 38**,** 957-970.

KARST, D. J., STEINEBACH, F., SOOS, M. & MORBIDELLI, M. 2017. Process performance and product quality in an integrated continuous antibody production process. *Biotechnology and bioengineering,* 114**,** 298-307.

KENDALL, D. G. 1989. A survey of the statistical theory of shape. *Statistical Science***,** 87-99.

KENNARD, R. W. & STONE, L. A. 1969. Computer aided design of experiments. *Technometrics,* 11**,** 137-148.

KENNEDY, R. M. 1990. [27] Hydrophobic chromatography. *Methods in enzymology*. Elsevier.

KERN, G. & KRISHNAN, M. 2006. Virus removal by filtration: points to consider. *BioPharm Int,* 19**,** 32-41.

KHALAF, R., HEYMANN, J., LESAOUT, X., MONARD, F., COSTIOLI, M. & MORBIDELLI, M. 2016. Model-based high-throughput design of ion exchange protein chromatography. *J Chromatogr A,* 1459**,** 67-77.

KHAWLI, L. A., GOSWAMI, S., HUTCHINSON, R., KWONG, Z. W., YANG, J., WANG, X., YAO, Z., SREEDHARA, A., CANO, T. & TESAR, D. B. Charge variants in IgG1: Isolation, characterization, in vitro binding properties and pharmacokinetics in rats. MAbs, 2010. Taylor & Francis, 613-624.

KIDERA, A., KONISHI, Y., OKA, M., OOI, T. & SCHERAGA, H. A. 1985. Statistical-Analysis of the Physical-Properties of the 20 Naturally-Occurring Amino-Acids. *Journal of Protein Chemistry,* 4**,** 23-55.

KILDEGAARD, H. F., FAN, Y. Z., SEN, J. W., LARSEN, B. & ANDERSEN, M. R. 2016. Glycoprofiling Effects of Media Additives on IgG Produced by CHO Cells in Fed-Batch Bioreactors. *Biotechnology and Bioengineering,* 113**,** 359-366.

KIM, S. J., PARK, Y. & HONG, H. J. 2005. Antibody engineering for the development of therapeutic antibodies. *Molecules & Cells (Springer Science & Business Media BV),* 20.

KITTELMANN, J., LANG, K. M., OTTENS, M. & HUBBUCH, J. 2017. Orientation of monoclonal antibodies in ion-exchange chromatography: A predictive quantitative structure–activity relationship modeling approach. *Journal of Chromatography A,* 1510**,** 33-39.

KIZHEDATH, A., WILKINSON, S. & GLASSEY, J. 2017. Applicability of predictive toxicology methods for monoclonal antibody therapeutics: status Quo and scope. *Arch Toxicol,* 91**,** 1595-1612.

KJELDAHL, K. & BRO, R. 2010. Some common misunderstandings in chemometrics. *Journal of Chemometrics,* 24**,** 558-564.

KMIECIK, S., GRONT, D., KOLINSKI, M., WIETESKA, L., DAWID, A. E. & KOLINSKI, A. 2016. Coarse-grained protein models and their applications. *Chemical reviews,* 116**,** 7898-7936.

KORTKHONJIA, E., BRANDMAN, R., ZHOU, J. Z., VOELZ, V. A., CHORNY, I., KABAKOFF, B., PATAPOFF, T. W., DILL, K. A. & SWARTZ, T. E. 2013. Probing antibody internal dynamics with fluorescence anisotropy and molecular dynamics simulations. *mAbs,* 5**,** 306-22.

KRISHNAN, V. & RUPP, B. 2012. Macromolecular structure determination: Comparison of x-ray crystallography and nmr spectroscopy. *eLS (John Wiley & Sons Ltd, Chichester, 2012). http://www. els. net. doi,* 10**,** a0002716.

KRUMMEN, L. 2013. Lessons Learned from Two Case Studies in the FDA QBD Biotech Pilot. *Case study presentation at CMC Forum Europe 2013*.

KRZYWINSKI, M. & ALTMAN, N. 2014a. Points of significance: Analysis of variance and blocking. *Nature Methods,* 11**,** 699–700.

KRZYWINSKI, M. & ALTMAN, N. 2014b. Points of significance: nonparametric tests. *Nature Methods,* 11**,** 467–468.

KUHN, H. W. & TUCKER, A. W. 2014. Nonlinear programming. *Traces and emergence of nonlinear programming.* Springer.

KUMAR, V., BHALLA, A. & RATHORE, A. S. 2014. Design of Experiments Applications in Bioprocessing: Concepts and Approach. *Biotechnology Progress,* 30**,** 86-99.

KUNERT, R. & REINHART, D. 2016. Advances in recombinant antibody manufacturing. *Applied microbiology and biotechnology,* 100**,** 3451-3461.

LADIWALA, A., REGE, K., BRENEMAN, C. M. & CRAMER, S. M. 2003. Investigation of mobile phase salt type effects on protein retention and selectivity in cation-exchange systems using quantitative structure retention relationship models. *Langmuir,* 19**,** 8443-8454.

LADIWALA, A., REGE, K., BRENEMAN, C. M. & CRAMER, S. M. 2005. A priori prediction of adsorption isotherm parameters and chromatographic behavior in ion-exchange systems. *Proceedings of the National Academy of Sciences of the United States of America,* 102**,** 11710-11715.

LADIWALA, A., XIA, F., LUO, Q., BRENEMAN, C. M. & CRAMER, S. M. 2006. Investigation of protein retention and selectivity in HIC systems using quantitative structure retention relationship models. *Biotechnology and bioengineering,* 93**,** 836-850.

LAFFLEUR, B., PASCAL, V., SIRAC, C. & COGNÉ, M. 2012. Production of human or humanized antibodies in mice. *Antibody Methods and Protocols.* Springer.

LARSON, S. C. 1931. The shrinkage of the coefficient of multiple correlation. *Journal of Educational Psychology,* 22**,** 45.

LAUER, T. M., AGRAWAL, N. J., CHENNAMSETTY, N., EGODAGE, K., HELK, B. & TROUT, B. L. 2012. Developability index: a rapid in silico tool for the screening of antibody aggregation propensity. *Journal of pharmaceutical sciences,* 101**,** 102-115.

LE, H., KABBUR, S., POLLASTRINI, L., SUN, Z., MILLS, K., JOHNSON, K., KARYPIS, G. & HU, W. S. 2012. Multivariate analysis of cell culture bioprocess data--lactate consumption as process indicator. *J Biotechnol,* 162**,** 210-23.

LEACH, A. R. 2001a. Computer Simulation Methods. *Molecular modelling: principles and applications.* 2nd ed. Harlow, England: Pearson Education Ltd.

LEACH, A. R. 2001b. Emperical Force Field Models: Molecular Mechanics. *Molecular modelling: principles and applications.* 2nd ed. Harlow, England: Pearson Education Ltd.

LEACH, A. R. 2001c. Energy Minimisation and Related Methods for Exploring the Energy Surface. *Molecular modelling: principles and applications.* 2nd ed. Harlow, England: Pearson Education Ltd.

LEACH, A. R. 2001d. An Introduction to Computational Quantum Mechanics. *Molecular modelling: principles and applications.* 2nd ed. Harlow, England: Pearson Education Ltd.

LEACH, A. R. 2001e. Monte Carlo Simulation Methods. *Molecular modelling: principles and applications.* 2nd ed. Harlow, England: Pearson Education Ltd.

LEARDI, R. 2000. Application of genetic algorithm–PLS for feature selection in spectral data sets. *Journal of Chemometrics,* 14**,** 643-655.

LEARDI, R. 2007. Genetic algorithms in chemistry. *Journal of Chromatography A,* 1158**,** 226-233.

LEARDI, R. 2009. Experimental design in chemistry: A tutorial. *Anal Chim Acta,* 652**,** 161-72.

LEE, J., FREDDOLINO, P. L. & ZHANG, Y. 2017. Ab initio protein structure prediction. *From protein structure to function with bioinformatics.* Springer.

LEFRANC, M.-P. & LEFRANC, G. 2012. Human Gm, Km, and Am allotypes and their molecular characterization: a remarkable demonstration of polymorphism. *Immunogenetics.* Springer.

LEFRANC, M. P., POMMIE, C., KAAS, Q., DUPRAT, E., BOSC, N., GUIRAUDOU, D., JEAN, C., RUIZ, M., DA PIEDADE, I., ROUARD, M., FOULQUIER, E., THOUVENIN, V. & LEFRANC, G. 2005. IMGT unique numbering for immunoglobulin and T cell receptor constant domains and Ig superfamily C-like domains. *Dev Comp Immunol,* 29**,** 185-203.

LEFRANC, M. P., POMMIE, C., RUIZ, M., GIUDICELLI, V., FOULQUIER, E., TRUONG, L., THOUVENIN-CONTET, V. & LEFRANC, G. 2003. IMGT unique numbering for immunoglobulin and T cell receptor variable domains and Ig superfamily V-like domains. *Dev Comp Immunol,* 27**,** 55-77.

LEVER, J., KRZYWINSKI, M. & ALTMAN, N. 2016. Points of significance: model selection and overfitting. *Nature Methods,* 13**,** 703-704.

LEVITT, M. 1992. Accurate modeling of protein conformation by automatic segment matching. *J Mol Biol,* 226**,** 507-33.

LI, W., COWLEY, A., ULUDAG, M., GUR, T., MCWILLIAM, H., SQUIZZATO, S., PARK, Y. M., BUSO, N. & LOPEZ, R. 2015. The EMBL-EBI bioinformatics web and programmatic tools framework. *Nucleic acids research,* 43**,** W580-W584.

LI, W., PRABAKARAN, P., CHEN, W., ZHU, Z., FENG, Y. & DIMITROV, D. S. 2016. Antibody aggregation: insights from sequence and structure. *Antibodies,* 5**,** 19.

LI, Z. & EASTON, R. Practical considerations in clinical strategy to support the development of injectable drug-device combination products for biologics. mAbs, 2018. Taylor & Francis, 18-33.

LIAO, C., SITZMANN, M., PUGLIESE, A. & NICKLAUS, M. C. 2011. Software and resources for computational medicinal chemistry. *Future Med Chem,* 3**,** 1057-85.

LINDORFF-LARSEN, K., PIANA, S., PALMO, K., MARAGAKIS, P., KLEPEIS, J. L., DROR, R. O. & SHAW, D. E. 2010. Improved side-chain torsion potentials for the Amber ff99SB protein force field. *Proteins: Structure, Function, and Bioinformatics,* 78**,** 1950-1958.

LIU, H., ELSTNER, M., KAXIRAS, E., FRAUENHEIM, T., HERMANS, J. & YANG, W. 2001. Quantum mechanics simulation of protein dynamics on long timescale. *Proteins,* 44**,** 484-9.

LIU, H. & MAY, K. 2012. Disulfide bond structures of IgG molecules: structural variations, chemical modifications and possible impacts to stability and biological function. *mAbs,* 4**,** 17-23.

LIU, H. F., MA, J., WINTER, C. & BAYER, R. Recovery and purification process development for monoclonal antibody production. MAbs, 2010. Taylor & Francis, 480-499.

LOUKATOU, S., PAPAGEORGIOU, L., FAKOURELIS, P., FILNTISI, A., POLYCHRONIDOU, E., BASSIS, I., MEGALOOIKONOMOU, V., MAKAŁOWSKI, W., VLACHAKIS, D. & KOSSIDA, S. 2014. Molecular dynamics simulations through GPU video games technologies. *Journal of molecular biochemistry,* 3**,** 64.

MACARTHUR, R. H. 1957. On the relative abundance of bird species. *Proceedings of the National Academy of Sciences of the United States of America,* 43**,** 293.

MALDONADO, S. & WEBER, R. 2009. A wrapper method for feature selection using support vector machines. *Information Sciences,* 179**,** 2208-2217.

MALMQUIST, G., NILSSON, U. H., NORRMAN, M., SKARP, U., STRÖMGREN, M. & CARREDANO, E. 2006. Electrostatic calculations and quantitative protein retention models for ion exchange chromatography. *Journal of Chromatography A,* 1115**,** 164-186.

MARCATILI, P., OLIMPIERI, P. P., CHAILYAN, A. & TRAMONTANO, A. 2014. Antibody modeling using the Prediction of ImmunoGlobulin Structure (PIGS) web server. *Nature protocols,* 9**,** 2771.

MARINI, F. 2017. *Discrimination and classification in nir spectroscopy* [Online]. Heliospir. Available: http://www.heliospir.net/medias/upload/files/18RENC.comMarini.pdf.

MARRINK, S. J. & TIELEMAN, D. P. 2013. Perspective on the Martini model. *Chem Soc Rev,* 42**,** 6801-22.

MARTI-RENOM, M. A., STUART, A. C., FISER, A., SANCHEZ, R., MELO, F. & SALI, A. 2000. Comparative protein structure modeling of genes and genomes. *Annu Rev Biophys Biomol Struct,* 29**,** 291-325.

MARTIN, T. M., HARTEN, P., YOUNG, D. M., MURATOV, E. N., GOLBRAIKH, A., ZHU, H. & TROPSHA, A. 2012. Does rational selection of training and test sets improve the outcome of QSAR modeling? *Journal of Chemical Information and Modeling,* 52**,** 2570-2578.

MARTINEZ-ROSELL, G., GIORGINO, T. & DE FABRITIIS, G. 2017. PlayMolecule ProteinPrepare: A Web Application for Protein Preparation for Molecular Dynamics Simulations. *J Chem Inf Model,* 57**,** 1511-1516.

MASON, M., SWEENEY, B., CAIN, K., STEPHENS, P. & SHARFSTEIN, S. T. 2012. Identifying bottlenecks in transient and stable production of recombinant monoclonal-antibody sequence variants in Chinese hamster ovary cells. *Biotechnology progress,* 28**,** 846-855.

MATTILA, J., CLARK, M., LIU, S., PIERACCI, J., GERVAIS, T. R., WILSON, E., GALPERINA, O., LI, X., ROUSH, D. & ZOELLER, K. 2016. Retrospective evaluation of low-pH viral inactivation and viral filtration data from a multiple company collaboration. *PDA journal of pharmaceutical science and technology,* 70**,** 293-299.

MAY, A., POOL, R., VAN DIJK, E., BIJLARD, J., ABELN, S., HERINGA, J. & FEENSTRA, K. A. 2013. Coarse-grained versus atomistic simulations: realistic interaction free energies for real proteins. *Bioinformatics,* 30**,** 326-334.

MAZZA, C. B., SUKUMAR, N., BRENEMAN, C. M. & CRAMER, S. 2001. Prediction of protein retention in ion-exchange systems using molecular descriptors obtained from crystal structure. *Analytical chemistry,* 73**,** 5457-5461.

MAZZER, A. R., PERRAUD, X., HALLEY, J., O'HARA, J. & BRACEWELL, D. G. 2015. Protein A chromatography increases monoclonal antibody aggregation rate during subsequent low pH virus inactivation hold. *Journal of Chromatography A,* 1415**,** 83-90.

MCWILLIAM, H., LI, W., ULUDAG, M., SQUIZZATO, S., PARK, Y. M., BUSO, N., COWLEY, A. P. & LOPEZ, R. 2013. Analysis Tool Web Services from the EMBL-EBI. *Nucleic Acids Res,* 41**,** W597-600.

MEINSHAUSEN, N. & YU, B. 2009. Lasso-type recovery of sparse representations for high-dimensional data. *The Annals of Statistics,* 37**,** 246-270.

MERCIER, S. M., DIEPENBROEK, B., DALM, M. C., WIJFFELS, R. H. & STREEFLAND, M. 2013. Multivariate data analysis as a PAT tool for early bioprocess development data. *J Biotechnol,* 167**,** 262-70.

MERCIER, S. M., DIEPENBROEK, B., WIJFFELS, R. H. & STREEFLAND, M. 2014. Multivariate PAT solutions for biopharmaceutical cultivation: current progress and limitations. *Trends in Biotechnology,* 32**,** 329-336.

MERK, A., BARTESAGHI, A., BANERJEE, S., FALCONIERI, V., RAO, P., DAVIS, M. I., PRAGANI, R., BOXER, M. B., EARL, L. A., MILNE, J. L. S. & SUBRAMANIAM, S. 2016. Breaking Cryo-EM Resolution Barriers to Facilitate Drug Discovery. *Cell,* 165**,** 1698-1707.

MOE 2018. Chemical Computing Group ULC. 1010 Sherbooke St. West, Suite #910, Montreal, QC, Canada, H3A 2R7.

MOMPO, S. M. & GONZALEZ-FERNANDEZ, A. 2014. Antigen-specific human monoclonal antibodies from transgenic mice. *Methods Mol Biol,* 1060**,** 245-76.

NIAZI, A. & LEARDI, R. 2012. Genetic algorithms in chemometrics. *Journal of Chemometrics,* 26**,** 345-351.

NOSÉ, S. 1984. A unified formulation of the constant temperature molecular dynamics methods. *The Journal of chemical physics,* 81**,** 511-519.

O'BOYLE, N. M., BANCK, M., JAMES, C. A., MORLEY, C., VANDERMEERSCH, T. & HUTCHISON, G. R. 2011. Open Babel: An open chemical toolbox. *J Cheminform,* 3**,** 33.

O'MALLEY, C. J. 2008. *Information extraction for enhanced bioprocess development.* UCL (University College London).

O'KENNEDY, R. D. 2016. Multivariate analysis of biological additives for growth media and feeds. *BioProcess Int,* 14.

OBREZANOVA, O., ARNELL, A., DE LA CUESTA, R. G., BERTHELOT, M. E., GALLAGHER, T. R. A., ZURDO, J. & STALLWOOD, Y. 2015. Aggregation risk prediction for antibodies and its application to biotherapeutic development. *mAbs,* 7**,** 352-363.

OLSSON, M. H., SONDERGAARD, C. R., ROSTKOWSKI, M. & JENSEN, J. H. 2011. PROPKA3: Consistent Treatment of Internal and Surface Residues in Empirical pKa Predictions. *J Chem Theory Comput,* 7**,** 525-37.

OOSTENBRINK, C., VILLA, A., MARK, A. E. & VAN GUNSTEREN, W. F. 2004. A biomolecular force field based on the free enthalpy of hydration and solvation: the GROMOS force-field parameter sets 53A5 and 53A6. *J Comput Chem,* 25**,** 1656-76.

OTAKI, J. M., TSUTSUMI, M., GOTOH, T. & YAMAMOTO, H. 2010. Secondary structure characterization based on amino acid composition and availability in proteins. *J Chem Inf Model,* 50**,** 690-700.

PANDEY, H. M., CHAUDHARY, A. & MEHROTRA, D. 2014. A comparative review of approaches to prevent premature convergence in GA. *Applied Soft Computing,* 24**,** 1047-1077.

PARRINELLO, M. & RAHMAN, A. 1981. Polymorphic transitions in single crystals: A new molecular dynamics method. *Journal of Applied physics,* 52**,** 7182-7190.

PEARSON, K. 1901. LIII. On lines and planes of closest fit to systems of points in space. *The London, Edinburgh, and Dublin Philosophical Magazine and Journal of Science,* 2**,** 559-572.

PEARSON, W. R. 1998. Empirical statistical estimates for sequence similarity searches. *J Mol Biol,* 276**,** 71-84.

PENCE, H. E. & WILLIAMS, A. 2010. ChemSpider: an online chemical information resource. ACS Publications.

PERES-NETO, P. R. & JACKSON, D. A. 2001. How well do multivariate data sets match? The advantages of a Procrustean superimposition approach over the Mantel test. *Oecologia,* 129**,** 169-178.

PEREZ, D. R. & NARASIMHAN 2018. So you think you know PLS-DA? *bioRxiv*.

PÉREZ, N. F., FERRÉ, J. & BOQUÉ, R. 2009. Calculation of the reliability of classification in discriminant partial least-squares binary classification. *Chemometrics and Intelligent Laboratory Systems,* 95**,** 122-128.

PETTERSEN, E. F., GODDARD, T. D., HUANG, C. C., COUCH, G. S., GREENBLATT, D. M., MENG, E. C. & FERRIN, T. E. 2004. UCSF Chimera--a visualization system for exploratory research and analysis. *J Comput Chem,* 25**,** 1605-12.

PHILLIPS, J. C., BRAUN, R., WANG, W., GUMBART, J., TAJKHORSHID, E., VILLA, E., CHIPOT, C., SKEEL, R. D., KALE, L. & SCHULTEN, K. 2005. Scalable molecular dynamics with NAMD. *J Comput Chem,* 26**,** 1781-802.

PLATT, J. 1998. Sequential minimal optimization: A fast algorithm for training support vector machines.

POVEY, J. F., O'MALLEY, C. J., ROOT, T., MARTIN, E. B., MONTAGUE, G. A., FEARY, M., TRIM, C., LANG, D. A., ALLDREAD, R. & RACHER, A. J. 2014. Rapid high-throughput characterisation, classification and selection of recombinant mammalian cell line phenotypes using intact cell MALDI-ToF mass spectrometry fingerprinting and PLS-DA modelling. *Journal of biotechnology,* 184**,** 84-93.

PYBUS, L. P., JAMES, D. C., DEAN, G., SLIDEL, T., HARDMAN, C., SMITH, A., DARAMOLA, O. & FIELD, R. 2014. Predicting the expression of recombinant monoclonal antibodies in Chinese hamster ovary cells based on sequence features of the CDR3 domain. *Biotechnology progress,* 30**,** 188-197.

RAJPAL, A., STROP, P., YEUNG, Y. A., CHAPARRO-RIGGERS, J. & PONS, J. 2014. Introduction: Antibody structure and function. *Therapeutic Fc-Fusion Proteins***,** 1-44.

RAJU, T. S. & JORDAN, R. E. 2012. Galactosylation variations in marketed therapeutic antibodies. *Mabs,* 4**,** 385-391.

RASCHKA, S. 2018. Model evaluation, model selection, and algorithm selection in machine learning. *arXiv preprint arXiv:1811.12808*.

RATHORE, A. S. 2009. Roadmap for implementation of quality by design (QbD) for biotechnology products. *Trends Biotechnol,* 27**,** 546-53.

RATHORE, A. S. 2014. QbD/PAT for bioprocessing: moving from theory to implementation. *Current Opinion in Chemical Engineering,* 6**,** 1-8.

RATHORE, A. S. 2016. Quality by design (QbD)-based process development for purification of a biotherapeutic. *Trends in biotechnology,* 34**,** 358-370.

RATHORE, A. S., KUMAR SINGH, S., PATHAK, M., READ, E. K., BRORSON, K. A., AGARABI, C. D. & KHAN, M. 2015. Fermentanomics: Relating Quality Attributes of a Monoclonal Antibody to Cell Culture Process Variables and Raw Materials Using Multivariate Data Analysis. *Biotechnology Progress,* 31**,** 1586-1599.

RATHORE, A. S., SINGH, S. K., KUMAR, J. & KAPOOR, G. 2018. Implementation of QbD for Manufacturing of Biologics—Has It Met the Expectations? *Biopharmaceutical Processing.* Elsevier.

RATHORE, A. S. & WINKLE, H. 2009. Quality by design for biopharmaceuticals. *Nature Biotechnology,* 27**,** 26-34.

RAUSCHER, S., GAPSYS, V., GAJDA, M. J., ZWECKSTETTER, M., DE GROOT, B. L. & GRUBMÜLLER, H. 2015. Structural ensembles of intrinsically disordered proteins depend strongly on force field: a comparison to experiment. *Journal of chemical theory and computation,* 11**,** 5513-5524.

READ, E. K., PARK, J. T., SHAH, R. B., RILEY, B. S., BRORSON, K. A. & RATHORE, A. S. 2010. Process Analytical Technology (PAT) for Biopharmaceutical Products: Part I. Concepts and Applications. *Biotechnology and Bioengineering,* 105**,** 276-284.

REICHERT, J. M. Marketed therapeutic antibodies compendium. MAbs, 2012. Taylor & Francis, 413-415.

RIFKIN, R. M. 2002. *Everything old is new again: a fresh look at historical approaches in machine learning.* MaSSachuSettS InStitute of Technology.

RINNAN, A., ANDERSSON, M., RIDDER, C. & ENGELSEN, S. B. 2014. Recursive weighted partial least squares (rPLS): an efficient variable selection method using PLS. *Journal of Chemometrics,* 28**,** 439-447.

ROBINSON, J. R., KARKOV, H. S., WOO, J. A., KROGH, B. O. & CRAMER, S. M. 2017. QSAR models for prediction of chromatographic behavior of homologous Fab variants. *Biotechnology and bioengineering,* 114**,** 1231-1240.

RODRIGUES DE AZEVEDO, C., VON STOSCH, M., COSTA, M. S., RAMOS, A. M., CARDOSO, M. M., DANHIER, F., PREAT, V. & OLIVEIRA, R. 2017. Modeling of the burst release from PLGA micro- and nanoparticles as function of physicochemical parameters and formulation characteristics. *Int J Pharm,* 532**,** 229-240.

ROSASCO, L., VITO, E. D., CAPONNETTO, A., PIANA, M. & VERRI, A. 2004. Are loss functions all the same? *Neural Computation,* 16**,** 1063-1076.

ROST, B. 1999. Twilight zone of protein sequence alignments. *Protein Eng,* 12**,** 85-94.

ROUET, R., LOWE, D. & CHRIST, D. 2014. Stability engineering of the human antibody repertoire. *FEBS letters,* 588**,** 269-277.

ROUILLER, Y., BIELSER, J. M., BRUHLMANN, D., JORDAN, M., BROLY, H. & STETTLER, M. 2016. Screening and assessment of performance and molecule quality attributes of industrial cell lines across different fed-batch systems. *Biotechnol Prog,* 32**,** 160-70.

ROUILLER, Y., PERILLEUX, A., COLLET, N., JORDAN, M., STETTLER, M. & BROLY, H. 2013. A high-throughput media design approach for high performance mammalian fed-batch cultures. *mAbs,* 5**,** 501-11.

ROUILLER, Y., PERILLEUX, A., VESIN, M. N., STETTLER, M., JORDAN, M. & BROLY, H. 2014. Modulation of mAb quality attributes using microliter scale fed-batch cultures. *Biotechnol Prog,* 30**,** 571-83.

RÜCKER, C., RÜCKER, G. & MERINGER, M. 2007. y-Randomization and its variants in QSPR/QSAR. *Journal of chemical information and modeling,* 47**,** 2345-2357.

RUIZ-BLANCO, Y. B., MARRERO-PONCE, Y., GARCIA-HERNANDEZ, E. & GREEN, J. 2017. Novel "extended sequons" of human N-glycosylation sites improve the precision of qualitative predictions: an alignment-free study of pattern recognition using ProtDCal protein features. *Amino Acids,* 49**,** 317-325.

RUIZ-BLANCO, Y. B., MARRERO-PONCE, Y., PAZ, W., GARCÍA, Y. & SALGADO, J. 2013. Global stability of protein folding from an empirical free energy function. *Journal of theoretical biology,* 321**,** 44-53.

RUIZ-BLANCO, Y. B., PAZ, W., GREEN, J. & MARRERO-PONCE, Y. 2015. ProtDCal: A program to compute general-purpose-numerical descriptors for sequences and 3D-structures of proteins. *BMC Bioinformatics,* 16**,** 162.

RUSTICUS, S. A. & LOVATO, C. Y. 2014. Impact of sample size and variability on the power and type I error rates of equivalence tests: A simulation study. *Practical Assessment, Research & Evaluation,* 19**,** 2.

SADOWSKI, M. I., GRANT, C. & FELL, T. S. 2016. Harnessing QbD, Programming Languages, and Automation for Reproducible Biology. *Trends Biotechnol,* 34**,** 214-27.

SALI, A. 1995. Comparative protein modeling by satisfaction of spatial restraints. *Mol Med Today,* 1**,** 270-7.

SALOMON-FERRER, R., CASE, D. A. & WALKER, R. C. 2013. An overview of the Amber biomolecular simulation package. *Wiley Interdisciplinary Reviews: Computational Molecular Science,* 3**,** 198-210.

SANCHEZ, R. & SALI, A. 1998. Large-scale protein structure modeling of the Saccharomyces cerevisiae genome. *Proc Natl Acad Sci U S A,* 95**,** 13597-602.

SANDBERG, M., ERIKSSON, L., JONSSON, J., SJOSTROM, M. & WOLD, S. 1998. New chemical descriptors relevant for the design of biologically active peptides. A multivariate characterization of 87 amino acids. *Journal of Medicinal Chemistry,* 41**,** 2481-2491.

SCHLICK, T. 1992. Optimization methods in computational chemistry. *In:* LIPOKOWITZ, K. & BOYD, D. (eds.) *Reviews in computational chemistry.* John Wiley & Sons.

SCHROEDER, H. W., JR. & CAVACINI, L. 2010. Structure and function of immunoglobulins. *J Allergy Clin Immunol,* 125**,** S41-52.

SCOTT, K. A., ALONSO, D. O., SATO, S., FERSHT, A. R. & DAGGETT, V. 2007. Conformational entropy of alanine versus glycine in protein denatured states. *Proceedings of the National Academy of Sciences,* 104**,** 2661-2666.

SEDGWICK, P. 2014. Multiple hypothesis testing and Bonferroni's correction. *BMJ: British Medical Journal (Online),* 349.

SHAHROKH, E., MOHAMMAD & DOUGHERTY, E. R. 2013. Effect of separate sampling on classification accuracy. *Bioinformatics,* 30**,** 242-250.

SHARMA, V. K., PATAPOFF, T. W., KABAKOFF, B., PAI, S., HILARIO, E., ZHANG, B., LI, C., BORISOV, O., KELLEY, R. F., CHORNY, I., ZHOU, J. Z., DILL, K. A. & SWARTZ, T. E. 2014. In silico selection of therapeutic antibodies for development: viscosity, clearance, and chemical stability. *Proc Natl Acad Sci U S A,* 111**,** 18601-6.

SHAWE-TAYLOR, J. & CRISTIANINI, N. 2004. Properties of kernels. *Kernel methods for pattern analysis.* Cambridge university press.

SHEN, M. Y. & SALI, A. 2006. Statistical potential for assessment and prediction of protein structures. *Protein Sci,* 15**,** 2507-24.

SHEVADE, S. K., KEERTHI, S. S., BHATTACHARYYA, C. & MURTHY, K. R. K. 2000. Improvements to the SMO algorithm for SVM regression. *IEEE transactions on neural networks,* 11**,** 1188-1193.

SHUKLA, A. A., HUBBARD, B., TRESSEL, T., GUHAN, S. & LOW, D. 2007. Downstream processing of monoclonal antibodies—application of platform approaches. *Journal of Chromatography B,* 848**,** 28-39.

SHUKLA, A. A., WOLFE, L. S., MOSTAFA, S. S. & NORMAN, C. 2017. Evolving trends in mAb production processes. *Bioengineering & translational medicine,* 2**,** 58-69.

SILVA, J. P., VETTERLEIN, O., JOSE, J., PETERS, S. & KIRBY, H. 2015. The S228P mutation prevents in vivo and in vitro IgG4 Fab-arm exchange as demonstrated using a combination of novel quantitative immunoassays and physiological matrix preparation. *J Biol Chem,* 290**,** 5462-9.

SIRCAR, A., KIM, E. T. & GRAY, J. J. 2009. RosettaAntibody: antibody variable region homology modeling server. *Nucleic Acids Res,* 37**,** W474-9.

SIVASUBRAMANIAN, A., SIRCAR, A., CHAUDHURY, S. & GRAY, J. J. 2009. Toward high-resolution homology modeling of antibody Fv regions and application to antibody-antigen docking. *Proteins,* 74**,** 497-514.

SNEATH, P. H. 1966. Relations between chemical structure and biological activity in peptides. *J Theor Biol,* 12**,** 157-95.

SNOEK, J., LAROCHELLE, H. & ADAMS, R. P. 2012. Practical bayesian optimization of machine learning algorithms. *Advances in neural information processing systems***,** 2951-2959.

SOKAL, R. R. & ROHLF, F. J. 1969. *The principles and practice of statistics in biological research*, WH Freeman and company San Francisco:.

SOKOLOV, M., RITSCHER, J., MACKINNON, N., BIELSER, J. M., BRUHLMANN, D., ROTHENHAUSLER, D., THANEI, G., SOOS, M., STETTLER, M., SOUQUET, J., BROLY, H., MORBIDELLI, M. & BUTTE, A. 2016. Robust factor selection in early cell culture process development for the production of a biosimilar monoclonal antibody. *Biotechnol Prog*.

SONDERGAARD, C. R., OLSSON, M. H., ROSTKOWSKI, M. & JENSEN, J. H. 2011. Improved Treatment of Ligands and Coupling Effects in Empirical Calculation and Rationalization of pKa Values. *J Chem Theory Comput,* 7**,** 2284-95.

SONG, M., BRENEMAN, C. M., BI, J., SUKUMAR, N., BENNETT, K. P., CRAMER, S. & TUGCU, N. 2002. Prediction of protein retention times in anion-exchange chromatography systems using support vector regression. *Journal of chemical information and computer sciences,* 42**,** 1347-1357.

SOUSA DA SILVA, A. W. & VRANKEN, W. F. 2012. ACPYPE - AnteChamber PYthon Parser interfacE. *BMC Res Notes,* 5**,** 367.

STATNIKOV, A., ALIFERIS, C. F., TSAMARDINOS, I., HARDIN, D. & LEVY, S. 2004. A comprehensive evaluation of multicategory classification methods for microarray gene expression cancer diagnosis. *Bioinformatics,* 21**,** 631-643.

STEINWART, I. & THOMANN, P. 2017. liquidSVM: A fast and versatile SVM package. *arXiv preprint arXiv:1702.06899*.

STOOPS, J., BYRD, S. & HASEGAWA, H. 2012. Russell body inducing threshold depends on the variable domain sequences of individual human IgG clones and the cellular protein homeostasis. *Biochimica et Biophysica Acta (BBA)-Molecular Cell Research,* 1823**,** 1643-1657.

SUTCLIFFE, M. J., HANEEF, I., CARNEY, D. & BLUNDELL, T. L. 1987. Knowledge based modelling of homologous proteins, Part I: Three-dimensional frameworks derived from the simultaneous superposition of multiple structures. *Protein Eng,* 1**,** 377-84.

SWOPE, W. C., ANDERSEN, H. C., BERENS, P. H. & WILSON, K. R. 1982. A computer simulation method for the calculation of equilibrium constants for the formation of physical clusters of molecules: Application to small water clusters. *The Journal of Chemical Physics,* 76**,** 637-649.

SYDOW, J. F., LIPSMEIER, F., LARRAILLET, V., HILGER, M., MAUTZ, B., MOLHOJ, M., KUENTZER, J., KLOSTERMANN, S., SCHOCH, J., VOELGER, H. R., REGULA, J. T., CRAMER, P., PAPADIMITRIOU, A. & KETTENBERGER, H. 2014. Structure-based prediction of asparagine and aspartate degradation sites in antibody variable regions. *PLoS One,* 9**,** e100736.

TAI, M., LY, A., LEUNG, I. & NAYAR, G. 2015. Efficient high-throughput biological process characterization: Definitive screening design with the Ambr250 bioreactor system. *Biotechnology Progress,* 31**,** 1388-1395.

TAYLOR, W. R. 1986. The classification of amino acid conservation. *J Theor Biol,* 119**,** 205-18.

TIAN, F. F., ZHOU, P. & LI, Z. L. 2007. T-scale as a novel vector of topological descriptors for amino acids and its application in QSARs of peptides. *Journal of Molecular Structure,* 830**,** 106-115.

TIEN, M. Z., MEYER, A. G., SYDYKOVA, D. K., SPIELMAN, S. J. & WILKE, C. O. 2013. Maximum allowed solvent accessibilites of residues in proteins. *PLoS One,* 8**,** e80635.

TILLER, K. E. & TESSIER, P. M. 2015. Advances in antibody design. *Annual review of biomedical engineering,* 17**,** 191-216.

TREXLER-SCHMIDT, M., SZE-KHOO, S., COTHRAN, A. R., THAI, B. Q., SARGIS, S., LEBRETON, B., KELLEY, B. & BLANK, G. S. 2009. Purification strategies to process 5 g/L titers of monoclonal antibodies. *BioPharm Intl Supplement March***,** 8-15.

TRYGG, J. & WOLD, S. 2002. Orthogonal projections to latent structures (O-PLS). *Journal of Chemometrics: A Journal of the Chemometrics Society,* 16**,** 119-128.

TUGCU, N., SONG, M. H., BRENEMAN, C. M., SUKUMAR, N., BENNETT, K. P. & CRAMER, S. M. 2003. Prediction of the effect of mobile-phase salt type on protein retention and selectivity in anion exchange systems. *Analytical Chemistry,* 75**,** 3563-3572.

U.S. DEPARTMENT OF OF HEALTH AND HUMAN SERVICES, FOOD AND DRUG ADMINISTRATION 2004. Guidance for Industry PAT — A Framework for Innovative Pharmaceutical Development, Manufacturing, and Quality Assurance

VAN DEN BERG, R. A., HOEFSLOOT, H. C., WESTERHUIS, J. A., SMILDE, A. K. & VAN DER WERF, M. J. 2006. Centering, scaling, and transformations: improving the biological information content of metabolomics data. *BMC genomics,* 7**,** 142.

VAN DER SPOEL, D., LINDAHL, E., HESS, B., GROENHOF, G., MARK, A. E. & BERENDSEN, H. J. 2005. GROMACS: fast, flexible, and free. *J Comput Chem,* 26**,** 1701-18.

VAN WESTEN, G. J. P., SWIER, R. F., CORTES-CIRIANO, I., WEGNER, J. K., OVERINGTON, J. P., IJZERMAN, A. P., VAN VLIJMEN, H. W. T. & BENDER, A. 2013a. Benchmarking of protein descriptor sets in proteochemometric modeling (part 2): modeling performance of 13 amino acid descriptor sets. *Journal of Cheminformatics,* 5.

VAN WESTEN, G. J. P., SWIER, R. F., WEGNER, J. K., IJZERMAN, A. P., VAN VLIJMEN, H. W. T. & BENDER, A. 2013b. Benchmarking of protein descriptor sets in proteochemometric modeling (part 1): comparative study of 13 amino acid descriptor sets. *Journal of Cheminformatics,* 5.

VAPNIK, V. & LERNER, A. Y. 1963. Recognition of patterns with help of generalized portraits. *Avtomat. i Telemekh,* 24**,** 774-780.

VEERASAMY, R., RAJAK, H., JAIN, A., SIVADASAN, S., VARGHESE, C. P. & AGRAWAL, R. K. 2011. Validation of QSAR models-strategies and importance. *International Journal of Drug Design & Discovery,* 3**,** 511-519.

VENCLOVAS, Č. 2011. Methods for sequence–structure alignment. *Homology Modeling.* Springer.

VERLET, L. 1968. Computer" experiments" on classical fluids. II. equilibrium correlation functions. *Physical Review,* 165**,** 201.

VIDARSSON, G., DEKKERS, G. & RISPENS, T. 2014. IgG subclasses and allotypes: from structure to effector functions. *Front Immunol,* 5**,** 520.

VON STOSCH, M., OLIVEIRA, R., PERES, J. & DE AZEVEDO, S. F. 2014. Hybrid semi-parametric modeling in process systems engineering: past, present and future. *Computers & Chemical Engineering,* 60**,** 86-101.

WALL, M. E., RECHTSTEINER, A. & ROCHA, L. M. 2003. Singular value decomposition and principal component analysis. *A practical approach to microarray data analysis.* Springer.

WANG, J., WOLF, R. M., CALDWELL, J. W., KOLLMAN, P. A. & CASE, D. A. 2004. Development and testing of a general amber force field. *Journal of computational chemistry,* 25**,** 1157-1174.

WANG, S., LIU, A. P., YAN, Y., DALY, T. J. & LI, N. 2018. Characterization of product-related low molecular weight impurities in therapeutic monoclonal antibodies using hydrophilic interaction chromatography coupled with mass spectrometry. *Journal of pharmaceutical and biomedical analysis,* 154**,** 468-475.

WEBB, B. & SALI, A. 2014. Comparative protein structure modeling using MODELLER. *Current protocols in bioinformatics,* 47**,** 5.6. 1-5.6. 32.

WESTERHUIS, J. A., HOEFSLOOT, H. C., SMIT, S., VIS, D. J., SMILDE, A. K., VAN VELZEN, E. J., VAN DUIJNHOVEN, J. P. & VAN DORSTEN, F. A. 2008. Assessment of PLSDA cross validation. *Metabolomics,* 4**,** 81-89.

WHITELEGG, N. R. & REES, A. R. 2000. WAM: an improved algorithm for modelling antibodies on the WEB. *Protein Eng,* 13**,** 819-24.

WOLD, S., ANTTI, H., LINDGREN, F. & ÖHMAN, J. 1998. Orthogonal signal correction of near-infrared spectra. *Chemometrics and Intelligent laboratory systems,* 44**,** 175-185.

WOLD, S., RUHE, A., WOLD, H. & DUNN, I., WJ 1984. The collinearity problem in linear regression. The partial least squares (PLS) approach to generalized inverses. *SIAM Journal on Scientific and Statistical Computing,* 5**,** 735-743.

WOLD, S., SJÖSTRÖM, M. & ERIKSSON, L. 2001. PLS-regression: a basic tool of chemometrics. *Chemometrics and intelligent laboratory systems,* 58**,** 109-130.

WONG, T.-T. 2015. Performance evaluation of classification algorithms by k-fold and leave-one-out cross validation. *Pattern Recognition,* 48**,** 2839-2846.

WOO, J., PARIMAL, S., BROWN, M. R., HEDEN, R. & CRAMER, S. M. 2015a. The effect of geometrical presentation of multimodal cation-exchange ligands on selective

recognition of hydrophobic regions on protein surfaces. *Journal of Chromatography a,* 1412**,** 33-42.

WOO, J. A., CHEN, H., SNYDER, M. A., CHAI, Y., FROST, R. G. & CRAMER, S. M. 2015b. Defining the property space for chromatographic ligands from a homologous series of mixed-mode ligands. *Journal of Chromatography A,* 1407**,** 58-68.

YAMASHITA, T. 2018. Toward rational antibody design: recent advancements in molecular dynamics simulations. *International immunology,* 30**,** 133-140.

YANG, T., BRENEMAN, C. M. & CRAMER, S. M. 2007a. Investigation of multi-modal high-salt binding ion-exchange chromatography using quantitative structure-property relationship modeling. *Journal of Chromatography A,* 1175**,** 96-105.

YANG, T., SUNDLING, M. C., FREED, A. S., BRENEMAN, C. M. & CRAMER, S. M. 2007b. Prediction of pH-dependent chromatographic behavior in ion-exchange systems. *Analytical Chemistry,* 79**,** 8927-8939.

YANG, X., XU, W., DUKLESKA, S., BENCHAAR, S., MENGISEN, S., ANTOCHSHUK, V., CHEUNG, J., MANN, L., BABADJANOVA, Z. & ROWAND, J. Developability studies before initiation of process development: improving manufacturability of monoclonal antibodies. MAbs, 2013. Taylor & Francis, 787-794.

ZALAI, D., DIETZSCH, C. & HERWIG, C. 2013. Risk-based Process Development of Biosimilars as Part of the Quality by Design Paradigm. *PDA J Pharm Sci Technol,* 67**,** 569-80.

ZALAI, D., GOLABGIR, A., WECHSELBERGER, P., PUTICS, A. & HERWIG, C. 2015. Advanced Development Strategies for Biopharmaceutical Cell Culture Processes. *Curr Pharm Biotechnol,* 16**,** 983-1001.

ZALIANI, A. & GANCIA, E. 1999. MS-WHIM scores for amino acids: A new 3D-description for peptide QSAR and QSPR studies. *Journal of Chemical Information and Computer Sciences,* 39**,** 525-533.

ZHANG, X., WU, Y., WANG, L. & LI, R. 2016. Variable selection for support vector machines in moderately high dimensions. *Journal of the Royal Statistical Society: Series B (Statistical Methodology),* 78**,** 53-76.

ZHAO, P. & YU, B. 2006. On model selection consistency of Lasso. *Journal of Machine learning research,* 7**,** 2541-2563.

ZHENG, K., BANTOG, C. & BAYER, R. 2011. The impact of glycosylation on monoclonal antibody conformation and stability. *mAbs,* 3**,** 568-576.

ZHOU, P., CHEN, X., WU, Y. Q. & SHANG, Z. C. 2010. Gaussian process: an alternative approach for QSAM modeling of peptides. *Amino Acids,* 38**,** 199-212.

ZHOU, P., TIAN, F. F., WU, Y. Q., LI, Z. L. & SHANG, Z. C. 2008. Quantitative Sequence-Activity Model (QSAM): Applying QSAR Strategy to Model and Predict Bioactivity and Function of Peptides, Proteins and Nucleic Acids. *Current Computer-Aided Drug Design,* 4**,** 311-321.

ZHU, J., ROSSET, S., TIBSHIRANI, R. & HASTIE, T. J. 1-norm support vector machines. Advances in neural information processing systems, 2004. 49-56.

ZIMMERMANN, H. F. & HENTSCHEL, N. 2011. Proposal on How To Conduct a Biopharmaceutical Process Failure Mode and Effect Analysis (FMEA) as a Risk Assessment Tool. *PDA J Pharm Sci Technol,* 65**,** 506-12.

ZURDO, J. 2013. Surviving the valley of death. *Eur Biopharmaceutical Rev,* 195**,** 50-4.

ZURDO, J., ARNELL, A., OBREZANOVA, O., SMITH, N., DE LA CUESTA, R. G., GALLAGHER, T. R. A., MICHAEL, R., STALLWOOD, Y., EKBLAD, C., ABRAHMSEN, L. & HOIDEN-GUTHENBERG, I. 2015. Early Implementation of QbD in Biopharmaceutical Development: A Practical Example. *Biomed Research International*.

Appendix A

A.1 Marketed mAbs

Table A.1. List of market approved and withdrawn mAbs in the EU and the US between 1986-2017 with their corresponding approval years from EMA and FDA, respectively. mAbs highlighted in blue are biosimilars.

Trade Name	INN	EMA Approval	FDA Approval	Comment
Amjevita	adalimumab	2017	2016	Biosimilar, same as Humira
Cyltezo	adalimumab	2017	2017	Biosimilar, same as Humira
Imraldi	adalimumab	2017	Not approved	Biosimilar, same as Humira
Zinplava	bezlotoxumab	2017	2016	
Bavencio	avelumab	Not approved	2017	
Dupixent	dupilumab	Not approved	2017	
Imfinzi	durvalumab	Not approved	2017	
Ocrevus	ocrelizumab	Not approved	2017	
Siliq	brodalumab	Not approved	2017	
Cinqair	reslizumab	2016	2016	
Lartruvo	olaratumab	2016	2016	
Darzalex	daratumumab	2016	2015	
Empliciti	elotuzumab	2016	2015	
Portrazza	necitumumab	2016	2015	
Inflectra (US), Remsima (EU)	infliximab	2013	2016	Biosimilar, same as Remicade
Ixifi	infliximab	Not approved	2017	Biosimilar, same as Remicade
Flixabi (EU), Renflexis (US)	infliximab	2016	2017	Biosimilar, same as Remicade
Anthim	obiltoxaximab	Not approved	2016	
Tecentriq	atezolizumab	Not approved	2016	
Cosentyx	secukinumab	2015	2015	
Nucala	mepolizumab	2015	2015	
Opdivo	nivolumab	2015	2015	
Praluent	alirocumab	2015	2015	
Praxbind	idarucizumab	2015	2015	
Repatha	evolocumab	2015	2015	
Unituxin	dinutuximab	2015	2015	Withdrawn from use in the European Union
Blincyto	blinatumomab	2015	2014	
Mvasi (US)	bevacizumab	Not approved	2017	Biosimilar, same as Avastin
Keytruda	pembrolizumab	2015	2014	
Cyramza	ramucirumab	2014	2014	
Entyvio	vedolizumab	2014	2014	
Sylvant	siltuximab	2014	2014	
Lemtrada	alemtuzumab	2013	2014	

Trade Name	INN	EMA Approval	FDA Approval	Comment
Kadcyla	trastuzumab emtansine	2013	2013	Conjugated antibody
Perjeta	pertuzumab	2013	2012	
Gazyvaro	obinutuzumab	Not approved	2013	
Adcetris	brentuximab vedotin	2012	2011	Conjugated antibody
Abthrax	raxibacumab	Not approved	2012	
Benlysta	belimumab	2011	2011	
Vervoy	ipilimumab	2011	2011	
Xgeva	denosumab	2011	2011	
Prolia	denosumab	2010	2010	
Arzerra	ofatumumab	2010	2009	
Scintimun	besilesomab	2010	Not approved	
RoActemra	tocilizumab	2009	2010	
Ilaris	canakinumab	2009	2009	
Simponi	golimumab	2009	2009	
Stelara	ustekinumab	2009	2009	
Cimzia	certolizumab pegol	2009	2008	PEG conjugated Fab fragment
Removab	catumaxomab	2009	Not approved	
Soliris	eculizumab	2007	2007	
Lucentis	ranibizumab	2007	2006	Fab fragment
Vectibix	panitumumab	2007	2006	
Tysabri	natalizumab	2006	2004	
Proxinium	catumaxomab	2005	2005	
Avastin	bevacizumab	2005	2004	
Xolair	omalizumab	2005	2003	
Erbitux	cetuximab	2004	2004	
Raptiva	efalizumab	2004	2003	Voluntarily withdrawn from the market in EU in 2009 and in US in 2009
Zevalin	ibritumomab tiuxetan	2004	2002	Conjugated antibody
NeutroSpec	fanolesomab	Not approved	2004	
Humira	adalimumab	2003	2002	
Bexxar	tositumomab	Not approved	2003	
Campath	alemtuzumab	2001	2001	
Herceptin	trastuzumab	2000	1998	
Ogivri	trastuzumab	Not approved	2017	Biosimilar, same as Herceptin
Ontruzant	trastuzumab	2017	Not approved	Biosimilar, same as Herceptin
Mylotarg	gemtuzumab ozogamicin	Not approved	2000	Conjugated antibody. Voluntarily withdrawn from the market in US in 2010.

Trade Name	INN	EMA Approval	FDA Approval	Comment
Remicade	infliximab	1999	1998	
Synagis	palivizumab	1999	1998	
Zenapax	daclizumab	1999	1997	Withdrawn from the market for commercial reasons in EU in 2009 and in US in 2009
Simulect	basiliximab	1998	1998	
Rituxan, MabThera	rituximab	1998	1997	
Rixathon	rituximab	2017	Not approved	Biosimilar, same as Rituxan
Truxima	rituximab	2017	Not approved	Biosimilar, same as Rituxan
Humaspect	votumumab	1998	Not approved	Withdrawn from the market in EU in 2003
LeukoScan	sulesomab	1997	Not approved	
CEA-scan	arcitumomab	1996	1996	Withdrawn from the market in EU in 2005
MyoScint	imiciromab	Not approved	1996	Has been discounted
ProstaScint	capromab	Not approved	1996	
Verluma	nofetumomab	Not approved	1996	
ReoPro	abciximab	1995	1994	Country-specific approval (prior to EMA Centralized Procedure).
OncoScint	satumomab	Not approved	1992	
Orthoclone OKT3	muromonab-CD3	1986	1986	Country-specific approval (prior to EMA Centralized Procedure).
Panorex	edrecolomab	1995	Not approved	Withdrawn from the market in EU in 2006
Centoxin	nebacumab	1991	Not approved	Withdrawn from the market in EU in 1993

A.2 IMGT mAbs

Table A.2. List of 273 mAbs collected from the IMGT database. The original chain isotypes, species origin and development status are given for each antibody.

INN	HC	LC	Species Origin	Development Status
abituzumab	IgG2	kappa	humanised	Phase I
abrilumab	IgG2	kappa	human	Phase II
actoxumab	IgG1	kappa	human	Phase III
adalimumab	IgG1	kappa	human	Phase M
aducanumab	IgG1	kappa	human	Phase III
afasevikumab	IgG1	kappa	human	Phase I
alemtuzumab	IgG1	kappa	humanised	Phase M
alirocumab	IgG1	kappa	human	Phase I
amatuximab	IgG1	kappa	chimeric	Phase II
andecaliximab	IgG4	kappa	chimeric	Phase II
anifrolumab	IgG1	kappa	human	Phase III
anrukinzumab	IgG1	kappa	humanised	Phase II
aprutumab	IgG1	lambda	human	Phase I
ascrinvacumab	IgG2	kappa	human	Phase II
atezolizumab	IgG1	kappa	humanised	Phase III
atinumab	IgG4	kappa	human	Phase I
avelumab	IgG1	lambda	human	Phase III
bapineuzumab	IgG1	kappa	humanised	Discontinued
basiliximab	IgG1	kappa	chimeric	Phase M
bavituximab	IgG1	kappa	chimeric	Phase II
benralizumab	IgG1	kappa	humanised	Phase III
bevacizumab beta	IgG1	kappa	humanised	Phase III
bevacizumab	IgG1	kappa	humanised	Phase M
bezlotoxumab	IgG1	kappa	human	Phase M
bimagrumab	IgG1	lambda	human	Phase II
bimekizumab	IgG1	kappa	humanised	Phase III
bleselumab	IgG4	kappa	human	Phase II
blosozumab	IgG4	kappa	humanised	Phase II
bococizumab	IgG2	kappa	humanised	Phase III
brazikumab	IgG2	lambda	human	Phase II
brentuximab vedotin	IgG1	kappa	chimeric	Phase II
briakinumab	IgG1	lambda	human	Phase I
brodalumab	IgG2	kappa	human	Phase II
brontictuzumab	IgG2	lambda	humanised	Phase I
burosumab	IgG1	kappa	human	Phase II
cabiralizumab	IgG4	kappa	humanised	Phase I
camrelizumab	IgG4	kappa	humanised	Phase I

INN	HC	LC	Species Origin	Development Status
canakinumab	IgG1	kappa	human	Phase II
cantuzumab ravtansine	IgG1	kappa	humanised	Phase II
carlumab	IgG1	kappa	human	Phase II
carotuximab	IgG1	kappa	chimeric	Phase II
cergutuzumab amunaleukin	IgG1	kappa	humanised	Phase II
cetuximab	IgG1	kappa	chimeric	Phase M
cixutumumab	IgG1	lambda	human	Phase II
clazakizumab	IgG1	kappa	humanised	Phase II
clivatuzumab tetraxetan	IgG1	kappa	humanised	Phase II
codrituzumab	IgG1	kappa	humanised	Phase II
coltuximab ravtansine	IgG1	kappa	chimeric	Phase II
conatumumab	IgG1	kappa	human	Discontinued
concizumab	IgG4	kappa	humanised	Phase I
cosfroviximab	IgG1	kappa	chimeric	Phase I/II
crenezumab	IgG4	kappa	humanised	Phase III
crizanlizumab	IgG2	kappa	humanised	Phase II
crotedumab	IgG4	kappa	human	Phase I
dacetuzumab	IgG1	kappa	humanised	Phase I
daclizumab	IgG1	kappa	humanised	Phase M
dalotuzumab	IgG1	kappa	humanised	Phase I
daratumumab	IgG1	kappa	human	Phase M
dectrekumab	IgG1	kappa	human	Phase II
demcizumab	IgG2	kappa	humanised	Phase I
denintuzumab mafodotin	IgG1	kappa	human	Phase I
denosumab	IgG2	kappa	humanised	Phase III
dezamizumab	IgG1	kappa	humanised	Phase I
dinutiximab beta	IgG1	kappa	chimeric	Phase I
dinutuximab	IgG1	kappa	chimeric	Phase M
diridavumab	IgG1	lambda	human	Not Stated
domagrozumab	IgG1	kappa	humanised	Phase II
drozitumab	IgG1	lambda	human	Phase I
duligotuzumab	IgG1	kappa	humanised	Phase II
dupilumab	IgG4	kappa	human	Phase III
durvalumab	IgG1	kappa	human	Phase III
dusigitumab	IgG2	lambda	human	Phase II
efalizumab	IgG1	kappa	humanised	Withdrawn
eldelumab	IgG1	kappa	human	Phase II
elezanumab	IgG1	lambda	human	Phase I
elgemtumab	IgG1	kappa	human	Phase I
elotuzumab	IgG1	kappa	humanised	Phase M

INN	HC	LC	Species Origin	Development Status
emactuzumab	IgG1	kappa	humanised	Phase I
emapalumab	IgG1	lambda	human	Phase III
emibetuzumab	IgG4	kappa	humanised	Phase II
emicizumab	IgG4	kappa	humanised	Phase M
enavatuzumab	IgG1	kappa	humanised	Phase I
enfortumab vedotin	IgG1	kappa	human	Phase I
enoblituzumab	IgG1	kappa	humanised	Phase I
enokizumab	IgG1	kappa	humanised	Phase II
enoticumab	IgG1	kappa	human	Phase I
ensituximab	IgG1	kappa	chimeric	Phase II
eptinezumab	IgG1	kappa	humanised	Phase III
erenumab	IgG2	lambda	human	Phase III
etaracizumab	IgG1	kappa	humanised	Phase II
etrolizumab	IgG1	kappa	humanised	Phase III
evinacumab	IgG4	kappa	human	Phase II
evolocumab	IgG2	lambda	human	Phase M
farletuzumab	IgG1	kappa	humanised	Phase III
fasinumab	IgG4	kappa	human	Phase III
fezakinumab	IgG1	lambda	human	Not Stated
ficlatuzumab	IgG1	kappa	humanised	Phase I
figitumumab	IgG2	kappa	human	Phase I
firivumab	IgG1	kappa	human	Not Stated
flanvotumab	IgG1	kappa	human	Phase I
fletikumab	IgG4	kappa	human	Phase II
foralumab	IgG1	kappa	human	Phase I
foravirumab	IgG1	kappa	human	Phase II
fremanezumab	IgG2	kappa	humanised	Phase III
fresolimumab	IgG4	kappa	human	Phase I
fulranumab	IgG2	kappa	human	Phase III
futuximab	IgG1	kappa	chimeric	Phase II
galcanezumab	IgG4	kappa	humanised	Phase II
ganitumab	IgG1	kappa	human	Phase I
gantenerumab	IgG1	kappa	human	Phase III
gatipotuzumab	IgG1	kappa	humanised	Phase I
gedivumab	IgG1	kappa	human	Phase II
gemtuzumab ozogamicin	IgG4	kappa	humanised	Phase M
gevokizumab	IgG2	kappa	humanised	Phase II
girentuximab	IgG1	kappa	chimeric	Phase III
glembatumumab vedotin	IgG2	kappa	human	Phase III
glembatumumab	IgG2	kappa	human	Phase II

INN	HC	LC	Species Origin	Development Status
guselkumab	IgG1	lambda	human	Phase M
ibalizumab	IgG4	kappa	humanised	Phase III
icrucumab	IgG1	kappa	human	Phase II
ifabotuzumab	IgG1	kappa	humanised	Phase I/II
imalumab	IgG1	kappa	human	Not Stated
imgatuzumab	IgG1	kappa	humanised	Phase II
inclacumab	IgG4	kappa	human	Phase II
indatuximab ravtansine	IgG4	kappa	chimeric	Phase II
indusatumab vedotin	IgG1	kappa	human	Phase I
indusatumab	IgG1	kappa	human	Not Stated
inebilizumab	IgG1	kappa	humanised	Phase II
infliximab	IgG1	kappa	chimeric	Phase M
intetumumab	IgG1	kappa	human	Not Stated
ipilimumab	IgG1	kappa	human	Phase M
iratumumab	IgG1	kappa	human	Phase II
isatuximab	IgG1	kappa	chimeric	Phase III
itolizumab	IgG1	kappa	humanised	Phase II
ixekizumab	IgG4	kappa	humanised	Phase II
labetuzumab govitecan	IgG1	kappa	humanised	Phase II
lacnotuzumab	IgG1	kappa	humanised	Phase II
lanadelumab	IgG1	kappa	human	Phase III
landogrozumab	IgG4	kappa	humanised	Phase II
laprituximab emtansine	IgG1	kappa	chimeric	Phase I
laprituximab	IgG1	kappa	chimeric	Phase I
larcaviximab	IgG1	kappa	chimeric	Phase I/II
lebrikizumab	IgG4	kappa	humanised	Phase III
lenzilumab	IgG1	kappa	human	Phase II
lesofavumab	IgG1	kappa	human	Preclinical
lexatumumab	IgG1	lambda	human	Phase I
lifastuzumab vedotin	IgG1	kappa	humanised	Phase II
ligelizumab	IgG1	kappa	humanised	Not Stated
lirilumab	IgG4	kappa	human	Phase II
lodelcizumab	IgG1	kappa	humanised	Phase II
lorvotuzumab mertansine	IgG1	kappa	humanised	Phase I/II
lucatumumab	IgG1	kappa	human	Phase I
lumretuzumab	IgG1	kappa	humanised	Phase I
lupartumab amadotin	IgG1	lambda	human	Phase I
lupartumab	IgG1	lambda	human	Phase I
margetuximab	IgG1	kappa	chimeric	Phase II
mavrilimumab	IgG4	lambda	human	Phase II

INN	HC	LC	Species Origin	Development Status
milatuzumab doxorubicin	IgG1	kappa	humanised	Phase I
mirvetuximab soravtansine	IgG1	kappa	chimeric	Phase III
mirvetuximab	IgG1	kappa	chimeric	Phase I
modotuximab	IgG1	kappa	chimeric	Phase II
mogamulizumab	IgG1	kappa	humanised	Phase I
monalizumab	IgG4	kappa	humanised	Phase I
motavizumab	IgG1	kappa	humanised	Phase III
namilumab	IgG1	kappa	human	Phase I
naratuximab	IgG1	kappa	chimeric	Phase II
narnatumab	IgG1	kappa	human	Phase I
natalizumab	IgG4	kappa	humanised	Phase M
navivumab	IgG1	kappa	human	Not Stated
necitumumab	IgG1	kappa	human	Phase M
nemolizumab	IgG2	kappa	humanised	Phase II
nesvacumab	IgG1	kappa	human	Phase I
nimotuzumab	IgG1	kappa	humanised	Phase M
nivolumab	IgG4	kappa	human	Phase M
obiltoxaximab	IgG1	kappa	chimeric	Phase I/II
obinutuzumab	IgG1	kappa	humanised	Phase M
ocaratuzumab	IgG1	kappa	humanised	Phase I/II
olaratumab	IgG1	kappa	human	Phase II
oleclumab	IgG1	lambda	human	Phase I
olokizumab	IgG4	kappa	humanised	Phase I
omalizumab	IgG1	kappa	humanised	Phase M
onartuzumab	IgG1	kappa	humanised	Phase M
opicinumab	IgG1	kappa	human	Phase II
orticumab	IgG1	lambda	human	Phase II
oxelumab	IgG1	kappa	human	Discontinued
ozanezumab	IgG1	kappa	humanised	Phase I
pamrevlumab	IgG1	kappa	human	Phase I
parsatuzumab	IgG1	kappa	humanised	Phase II
pateclizumab	IgG1	kappa	humanised	Phase II
patritumab	IgG1	kappa	human	Phase III
pembrolizumab	IgG4	kappa	humanised	Phase III
perakizumab	IgG1	kappa	humanised	Phase I
pidilizumab	IgG1	kappa	humanised	Phase II
pinatuzumab vedotin	IgG1	kappa	humanised	Phase I
plozalizumab	IgG1	kappa	humanised	Phase II
polatuzumab vedotin	IgG1	kappa	humanised	Phase I
ponezumab	IgG2	kappa	humanised	Phase II

INN	HC	LC	Species Origin	Development Status
porgaviximab	IgG1	kappa	chimeric	Phase I/II
prezalumab	IgG2	kappa	human	Phase I
pritoxaximab	IgG1	kappa	chimeric	Phase II
quilizumab	IgG1	kappa	humanised	Phase II
rafivirumab	IgG1	lambda	human	Phase II
ralpancizumab	IgG2	kappa	humanised	Phase I
ramucirumab	IgG1	kappa	human	Phase II
refanezumab	IgG1	kappa	humanised	Phase II
rilotumumab	IgG2	kappa	human	Phase II
rinucumab	IgG4	kappa	human	Phase I
risankizumab	IgG1	kappa	humanised	Phase III
rituximab	IgG1	kappa	chimeric	Phase M
robatumumab	IgG1	kappa	human	Preclinical
roledumab	IgG1	kappa	human	Phase II
romosozumab	IgG2	kappa	humanised	Phase III
rontalizumab	IgG1	kappa	humanised	Phase II
rosmantuzumab	IgG1	kappa	humanised	Phase I
rovalpituzumab	IgG1	kappa	humanised	Not Stated
sacituzumab govitecan	IgG1	kappa	humanised	Phase III
sacituzumab	IgG1	kappa	humanised	Not Stated
sarilumab	IgG1	kappa	human	Phase M
satralizumab	IgG2	kappa	humanised	Phase III
secukinumab	IgG1	kappa	human	Phase M
selicrelumab	IgG2	kappa	human	Phase I
seribantumab	IgG2	lambda	human	Phase II
setoxaximab	IgG1	kappa	chimeric	Phase II
sifalimumab	IgG1	kappa	human	Phase I
siltuximab	IgG1	kappa	chimeric	Phase II
simtuzumab	IgG4	kappa	humanised	Phase II
sirukumab	IgG1	kappa	human	Phase III
solanezumab	IgG1	kappa	humanised	Phase III
suptavumab	IgG1	kappa	human	Discontinued
suvizumab	IgG1	kappa	humanised	Phase I
suvratoxumab	IgG1	kappa	human	Phase II
tabalumab	IgG4	kappa	human	Phase III
tanezumab	IgG2	kappa	humanised	Phase III
tarextumab	IgG2	kappa	human	Phase I/II
telisotuzumab	IgG1	kappa	humanised	Phase I
teplizumab	IgG1	kappa	humanised	Phase III
teprotumumab	IgG1	kappa	human	Phase I

INN	HC	LC	Species Origin	Development Status
tesidolumab	IgG1	lambda	human	Phase II
tezepelumab	IgG2	lambda	human	Phase III
TGN1412	IgG4	kappa	humanised	Phase III
tigatuzumab	IgG1	kappa	humanised	Phase II
tildrakizumab	IgG1	kappa	humanised	Phase III
timigutuzumab	IgG1	kappa	humanised	Phase I
timolumab	IgG4	kappa	human	Phase I
tisotumab	IgG1	kappa	human	Not Stated
tocilizumab	IgG1	kappa	humanised	Phase M
tomuzotuximab	IgG1	kappa	chimeric	Phase II
tosatoxumab	IgG1	lambda	human	Phase I/II
tovetumab	IgG2	kappa	human	Phase I/II
tralokinumab	IgG4	lambda	human	Withdrawn
trastuzumab emtansine	IgG1	kappa	humanised	Phase III
trastuzumab	IgG1	kappa	humanised	Phase M
tregalizumab	IgG1	kappa	humanised	Phase II
tremelimumab	IgG2	kappa	human	Phase III
trevogrumab	IgG4	kappa	human	Phase II
ublituximab	IgG1	kappa	chimeric	Phase I
ulocuplumab	IgG4	kappa	human	Phase I
urelumab	IgG4	kappa	human	Phase II
ustekinumab	IgG1	kappa	human	Phase M
utomilumab	IgG2	lambda	human	Phase I
vadastuximab talirine	IgG1	kappa	chimeric	Phase III
vadastuximab	IgG1	kappa	chimeric	Not Stated
vantictumab	IgG2	lambda	human	Phase I
varisacumab	IgG1	kappa	human	Phase I
varlilumab	IgG1	kappa	human	Phase I
vatelizumab	IgG4	kappa	humanised	Phase I
vedolizumab	IgG1	kappa	humanised	Phase M
veltuzumab	IgG1	kappa	humanised	Phase I
vesencumab	IgG1	kappa	human	Phase I
vonlerolizumab	IgG1	kappa	humanised	Phase I
vorsetuzumab	IgG1	kappa	humanised	Phase I
vunakizumab	IgG1	kappa	humanised	Not Stated
xentuzumab	IgG1	lambda	human	Phase I

A.3 Predictive Modelling mAbs

Table A.3. List of 137 mAbs from Jain et al (2017) "Biophysical properties of the clinical-stage antibody landscape" PNAS. The original chain isotypes and species origin is given for each mAb along with the corresponding experimental measurements for melting point (Tm), HIC retention times and mAb yield from HEK cell line. The two last columns indicate if either primary sequence-based or MD based descriptors were generated for a sample and then used for model development.

Name	HC	LC	Species Origin	Tm	HIC	Yield	Primary	MD
abituzumab	IgG2	kappa	humanised	75.50	9.23	89.56	●	●
abrilumab	IgG2	kappa	human	71.00	9.41	100.22	●	●
adalimumab	IgG1	kappa	human	71.00	8.82	134.93	●	●
alemtuzumab	IgG1	kappa	humanised	74.50	8.77	144.65	●	●
alirocumab	IgG1	kappa	human	71.50	9.04	69.23	●	●
anifrolumab	IgG1	kappa	human	62.50	8.80	82.05	●	●
atezolizumab	IgG1	kappa	humanised	73.50	13.35	164.09	●	
bapineuzumab	IgG1	kappa	humanised	73.00	8.86	151.09	●	●
basiliximab	IgG1	kappa	chimeric	60.50	9.58	107.46	●	●
bavituximab	IgG1	kappa	chimeric	59.50	11.50	45.11	●	●
belimumab	IgG1	lambda	human	60.00	10.46	10.47	●	●
benralizumab	IgG1	kappa	humanised	76.00	9.47	146.71	●	●
bevacizumab	IgG1	kappa	humanised	63.50	11.77	49.98	●	●
bimagrumab	IgG1	lambda	human	72.00	10.13	150.24	●	●
blosozumab	IgG4	kappa	humanised	70.50	9.24	120.01	●	●
bococizumab	IgG2	kappa	humanised	67.00	10.18	95.79	●	●
brentuximab	IgG1	kappa	chimeric	72.00	10.54	268.06	●	●
briakinumab	IgG1	lambda	human	71.50	9.36	121.99	●	●
brodalumab	IgG2	kappa	human	74.50	9.08	150.86	●	●
canakinumab	IgG1	kappa	human	72.00	9.32	45.72	●	●
carlumab	IgG1	kappa	human	69.50	11.17	243.32	●	●
certolizumab	IgG1	kappa	humanised	81.50	11.48	186.71	●	●
cetuximab	IgG1	kappa	chimeric	68.50	10.11	109.16	●	●
cixutumumab	IgG1	lambda	human	73.50	11.76	154.26	●	●
clazakizumab	IgG1	kappa	humanised	69.50	9.57	113.48	●	●
codrituzumab	IgG1	kappa	humanised	73.00	8.84	66.35	●	●
crenezumab	IgG4	kappa	humanised	72.00	10.03	149.27	●	●
dacetuzumab	IgG1	kappa	humanised	68.00	8.47	128.45	●	●
daclizumab	IgG1	kappa	humanised	74.00	9.29	245.11	●	●
dalotuzumab	IgG1	kappa	humanised	77.00	9.89	82.42	●	●
daratumumab	IgG1	kappa	human	71.00	9.51	233.33	●	●
denosumab	IgG2	kappa	human	69.50	8.50	134.17	●	●
dinutuximab	IgG1	kappa	chimeric	69.00	9.83	76.43	●	●
drozitumab	IgG1	lambda	human	63.00	9.29	22.07	●	●
duligotuzumab	IgG1	kappa	humanised	67.50	10.21	192.58	●	●

Name	HC	LC	Species Origin	Tm	HIC	Yield	Primary	MD
dupilumab	IgG4	kappa	human	76.50	10.16	163.55	●	●
eculizumab	IgG2/G4	kappa	humanised	66.00	10.61	226.47		
efalizumab	IgG1	kappa	humanised	72.50	8.67	166.99	●	●
eldelumab	IgG1	kappa	human	59.50	12.42	89.25	●	●
elotuzumab	IgG1	kappa	humanised	83.50	10.31	213.19	●	●
emibetuzumab	IgG4	kappa	humanised	71.50	9.64	98.75	●	●
enokizumab	IgG1	kappa	humanised	68.00	12.93	239.82	●	●
epratuzumab	IgG1	kappa	humanised	65.00	9.19	78.23	●	●
etrolizumab	IgG1	kappa	humanised	76.00	9.32	173.84	●	●
evolocumab	IgG2	lambda	human	65.00	10.36	260.68	●	●
farletuzumab	IgG1	kappa	humanised	75.50	9.49	220.82	●	●
fasinumab	IgG4	kappa	human	71.00	10.03	110.37	●	●
fezakinumab	IgG1	lambda	human	69.00	11.80	141.45	●	●
ficlatuzumab	IgG1	kappa	humanised	75.00	9.42	249.03	●	●
figitumumab	IgG2	kappa	human	66.50	10.75	119.92	●	●
fletikumab	IgG4	kappa	human	71.50	11.04	220.38	●	●
foralumab	IgG1	kappa	human	66.00	9.84	174.44	●	●
fresolimumab	IgG4	kappa	human	74.00	10.88	166.04	●	●
fulranumab	IgG2	kappa	human	68.50	9.33	142.02	●	●
galiximab	IgG1	lambda	chimeric	67.50	12.20	174.12	●	●
ganitumab	IgG1	kappa	human	78.50	9.33	229.44	●	●
gantenerumab	IgG1	kappa	human	77.50	9.00	162.66	●	●
gemtuzumab	IgG4	kappa	humanised	72.50	12.26	171.30	●	●
gevokizumab	IgG2	kappa	humanised	71.50	8.83	136.36	●	●
girentuximab	IgG1	kappa	chimeric	63.00	9.08	30.72	●	●
glembatumumab	IgG2	kappa	human	70.50	13.68	152.71	●	●
golimumab	IgG1	kappa	human	70.00	11.36	163.24	●	●
guselkumab	IgG1	lambda	human	69.50	11.40	167.34	●	●
ibalizumab	IgG4	kappa	humanised	72.00	10.24	133.28	●	●
imgatuzumab	IgG1	kappa	humanised	71.50	10.09	187.71	●	●
infliximab	IgG1	kappa	chimeric	64.50	10.36	6.58	●	●
inotuzumab	IgG4	kappa	humanised	83.00	9.72	169.77	●	●
ipilimumab	IgG1	kappa	human	73.00	11.57	169.56	●	●
ixekizumab	IgG4	kappa	humanised	83.00	10.94	97.28	●	●
lampalizumab	IgG1	kappa	humanised	67.00	9.25	187.08	●	●
lebrikizumab	IgG4	kappa	humanised	66.00	12.38	61.61	●	●
lenzilumab	IgG1	kappa	human	74.00	8.72	184.74	●	●
lintuzumab	IgG1	kappa	humanised	75.50	10.87	229.97	●	●
lirilumab	IgG4	kappa	human	70.00	25.00	270.48		
lumiliximab	IgG1	kappa	chimeric	64.50	9.55	86.27	●	●

Name	HC	LC	Species Origin	Tm	HIC	Yield	Primary	MD
matuzumab	IgG1	kappa	humanised	72.00	9.84	224.33	●	●
mavrilimumab	IgG4	lambda	human	68.50	10.30	150.55	●	●
mepolizumab	IgG1	kappa	humanised	78.50	9.24	221.48	●	●
mogamulizumab	IgG1	kappa	humanised	68.50	9.64	89.77	●	●
motavizumab	IgG1	kappa	humanised	86.00	9.69	133.55	●	●
muromonab	IgG2	kappa	chimeric	74.50	8.90	113.52	●	
natalizumab	IgG4	kappa	humanised	79.50	9.70	251.75	●	●
necitumumab	IgG1	kappa	human	76.50	10.81	198.60	●	●
nimotuzumab	IgG1	kappa	humanised	65.50	25.00	15.13		
nivolumab	IgG4	kappa	human	66.00	9.02	178.81	●	●
obinutuzumab	IgG1	kappa	humanised	73.00	10.64	176.44	●	●
ocrelizumab	IgG1	kappa	humanised	70.50	9.91	137.77	●	●
ofatumumab	IgG1	kappa	human	68.00	9.73	249.75	●	●
olaratumab	IgG1	kappa	human	62.50	10.61	141.94	●	●
olokizumab	IgG4	kappa	humanised	69.00	9.91	115.26	●	●
omalizumab	IgG1	kappa	humanised	77.50	9.52	150.45	●	●
onartuzumab	IgG1	kappa	humanised	80.00	9.92	147.93	●	●
otelizumab	IgG1	lambda	humanized/ chimeric	75.50	9.08	152.08		
otlertuzumab	IgG1	kappa	humanised	68.50	10.96	149.60	●	●
ozanezumab	IgG1	kappa	humanised	67.00	10.03	97.07	●	●
palivizumab	IgG1	kappa	humanised	79.50	9.33	243.12	●	●
panitumumab	IgG2	kappa	human	78.50	9.48	179.59	●	●
panobacumab	IgM	kappa	human	69.00	9.83	107.60		
parsatuzumab	IgG1	kappa	humanised	64.50	9.11	40.02	●	●
patritumab	IgG1	kappa	human	71.50	10.15	68.77	●	●
pembrolizumab	IgG4	kappa	humanised	66.00	11.07	64.91	●	●
pertuzumab	IgG1	kappa	humanised	78.50	10.11	31.43	●	●
pinatuzumab	IgG1	kappa	humanised	79.00	9.22	130.58	●	●
polatuzumab	IgG1	kappa	humanised	74.00	8.76	225.06	●	●
ponezumab	IgG2	kappa	humanised	61.00	10.50	16.96	●	●
radretumab	IgE	kappa	human	77.00	9.51	151.17		
ramucirumab	IgG1	kappa	human	66.00	9.43	90.67	●	●
ranibizumab	IgG1	kappa	humanised	65.00	12.14	41.45	●	●
reslizumab	IgG4	kappa	humanised	75.50	9.82	191.57	●	●
rilotumumab	IgG2	kappa	human	79.00	12.63	173.08	●	●
rituximab	IgG1	kappa	chimeric	69.00	10.80	164.14	●	●
robatumumab	IgG1	kappa	human	80.00	9.51	117.12	●	●
romosozumab	IgG2	kappa	humanised	76.00	9.18	227.69	●	●
sarilumab	IgG1	kappa	human	64.00	8.99	181.79	●	●

Name	HC	LC	Species Origin	Tm	HIC	Yield	Primary	MD
secukinumab	IgG1	kappa	human	72.00	11.39	148.96	●	●
seribantumab	IgG2	lambda	human	77.50	10.42	189.98	●	●
sifalimumab	IgG1	kappa	human	67.00	9.65	158.63	●	●
siltuximab	IgG1	kappa	chimeric	64.50	11.00	95.67	●	●
simtuzumab	IgG4	kappa	humanised	66.50	10.41	191.44	●	●
sirukumab	IgG1	kappa	human	68.00	11.26	109.81	●	●
tabalumab	IgG4	kappa	human	64.00	10.85	121.60	●	●
tanezumab	IgG2	kappa	humanised	75.50	12.39	48.86	●	●
teplizumab	IgG1	kappa	humanised	64.50	8.79	150.88	●	
tigatuzumab	IgG1	kappa	humanised	64.50	10.02	178.97	●	●
tildrakizumab	IgG1	kappa	humanised	77.50	11.08	181.89	●	●
tocilizumab	IgG1	kappa	humanised	91.50	9.09	139.65	●	●
tovetumab	IgG2	kappa	human	63.50	8.67	277.18	●	●
tralokinumab	IgG4	lambda	human	63.00	10.26	121.43	●	●
trastuzumab	IgG1	kappa	humanised	78.50	9.66	159.48	●	●
tremelimumab	IgG2	kappa	human	75.00	11.56	229.59	●	●
urelumab	IgG4	kappa	human	66.00	11.16	143.92	●	●
ustekinumab	IgG1	kappa	human	69.50	8.78	152.72	●	●
vedolizumab	IgG1	kappa	humanised	80.50	10.94	221.76	●	●
veltuzumab	IgG1	kappa	humanised	70.00	11.09	224.95	●	●
visilizumab	IgG2	kappa	humanised	71.00	9.01	242.01	●	●
zalutumumab	IgG1	kappa	human	72.50	9.34	200.51	●	●
zanolimumab	IgG1	kappa	human	80.50	9.59	116.37	●	●

Appendix B

B.1 MATLAB Scripts

Code B.1. MATLAB script for implementation of OVR classification strategy in SVC function from LibSVM toolbox for model fitting.

```
function [assignedClass,prob,model] = fitSVC_ovr(X,labels,svmcmd)

nSam = size(X,1);
labelSet = unique(labels);
nClasses = length(labelSet);

% MEMORY ALLOCATION
SVC = cell(nClasses,1);
prob = zeros(nSam,nClasses);
decv = zeros(nSam,nClasses);

for i=1:nClasses
    % MODEL DEVELOPMENT
    SVC{i} = svmtrain(double(labels == labelSet(i)),pX,svmcmd);

    % PREDICTION OF SAMPLES
    [~,~,prob(:,i)] = svmpredict(double(labels == labelSet(i)), ...
                      X,SVC{i},'-q');

    % DECISION VALUES
    decv(:, i) = prob(:,i) * (2 * SVC{i}.Label(1) - 1);
end

% CLASS ASSIGNMENT
[~,assignedClass] = max(decv,[],2);
assignedClass = labelSet(assignedClass);

model.SVC = SVC;
model.labelSet = labelSet;
end
```

Code B.2. MATLAB script for implementation of OVR classification strategy in SVC function from LibSVM toolbox for model prediction.

```
function [assignedClass,prob] = predictSVC_ovr(X,labels,model)

SVC = model.SVC;
nSam = size(X,1);
labelSet = model.labelSet;
nClasses = length(labelSet);

% MEMORY ALLOCATION
prob = zeros(nSam,nClasses);
decv = zeros(nSam,nClasses);

for i=1:nClasses
    % PREDICTION OF SAMPLES
    [~,~,prob(:,i)] = svmpredict(double(labels == labelSet(i)), ...
                      X,SVC{i},'-q');

    % DECISION VALUES
    decv(:, i) = prob(:,i) * (2 * SVC{i}.Label(1) - 1);
end

% CLASS ASSIGNMENT
[~,assignedClass] = max(decv,[],2);
assignedClass = labelSet(assignedClass);
end
```

B.2 GROMACS Parameters

Code B.3. Energy minimisation parameters in EM.mdp.

```
integrator                      = steep
emstep                          = 0.002
nsteps                          = 50000
emtol                           = 20.0

; Parameters for atom neighbour search and interaction calculations
nstxout                         = 800
nstlist                         = 1
cutoff-scheme                   = Verlet
ns_type                         = grid
coulombtype                     = PME
rcoulomb                        = 1.0
rvdw                            = 1.0
pbc                             = xyz
```

Code B.4. NVT parameters with defined volume and temperature (NVT.mdp).

```
title                    = NVT equilibration
define                   = -DPOSRES

; Run parameters
integrator               = md       ; leap-frog integrator
nsteps                   = 5000     ; 2 * 5000 = 10 ps
dt                       = 0.002    ; 2 fs

; Output control (saves coordinates, velocities and energies to log file)
nstxout                  = 5000
nstvout                  = 5000
nstenergy                = 5000
nstlog                   = 5000

; Bond parameters
Continuation             = no
constraint_algorithm     = lincs
constraints              = all-bonds
lincs_iter               = 1
lincs_order              = 4

; Neighborsearching
cutoff-scheme            = Verlet
ns_type                  = grid
nstlist                  = 10
rcoulomb                 = 1.0
rvdw                     = 1.0

; Electrostatics
Coulombtype              = PME
pme_order                = 4
fourierspacing           = 0.16

; Temperature coupling is on
tcoupl                   = V-rescale
tc-grps                  = Protein Non-Protein
tau_t                    = 0.1      0.1
ref_t                    = 300      300

; Pressure coupling is off
pcoupl                   = no

; Periodic boundary conditions
Pbc                      = xyz

; Dispersion correction
DispCorr                 = EnerPres

; Velocity generation
gen_vel                  = yes
gen_temp                 = 300
gen_seed                 = -1
```

Code B.5. NPT parameters with defined pressure (NPT.mdp). Resumes after end of NVT simulation.

```
title                    = NPT equilibration
define                   = -DPOSRES

; Run parameters
integrator               = md       ; leap-frog integrator
nsteps                   = 5000     ; 2 * 5000 = 10 ps
dt                       = 0.002    ; 2 fs

; Output control (saves coordinates, velocities and energies to log file)
nstxout                  = 5000
nstvout                  = 5000
nstenergy                = 5000
nstlog                   = 5000

; Bond parameters
continuation             = yes      ; Restarting after NVT
constraint_algorithm     = lincs
constraints              = all-bonds
lincs_iter               = 1
lincs_order              = 4

; Neighborsearching
cutoff-scheme            = Verlet
ns_type                  = grid
nstlist                  = 10
rcoulomb                 = 1.0
rvdw                     = 1.0

; Electrostatics
coulombtype              = PME
pme_order                = 4
fourierspacing           = 0.16

; Temperature coupling is on
Tcoupl                   = V-rescale
tc-grps                  = Protein Non-Protein
tau_t                    = 0.1      0.1
ref_t                    = 300      300

; Pressure coupling is on
pcoupl                   = Parrinello-Rahman
pcoupltype               = isotropic
tau_p                    = 2.0
ref_p                    = 1.0
compressibility          = 4.5e-5
refcoord_scaling         = com
```

Code B.5 Continued. NPT parameters with defined pressure (NPT.mdp). Resumes after end of NVT simulation.

```
; Periodic boundary conditions
pbc                              = xyz

; Dispersion correction
DispCorr                         = EnerPres

; Velocity generation
gen_vel                          = no
```

Code B.6. Production run parameters (MD.mdp). Resumes after end of NPT simulation.

```
title                       = MD simulation

; Run parameters
integrator                  = md       ; leap-frog integrator
nsteps                      = 25000000 ; 2 * 25000000 = 100 ns
dt                          = 0.002    ; 2 fs

; Output control
nstxout                     = 20000
nstvout                     = 20000
nstenergy                   = 20000
nstlog                      = 20000

; Bond parameters
continuation                = yes      ; Restarting after NPT
constraint_algorithm        = lincs
constraints                 = all-bonds
lincs_iter                  = 1
lincs_order                 = 4

; Neighborsearching
cutoff-scheme               = Verlet
ns_type                     = grid
nstlist                     = 10
rcoulomb                    = 1.0
rvdw                        = 1.0

; Electrostatics
coulombtype                 = PME
pme_order                   = 4
fourierspacing              = 0.16

; Temperature coupling is on
tcoupl                      = V-rescale
tc-grps                     = Protein Non-Protein
tau_t                       = 0.1      0.1
ref_t                       = 300      300

; Pressure coupling is on
Pcoupl                      = Parrinello-Rahman
Pcoupltype                  = isotropic
tau_p                       = 2.0
ref_p                       = 1.0
compressibility             = 4.5e-5

; Periodic boundary conditions
pbc                         = xyz

; Dispersion correction
DispCorr                    = EnerPres

; Velocity generation
gen_vel                     = no
```

Appendix C

C.1 Chapter 4 Modelling Results

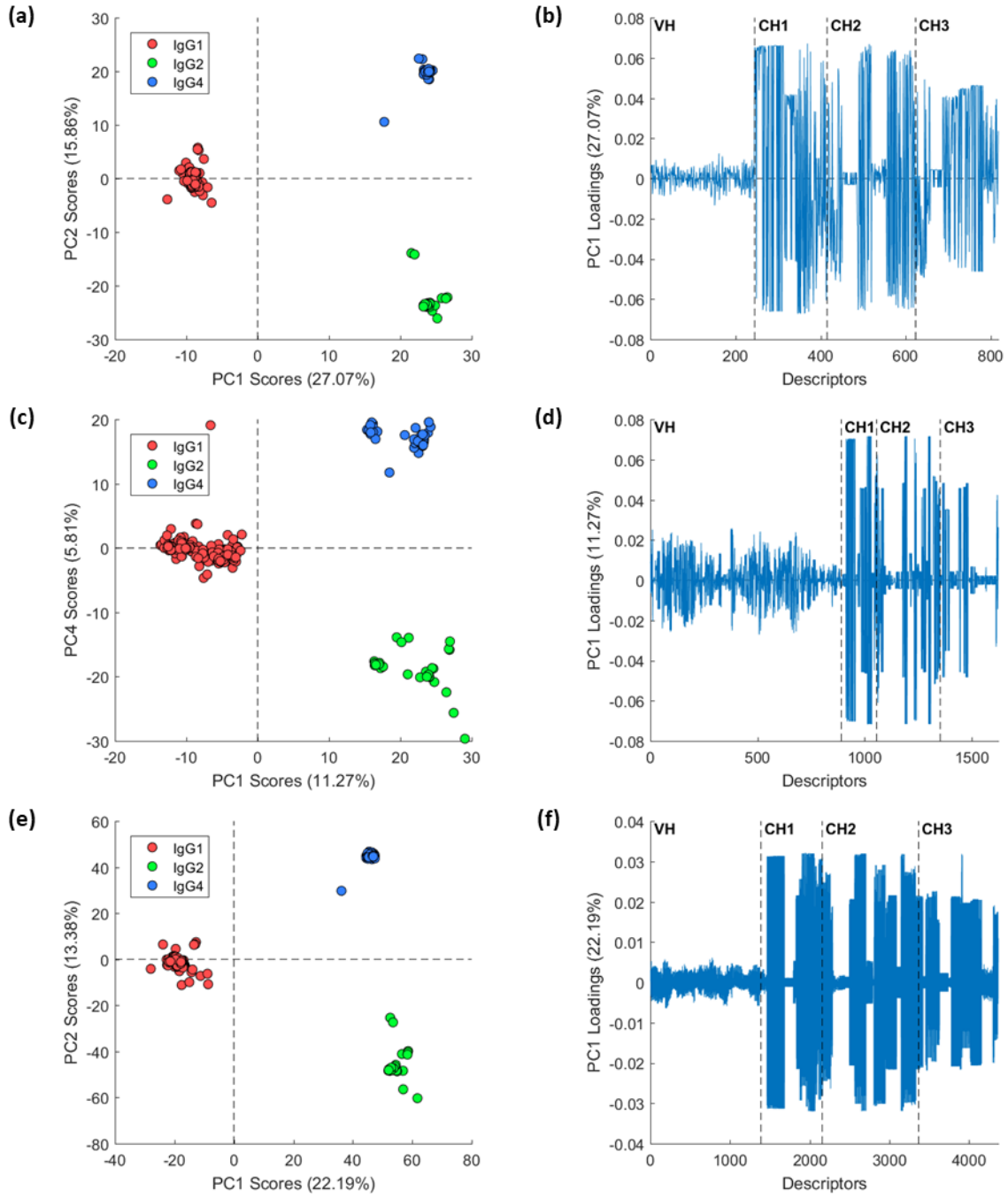

Figure C.1. PCA exploration of descriptors from V_H, C_H1, C_H2 and C_H3 heavy chain domains with a clear separation of IgG1 (red), IgG2 (green) and IgG4 (blue) occurred in the scores generated from PSD2 **(a)**, PSD3 **(c)** and PSD4 **(e)**. The vast majority of domain contribution for the HC isotype separation of the scores originated from the constant domains for the descriptor sets PSD2 **(b)**, PSD3 **(d)** and PSD4 **(f)**.

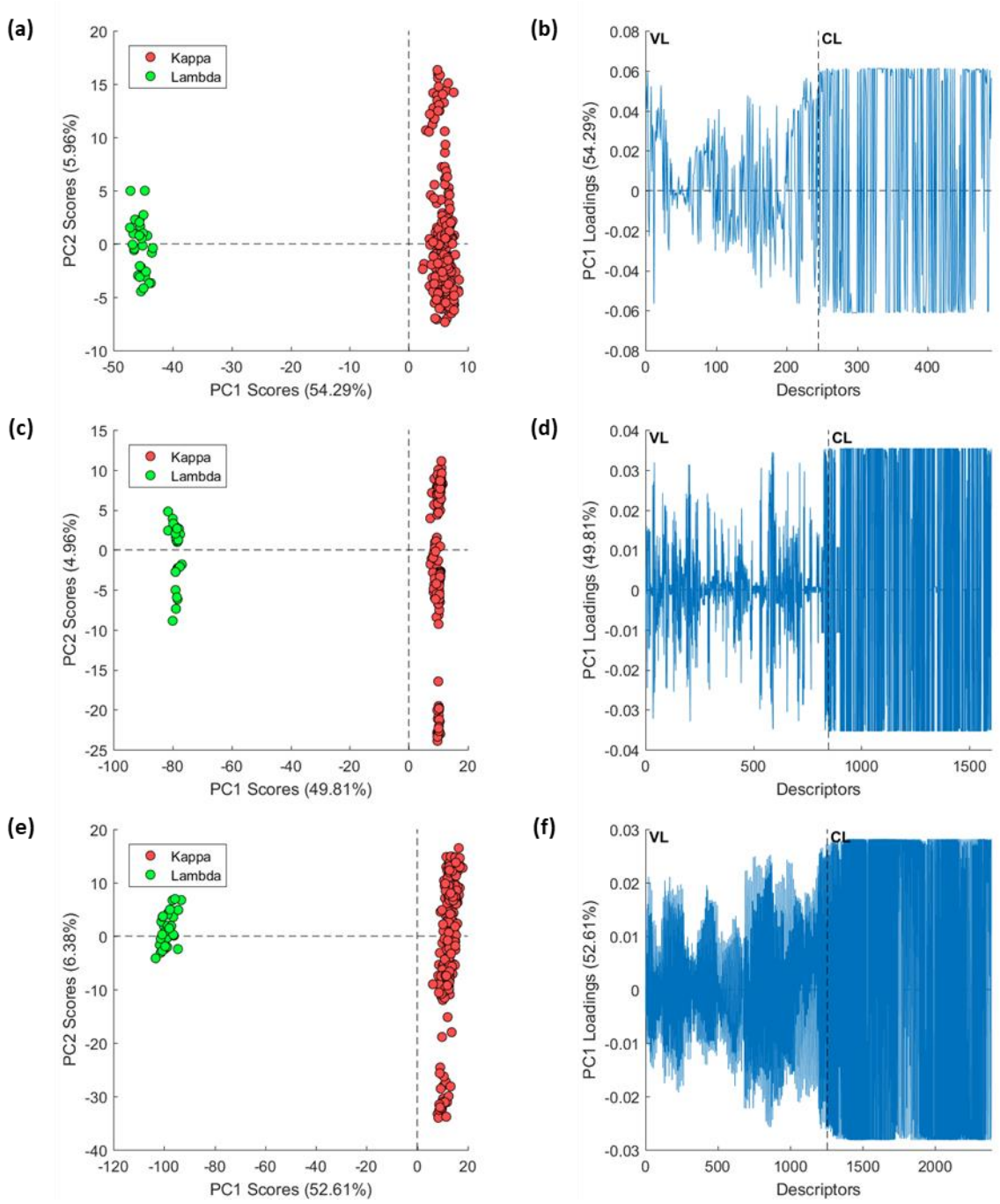

Figure C.2. PCA exploration of descriptors from V_L and C_L light chain domains with a clear separation of kappa (red) and lambda (green) occurred in the scores generated from PSD2 **(a)**, PSD3 **(c)** and PSD4 **(e)**. Both V_L and C_L domains contributed to the LC isotype separation of the scores for the descriptor sets PSD2 **(b)**, PSD3 **(d)** and PSD4 **(f)**.

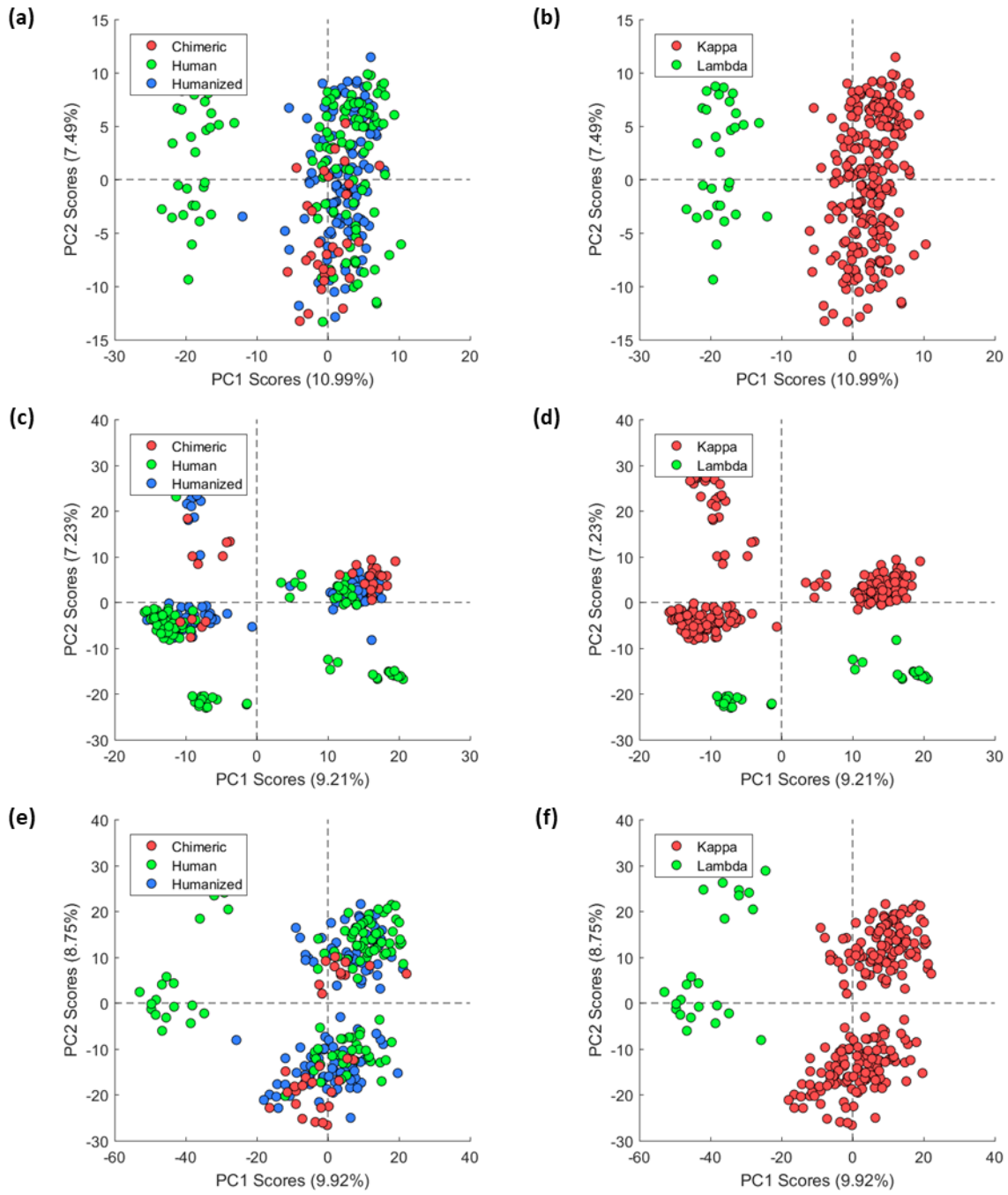

Figure C.3. Impact of LC isotype from the V_L domain on the PCA exploration with two principal components. No clear separation of the species origins: chimeric (red), human (green) and humanised (blue) samples were apparent in PSD2 **(a)**, PSD3 **(c)** and PSD4 **(e)**. Instead, structural features related to the LC isotype from the V_L domain had a larger impact on the PCA scores in descriptor set PSD2 **(b)**, PSD3 **(d)** and PSD4 **(f)**.

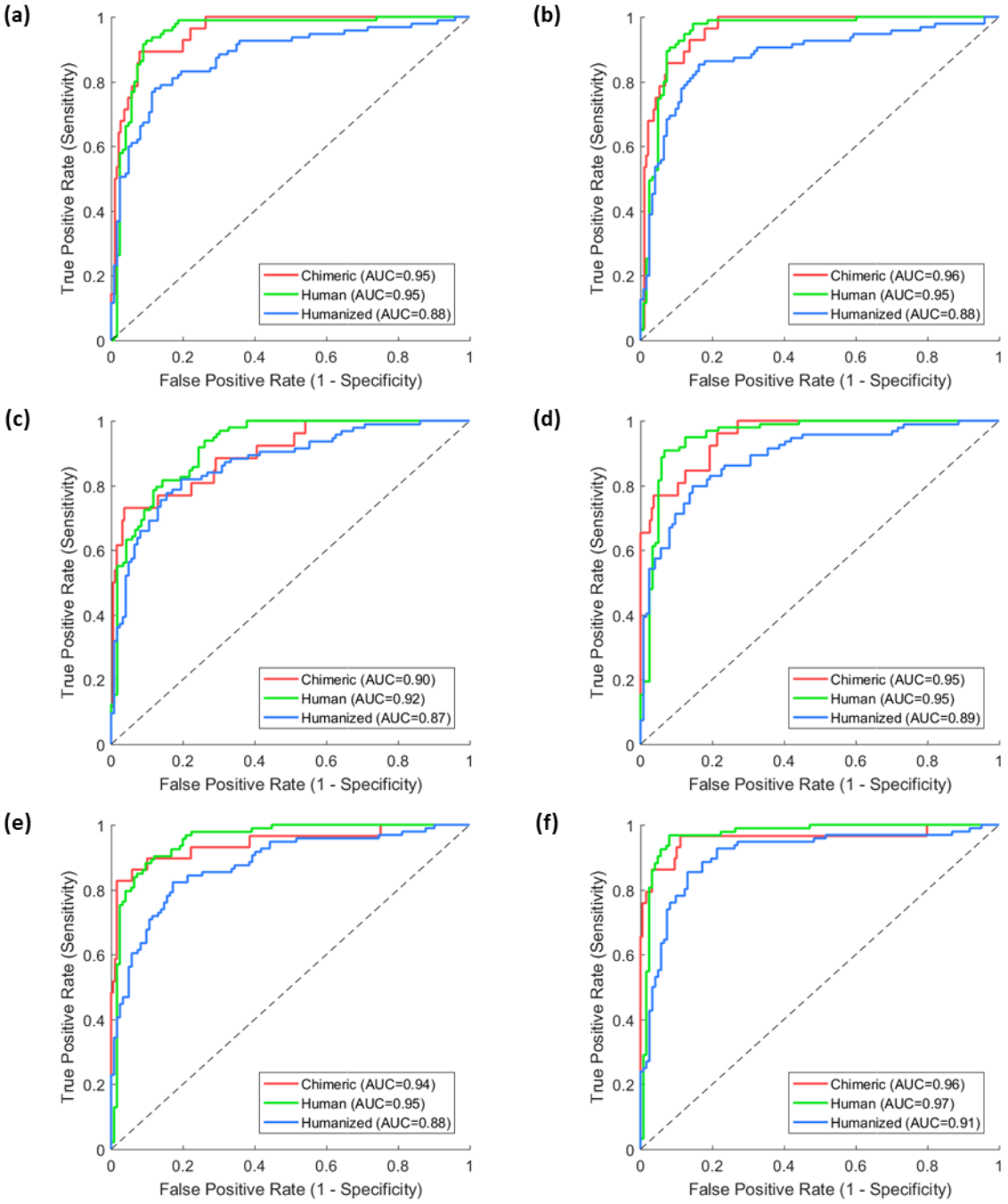

Figure C.4. ROC curves and AUC of cross-validation for chimeric (red line), human (green line) and humanised (blue line) with PLS-DA developed on **(a)** PSD1, **(c)** PSD2 and **(e)** PSD4 as well as SVC developed on **(b)** PSD1, **(d)** PSD2 and **(f)** PSD4.

C.2 Chapter 5 Modelling Results

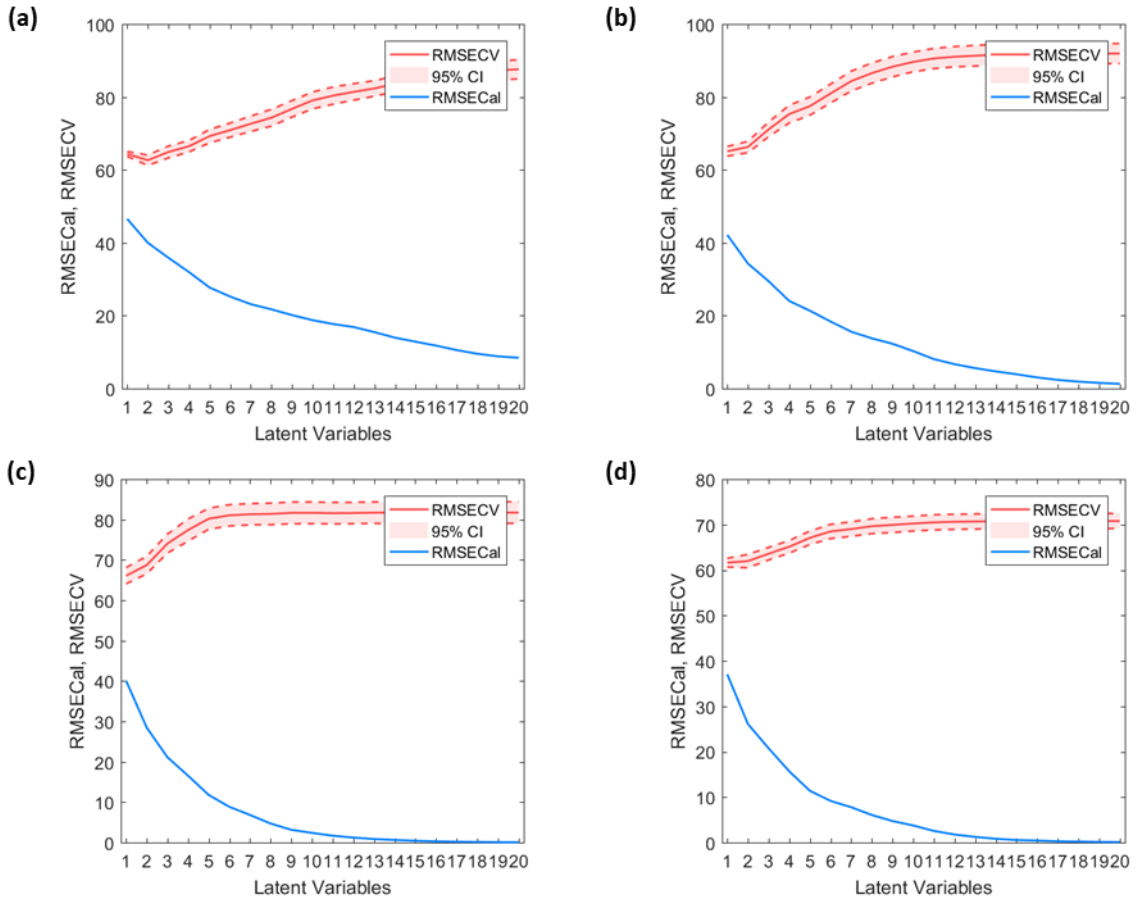

Figure C.5. PLS error for prediction of mAb yields in the calibration (blue line) and the cross-validation (red line) with regards to the number of latent variables developed from the V-WSP reduced descriptor sets of (**a**) PSD1, (**b**) PSD2, (**c**) PSD3 and (**d**) PSD4.

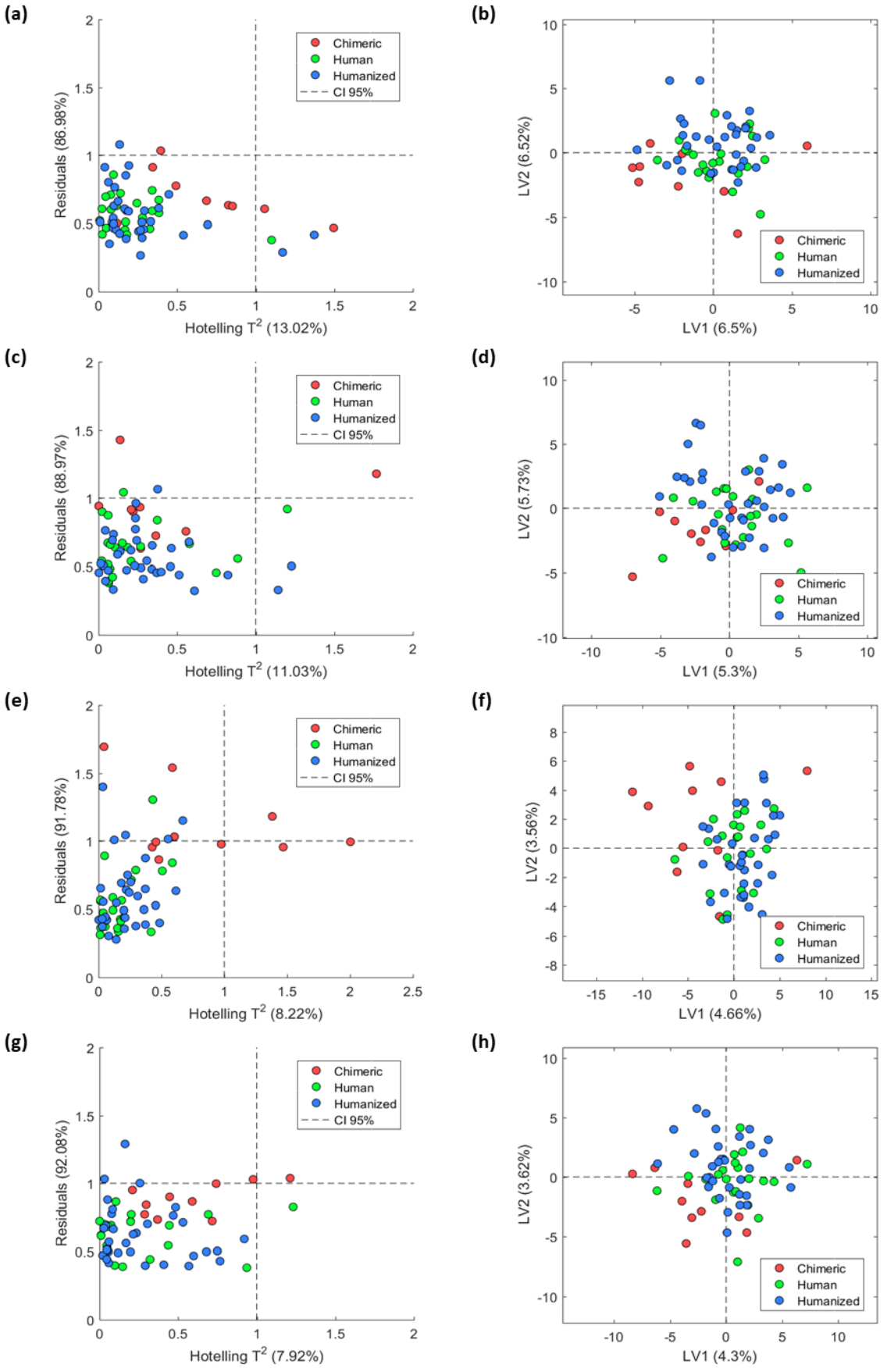

Figure C.6. Impact of species on PLS models developed on the mAb yield where chimeric samples are coloured red, human samples in green and humanised in blue. PLS Influence plots for PSD1 **(a)**, PSD2 **(c)**, PSD3 **(e)** and PSD4 **(g)**. PLS scores, ***T***, for the individual samples for PSD1 **(b)**, PSD2 **(d)**, PSD3 **(f)** and PSD4 **(h)**.

Table C.1. Hypothesis testing of heavy and light chain isotypes using Anderson-Darling Normality Test with a significance level of 0.05. H_0 represents that the data follows a normal distribution.

Factor	Level	Samples	HIC		Yield	
			p	Decision	p	Decision
Species	chimeric	10	0.9900	Keep H_0	0.2387	Keep H_0
	humanised	45	0.0007	Reject H_0	0.1195	Keep H_0
	human	26	0.0050	Reject H_0	0.8751	Keep H_0

Table C.2. Hypothesis testing of with a significance level of 0.05. H_o represents that there is no significant difference between means of different species origins. Non-parametric tests are referred to as NP and parametric test as P.

Response	Factor	Levels	Type	Test	Equal Variance	p	Decision
HIC	Species	3	NP	Kruskal-Wallis	-	0.3923	Keep H0
Yield	Species	3	P	1-Way ANOVA	Yes (p=0.9315)	0.0244	Reject H0

Table C.3. Multiple comparison hypothesis testing with 2-sample T-test with an effective significance level of 0.0133 according to Bonferroni Correction. H_0 represents that no difference between means can be observed.

First Level	Second Level	Equal variance	p	Decision
chimeric	human	Yes (p=0.7314)	0.0313	Keep H0
chimeric	humanised	Yes (p=0.8420)	0.0093	Reject H0
human	humanised	Yes (p=0.7917)	0.6086	Keep H0

Table C.4. Model benchmarking table for HIC retention times. **(a)** Performance of all model permutations and descriptor sets in the Cross validation and Test set when all samples were used ($N = 81$). **(b)** Performance of all model permutations and descriptor sets in the Cross validation and Test set after sample selection ($n = 45$). Colouring was applied conforming to the OECD guidelines. Green indicates values higher than 0.5 and 0.6 in the cross validation and Test set, respectively. Yellow indicates values between 0.3 and 0.5 in the cross validation as well as between 0.3 and 0.6 in the Test set. Red indicates values below 0.3.

(a)

			Cross Validation								Test Set							
			PSD1		PSD2		PSD3		PSD4		PSD1		PSD2		PSD3		PSD4	
			R^2	Q^2	R^2	Q^2	R^2	Q^2	R^2	Q^2	R^2	Q^2	R^2	Q^2	R^2	Q^2	R^2	Q^2
All samples (n = 81)	PLS	Full	0.20	0.18	0.16	0.00	0.05	-0.13	0.06	-0.02	0.22	0.21	0.59	0.51	0.07	-0.25	0.30	0.24
		V-WSP	0.17	0.14	0.03	-0.12	0.05	-0.15	0.05	-0.04	0.33	0.32	0.03	-0.14	0.24	0.23	0.39	0.36
		rPLS	0.29	0.28	0.25	0.24	0.63	0.62	0.37	0.37	0.26	0.26	0.02	-0.11	0.28	0.27	0.33	0.31
		GA	0.48	0.46	0.59	0.57	0.57	0.57	0.74	0.73	0.53	0.53	0.34	0.03	0.37	0.33	0.53	0.41
	SVR	Full	0.17	0.15	0.15	0.06	0.03	-0.04	0.08	0.05	0.23	0.12	0.33	0.26	0.06	-0.05	0.17	0.01
		V-WSP	0.27	0.25	0.01	-0.02	0.02	-0.03	0.07	0.04	0.40	0.28	0.08	0.00	0.21	0.00	0.23	0.08
		L1-SVR	0.34	0.33	0.27	0.25	0.04	-0.03	0.42	0.39	0.28	0.22	0.12	-0.02	0.24	-0.06	0.18	0.17
		GA	0.39	0.37	0.54	0.53	0.54	0.46	0.69	0.67	0.65	0.63	0.36	0.20	0.32	0.15	0.40	0.19

(b)

			Cross Validation								Test Set							
			PSD1		PSD2		PSD3		PSD4		PSD1		PSD2		PSD3		PSD4	
			R^2	Q^2	R^2	Q^2	R^2	Q^2	R^2	Q^2	R^2	Q^2	R^2	Q^2	R^2	Q^2	R^2	Q^2
Humanized samples (n = 45)	PLS	Full	0.22	0.13	0.08	-0.09	0.04	-0.09	0.20	0.14	0.73	0.69	0.25	0.06	0.02	-0.06	0.70	0.65
		V-WSP	0.28	0.22	0.03	-0.18	0.04	-0.49	0.13	0.10	0.79	0.66	0.03	-0.20	0.18	0.14	0.24	0.20
		rPLS	0.55	0.53	0.28	0.26	0.92	0.91	0.84	0.83	0.75	0.63	0.04	-0.09	0.25	0.22	0.52	0.26
		GA	0.63	0.62	0.90	0.89	0.89	0.89	0.94	0.92	0.78	0.69	0.51	-0.01	0.45	0.34	0.72	0.69
	SVR	Full	0.23	0.17	0.04	0.01	0.02	-0.01	0.18	0.13	0.64	0.62	0.12	-0.32	0.09	-0.01	0.70	0.65
		V-WSP	0.30	0.18	0.02	-0.04	0.04	-0.03	0.08	0.02	0.52	0.50	0.00	-0.58	0.10	-0.04	0.46	0.42
		L1-SVR	0.29	0.16	0.02	-0.05	0.04	-0.02	0.30	0.27	0.52	0.50	0.00	-0.58	0.10	-0.04	0.56	0.50
		GA	0.59	0.57	0.85	0.84	0.89	0.88	0.92	0.91	0.85	0.81	0.47	-0.17	0.49	0.38	0.75	0.71

Table C.5. Model benchmarking table for mAb yields. **(a)** Performance of all model permutations and descriptor sets in the Cross validation and Test set when all samples were used ($N = 81$). **(b)** Performance of all model permutations and descriptor sets in the Cross validation and Test set after sample selection ($N = 55$). Colouring was applied conforming to the OECD guidelines. Green indicates values higher than 0.5 and 0.6 in the cross validation and Test set, respectively. Yellow indicates values between 0.3 and 0.5 in the cross validation as well as between 0.3 and 0.6 in the Test set. Red indicates values below 0.3

(a)

			Cross Validation								Test Set							
			PSD1		PSD2		PSD3		PSD4		PSD1		PSD2		PSD3		PSD4	
			R^2	Q^2	R^2	Q^2	R^2	Q^2	R^2	Q^2	R^2	Q^2	R^2	Q^2	R^2	Q^2	R^2	Q^2
All samples (n = 81)	PLS	Full	0.17	0.09	0.22	0.15	0.04	-0.06	0.12	0.02	0.01	-0.50	0.00	-0.64	0.12	-0.13	0.12	0.02
		V-WSP	0.19	0.10	0.08	0.00	0.05	-0.08	0.06	-0.04	0.01	-0.53	0.00	-0.36	0.08	-0.06	0.18	0.03
		rPLS	0.35	0.34	0.39	0.39	0.41	0.31	0.39	0.38	0.02	-0.64	0.06	-0.15	0.34	0.02	0.20	0.06
		GA	0.49	0.48	0.58	0.58	0.71	0.70	0.81	0.81	0.01	-0.66	0.09	-0.33	0.11	-0.10	0.34	0.30
	SVR	Full	0.21	0.15	0.16	0.16	0.06	0.02	0.04	0.03	0.01	-0.78	0.00	-0.23	0.24	0.07	0.23	0.08
		V-WSP	0.17	0.16	0.08	0.08	0.06	0.05	0.03	0.01	0.01	-0.07	0.01	-0.09	0.19	-0.24	0.12	0.01
		L1-SVR	0.17	0.15	0.31	0.28	0.07	0.07	0.05	0.04	0.01	-0.07	0.04	-0.08	0.19	-0.24	0.12	0.01
		GA	0.45	0.43	0.52	0.48	0.63	0.62	0.78	0.78	0.00	-0.64	0.07	-0.45	0.02	-0.72	0.31	0.24

(b)

			Cross Validation								Test Set							
			PSD1		PSD2		PSD3		PSD4		PSD1		PSD2		PSD3		PSD4	
			R^2	Q^2	R^2	Q^2	R^2	Q^2	R^2	Q^2	R^2	Q^2	R^2	Q^2	R^2	Q^2	R^2	Q^2
Chimeric and Humanized samples (n = 55)	PLS	Full	0.46	0.45	0.36	0.33	0.06	-0.03	0.18	0.13	0.00	-0.54	0.01	-0.51	0.76	0.25	0.22	0.19
		V-WSP	0.46	0.42	0.33	0.25	0.08	-0.03	0.09	0.01	0.10	-0.75	0.03	-1.04	0.22	0.01	0.40	0.34
		rPLS	0.73	0.73	0.91	0.91	0.72	0.72	0.87	0.87	0.24	-0.48	0.00	-0.45	0.11	-0.38	0.31	0.26
		GA	0.69	0.68	0.94	0.94	0.92	0.91	0.95	0.94	0.29	-0.58	0.01	-0.88	0.69	0.37	0.51	0.50
	SVR	Full	0.45	0.44	0.35	0.34	0.01	-0.01	0.21	0.18	0.03	-0.37	0.00	-0.29	0.57	-0.14	0.17	0.13
		V-WSP	0.42	0.40	0.34	0.30	0.05	0.01	0.08	0.07	0.01	-0.80	0.02	-0.80	0.64	-0.17	0.28	0.19
		L1-SVR	0.46	0.44	0.36	0.34	0.06	-0.03	0.09	0.08	0.01	-0.80	0.02	-0.80	0.00	-0.15	0.28	0.19
		GA	0.68	0.68	0.94	0.93	0.92	0.91	0.95	0.95	0.16	-0.85	0.00	-0.73	0.68	0.35	0.48	0.47

C.3 Chapter 7 Modelling Results

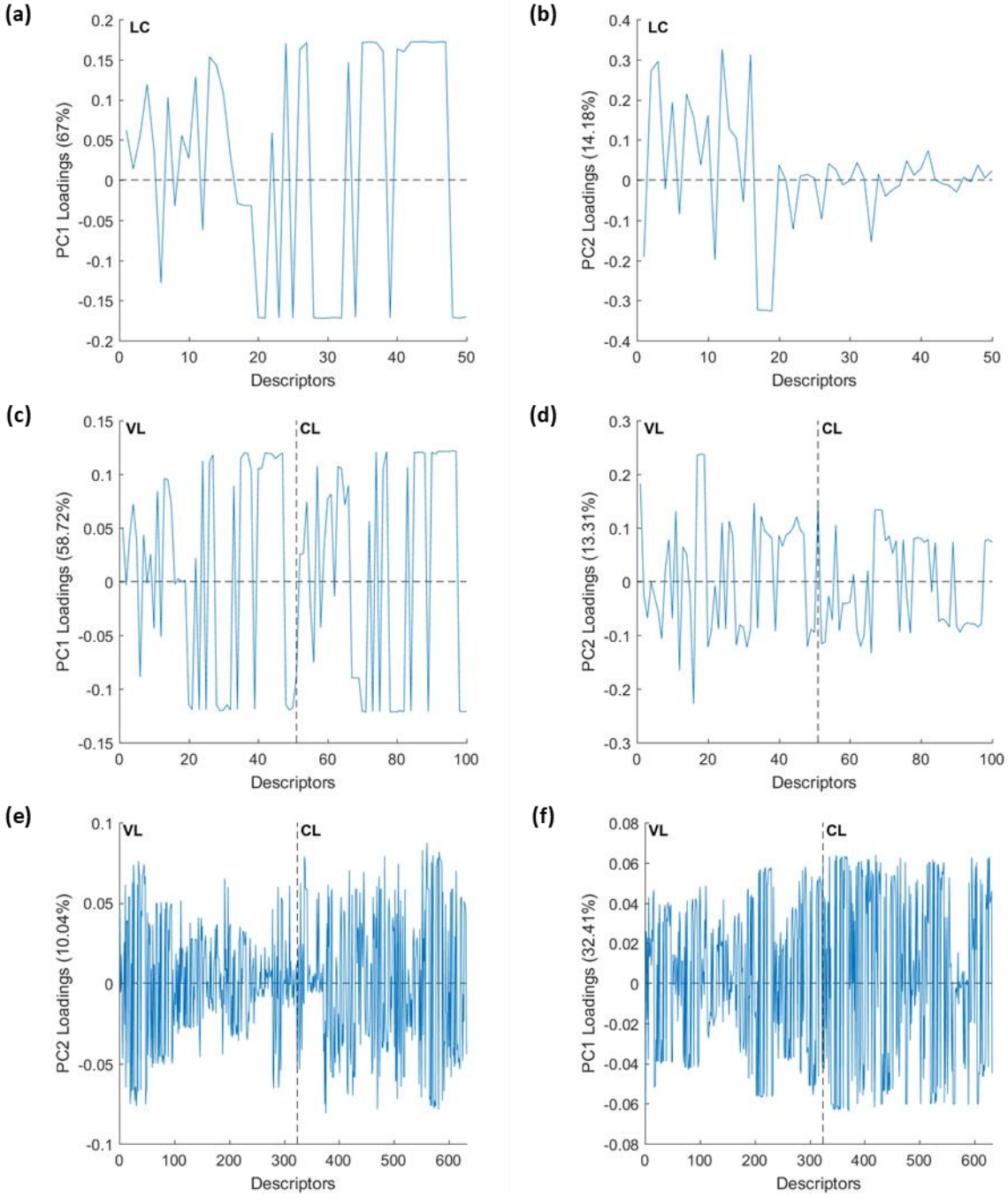

Figure C.7. PCA loadings of light chain descriptors from MSD1, MSD2 and MSD3. The first **(a)** and second **(b)** component of MSD1 calculated from descriptor generated from the entire light chain. The first **(c)** and second **(d)** component of MSD2 were calculated from descriptors generated individually from the V_L and C_L domains. The first **(e)** and second **(f)** component of MSD3 were calculated from descriptors generated from individual substructures in the V_L and C_L domains. Domain specific descriptors are separated by the black vertical dashed line in MSD2 and MSD3.

Table C.6. 80/20 sample splitting of the 79 selected IgG1-kappa samples. Splitting was performed with the CADEX algorithm on the three descriptor resolutions MSD1, MSD2 and MSD3 generated from the variable domains V_H and V_L. The splitting results of a stratified and non-stratified strategy is presented. The implemented sample stratification strategy was designed to place approximately 20% of each species origin in the test set for model validation.

Descriptor Set	Species origin	Not Stratified			Stratified		
		Calibration	Test	Ratio (Test)	Calibration	Test	Ratio (Test)
MSD1	chimeric	10	0	0.00	8	2	0.20
	human	23	3	0.12	20	6	0.23
	humanised	30	13	0.30	34	9	0.21
MSD2	chimeric	9	1	0.10	8	2	0.20
	human	23	3	0.12	20	6	0.23
	humanised	31	12	0.28	34	9	0.21
MSD3	chimeric	9	1	0.10	8	2	0.20
	human	21	5	0.19	20	6	0.23
	humanised	34	9	0.23	34	9	0.21

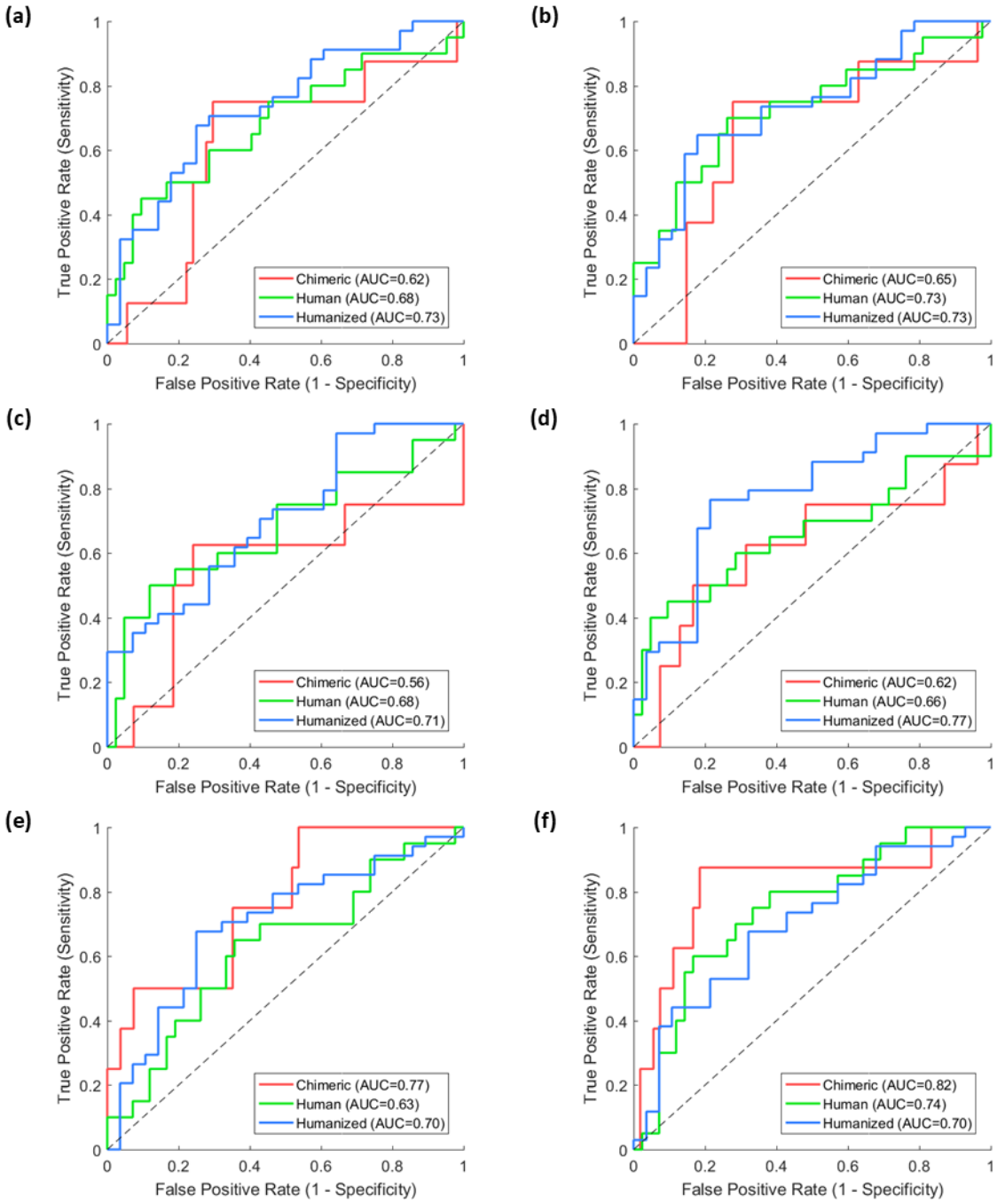

Figure C.8. ROC curves and AUC of cross-validation for chimeric (red line), human (green line) and humanised (blue line) with PLS-DA developed on **(a)** MSD1, **(c)** MSD2 and **(e)** MDS3 as well as SVC developed on **(b)** MSD1, **(d)** MSD2 and **(f)** MDS3.

Table C.7. Model benchmarking table for **(a)** HIC retention times and **(b)** mAb yields. Performance of all model permutations and descriptor sets in the Cross validation and Test set developed from 79 IgG1-kappa samples have been presented. Colouring was applied conforming to the OECD guidelines. Green indicates values higher than 0.5 and 0.6 in the cross validation and Test set, respectively. Yellow indicates values between 0.3 and 0.5 in the cross validation as well as between 0.3 and 0.6 in the Test set. Red indicates values below 0.3.

(a)

			Cross Validation						Test Set					
			MSD1		MSD2		MSD3		MSD1		MSD2		MSD3	
			R^2	Q^2	R^2	Q^2	R^2	Q^2	R^2	Q^2	R^2	Q^2	R^2	Q^2
HIC Retention Time (n = 79)	PLS	Full	0.04	-0.06	0.07	-0.07	0.03	-0.12	0.09	-0.11	0.04	-0.19	0.12	0.11
		V-WSP	0.06	-0.08	0.03	-0.17	0.01	-0.23	0.16	-0.03	0.05	-0.33	0.16	0.12
		rPLS	0.12	0.11	0.13	0.10	0.56	0.55	0.02	-0.08	0.03	-0.18	0.07	0.02
		GA	0.19	0.16	0.39	0.34	0.75	0.71	0.24	0.06	0.10	-0.33	0.66	0.65
	SVR	Full	0.04	-0.03	0.05	-0.04	0.05	-0.04	0.02	-0.05	0.05	-0.06	0.01	-0.04
		V-WSP	0.08	-0.05	0.01	-0.03	0.06	-0.04	0.14	-0.05	0.06	-0.04	0.03	-0.04
		L1-SVR	0.05	-0.04	0.13	0.09	0.07	-0.05	0.00	-0.05	0.08	0.01	0.00	-0.04
		GA	0.22	0.18	0.30	0.29	0.77	0.75	0.22	0.06	0.09	-0.18	0.64	0.63

(b)

			Cross Validation						Test Set					
			MSD1		MSD2		DS3		MSD1		MSD2		MSD3	
			R^2	Q^2	R^2	Q^2	R^2	Q^2	R^2	Q^2	R^2	Q^2	R^2	Q^2
Antibody Yield (n = 79)	PLS	Full	0.01	-0.25	0.04	-0.21	0.02	-0.21	0.00	-0.15	0.01	-0.28	0.00	-0.82
		V-WSP	0.01	-0.23	0.01	-0.14	0.07	0.00	0.00	-0.14	0.00	-0.24	0.00	-1.06
		rPLS	0.06	0.05	0.10	0.08	0.59	0.58	0.06	-0.18	0.01	-0.42	0.03	-0.71
		GA	0.08	0.04	0.19	0.11	0.69	0.68	0.28	-0.34	0.01	-0.63	0.11	-0.92
	SVR	Full	0.07	0.00	0.03	-0.02	0.01	-0.02	0.25	-0.43	0.09	-0.15	0.02	-0.59
		V-WSP	0.04	-0.02	0.01	-0.01	0.10	0.04	0.01	0.00	0.02	-0.17	0.00	-0.97
		L1-SVR	0.04	-0.03	0.04	-0.03	0.36	0.34	0.00	0.00	0.00	-0.15	0.03	-0.67
		GA	0.06	0.04	0.24	0.15	0.64	0.63	0.33	-0.26	0.06	-0.96	0.18	-0.81

Table C.8. List of descriptors from PLS model developed with GA for prediction of HIC retention times (LVs = 9). The descriptor names and types have been given as well as which domain and substructure the descriptors were generated from.

Index	Descriptor	Type	Domain	Substructure	Regression Coefficient
1	$G_C(F)$	Energy	V_H	FW1	0.0673
2	SIEP	TAE	V_H	FW1	-0.0892
3	W(F)	Energy	V_H	CDR1	-0.0867
4	$SASA_{non\text{-}polar}$	Topo	V_H	CDR1	0.0235
5	SIEPMax	TAE	V_H	CDR1	-0.0898
6	$G_C(F)$	Energy	V_H	FW2	0.1844
7	ΔG_s	Energy	V_H	FW2	0.1245
8	ln(FD)	Topo	V_H	FW2	0.0534
9	Del(K)IA	TAE	V_H	FW2	-0.1129
10	$G_c(F)$	Energy	V_H	CDR2	0.2312
11	VOLTAE	TAE	V_H	CDR2	0.0738
12	SIEPMax	TAE	V_H	CDR2	0.0272
13	VOLTAE	TAE	V_H	FW3	-0.0655
14	Del(G)NMax	TAE	V_H	FW3	-0.0755
15	$G_C(F)$	Energy	V_H	CDR3	0.1747
16	$G_W(F)$	Energy	V_H	CDR3	0.2325
17	ΔG_s	Energy	V_H	CDR3	-0.0820
18	ΔG_{el}	Energy	V_H	CDR3	0.1667
19	$SASA_{polar}$	Topo	V_H	CDR3	0.3130
20	S_{polar}	Topo	V_H	CDR3	0.0776
21	$S_{non\text{-}polar}$	Topo	V_H	CDR3	-0.1258
22	VOLTAE	TAE	V_H	CDR3	0.0730
23	SIEPMax	TAE	V_H	CDR3	-0.0948
24	$G_C(F)$	Energy	V_H	FW4	0.0297
25	$SASA_{polar}$	Topo	V_L	FW1	0.1018
26	$G_c(F)$	Energy	V_L	CDR1	0.1803
27	$SASA_{non\text{-}polar}$	Topo	V_L	CDR1	0.0818
28	$S_{non\text{-}polar}$	Topo	V_L	CDR1	0.0066
29	ln(FD)	Topo	V_L	CDR1	0.1763
30	Del(Rho)NMax	TAE	V_L	CDR1	-0.1068
31	ΔG_s	Energy	V_L	FW2	-0.1137
32	HBd	Energy	V_L	FW2	-0.1156
33	SIDel(K)N	TAE	V_L	FW2	-0.1292
34	ΔG_{Tors}	Energy	V_L	CDR2	0.2147
35	$SASA_{non\text{-}polar}$	Topo	V_L	CDR2	0.2519
36	$S_{non\text{-}polar}$	Topo	V_L	CDR2	0.1550
37	$G_c(F)$	Energy	V_L	FW3	0.1116

Index	Descriptor	Type	Domain	Substructure	Regression Coefficient
38	$G_c(F)$	Energy	V_L	FW4	0.2662
39	ΔG_W	Energy	V_L	FW4	0.0374
40	$G_C(F)$	Energy	C_H1	A-Strand	0.1552
41	$G_c(F)$	Energy	C_H1	B-Strand	-0.1913
42	SIEP	TAE	C_H1	B-Strand	0.0681
43	HBd	Energy	C_H1	D-Strand	0.0992
44	$SASA_{polar}$	Topo	C_H1	E-Strand	-0.2145
45	Del(K)Max	TAE	C_H1	E-Strand	-0.0814
46	ΔG_{LJ}	Energy	C_H1	G-Strand	-0.1064
47	Del(K)Max	TAE	C_H1	G-Strand	-0.1336
48	Del(K)Max	TAE	C_L	A-Strand	0.1670
49	W(F)	Energy	C_L	C-Strand	0.1686
50	ΔG_{Tors}	Energy	C_L	F-Strand	-0.2348
51	$G_C(F)$	Energy	C_L	G-Strand	0.0874

Appendix D

D.1 Eigenvectors and Eigenvalues

Eigenvectors are a special case of matrix multiplication where a transformation of these vectors only changes their magnitude where their original direction is retained. Eigenvectors can only be calculated for square matrices, but it should be noted that not all square matrices have them (Abdi, 2007). The definition of eigenvectors is presented in eq.(D.1).

$$\boldsymbol{A}\boldsymbol{v} = \lambda\boldsymbol{v}, \qquad \boldsymbol{v} \neq \boldsymbol{0} \tag{D.1}$$

Here, $\boldsymbol{A}$ is an arbitrary non-symmetric transformation matrix with M rows and M columns, $\boldsymbol{v}$ is the eigenvector and λ is the eigenvalue. Given the square form of the transformation matrix, $\boldsymbol{A}$, there will be m eigenvectors and eigenvalues. Eq.(D.1) can then be rewritten to include all eigenvectors and eigenvalues according to eq.(D.2) and is referred to as the eigen space of $\boldsymbol{A}$.

$$\boldsymbol{A}\boldsymbol{V} = \boldsymbol{V}\boldsymbol{\Lambda} \tag{D.2}$$

Where, $\boldsymbol{V} = [\boldsymbol{v}_1 \quad \dots \quad \boldsymbol{v}_M]$ is the eigenvector matrix and $\boldsymbol{\Lambda} = \text{diag}(\lambda_1, \dots, \lambda_M)$ is a diagonal matrix consisting of the eigenvalues. $\boldsymbol{V}$ is invertible if, and only if all eigenvectors are linearly independent, then the transformation matrix, $\boldsymbol{A}$ can be decomposed according to eq.(D.3) which is also called the eigen-decomposition of $\boldsymbol{A}$.

$$\boldsymbol{A} = \boldsymbol{V}\boldsymbol{\Lambda}\boldsymbol{V}^{-1} \tag{D.3}$$

However, for a special type of matrices often used in statistics called positive semi-definite, the eigen-decomposition will always exist. A matrix, $\boldsymbol{A}$, is positive semi-definite if obtained as the product of some matrix $\boldsymbol{X}$ and its transpose according to eq.(D.4).

$$\boldsymbol{A} = \boldsymbol{X}\boldsymbol{X}^T \text{ or } \boldsymbol{A} = \boldsymbol{X}^T\boldsymbol{X} \tag{D.4}$$

The positive semi-definite matrices are therefore always symmetric which results in all eigenvectors becoming orthonormal, meaning that pair-wise eigenvectors are orthogonal, eq.(D.5), and that the magnitude of each eigenvector is equal to one, eq.(D.6). The eigenvalues obtained from a positive semi-definite matrix will always be larger or equal to zero, eq.(D.7).

$$\boldsymbol{v}_k^T \boldsymbol{v}_l = 0 \text{ if } k \neq l, \qquad k, l = 1, \ldots, M \tag{D.5}$$

$$\|\boldsymbol{v}_k\| = \boldsymbol{v}_k^T \boldsymbol{v}_k = 1 \tag{D.6}$$

$$\lambda_k \geq 0 \tag{D.7}$$

The orthogonality of the eigenvectors implies that $\boldsymbol{V}^{-1} = \boldsymbol{V}^T$ and greatly simplifies the eigen-decomposition of $\boldsymbol{A}$ due to that the inverse does not need to be calculated. The expression in eq.(D.3) can be rewritten according to eq.(D.8). In statistics, common positive semi-definite matrices include the covariance, $\boldsymbol{\Sigma}$, matrix and the correlation matrix.

$$\boldsymbol{A} = \boldsymbol{V}\boldsymbol{\Lambda}\boldsymbol{V}^T \tag{D.8}$$

D.2 Singular Value Decomposition

The Singular Value Decomposition (SVD) is another common technique that is used for calculating the principal components in PCA where $\boldsymbol{X}$ is decomposed according to:

$$\boldsymbol{X}_{Cent} = \boldsymbol{USV}^T \tag{D.9}$$

where $\boldsymbol{U}$ (N x N) is unitary matrix, $\boldsymbol{S} = \text{diag}\left(s_1, s_2, \dots, s_{min(N,M)}\right)$ (N x M) is a diagonal matrix which will contain extra rows or columns of zeros if N > M or N < M, respectively. The matrix $\boldsymbol{V}$ is the eigenvector matrix and is equal to $\boldsymbol{V}$ in the eigen-decomposition in eq.(2.12) only when $\boldsymbol{X}$ has been mean centred prior to SVD decomposition (Wall et al., 2003). Through substitution of eq.(D.9) into eq.(2.11), the relationship between the eigenvalues and the and the singular values can be calculated to:

$$\boldsymbol{\Lambda} = \frac{\boldsymbol{\Sigma}^2}{N-1}, \qquad \lambda_k = \frac{s_k^2}{N-1}, \qquad k = 1, \dots, \min\,(\mathrm{N}, \mathrm{M}) \tag{D.10}$$

The PC loadings will be the eigenvector matrix as stated in eq.(2.13) which means that the PC scores are calculated as the product of $\boldsymbol{U}$ and $\boldsymbol{S}$ according to:

$$\boldsymbol{T} = \boldsymbol{US} \tag{D.11}$$

D.3 Lagrange Multipliers in SVC

Application of Lagrange multipliers is described here for the soft-margin SVC classifier covered in Section 2.3.2.2. In its essence the Lagrange multipliers reformulates the primal optimisation problem by adding the constraints to the maximisation or minimisation expression according to:

$$\begin{aligned}\mathcal{L}(\boldsymbol{\omega}, b, \boldsymbol{\xi}) &= \frac{1}{2}\|\boldsymbol{\omega}\|_2^2 + \mathrm{C}\sum_{i=1}^{N}\xi_i - \sum_{i=1}^{N}\alpha_i\big(y_i(\boldsymbol{\omega}^T\boldsymbol{x}_i + b) - (1-\xi_i)\big) \\ &= -\sum_{i=1}^{N}\beta_i\xi_i\end{aligned} \tag{D.12}$$

where the constraints for the class boundaries have been multiplied by α_i and the constraints for the slack variables have been multiplied by β_i. This is necessary in order to formulate the dual problem where optimisation is performed with regards to the samples instead of the variables. For the SVC algorithm to properly select the optimal solution, the Karush–Kuhn–Tucker (KKT) conditions must hold true (Kuhn and Tucker, 2014). This means that the resulting Lagrangian, $\mathcal{L}$, in expression in eq.(D.9) must be differentiable as presented in KKT condition 1. The initial constraints from the primal must also hold true in the solution and is represented as KKT condition 2. KKT condition 3 is called the complementary slackness condition and is necessary in order to have a strong duality, meaning that the solution of the dual is equal to that of the primal.

KKT condition 1

$$\frac{\partial\mathcal{L}(\boldsymbol{\omega}, b, \boldsymbol{\xi})}{\partial\boldsymbol{\omega}} = \boldsymbol{\omega} - \sum_{i=1}^{N}\alpha_i y_i \boldsymbol{x}_i = 0 \tag{D.13}$$

$$\frac{\partial\mathcal{L}(\boldsymbol{\omega}, b, \boldsymbol{\xi})}{\partial b} = -\sum_{i=1}^{N}\alpha_i y_i = 0 \tag{D.14}$$

$$\frac{\partial\mathcal{L}(\boldsymbol{\omega}, b, \boldsymbol{\xi})}{\partial\xi_i} = C - \alpha_i - \beta_i = 0 \tag{D.15}$$

KKT condition 2

$$y_i(\boldsymbol{\omega} \cdot \boldsymbol{x}_i + b) - 1 \geq 0 \tag{D.16}$$

$$\xi_i \geq 0 \tag{D.17}$$

KKT condition 3

$$\alpha_i(y_i(\boldsymbol{\omega}^T \boldsymbol{x}_i + b) - (1 - \xi_i)) = 0 \tag{D.18}$$

$$\beta_i \xi_i = 0 \tag{D.19}$$

Through substitution with eq.(D.13) into eq.(D.12), the expression can be rewritten into the form of the Wolf dual according to:

$$\begin{aligned} \underset{\boldsymbol{\alpha}}{\text{maximise}} &= W(\boldsymbol{\alpha}) = \sum_{i=1}^{N} \alpha_i - \frac{1}{2} \sum_{i,j=1}^{N} \alpha_i \alpha_j y_i y_j \boldsymbol{x}_i \cdot \boldsymbol{x}_j \\ \text{subject to} &= 0 \leq \alpha_i \leq C \\ &= \sum_{i=1}^{n} \alpha_i y_i = 0 \end{aligned} \tag{D.20}$$

The resulting constraints in eq.(D.17) are formulated based on eq.(D.13) and eq.(D.14) in KKT condition 2 as well as eq.(D.15) and eq.(D.16) in KKT condition 3. An example of the potential solutions for the Wolf dual is illustrated in Figure D.1 which is only dependent on the values α_i. For more details on Lagrange multiplier in SVC, refer to the work of Hastie et al. (2009b).

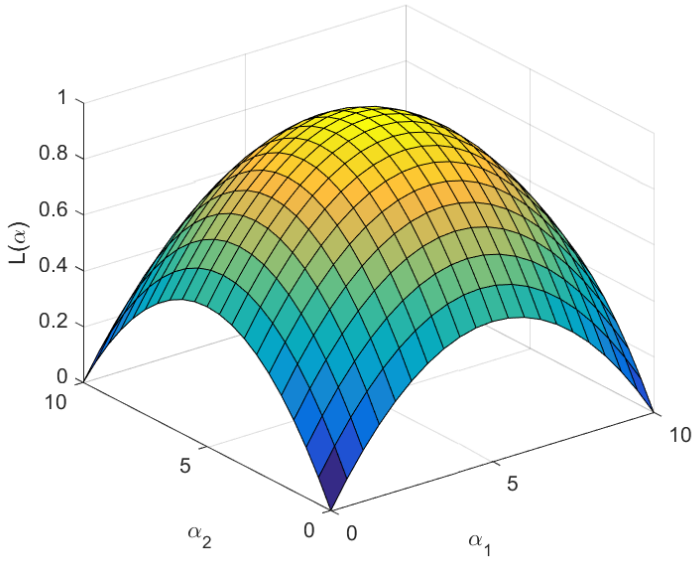

Figure D.1. Example of optimisation solutions for the Lagrange dual which is only dependent on the values of α_i as well as the samples in the data set.